.

NASA Program: Causes and Consequences of the Minimum of Solar Cycle 23/24 (CCMSC)

NASA Contract Number: NNH10CC96C

Contract Title: Using Global MHD Simulations and Comparisons with Solar and in situ Observations to Understand the Origins and Properties of the Minimum of Solar Cycle 24

Principal Investigator: Pete Riley, Predictive Science Inc., San Diego

FINAL REPORT

Covering the period AUGUST 9, 2010 - AUGUST 8, 2013

1. Overview

This report summarizes the technical progress made during all three years of the contract "Using Global MHD Simulations and Comparisons with Solar and in situ Observations to Understand the Origins and Properties of the Minimum of Solar Cycle 24," (Contract NNH10CC96C) between NASA and Predictive Science, and covers the period from AUGUST 9, 2010 to AUGUST 8, 2013. Under this contract, Predictive Science Inc. (PSI) has conducted numerical and data analysis related to issues concerning origins and properties of the minimum of solar cycle 24. The results of our studies were presented at over a dozen scientific meetings, and have resulted in more than 16 first-authored peer-reviewed publications with at least as many co-authored publications. In the sections that follow, we summarize the main components of this work, the meetings at which this work was presented, and, in the appendices, provide copies of the publications that resulted from this work.

2. Summary of Work

2.1. Global MHD Modeling of the Solar Corona and Inner Heliosphere for the Whole Heliosphere Interval

With the goal of understanding the three-dimensional structure of the solar corona and inner heliosphere during the Whole Heliosphere Interval (WHI), we developed a global MHD solution for Carrington rotation (CR) 2068. Our model, which includes energy transport processes, such as coronal heating, conduction of heat parallel to the magnetic field, radiative losses, and the effects of Alfvn waves, is capable of producing significantly better estimates of the plasma temperature and density in the corona than have been possible in the past. With such a model, we can compute emission in extreme ultraviolet (EUV) and X-ray wavelengths, as well as scattering in polarized white light. Additionally, from our heliospheric solutions, we can deduce magnetic field and plasma parameters along specific spacecraft trajectories. We made detailed comparisons of both remote solar and in situ observations with the model results, allowing us to: (1) Connect these disparate sets of observations; (2) Infer the global structure of the inner heliosphere; and (3) Provide support for (or against) assumptions in the MHD model, such as the empirically-based coronal heating profiles.

This work is described in more detail by Riley et al. (2010a) and provided in Appendix A.

2.2. The Three-Dimensional Structure of the Inner Heliosphere

We reviewed our current knowledge regarding the three-dimensional structure of the quasi-steady, large-scale inner heliosphere. This understanding is based on the interpretation of a wide array of remote and in situ measurements, in conjunction with sophisticated numerical models. Observations by the Ulysses spacecraft, in particular, have provided an unprecedented set of measurements for more than 18 years, and observations by the STEREO spacecraft promise no less. Global MHD models of the solar corona and heliosphere have matured to the point that a wide range of measurements can now be reproduced with reasonable fidelity. In the absence of transient effects, this structure is dominated by corotating interaction regions which can be understood-to a large extent-from the consequence of solar rotation on a spatially-variable velocity profile near the Sun, leading to parcels of plasma with different plasma and magnetic properties becoming radially aligned. This interaction is one of the principal dynamic processes that shape the structure of the interplanetary medium. To illustrate some of these phenomena, we discussed the structural features of the current solar minimum, which has, thus far, displayed a number of distinct characteristics in relation to recent previous minima of the space age.

This work is described in more detail by Riley (2010) and provided in Appendix B.

2.3. On the relationship between coronal heating, magnetic flux, and the density of the solar wind

The stark differences between the current solar minimum and the previous one offered a unique opportunity to develop new constraints on mechanisms for heating and acceleration of the solar wind. We used a combination of numerical simulations and analysis of remote solar and in situ observations to infer that the coronal heating rate, H, scales with the average magnetic field strength within a coronal hole, Bch. This was accomplished in three steps. First, we analyzed Ulysses measurements made during its first and third orbit southern and northern polar passes (i.e., during near-solar minimum conditions) to deduce a linear relationship between proton number density (np) and radial magnetic field strength (Br) in the high-speed quiescent solar wind, consistent with the results of McComas et al. (2008) and Ebert et al. (2009). Second, we used Wilcox Solar Observatory measurements of the photospheric magnetic field to show that the magnetic field strength within coronal holes (Bch) is approximately correlated with the strength of the interplanetary field at the location of Ulysses. Third, we used hydrodynamic simulations to show that np in the solar wind scales linearly with H. Taken together, these results imply the chain: $H \propto np \propto Br \propto Bch$. We also explored ideas that the correlation between np and Br could have resulted from interplanetary

processes, or from the superradial expansion of the coronal magnetic field close to the Sun, but find that neither possibility can produce the observed relationship. The derived heating relationship is consistent with (1) empirical heating laws derived for closed-field line regions and (2) theoretical models aimed at understanding both the heating and acceleration of the solar wind.

This work is described in more detail by Riley et al. (2010c) and provided in Appendix C.

2.4. Interpretation of the cross-correlation function of ACE and STEREO solar wind velocities using a global MHD Model

Measurements from the ACE and STEREO A and B spacecraft are allowing an unprecedented view of the structure of the three-dimensional heliosphere. One aspect of this is the degree to which the measurements at one spacecraft correlate with those at the other. We have computed the cross-correlation functions (CCFs) for all three combinations of ACE and STEREO A and B in situ observations of the bulk solar wind velocity as the spacecraft moved progressively farther away from one another. Our results confirm previous studies that the phase lag between the signals becomes linearly larger with time. However, we have identified two intervals where this appears to break down. During these "lulls," the CCF reveals a phase lag considerably less than that which would be predicted based only on the angular separation of the spacecraft. We modeled the entire STEREO time period using a global MHD model to investigate the cause for these "lulls." We find that a combination of time-dependent evolution of the streams as well as spatial inhomogeneities, due to the latitudinal separation of the spacecraft, are sufficient to explain them.

This work is described in more detail by Riley et al. (2010b) and provided in Appendix D.

2.5. Mapping Solar Wind Streams from the Sun to 1 AU: A Comparison of Techniques

A variety of techniques exist for mapping solar wind plasma and magnetic field measurements from one location to another in the heliosphere. Such methods are either applied to extrapolate solar data or coronal model results from near the Sun to 1 AU (or elsewhere), or to map in-situ observations back to the Sun. In this study, we estimated the sensitivity of four models for evolving solar wind streams from the Sun to 1 AU. In order of increas-

ing complexity, these are: i) ballistic extrapolation; ii) ad hoc kinematic mapping; iii) 1-D upwinding propagation; and iv) global heliospheric MHD modeling. We also consider the effects of the interplanetary magnetic field on the evolution of the stream structure. The upwinding technique is a new, simplified method that bridges the extremes of ballistic extrapolation and global heliospheric MHD modeling. It can match the dynamical evolution captured by global models, but is almost as simple to implement and as fast to run as the ballistic approximation.

This work is described in more detail by Riley & Lionello (2011) and provided in Appendix E.

2.6. Global MHD modeling of the solar corona and inner heliosphere for the whole heliosphere interval

In an effort to understand the three-dimensional structure of the solar corona and inner heliosphere during the Whole Heliosphere Interval (WHI), we have developed a global magnetohydrodynamics (MHD) solution for Carrington rotation (CR) 2068. Our model, which includes energy-transport processes, such as coronal heating, conduction of heat parallel to the magnetic field, radiative losses, and the effects of Alfvn waves, is capable of producing significantly better estimates of the plasma temperature and density in the corona than have been possible in the past. With such a model, we can compute emission in extreme ultraviolet (EUV) and X-ray wavelengths, as well as scattering in polarized white light. Additionally, from our heliospheric solutions, we can deduce magnetic-field and plasma parameters along specific spacecraft trajectories. In this paper, we present a general analysis of the large-scale structure of the solar corona and inner heliosphere during WHI, focusing, in particular, on i) helmet-streamer structure; ii) the location of the heliospheric current sheet; and iii) the geometry of corotating interaction regions. We also compare model results with i) EUV observations from the EIT instrument onboard SOHO; and ii) in-situ measurements made by the STEREO-A and B spacecraft. Finally, we contrast the global structure of the corona and inner heliosphere during WHI with its structure during the Whole Sun Month (WSM) interval. Overall, our model reproduces the essential features of the observations; however, many discrepancies are present. We discuss several likely causes for them and suggest how model predictions may be improved in the future.

This work is described in more detail by Riley et al. (2012a) and provided in Appendix F.

2.7. Global MHD modeling of the solar corona and inner heliosphere for the whole heliosphere interval

In an effort to understand the three-dimensional structure of the solar corona and inner heliosphere during the Whole Heliosphere Interval (WHI), we have developed a global magnetohydrodynamics (MHD) solution for Carrington rotation (CR) 2068. Our model, which includes energy-transport processes, such as coronal heating, conduction of heat parallel to the magnetic field, radiative losses, and the effects of Alfvn waves, is capable of producing significantly better estimates of the plasma temperature and density in the corona than have been possible in the past. With such a model, we can compute emission in extreme ultraviolet (EUV) and X-ray wavelengths, as well as scattering in polarized white light. Additionally, from our heliospheric solutions, we can deduce magnetic-field and plasma parameters along specific spacecraft trajectories. In this paper, we present a general analysis of the large-scale structure of the solar corona and inner heliosphere during WHI, focusing, in particular, on i) helmet-streamer structure; ii) the location of the heliospheric current sheet; and iii) the geometry of corotating interaction regions. We also compare model results with i) EUV observations from the EIT instrument onboard SOHO; and ii) in-situ measurements made by the STEREO-A and B spacecraft. Finally, we contrast the global structure of the corona and inner heliosphere during WHI with its structure during the Whole Sun Month (WSM) interval. Overall, our model reproduces the essential features of the observations; however, many discrepancies are present. We discuss several likely causes for them and suggest how model predictions may be improved in the future.

This work is described in more detail by Riley et al. (2012a) and provided in Appendix F.

2.8. Modeling the global structure of the heliosphere during the recent solar minimum: Model improvements and unipolar streamer

The recent solar minimum, marking the end of solar cycle 23, has been unique in a number of ways. In particular, the polar photospheric flux was substantially weaker, coronal holes were notably smaller, and unipolar streamers were considerably more prevalent than previous minima. To understand the origins of some of these phenomena, we have computed global solutions using a three-dimensional, time-dependent MHD model of the solar corona and heliosphere. In this report, we present a brief overview of a selection of model results, illustrating: (1) how observations are being used to better constrain model properties; and (2) how the model results can be applied to understanding complex coronal and interplanetary phenomena, and, specifically, unipolar streamers.

This work is described in more detail by Riley et al. (2012b) and provided in Appendix G.

2.9. Interpreting some properties of CIRs and their associated shocks during the last two solar minima using global MHD simulations

In this part of the study, we investigated some properties of corotating interaction regions (CIRs) during the recent solar minimum (December 2008), and compared them to CIRs observed during the previous minimum (September 1996). In particular, we focused on the orientation of stream interfaces (SIs), which separate wind that was originally slow and dense from wind that was originally fast and tenuous. We found that while the east-west flow deflections imply a systematic tilt of CIRs such that they are aligned with the nominal Parker spiral direction, the north-south flow deflections are much more irregular and show no discernible patterns. Comparison with global MHD model results suggested that this is a consequence of the spacecraft intercepting the equatorward flanks of the CIRs. We also studied the solar-cycle variations of CIR-associated shocks over the last cycle, finding that forward (F) shocks tended to occur approximately three times more frequently than reverse (R) shocks, and, moreover, during the recent minimum, there were approximately 3-4 times more R shocks than during the previous minimum. We showed that this too is likely due to the orientation of CIRs and Earth's limited vantage point in the ecliptic plane.

This work is described in more detail by Riley et al. (2012a) and provided in Appendix H.

2.10. Corotating interaction regions during the recent solar minimum: The power and limitations of global MHD modeling

The declining phase of solar activity cycle 23 has provided an unprecedented opportunity to study the evolution and properties of corotating interaction regions (CIRs) during unique and relatively steady conditions. The absence of significant transient activity has allowed modelers to test ambient solar wind models, but has also challenged them to reproduce structure that was qualitatively different than had been observed previously (at least within the space era). In this part of our investigation, we analyzed global magnetohydrodynamic (MHD) solutions of the inner heliosphere (from 1RS to 1 AU) for several intervals defined as part of a Center for Integrated Space weather Modeling (CISM) interdisciplinary campaign study, and, in particular, Carrington rotation 2060. We compared in situ measurements from

ACE and STEREO A and B with the model results to illustrate both the capabilities and limitations of current numerical techniques. We showed that, overall, the models do capture the essential structural features of the solar wind for specific time periods; however, there are times when the models and observations diverge. We described, and, to some extent assessed the sources of error in the modeling chain from the input photospheric magnetograms to the numerical schemes used to propagate structure through the heliosphere, and speculated on how they may be resolved, or at least mitigated in the future.

This work is described in more detail by Riley et al. (2012b) and provided in Appendix I.

2.11. Interplanetary Signatures of Unipolar Streamers and the Origin of the Slow Solar Wind

Unipolar streamers (also known as pseudo-streamers) are coronal structures that, at least in coronagraph images, and when viewed at the correct orientation, are often indistinguishable from dipolar (or "standard") streamers. When interpreted with the aid of a coronal magnetic field model, however, they are shown to consist of a pair of loop arcades. Whereas dipolar streamers separate coronal holes of the opposite polarity and whose cusp is the origin of the heliospheric current sheet, unipolar streamers separate coronal holes of the same polarity and are therefore not associated with a current sheet. In this portion of our study, we investigated the interplanetary signatures of unipolar streamers. Using a global MHD model of the solar corona driven by the observed photospheric magnetic field for Carrington rotation 2060, we mapped the ACE trajectory back to the Sun. The results suggested that ACE fortuitously traversed through a large and well-defined unipolar streamer. We also compared heliospheric model results at 1 AU with ACE in-situ measurements for Carrington rotation 2060. The results strongly suggested that the solar wind associated with unipolar streamers is slow. We also compared predictions using the original Wang-Sheeley (WS) empirically determined inverse relationship between solar wind speed and expansion factor. Because of the very low expansion factors associated with unipolar streamers, the WS model predicts high speeds, in disagreement with the observations. We discussed the implications of these results in terms of theories for the origin of the slow solar wind. Specifically, premises relying on the expansion factor of coronal flux tubes to modulate the properties of the plasma (and speed, in particular) must address the issue that while the coronal expansion factors are significantly different at dipolar and unipolar streamers, the properties of the measured solar wind are, at least qualitatively, very similar.

This work is described in more detail by Riley & Luhmann (2012) and provided in

Appendix J.

2.12. Ensemble Modeling of the Ambient Solar Wind

Ensemble modeling is a method of prediction based on the use of a representative sample of possible future states. Global models of the solar corona and inner heliosphere are now maturing to the point of becoming predictive tools, thus, it is both meaningful and necessary to quantitatively assess their uncertainty and limitations. In this study, we apply simple ensemble modeling techniques in a first step towards these goals. We focus on one relatively quiescent time period, Carrington rotation 2062, which occurred during the late declining phase of solar cycle 23 and assess the sensitivity of the model results to variations in boundary conditions, models, and free parameter values. We present variance maps, "whisker" plots, and Taylor diagrams to estimate the accuracy of the solutions, which demonstrate that the ensemble mean solution outperforms any of the individual realizations. Our results provide a baseline against which future model improvements can be compared.

This work is described in more detail by Riley et al. (2012) and provided in Appendix K.

2.13. Ensemble Modeling of the Ambient Solar Wind

In this study, we further applied simple ensemble modeling techniques to solar wind models. We focused on two relatively quiescent time periods, Carrington rotation 2058 and 2062, which occurred during the late declining phase of solar cycle 23. To illustrate and assess the sensitivity of the model results to variations in boundary conditions, we computed solutions using synoptic magnetograms from seven solar observatories. Model sensitivity was explored using: (1) different combinations of models; (2) perturbations in the base coronal temperature, a free parameter in one of the model approximations; and (3) the spatial resolution of the numerical grid. We constructed variance maps, "whisker" plots, and Taylor diagrams to summarize the accuracy of the solutions and computed skill scores, which demonstrated that the ensemble mean solution outperforms any of the individual realizations. Our results provide a baseline against which future model improvements can be compared.

This work is described in more detail by Riley et al. (2013) and provided in Appendix L.

2.14. A Multi-Observatory Inter-Comparison of Line-of-Sight Synoptic Solar Magnetograms

The observed photospheric magnetic field is a crucial parameter for understanding a range of fundamental solar and heliospheric phenomena. Synoptic maps, in particular, which are derived from the observed line-of-sight photospheric magnetic field and built up over a period of 27 days, are the main driver for global numerical models of the solar corona and inner heliosphere. Yet, in spite of 60 years of measurements, quantitative estimates remain elusive. In this study, we compare maps from seven solar observatories (Stanford/WSO, NSO/KPVT, NSO/SOLIS, NSO/GONG, SOHO/MDI, UCLA/MWO, and SDO /HMI) to identify consistencies and differences among them. We find that while there is a general qualitative consensus, there are also some significant differences. We compute conversion factors that relate measurements made by one observatory to another using both synoptic map pixel-by-pixel and histogram-equating techniques, and we also estimate the correlation between datasets. For example, Wilcox Solar Observatory (WSO) synoptic maps must be multiplied by a factor of 3??4 to match Mount Wilson Observatory (MWO) estimates. Additionally, we find no evidence that the MWO saturation correction factor should be applied to WSO data, as has been done in previous studies. Finally, we explore the relationship between these datasets over more than a solar cycle, demonstrating that, with a few notable exceptions, the conversion factors remain relatively constant. While our study was able to quantitatively describe the relationship between the datasets, it did not uncover any obvious ground truth. We offer several suggestions for how this may be addressed in the future.

This work is described in more detail by Riley et al. (2013) and provided in Appendix M.

2.15. The Structure of the Solar Corona and Inner Heliosphere during the Maunder Minimum

The period known as the "Maunder Minimum" (1645-1715) has been the source of considerable scientific research and debate, particularly with regard to the potential causal relationship between the Sun and Earth's climate. However, the structure and properties of the Sun's extended corona have remained elusive. By assembling, and interpreting a comprehensive set of observations associated with this interval and simulating a suite of plausible model reconstructions, we have been able to determine the most likely state of the corona. We found that the Maunder Minimum corona was substantially different from anything we have observed in modern times, and these differences are sufficiently large that they may have had a noticeable effect on Earths climate. If, has been suggested, we are

currently entering another period of solar inactivity, these results may provide a basis for predicting the long-term behavior of the Sun.

This work is currently being reviewed by co-authors and will be submitted to Astrophysical Journal. A pre-print is provided in Appendix N.

2.16. Presentations and Publications

The work performed as part of this investigation were presented at more than a dozen conferences and workshops over the 36-month duration of the contract. These included:

1. 10th Annual ICNS Huntsville Workshop. Pete Riley presented modeling and data analysis of the cycle 23-23 solar minimumm (March, 2011).

2. CCMSC24 Workshop. Pete Riley summarized the main results from this investigation (May, 2011).

3. IUGG Meeting. Pete Riley gave an invited talk summarizing much of the work performed under this contract (August, 2011).

4. Space Weather Workshop, Boulder, Colorado. Pete Riley gave an invited talk on modeling the corona during the recent minimum and transitioning scientific models to operational tools (April, 2012).

5. Seminar at the Universidad National Autonoma de Mexico at Morelia, Mexico. Pete Riley summarized our group's CIR modeling effort, particularly during the recent solar minimum (August, 2011).

6. Space Weather Workshop. Pete Riley presented large-scale modeling results for the recent, unusual solar minimum (April, 2012).

7. ISSI workshop, Berne, Switzerland. Pete Riley gave a talk on the structure of the solar corona during the recent solar minimum and the implications for other periods of low solar activity over the last 400 years (May, 2012).

8. Solar Wind 13 Conference, Hawaii. Pete Riley gave a talk on ensemble modeling of the ambient solar wind (June, 2012)

9. SHINE workshop, Hawaii. Pete Riley gave a talk on large-scale modeling and validation of periods during the recent solar minimum (June, 2012)

10. Hinode Workshop, Scotland. Pete Riley gave a talk on the structure of the solar corona and inner heliosphere during the Maunder Minimum (August, 2012)

11. Fall AGU Meeting. Pete Riley presented results from an analysis of MHD solutions mimicking the structure of the corona during the Maunder Minimum (December, 2012).

12. Chapman Conference on the unusual 23-24 solar cycle. Pete Riley gave a talk on the likely structure of the heliosphere during the Maunder Minimum (March, 2013).

13. ISSI Workshop, Bern, Switzerland. Pete Riley gave several talks on the likely structure of the solar corona during the Maunder Minimum (April, 2013).

The work performed under this contract resulted in 16 first-authored publications, together with at least as many more co-authored publications. Additionally, a number of other studies and resulting papers benefitted from the work performed under this contract. The main papers are listed in the reference section and reproduced in Appendices A through O.

REFERENCES

Riley, P. 2010, in Twelfth International Solar Wind Conference, Am. Inst. Phys. Conf. Proc., ed. M. Maksimovic, K. Issautier, N. Meyer-Vernet, M. Moncuquet, & F. Pantellini, Vol. 1216, 323

Riley, P., Ben-Nun, M., Linker, J., Mikic, Z., Svalgaard, L., Harvey, J., Bertello, L., Hoeksema, T., Liu, Y., & Ulrich, R. 2013, Solar Physics, 1

Riley, P., Linker, J. A., Americo Gonzalez Esparza, J., Jian, L. K., Russell, C. T., & Luhmann, J. G. 2012a, J. of Atmos. and Solar-Terr. Phys., 83, 11

Riley, P., Linker, J. A., Lionello, R., & Mikic, Z. 2012b, J. Atmos. Solar-Terr. Phys., 83, 1

Riley, P., Linker, J. A., & Mikic, Z. 2010a, Highlights of Astronomy, 15, 491

Riley, P., Linker, J. A., & Mikic, Z. 2012, in Solar Wind 13, ed. G. P. Zank (AIP)

Riley, P., Linker, J. A., & Mikić, Z. 2013, Journal of Geophysical Research (Space Physics), 118, 600

Riley, P., & Lionello, R. 2011, Solar Phys., 270, 575

Riley, P., Lionello, R., Linker, J. A., Mikic, Z., Luhmann, J., & Wijaya, J. 2012a, Solar Phys., 274

Riley, P., Luhmann, J., Opitz, A., Linker, J. A., & Mikic, Z. 2010b, J. Geophys. Res. (Space Physics), 115, 11104

Riley, P., & Luhmann, J. G. 2012, Solar Phys., 277, 355

Riley, P., Mikic, Z., Lionello, R., Linker, J. A., Schwadron, N. A., & McComas, D. J. 2010c, J. Geophys. Res., 115, 6104

Riley, P., Stevens, M., Linker, J. A., Lionello, R., Mikic, Z., & Luhmann, J. G. 2012b, in American Institute of Physics Conference Series, Vol. 1436, American Institute of Physics Conference Series, ed. J. Heerikhuisen, G. Li, N. Pogorelov, & G. Zank, 337–343

Appendix A

Global MHD Modeling of the Solar Corona and Inner Heliosphere for the Whole Heliosphere Interval

Riley, P. and Linker, J. A. and Mikic, Z.

Published in Highlights of Astronomy, 2010.

Highlights of Astronomy, Volume 15
XXVIIth IAU General Assembly, August 2009
Ian F. Corbett, ed.

doi:10.1017/S1743921310010367

Global MHD Modeling of the Solar Corona and Inner Heliosphere for the Whole Heliosphere Interval

Pete Riley, Jon A. Linker and Zoran Mikic

Predictive Science, Inc.
9990 Mesa Rim Road, Suite 170, San Diego, CA 92121, USA.

Abstract. With the goal of understanding the three-dimensional structure of the solar corona and inner heliosphere during the "Whole Heliosphere Interval" (WHI), we have developed a global MHD solution for Carrington rotation (CR) 2068. Our model, which includes energy transport processes, such as coronal heating, conduction of heat parallel to the magnetic field, radiative losses, and the effects of Alfvén waves, is capable of producing significantly better estimates of the plasma temperature and density in the corona than have been possible in the past. With such a model, we can compute emission in extreme ultraviolet (EUV) and X-ray wavelengths, as well as scattering in polarized white light. Additionally, from our heliospheric solutions, we can deduce magnetic field and plasma parameters along specific spacecraft trajectories. We have made detailed comparisons of both remote solar and *in situ* observations with the model results, allowing us to: (1) Connect these disparate sets of observations; (2) Infer the global structure of the inner heliosphere; and (3) Provide support for (or against) assumptions in the MHD model, such as the empirically-based coronal heating profiles.

Keywords. Sun: corona, Sun: evolution, Sun: magnetic fields, Sun: solar wind, interplanetary medium

1. Introduction

Whole Heliosphere Interval (WHI), which ran from March 20 through April 16, 2008, and coincided with Carrington Rotation (CR) 2068, is providing a unique opportunity for both observers and modelers to collaborate in an effort to understand the three-dimensional structure and evolution of the solar corona and inner heliosphere. It builds on the previous Whole Sun Month (WSM) interval, which proved to be exceptionally successful. WHI occurred on the way to the current solar minimum, which has, thus far, been unique in a number of ways. For example, the polar photospheric flux is lower than the previous minimum by $\sim$40% (Svalgaard and Cliver 2007) and the coronal holes are noticeably smaller Kirk *et al.* (2009). Measurements by *in situ* spacecraft show substantial differences between the current minimum and the previous three. As of late 2008, Ulysses polar observations, in particular, suggested that: (1) The interplanetary magnetic field (IMF) was $\sim$36% lower than the previous minimum Smith and Balogh (2008); (2) The scaled number density was $\sim$17% lower McComas *et al.* (2008); and (3) The scaled temperature was $\sim$14% lower McComas *et al.* (2008). It was also determined that the bulk solar wind speed was $\sim$3% lower, although this may not represent a statistically significant change. The profiles of high-speed streams upstream of Earth also seem to be unique, being stronger, longer in duration, and more recurrent than the previous minimum Gibson *et al.* (2009).

To understand the three-dimensional structure during the WHI, and, more generally, the unique features of the current solar minimum, we have undertaken a detailed

Pete Riley , Jon A. Linker & Zoran Mikic

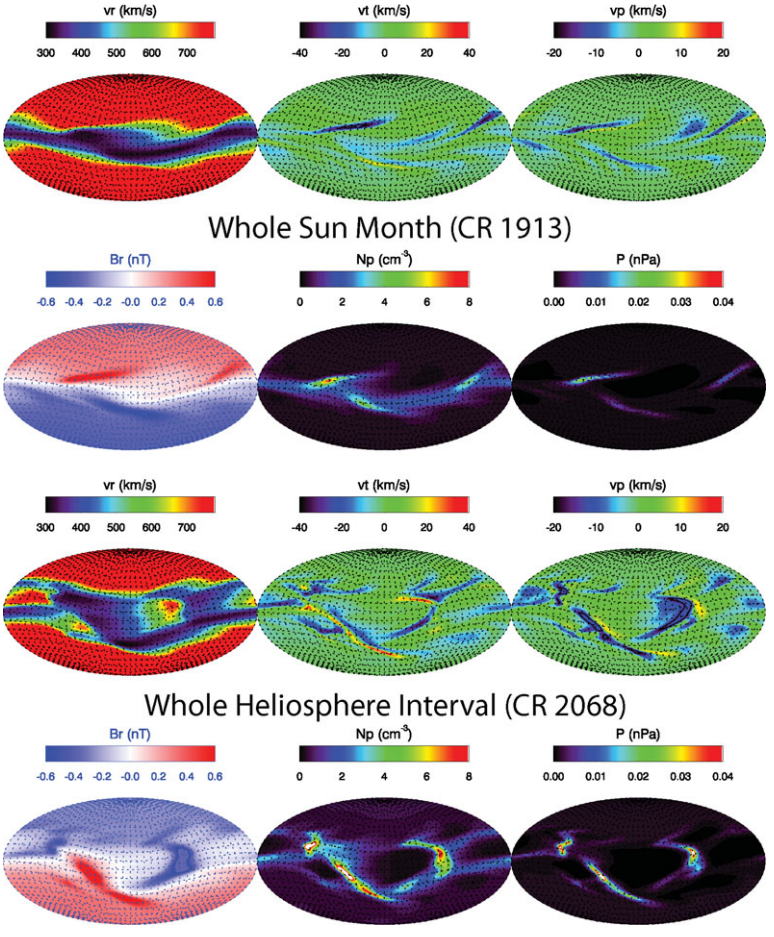

Figure 1. Mollweide projection maps of radial speed (v_r), meridional speed (v_r), azimuthal speed (v_p), radial magnetic field (B_r), number density (N_p), and thermal pressure (P) for Carrington rotation 1913 (top), corresponding to the Whole Sun Month (WSM) interval, and 2068 (bottom), corresponding to the Whole Heliosphere Interval (WHI).

investigation involving magnetohydrodynamic (MHD) modeling of the global structure of the corona and inner heliosphere, analysis of remote solar and *in situ* measurements, and interpretation and connection of the data using the simulation results. Our model results allow us to explore the physical connections between the various phenomena and synthesize these diverse observations into a coherent picture. In this brief report, we highlight one specific aspect of this study: A comparison of the large-scale three-dimensional structure of the inner heliosphere during WHI and WSM.

2. Modeling the Large-Scale Structure of the Heliosphere during WSM and WHI

MHD models have proven highly successful in interpreting and understanding a wide array of solar and heliospheric phenomena. They provide a global context for connecting diverse datasets and understanding the physical interrelationship between often dissimilar phenomena Riley *et al.* (1996, 2001a,b, 2002, 2003); Riley (2007). Our group has studied

the properties of the ambient solar wind for a number of years, and found that, in general, our model can reproduce the essential large-scale features of the solar wind. While these past comparisons demonstrate the success of the MHD model, the simplified polytropic approximation used has limitations. In the current study, we have developed coupled global thermodynamic MHD simulations driven by observed photospheric magnetic fields to study the large-scale, quasi-stationary properties of the WHI and understand the differences between the current solar minimum and the previous one, as characterized by the Whole Sun Month (WSM) interval (August/September, 1996).

In Figure 1, we show the three components of speed, together with the radial magnetic field strength, number density, and thermal pressure for WSM and WHI. The differences are quite remarkable. First, the "band of solar wind variability," that is, the region of typically slower, but more variable solar wind, and roughly centered about the helio-equator, extends to significantly higher latitudes during WHI. Second, the polar speeds are essentially the same for the two minima (confirmed by Ulysses observations). Third, a significant source of fast solar wind in the ecliptic plane derives from equatorial coronal holes during WHI. Fourth, the structure of CIRs is more complex during WHI: The systematic, opposed tilts observed during the declining phase of solar cycle 22 Gosling *et al.* (1995); Riley *et al.* (1996, 2001a,b) are not nearly as well defined during WHI; the equatorial coronal holes producing more localised "U" shaped interaction regions Riley *et al.* (2003).

3. Closing Remarks

In this brief report, we have summarized one aspect of our modeling effort to support the goals of the WHI Campaign. Model results will be contributed to the WHI repository (http://ihy2007.org/WHI/obs_models.shtml) and will be made available through Predictive Science's website (http://www.predsci.com).

References

Kirk, M. S., W. D. Pesnell, C. A. Young, & S. A. Hess Webber, *ArXiv e-prints* (2009), 0901.1158.

Gibson, S. E., J. U. Kozyra, G. d. Toma, B. A. Emery, T. Onsager, & B. J. Thompson, *Geophys. Res. Lett.* **114**, A09105 (2009).

Gosling, J. T., S. J. Bame, D. J. McComas, J. L. Phillips, V. J. Pizzo, B. E. Goldstein, & M. Neugebauer, *SSR* **72**, 99 (1995).

McComas, D. J., R. W. Ebert, H. A. Elliott, B. E. Goldstein, J. T. Gosling, N. A. Schwadron, & R. M. Skoug, *Geophys. Res. Lett.* **35**, 18103–+ (2008).

Riley, P., J. T. Gosling, L. A. Weiss, & V. J. Pizzo, *J. Geophys. Res.* **101**, 24349 (1996).

Riley, P., J. A. Linker, & Z. Mikić, *J. Geophys. Res.* **106**, 15889 (2001a).

Riley, P., J. A. Linker, Z. Mikić, & R. Lionello, "MHD Modeling of the Solar Corona and Inner Heliosphere: Comparison with Observations," in *Space Weather, Geophysical Monograph Series*, edited by P. Song, H. J. Singer, and G. L. Siscoe, AGU, Washington, DC, 2001b, vol. 125, p. 159.

Riley, P., J. A. Linker, & Z. Mikić, *J. Geophys. Res.* **107**, DOI 10.1029/2001JA000299 (2002).

Riley, P., Z. Mikić, & J. A. Linker, *Ann. Geophys.* **21**, 1347 (2003).

Riley, P., J. A. Linker, Z. Mikić, D. Odstrcil, T. H. Zurbuchen, D. Lario, & R. P. Lepping, *J. Geophys. Res.* **108**, 2 (2003).

Riley, P. *Journal of Atmospheric and Terrestrial Physics* **69**, 32–42 (2007).

Smith, E. J. & A. Balogh, *Geophys. Res. Lett.* **35**, 22103–+ (2008).

Svalgaard, L. & E. W. Cliver, *Ap. J. Lett.* **661**, L203–L206 (2007).

Appendix B

The three-dimensional structure of the inner heliosphere

Riley, P.

Published in Twelfth International Solar Wind Conference, 2010.

The Three-Dimensional Structure of the Inner Heliosphere

Pete Riley

Predictive Science, San Diego, California.

Abstract. In this review we summarize our current knowledge regarding the three-dimensional structure of the quasi-steady, large-scale inner heliosphere. This understanding is based on the interpretation of a wide array of remote and *in situ* measurements, in conjunction with sophisticated numerical models. Observations by the Ulysses spacecraft, in particular, have provided an unprecedented set of measurements for more than 18 years, and observations by the STEREO spacecraft promise no less. Global MHD models of the solar corona and heliosphere have matured to the point that a wide range of measurements can now be reproduced with reasonable fidelity. In the absence of transient effects, this structure is dominated by corotating interaction regions which can be understood - to a large extent - from the consequence of solar rotation on a spatially-variable velocity profile near the Sun, leading to parcels of plasma with different plasma and magnetic properties becoming radially aligned. This interaction is one of the principal dynamic processes that shape the structure of the interplanetary medium. To illustrate some of these phenomena, we discuss the structural features of the current solar minimum, which has, thus far, displayed a number of distinct characteristics in relation to recent previous minima of the space age.

Keywords: Structure of the Heliosphere; Corotating Interaction Regions; Stream Interface; Heliospheric Current Sheet
PACS: 96.50.Qx, 96.60.P-, 96.60.pf, 96.60.Q-, 96.60.Vg, 96.50.sh, 96.50.Ci, 96.50.Bh

INTRODUCTION

The aim of this review is to describe our current understanding of the three-dimensional, large-scale, quasi-steady structure of the inner heliosphere. Given the limited space, we must necessarily be selective. In particular, there are a number of topics related to heliospheric structure that we cannot cover: the origin of solar wind streams [1]; energetic particles at CIRs [2]; stream interactions in the outer heliosphere [3]; and the geomagnetic consequences of CIRs [4]. Instead, we focus on the main features of heliospheric structure, including the stream interface (SI), compression and rarefaction regions, the associated forward (F) and reverse (R) shocks, and the heliospheric current sheet (HCS). We consider how they form and evolve at various phases of the solar cycle. Finally, we compare some of the properties of the current minimum with previous minima of the space age. Given the unique conditions of the current solar minimum, such a review would appear to be timely.

The word “Structure" implies the way parts are arranged, or put together, to form a whole. By “large-scale," we refer to structure (and the underlying processes or mechanisms that lead to that structure) on spatial scales of, say, 1 solar radius (R_S) or larger. That is, structures that convect past a spacecraft on a timescale of say 30 mins or more. Structures that are discontinuous along one direction, such as shocks, the stream interface, and the HCS are also considered. Conveniently, current global MHD models address these constructs. By “quasi-steady" we avoid having to discuss any overtly time-dependent phenomena, such as coronal mass ejections [5] and interchange reconnection [6], with the acknowledgement that it is quite likely that much of the plasma we see in the solar wind may depend sensitively on such processes for its presence. In spite of this, to a large extent, we can understand how the large-scale structure arises using quasi-steady ideas and models.

It should be emphasized that “structure" is dependent upon, or even defined by the observations that describe it. Often, that same, or similar, structure is seen through a variety of observations. Sometimes different names are given to the same structure. Prominences, for example, are called filaments when observed on the solar disk. This can be a useful distinction, but can sometimes be confusing.

The structure in the heliosphere, while ultimately controlled by the Sun's magnetic field, can be conveniently described by the combination of two effects. The first is that, beyond $\sim 10R_S$, solar material streams away from the Sun along roughly radial trajectories with a range of speeds. The second is simply that the Sun rotates: solar rotation acts to replace plasma on the same radial trajectory with faster or slower wind. Faster wind overtaking slower wind leads to a compression front, while slower material being outrun by faster material leads to a rarefaction region, or expansion wave ([7]). The boundary within the compression region, separating the slow and fast wind, is known as a stream interface (SI) [8]. In the simplest possible scenario, where speed variations depend only on their source location at the Sun, that is, the flow pattern does not vary significantly on the timescale of a solar rotation (such as at solar minimum), the large-scale compressive structures created by the interactions

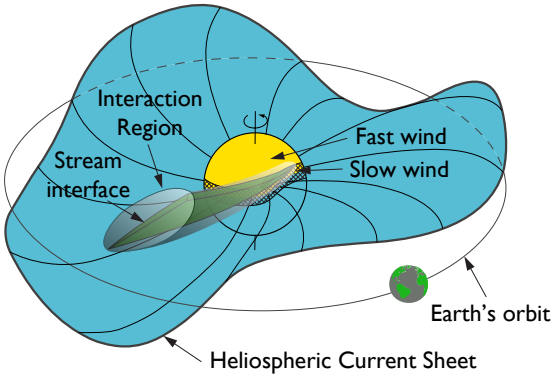

FIGURE 1. Illustration of the principal features associated with quasi-stready, large-scale heliospheric structure.

of these streams are fixed in a frame corotating with the Sun, and they are known as corotating interaction regions (CIRs) [9]. If the speed difference is sufficiently large, and typically beyond about 2 AU, a pair of shocks may form bounding the CIR (e.g., Pizzo [10]). These components are summarized in Figure 1.

The HCS, which is the natural extension of the neutral line, is a structure demarking the boundary between outwardly and inwardly directed magnetic field lines. It is not directly observable, except in a very localized sense by spacecraft in the heliosphere, yet it is undoubtedly one of the most important structures within the heliosphere. For practical purposes, it can be defined as the isosurface where $B_r = 0$. Although passive, the HCS is the single largest structure in the heliosphere and can be thought of as a "frame" on which stream structure "hangs." The SI and HCS are often confused as being colocated. However, as even the simple cartoon of Figure 1 demonstrates, they are distinct entities. Here, the HCS precedes the SI by approximately one day. Moreover, it is quite possible for the two structures to be completely unrelated, such as in the case of pseudostreamers, which lie over double-loop arcades and separate coronal holes of the same magnetic polarity [11, 12, 13].

HELIOSPHERIC OBSERVATIONS

The building block of heliospheric structure is the SI, which separates what was originally slow, dense wind with fast, tenuous wind [14, 15]. Here we focus on SIs on the leading edge of high-speed streams, but note that SIs also exist on the trailing edge of high-speed streams too, being revealed primarily through abrupt changes in composition and specific entropy [16]. In a detailed superposed epoch study, Gosling et al. [8] identified the crucial properties of abrupt SIs. Among their results, they found that the SI was associated with: (1) a discontinuous drop/rise in density/temperature (moving from the slow to fast wind, that is, in the same direction as time, as measured by an *in situ* spacecraft); (2) a discontinuous shear in the solar wind flow, observed as a discontinuous shift in flow angle from east to west; (3) an in-ecliptic orientation of $\sim 45^\circ$, relative to the radial direction, at 1 AU; (4) an abrupt change in both the alpha particle fraction as well as the relative flow speed of the alpha particles to protons; (5) the presence of sector boundaries (crossings of the heliospheric current sheet), which appear before the SI; and (6) the presence of stream-associated reverse shocks, but absence of forward shocks. Many of these features can be explained from simple 1-D hydrodynamic simulations (e.g., Hundhausen and Gentry [17]) as the result of fast solar wind compressing slower wind ahead and generating forward and reverse waves that later steepen into shocks ([18]). Two-and three-dimensional hydrodynamic simulations [19] supported the interpretation of the flow deflections at the SI being due to a velocity shear. In a frame corotating with the Sun, there is no flow angle change; the flow vectors are parallel but of different magnitude [8]. Such was our understanding in a two-dimensional "ecliptic plane" sense.

The Ulysses mission revolutionized our understanding of stream structure in three dimensions. Much of the basic structure had been predicted by global MHD simulations performed by V. Pizzo [20]. However, it was not until Ulysses measurements began to uncover a systematic picture of the properties of CIRs at mid latitudes during the declining phase of solar cycle 22, that these earlier numerical results began to be appreciated [21]. Several studies deserve mention. First, Gosling et al. [22] found that CIR-associated forward shocks disappeared at heliolatitudes in excess of $\sim 26^\circ$, which corresponded roughly to the tilt of the solar magnetic dipole. Additionally, R shocks continued to be observed frequently, up to latitudes of $\sim 42^\circ$, after which their presence became rarer. Further confirmation of the model predictions came from the flow deflections observed at the shocks, suggesting that the F shocks were oriented such that their outward normals were tilted toward the equator, and hence were propagating equatorward, while the R shock normals were tilted poleward [23].

STEREO observations promise a similar revolution in our understanding of stream structure. For the first time, observations by the HI2 A and B instruments are allowing us to directly connect disk and low-corona observations of solar structure with *in situ* observations at 1 AU [24, 25, 26]. Such studies are still in their infancy but will likely produce significant, and as yet unforeseen results. Rouillard [27] has summarized the results thus far.

THE UNDERLYING CAUSES OF THE 3-D STRUCTURE

Sophisticated numerical models have explored, described and explained many aspects of stream dynamics and evolution [28, 29]. Here we provide a heuristic discussion aimed at understanding these phenomena in a more intuitive manner. For simplicity, we consider the development of heliospheric structure from a prescribed velocity profile close to (but sufficiently far that the flow field is radial) the sun, say 20 R_s. We consider two idealized scenarios: the declining phase of the solar cycle and a simplified equatorial coronal hole configuration mimicking one aspect of solar maximum conditions.

Figure 2 (top), which is a generalization of a schematic presented by Gosling et al. [30], illustrates how compression regions and rarefaction regions are generated during the declining phase of the solar cycle. Consider this idealized picture of a band of slow solar wind organized about the heliomagnetic equator, which is tilted by some modest amount relative to the rotation axis. A parcel of plasma launched from the northern edge of the slow flow band will eventually be caught by plasma to the east (left) of it, as the Sun rotates underneath and populates that radial trajectory with faster material. The net effect is that, far from the Sun, a compression region builds up organized about this interface, the so-called SI. When mapped back to our reference surface, at 20 R_s, the compression region would be located as shown in Figure 2 (top). On the other hand, in the southern hemisphere, a similar argument leads to the formation of a rarefaction region (or expansion wave), as fast flow now outruns slower flow to the east. Finally, if we consider the opposite side of the Sun, the processes are reversed, with a rarefaction region being set up in the northern hemisphere and a compression region in the southern hemisphere Figure 2 (bottom). We can extend the argument to account for more complex shapes of the slow-flow band. In particular, if it is warped or contains more than a single sinusoidal variation with respect to heliographic latitude, the resulting patterns will be richer. Patterns for equatoward extensions of polar coronal holes, which were common near the previous minimum, can also be deduced. In summary then, given the flow speed at some inner radial boundary, such as 20R_S, it is relatively straightforward to infer the resulting dynamical pattern.

At, and surrounding solar maximum, the solar wind flow pattern is considerably more complex, and, likely, more time-dependent. Nevertheless, we can break the pattern into several basic building blocks. In particular, in Figure 3 we illustrate how an equatorial coronal hole drives solar wind structure. Using similar arguments, we deduce that a "U"-shaped internal region forms at the western edge of the coronal hole. On the eastern edge,

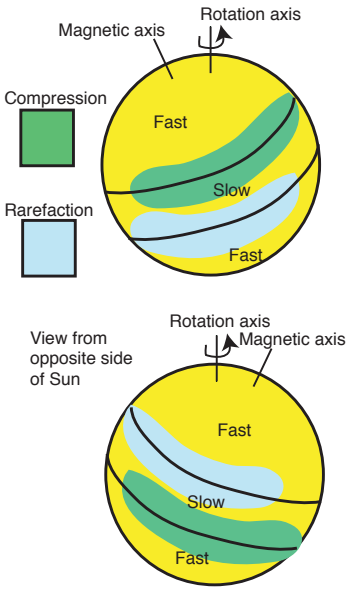

FIGURE 2. Evolution of solar wind streams for tilted-dipole geometry, representative of the declining phase of the solar cycle.

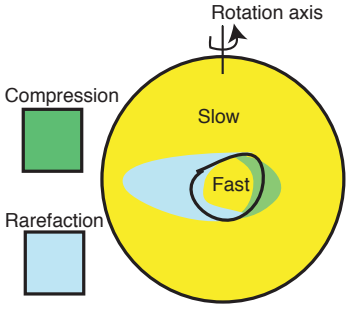

FIGURE 3. Evolution of solar wind streams for a fast, confined equatorial coronal hole.

an elongated rarefaction region develops. The effects of more complex flows can be inferred by assembling the various components. Of course, this heuristic approach is limited, and can only be applied to cases where the compression regions do not interact with one another. Yet although these examples are highly idealized, they provide the basic conceptual views for interpreting 3-D heliospheric structures over much of the solar cycle.

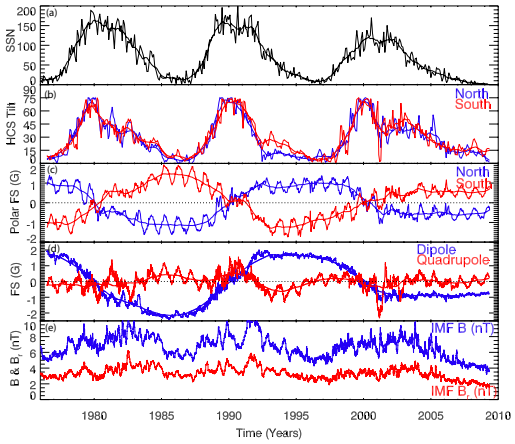

FIGURE 4. Time series of: (a) Sunspot Number (SSN); (b) Heliospheric Current Sheet (HCS) tilt, as inferred from PFSS solutions driven by WSO data; (c) Northern and Southern polar Field Strengths (FS); (d) Axial dipole and zonal quadrupole contributions to the field strength; and (e) total and radial Interplanetary Magnetic Field (IMF), as measured by the many spacecraft contributing to the OMNI dataset. Data for (b) through (d) provided by T. Hoeksema.

THE UNIQUE STRUCTURE OF THE CURRENT SOLAR MINIMUM

The current solar minimum, marking the end of solar cycle 23, has thus far been unique in a number of ways. As of August 21st, 2009, 183 days (79%) in 2009 have been spotless (Figure 4). Since 2004, 694 days have been spotless (see http://spaceweather.com) making the current solar minimum the most prolonged and quiet in a century. The polar photospheric flux has decreased by 40% [31] (see Figure 4) and the coronal holes are noticeably smaller [32]. Measurements by *in situ* spacecraft show substantial differences between the current minimum and the previous three. As of late 2008, Ulysses polar observations, in particular, suggest that: (1) the interplanetary magnetic field (IMF) was 36% lower than during its first polar passes in late 1994-1995, just prior to the previous solar minimum [33]; (2) the scaled number density was 17% lower [34, 35]; and (3) the scaled temperature was 14% lower [35]. It was also determined that the bulk solar wind speed was 3% lower (although this may not represent a statistically significant change). From these measurements it was inferred that: (1) the dynamic pressure decreased by 22%; (2) the proton thermal pressure decreased by 25%; and (3) the magnetic pressure decreased by 87% [35]. The profiles of high-speed streams upstream of Earth also seem to be unique, being of higher-speed, longer in duration, and more recurrent than the previous minimum [36]. In addition, strong periodicities were also found in early-mid 2008, with periods of 9, 13.5, and 27 days [37]; No comparable patterns were found during the previous minimum. It appears that the solar wind at Earth is 47% less dense, 13% faster, and the IMF is reduced by 11% [36].

Here we focus on structural differences between the current and previous minima. To address this, we have developed preliminary thermodynamic solutions for the two time periods: Carrington rotation 1913 (August/September, 1996), corresponding to the "Whole Sun Month" (WSM), and 2083 (May, 2009), which coincided roughly with Ulysses' traversals over the Sun's poles during its 1st and 3rd orbit. Figures 5 and 6 summarize the large-scale structure of the inner heliosphere during these two intervals. The top panels show the three components of solar wind velocity (in a helio-based spherical coordinate system: r, θ, ϕ), while the bottom panels show: the radial component of the magnetic field, the number density, and the plasma thermal pressure at 2.6 AU. Contrasting the two solutions, we note several points. First, the "band of solar wind variability" extended to higher heliographic latitudes during CR 2083. Second, the polar speeds are essentially the same for the two minima. Third, a significant source of fast solar wind in the ecliptic plane during CR 2083 derives from equatorial coronal holes. Fourth, the computed tilt (maximum extent) of the HCS (not shown) matches the values shown in Figure 4. Fifth, the values of B and B_r roughly match the OMNI measurements, although the CR 2083 predict values that are lower than were observed. However, since then, the measured IMF has continued to decrease in strength (Figure 4), reaching values commensurate with the model. We believe this is due to the residual effects of ICMEs in the observations, which are not included in the model solutions [38]. We note also that the tilts of the interaction regions are much less distinct for CR 2083 than for CR 1913, although they are still present. During CR 2083, the interaction regions are more localized and have the "U"-shaped profiles consistent with the schematic in Figure 3, that is, due to localized equatorial (and mid-latitude) coronal holes, "punching" through the otherwise slower wind.

CLOSING REMARKS

In this review, we have summarized the key processes leading to the large-scale, quasi-steady structure we observe in the inner heliosphere. Three-dimensional, global MHD simulations suggest that these processes do in fact produce the observed properties of CIRs.

The current solar minimum (defining the end of solar cycle 23) is unique in a number of respects, not least of which includes the structure of the heliosphere. The lower polar field strengths, presence of pseudostream-

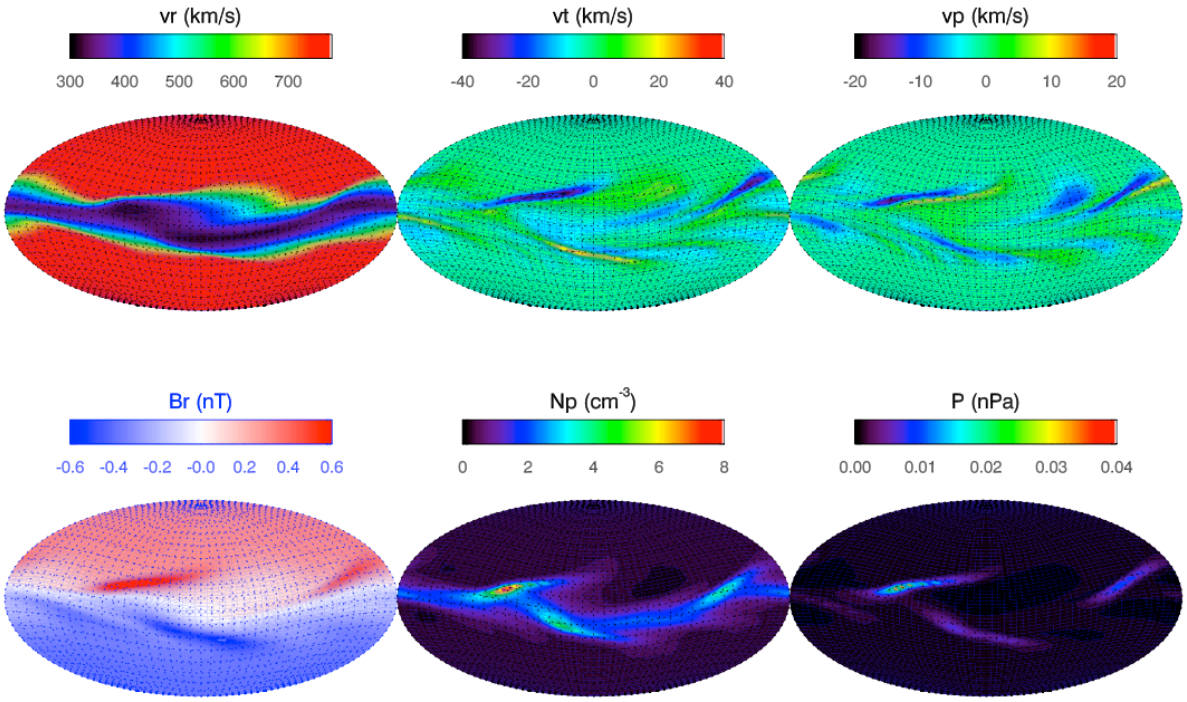

FIGURE 5. Mollweide projection maps of radial speed (v_r), meridional speed (v_t), azimuthal speed (v_p), radial magnetic field (B_r), number density (N_p), and thermal pressure (P) for Carrington rotation 1913, corresponding to August/September 1996.

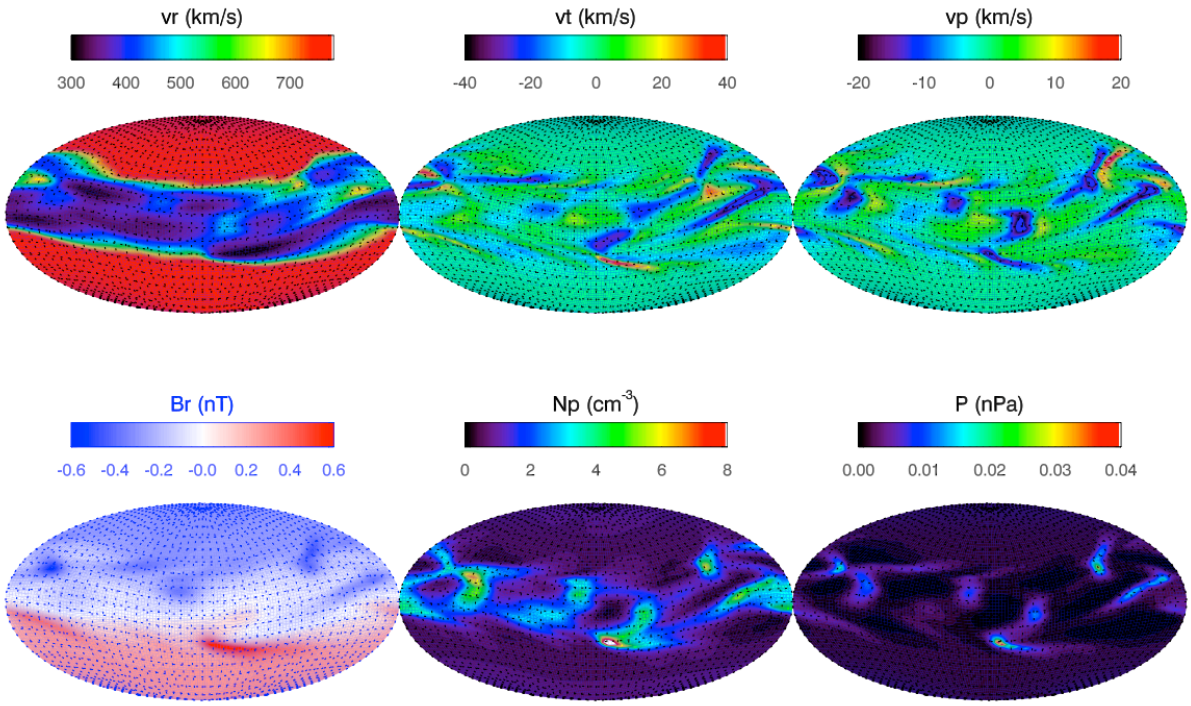

FIGURE 6. As Figure 5, for Carrington rotation 2083, corresponding to May 2009.

ers [13], and large current sheet tilt have contributed to a more complex pattern in the heliosphere. The band of solar wind variability extends to higher heliographic latitudes, as does the HCS, which is also composed of more vertical structure. Finally, the presence of equatorial and mid-latitude coronal holes, as well as polar coronal hole extensions is driving near-equatorial fast solar wind streams that are stronger, longer in duration, and more recurrent than have been observed in any of the previous three solar minima.

ACKNOWLEDGMENTS

PR gratefully acknowledges the support of NASA (SR&T and Theory programs) and NSF (CISM and SHINE programs). Support for some of the numerical simulations was provided through NASA's Advanced Supercomputing Division and NSF's Teragrid.

REFERENCES

1. Y.-M. Wang, *Ap. J. Lett.* **437**, L67–L70 (1994).
2. D. Lario, and E. C. Roelof, *Journal of Geophysical Research (Space Physics)* **112**, 9107–+ (2007).
3. A. J. Lazarus, J. D. Richardson, R. B. Decker, and F. B. McDonald, *Space Science Reviews* **89**, 53–59 (1999).
4. B. T. Tsurutani, W. D. Gonzalez, A. L. C. Gonzalez, F. L. Guarnieri, N. Gopalswamy, M. Grande, Y. Kamide, Y. Kasahara, G. Lu, I. Mann, R. McPherron, F. Soraas, and V. Vasyliunas, *J. Geophys. Res.* **111**, 7–+ (2006).
5. J. A. Linker, Z. Mikic, R. Lionello, P. Riley, T. Amari, and D. Odstrcil, *Phys. Plasmas* **10**, 1971 (2003).
6. N. U. Crooker, and G. L. Siscoe, *AGU Fall Meeting Abstracts* pp. B5+ (2004).
7. V. Sarabhai, *J. Geophys. Res.* **68**, 1555 (1963).
8. J. T. Gosling, J. R. Asbridge, S. J. Bame, and W. C. Feldman, *J. Geophys. Res.* **83**, 1401–1412 (1978).
9. E. J. Smith, and J. H. Wolfe, *Geophys. Res. Lett.* **3**, 137 (1976).
10. V. J. Pizzo, *IN: Collisionless Shocks in the Heliosphere: Reviews of Current Research* **35**, 51 (1985).
11. M. Neugebauer, P. C. Liewer, B. E. Goldstein, X. Zhou, and J. T. Steinberg, *Journal of Geophysical Research (Space Physics)* **109**, 10102–+ (2004).
12. X. P. Zhao, and D. F. Webb, *Journal of Geophysical Research (Space Physics)* **108**, 1234–+ (2003).
13. Y.-M. Wang, N. R. Sheeley, Jr., and N. B. Rich, *Ap. J.* **658**, 1340–1348 (2007).
14. C. P. Sonett, and D. S. Colburn, *Plan. Space. Sci.* **13**, 675–+ (1965).
15. H. Razdan, D. S. Colburn, and C. P. Sonett, *Plan. Spac. Sci.* **13**, 1111–+ (1965).
16. M. E. Burton, M. Neugebauer, N. U. Crooker, R. von Steiger, and E. J. Smith, *J. Geophys. Res.* **104**, 9925–9932 (1999).
17. A. J. Hundhausen, and R. A. Gentry, *J. Geophys. Res.* **74**, 2908 (1969).
18. P. Riley, J. T. Gosling, D. J. McComas, V. J. Pizzo, J. G. Luhmann, D. Biesecker, R. J. Forsyth, J. T. Hoeksema, A. Lecinski, and B. J. Thompson, *J. Geophys. Res.* **104**, 9871 (1999).
19. V. J. Pizzo, *A three-dimensional model of high-speed streams in the solar wind*, Ph.D. thesis, AA(Colorado Univ., Boulder.) (1977).
20. V. J. Pizzo, *J. Geophys. Res.* **96**, 5405–5420 (1991).
21. V. J. Pizzo, and J. T. Gosling, *Geophys. Res. Lett.* **21**, 2063 (1994).
22. J. T. Gosling, W. C. Feldman, D. J. McComas, J. L. Phillips, V. J. Pizzo, and R. J. Forsyth, *Geophys. Res. Lett.* **22**, 3333 (1995).
23. P. Riley, J. T. Gosling, L. A. Weiss, and V. J. Pizzo, *J. Geophys. Res.* **101**, 24349 (1996).
24. N. R. Sheeley, Jr., A. D. Herbst, C. A. Palatchi, Y.-M. Wang, R. A. Howard, J. D. Moses, A. Vourlidas, J. S. Newmark, D. G. Socker, S. P. Plunkett, C. M. Korendyke, L. F. Burlaga, J. M. Davila, W. T. Thompson, O. C. St Cyr, R. A. Harrison, C. J. Davis, C. J. Eyles, J. P. Halain, D. Wang, N. B. Rich, K. Battams, E. Esfandiari, and G. Stenborg, *Ap. J.* **675**, 853–862 (2008).
25. A. P. Rouillard, J. A. Davies, R. J. Forsyth, A. Rees, C. J. Davis, R. A. Harrison, M. Lockwood, D. Bewsher, S. R. Crothers, C. J. Eyles, M. Hapgood, and C. H. Perry, *Geophys. Res. Lett.* **35**, 10110–+ (2008).
26. A. P. Rouillard, N. P. Savani, J. A. Davies, B. Lavraud, R. J. Forsyth, S. K. Morley, A. Opitz, N. R. Sheeley, L. F. Burlaga, J.-A. Sauvaud, K. D. C. Simunac, J. G. Luhmann, A. B. Galvin, S. R. Crothers, C. J. Davis, R. A. Harrison, M. Lockwood, C. J. Eyles, D. Bewsher, and D. S. Brown, *Sol. Phys.* **256**, 307–326 (2009).
27. A. P. Rouillard, "STEREO HI Observations," in *Solar Wind 12*, edited by M. Maksimovic, AIP, Saint-Malo, 2009.
28. V. Pizzo, *J. Geophys. Res.* **83**, 5563–5572 (1978).
29. P. Riley, J. A. Linker, and Z. Mikić, *J. Geophys. Res.* **106**, 15889 (2001).
30. J. T. Gosling, S. J. Bame, W. C. Feldman, D. J. McComas, J. L. Phillips, and B. E. Goldstein, *Geophys. Res. Lett.* **20**, 2335 (1993).
31. L. Svalgaard, and E. W. Cliver, *Ap. J. Lett.* **661**, L203–L206 (2007).
32. M. S. Kirk, W. D. Pesnell, C. A. Young, and S. A. Hess Webber, *ArXiv e-prints* (2009), 0901.1158.
33. E. J. Smith, and A. Balogh, *Geophys. Res. Lett.* **35**, 22103–+ (2008).
34. K. Issautier, G. Le Chat, N. Meyer-Vernet, M. Moncuquet, S. Hoang, R. J. MacDowall, and D. J. McComas, *Geophys. Res. Lett.* **35**, 19101–+ (2008).
35. D. J. McComas, R. W. Ebert, H. A. Elliott, B. E. Goldstein, J. T. Gosling, N. A. Schwadron, and R. M. Skoug, *Geophys. Res. Lett.* **35**, 18103–+ (2008).
36. S. E. Gibson, G. d. Toma, B. A. Emery, T. Onsager, and B. J. Thompson, *Submitted to Geophys. Res. Lett.* (2009).
37. B. A. Emery, I. G. Richardson, D. S. Evans, F. J. Rich, and G. Wilson, *AGU Fall Meeting Abstracts* pp. B1640+ (2008).
38. P. Riley, *Ap. J. Lett.* **667**, L97–L100 (2007).

Appendix C

On the relationship between coronal heating, magnetic flux, and the density of the solar wind

Riley, P. and Mikic, Z. and Lionello, R. and Linker, J. A. and Schwadron, N. A. and McComas, D. J.

Published in J. Geophys. Res., 2010.

JOURNAL OF GEOPHYSICAL RESEARCH, VOL. 115, A06104, doi:10.1029/2009JA015131, 2010

On the relationship between coronal heating, magnetic flux, and the density of the solar wind

Pete Riley,[1] Z. Mikic,[1] R. Lionello,[1] J. A. Linker,[1] N. A. Schwadron,[2] and D. J. McComas[3,4]

Received 25 November 2009; revised 13 January 2010; accepted 28 January 2010; published 8 June 2010.

[1] The stark differences between the current solar minimum and the previous one offer a unique opportunity to develop new constraints on mechanisms for heating and acceleration of the solar wind. We have used a combination of numerical simulations and analysis of remote solar and in situ observations to infer that the coronal heating rate, H, scales with the average magnetic field strength within a coronal hole, B_{ch}. This was accomplished in three steps. First, we analyzed Ulysses measurements made during its first and third orbit southern and northern polar passes (i.e., during near-solar minimum conditions) to deduce a linear relationship between proton number density (n_p) and radial magnetic field strength (B_r) in the high-speed quiescent solar wind, consistent with the results of McComas et al. (2008) and Ebert et al. (2009). Second, we used Wilcox Solar Observatory measurements of the photospheric magnetic field to show that the magnetic field strength within coronal holes (B_{ch}) is approximately correlated with the strength of the interplanetary field at the location of Ulysses. Third, we used hydrodynamic simulations to show that n_p in the solar wind scales linearly with H. Taken together, these results imply the chain: $H \propto n_p \propto B_r \propto B_{ch}$. We also explored ideas that the correlation between n_p and B_r could have resulted from interplanetary processes, or from the superradial expansion of the coronal magnetic field close to the Sun, but find that neither possibility can produce the observed relationship. The derived heating relationship is consistent with (1) empirical heating laws derived for closed-field line regions and (2) theoretical models aimed at understanding both the heating and acceleration of the solar wind.

Citation: Riley, P., Z. Mikic, R. Lionello, J. A. Linker, N. A. Schwadron, and D. J. McComas (2010), On the relationship between coronal heating, magnetic flux, and the density of the solar wind, *J. Geophys. Res.*, *115*, A06104, doi:10.1029/2009JA015131.

1. Introduction

[2] A number of promising ideas for the underling physical mechanism(s) that heat the corona have been proposed [*Klimchuk*, 2006]. Undoubtedly, magnetic fields must play a crucial role, yet how energy from them is dissipated into heat in the corona remains poorly known. Additionally, there may be more than one mechanism at work, different subsets of which may operate in different regions of the Sun, such as active regions (ARs), the quiet sun (QS), and coronal holes (CHs). Most empirically based studies have focused on heating within ARs and the QS, that is, regions of closed magnetic field. Indeed, the absence of emission from coronal holes makes them intrinsically difficult to study.

[3] Although the mechanisms that heat open and closed regions may be fundamentally different, and our focus in this study will be on CHs, it is instructive to review studies of the heating of coronal loops. For the sake of simplicity, we group heating models into two types; wave heating and stress heating [*Fisher et al.*, 1998]. Wave-heating models obviously rely on the production of heat from damping of waves, while stress-heating models, also known as nanoflare heating [*Parker*, 1988], rely on magnetic reconnection to produce the energy necessary to heat the coronal plasma. *Fisher et al.* [1998] correlated a range of globally derived solar corona magnetic variables with X-ray luminosities, L_x (derived from observations by the SXT telescope aboard the Yohkoh spacecraft) finding that L_x is most highly correlated with the total unsigned magnetic flux, Φ_{tot}. Assuming L_x was a reasonable proxy for the power dissipated through coronal heating, they concluded that these results favored a wave-heating model, for which the total power dissipated in an active region scales as $\Phi_{tot}^{1.2}$. However, as *Fisher et al.* [1998] pointed out, there does not appear to be enough energy in the

[1]Predictive Science, San Diego, California, USA.
[2]Department of Astronomy, Boston University, Boston, Massachusetts, USA.
[3]Southwest Research Institute, San Antonio, Texas, USA.
[4]Physics and Astronomy Department, University of Texas at San Antonio, San Antonio, Texas, USA.

0148-0227/10/2009JA015131

waves to produce the observed level of heating. In contrast, a stress-heating (nanoflare) model [*Parker*, 1988], suggests a stronger correlation with $B^2_{z,tot}$ (= $\int dAB^2_z$, where the integral runs over the entire magnetogram) than with Φ_{tot}, which was not found (a correlation coefficient of 0.77 for $B^2_{z,tot}$ versus 0.83 for Φ_{tot}). Moreover, the stress-heating model suggests significantly more energy should be radiated than is observed [*Fisher et al.*, 1998]. *Pevtsov et al.* [2003] generalized this study to show that Φ_{tot} scaled approximately linearly (over more than 12 orders of magnitude) with L_x for a wide range of active stars, as well as the Sun. The relationship, however, was not without significant scatter. Limited to solar data, they found power law indices to the relationship $L_x \propto \Phi^p_{tot}$ ranging from $p \sim 0.93$–2.02, and concluded that the most likely relationship (should a single one exist) was $L_x \propto \Phi^{1.13}_{tot}$.

[4] The study of coronal heating within coronal holes has received less attention. Given the relative lack of observational constraints, it is not surprising that most research has focused on developing theoretical models. Early research, following the pioneering work of E. N. Parker [*Parker*, 1958, 1963, 1965] focused on the basic effects of depositing momentum and/or energy at different heights in the corona and understanding their effects on the properties of the solar wind at 1 AU (see review by *Leer et al.* [1982]), and elucidated a number of important, and perhaps counterintuitive results. *Holzer and Leer* [1980], for example, showed rapidly diverging flow geometries did not significantly affect solar wind speed at 1 AU; however, they did decrease the solar wind mass flux. *Leer and Holzer* [1980] showed that the height in the corona where energy is deposited can have a significant effect on the properties of the solar wind at 1 AU. Specifically, depositing energy low in the corona (below the sonic point) increases the mass flux, but not speed of the solar wind at 1 AU, whereas depositing that energy above the sonic point increases the flow speed of the solar wind, but has little effect on its mass flux. In these early studies, little consideration was paid on how this heat was generated. More recent work has addressed the issue of how the energy stored in the magnetic field is converted into heat, and there are two analogous categories that match the wave- and stress-heating models discussed above for closed field regions. Wave/turbulence-driven (WTD) models [*Cranmer et al.*, 2007; *Cranmer*, 2009] are an extension of the wave-heating models, which attempt to provide a self-consistent description of both the acceleration and heating of solar wind plasma through the combined effects of wave damping and turbulent cascade. Similarly, stress-heating models have been generalized in an attempt to explain the differences in the properties of the slow and fast solar wind [*Fisk et al.*, 1999; *Fisk*, 2003; *Fisk and Zurbuchen*, 2006]. These have been labeled reconnection/loop-opening (RLO) models by *Cranmer et al.* [2007]. Clearly, both ideas rely heavily on the strength of the local magnetic field to fuel the heating of the coronal plasma. *Cranmer* [2009] has shown that, for the WTD model, the volumetric heating rate, H scales with the average low-coronal magnetic field, B. *Schwadron et al.* [2006] showed that, for an RLO-type model, the total power available to drive the solar wind (P_{SW}) scales linearly with the base magnetic field flux of the open field carrying that parcel of solar wind. Moreover, assuming that the same process that powers the solar wind also heats the corona, they derived an estimate for the soft X-ray luminosity of the Sun of ~0.01 P_{SW}. This estimate agreed remarkably well with X-ray observations over 12 orders of magnitude in magnetic flux [*Pevtsov et al.*, 2003]. Thus, in their model, H is also proportional to B.

[5] Although the WTD and RLO models suggest the same basic relationship between H and B_{ch}, it is worth remarking that they suggest distinctly different origins for the slow solar wind. In the RLO view, the slow solar wind is produced initially in closed field regions (which may have a fundamentally different type of heating) that are then opened the plasma released [*Fisk et al.*, 1999]. This naturally accounts for the striking composition differences that are observed between slow and fast wind [*Geiss et al.*, 1995]. In the WTD view, the slow solar wind results from the large expansion factor of open field lines located near to the boundary between open and closed field lines [*Wang and Sheeley*, 1990; *Cranmer et al.*, 2007]. To produce the large variations that are seen between slow and fast wind, the coronal heating rate must be a function of the local magnetic field strength [*Pinto et al.*, 2009]. *Wang et al.* [2009] have further argued that the unique compositional signatures of the slow and fast wind can be accounted for by varying the amount of energy deposited and the range over which it is deposited. Fast wind from large polar coronal holes, for example, must be heated over a relatively large spatial range, but the amount of heat deposited must be small in comparison to heating associated with, say, AR holes.

[6] Global MHD models, which include energy transport processes, and ad hoc coronal heating profiles, in particular, have adopted a variety of heating functions to match emission measurements in the QS, ARs, and coronal holes [*Lionello et al.*, 2009; *Riley et al.*, 2009; *Riley*, 2010] and are roughly consistent with empirically based functions [*Fisher et al.*, 1998; *Pevtsov et al.*, 2003]. Such models represent a pragmatic compromise motivated by the objective of producing accurate simulated emission images (both EUV and soft X-ray) at the potential expense of not understanding the heating mechanism(s). Moreover, although the profiles chosen may lead to relatively accurate solutions, the question of uniqueness remains present. That is, are there another sets of parameters, which, while substantially different, would lead to equivalently accurate solutions, as assessed by, say, comparison between simulated and observed emission? Given the computational expense of running a single case, it is currently not feasible to systematically explore the full parameter space for global models. One-dimensional models, however, while limited in scope, can perform such parametric sensitivity studies.

[7] Bridging the gap between fully self-consistent global models and observations are a range of so-called empirically based models [*Wang and Sheeley*, 1990; *Arge and Pizzo*, 2000; *Riley et al.*, 2001]. The Wang-Sheeley-Arge (WSA) model [*Wang and Sheeley*, 1990; *Arge and Pizzo*, 2000] is perhaps the most widely known and implemented, and relies on an inverse correlation between coronal magnetic field expansion factor and solar wind speed at 1 AU. Intuitively, one can make the analogy with fluid (Bernoulli) flow through a diverging pipe: Provided density does not change appreciably, a more rapid divergence of the field suggests a slower asymptotic speed. In reality, the combination of the spherical

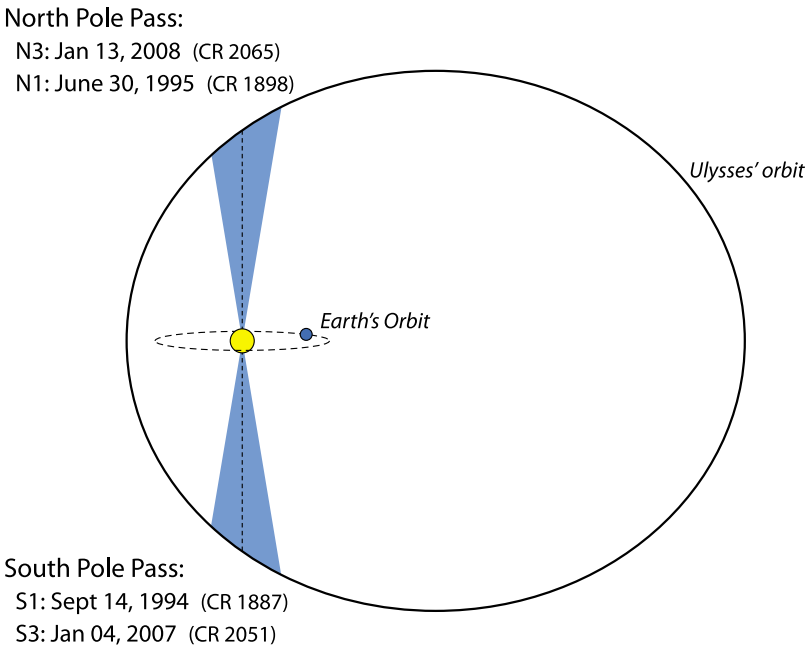

Figure 1. Schematic of Ulysses' orbit showing the relative position of Earth's ecliptic orbit and dates of polar crossings.

geometry, compressible flow, and transonic transition limits this analogy. Furthermore, what effects do remain, cannot directly account for the approximate factor of two difference in speed between the slow and fast wind [*Holzer and Leer*, 1980]. More sophisticated extrapolations have also been proposed. *Suzuki* [2006], for example, have derived an estimate for the solar wind speed at 1 AU based on E. Parker's implementation of Bernoulli equation [*Parker*, 1963], which posits that the kinetic energy of the solar wind can be inferred from a knowledge of the Alfvén wave energy at the Sun, the thermal pressure of the corona, and the solar gravitational potential. In particular, they derive an interplanetary speed that depends on B_{corona} and inversely with f.

[8] Ulysses observations made during its first and third polar passes showed that while the solar wind speed did not change appreciably between 1994–1995 and 2007–2008, the plasma number density decreased by ~17% [*McComas et al.*, 2008]. Based on the 1-D hydrodynamic models of solar wind flow by *Leer and Holzer* [1980], McComas et al. argued that: (1) the wind of the current minimum was heated less than during the previous minimum; and (2) this heating must have occurred below the critical point. As noted earlier, adding heat below the sonic point increases mass flux and momentum flux comparably, whereas adding heat above the sonic point increases solar wind speed.

[9] In this study, we analyze Ulysses observations over both poles of the Sun during its first and third orbit. We show that a relatively linear relationship exists between solar wind density, scaled to 1 AU (n_p) and the radial component of the magnetic field, B_r. We also show that the field strength within coronal holes (B_{ch}) during these passes approximately correlates with the IMF B_r measured at Ulysses. Finally, using 1-D numerical thermodynamic solutions of coronal-hole field lines with a variety of heating and geometrical properties, we show that n_p scales linearly with heating rate. These results suggest that the Ulysses polar measurements during the previous and current solar minimum are consistent with a CH heating rate, $H \propto B_{ch}$.

2. Ulysses Polar Observations During First and Third Orbits

[10] Following its rendezvous with Jupiter in February 1992, the Ulysses spacecraft began its epic journey to sample solar wind over the southern and northern poles of the Sun. This is summarized schematically in Figure 1. Perhaps both by design as well as serendipity, the spacecraft has continued to return valuable data through June, 2009, translating into almost 19 years, and three complete polar orbits. The first and third of these occurred during predominantly "minimum" activity conditions, while the second orbit encompassed the maximum of solar cycle 23.

[11] Figure 2 summarizes the principal plasma and magnetic field measurements made by the Ulysses spacecraft from 1993 through 2009. The orbital parameters of the spacecraft are summarized in the first and second panels, while the third, fourth, fifth, and sixth panels show the bulk solar wind speed, proton number density and temperature, and the radial component of the magnetic field, color-coded with the polarity of the field: Red indicates an outwardly directed field, while blue indicates an inwardly directed field. The values, variability, and trends in these data have been described in many studies over the past 15 years or so [e.g., *McComas et al.*, 2008, and references therein]. In this study, we focus on the poleward excursions centered around 1995 and 2007–2008, corresponding to orbits 1 and 3 of the spacecraft, and coinciding with the minima of the ends of solar cycles 22 and 23. The yellow-shaded boxes mark the regions poleward of 70° in the southern and northern hemispheres for orbits 1 and 3. We denote these intervals, which follow one another in time, as: S1, N1, S3, and N3.

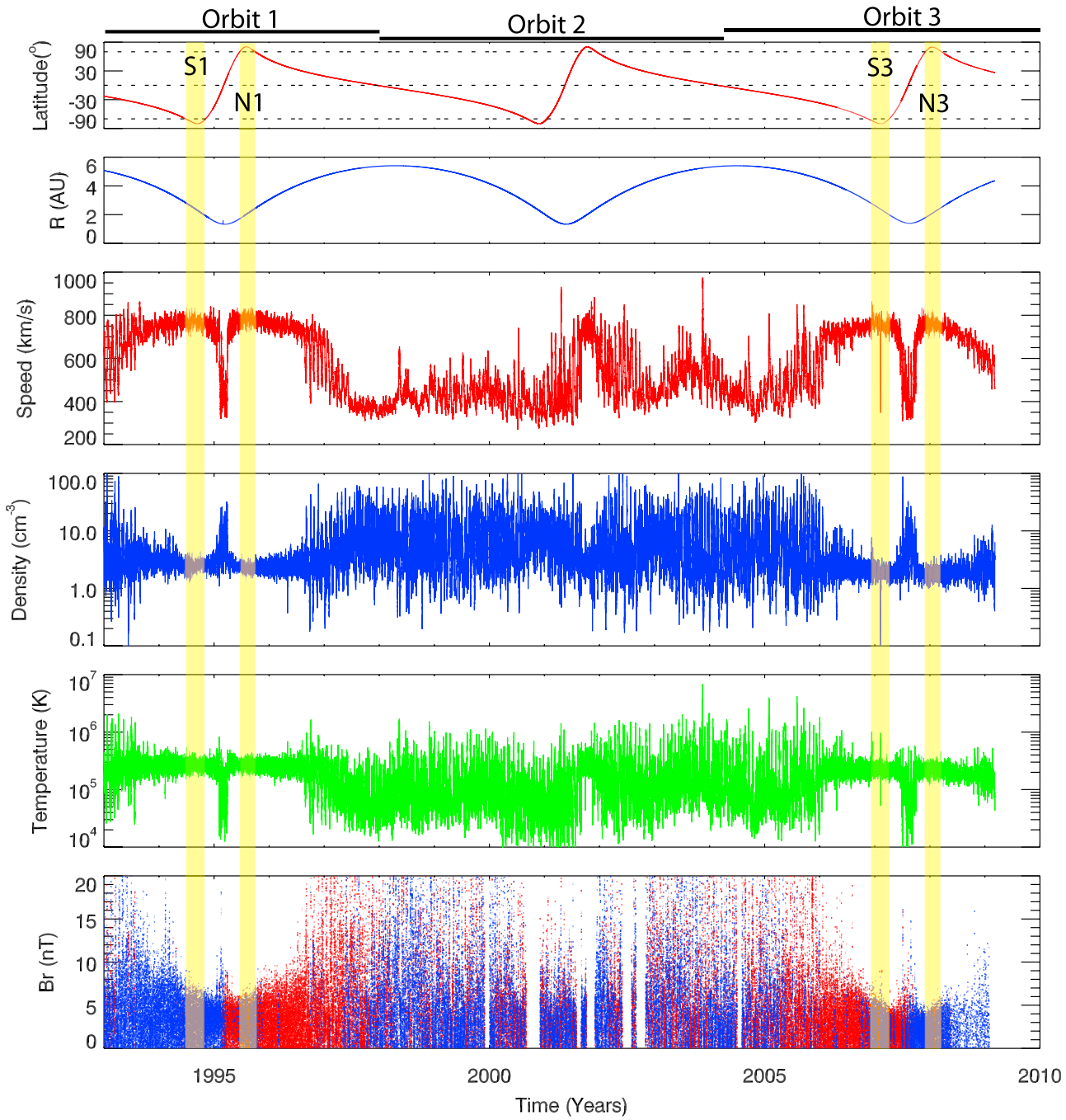

Figure 2. Summary of Ulysses measurements from 1993 through 2009. (top to bottom) The latitude and heliocentric distance of the spacecraft; the bulk solar wind speed; the proton number density; the proton temperature; and the radial component of the interplanetary magnetic field, color-coded with the polarity of the field (red indicating outward and blue indicating inward polarity). The yellow-shaded boxes mark the intervals: S1, N1, S3, and N3. The three polar orbits are indicated by the horizontal bars along the top.

[12] To explore the variability and relationship between various plasma and magnetic field quantities, we computed their mean values for intervals S1 through N3. We limited each interval to latitudes of greater than 70°, and, further, to the perihelion side of the polar pass, thus providing a more localized snapshot in time. Our results are consistent with the study by *Ebert et al.* [2009]. In comparing density, temperature, velocity, and magnetic field variations, we found that only n_p and B_r showed any systematic variations, both of which decreased in time, consistent with the results of *Ebert et al.* [2009]. This trend is summarized in Figure 3, which suggests a relatively linear correlation between n_p and B_r. A least squares fit to the Ulysses data has also been applied, which naturally intercepts the origin (0,0). Since the time between S1 and N1 is much shorter than the time between N1 and S3, it is worth considering the variation of B_r (and, implicitly n_p) as a function of time. This is shown in Figure 4. Perhaps counterintuitively, the largest temporal gradients

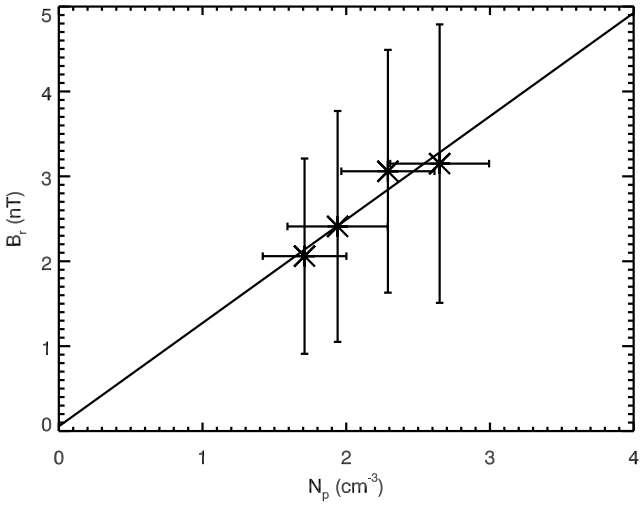

Figure 3. Variation of B_r versus n_p for the four intervals S1, N1, S3, and N3 defined in Figure 2. A least squares fit to the data has been drawn. The vertical and horizontal bars indicate ±1 standard deviation in the measurements; that is, 95% of the data contributing to each point fell within these bars.

occur from S1 to N1 and 3S to 3N, and not between the two solar minima, which span a significantly larger range in time. However, given the limited number of points, we would not conclude that this represents a long-term linear trend.

[13] Next, we consider the relationship between the in situ magnetic fields measured by Ulysses and the solar magnetic fields, presumed to drive the heating of the corona. This connection is not without controversy [*Riley*, 2007]. Nevertheless, we can assess (at least in a rudimentary way) whether a basic correlation exists between the two. Figure 5 compares the measured value of B_r at Ulysses for each of the four polar passes with the inferred magnitude of the solar polar fields corresponding to each epoch, as determined from photospheric magnetic field observations made at the Wilcox Solar Observatory (WSO). We infer that a reasonable, linear correlation exists between the interplanetary magnetic field and

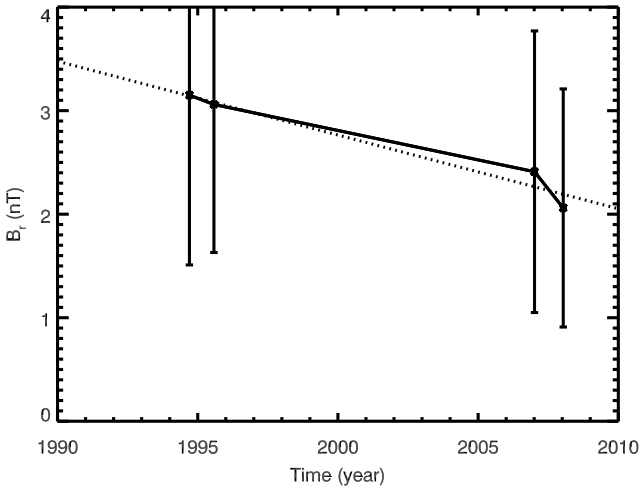

Figure 4. Variation of B_r as a function of time for the four intervals defined in Figure 2. The vertical bars are as defined in Figure 3.

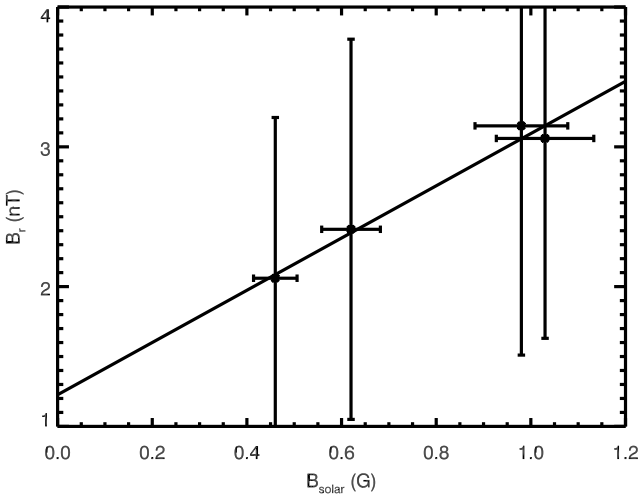

Figure 5. Variation of IMF B_r versus polar photospheric line-of-sight field, B_{ch} (as determined from WSO magnetograms) for the four intervals defined in Figure 2. A least squares fit to the data has been drawn. The vertical bars are as defined in Figure 3, while the horizontal bars have been set at 10% of the value of the data point, approximately consistent with variations seen surrounding each interval.

the large-scale solar photospheric field, and thus, that the former can act as a rough proxy of the latter. The coronal hole field estimates, however, contain several potentially significant sources of error. First, the polar field strength shown is the average of the northern and southern measurements. Observations of the Sun's poles are sensitive to the tilt of the Sun's rotation axis relative to the ecliptic plane (the B_o angle), with one polar region typically being tilted toward the Earth and the other away, and reversing every six months. Second, polar values are an average of the line-of-sight (not radial) field made using all data poleward of ±55°, which corresponds to the polemost 3′ apertures at WSO. For solar minimum conditions, when large polar coronal holes are established midlatitude structure should not affect the average; however, the limited number of points making up the average suggests a potentially nonnegligible noise component to the data. Finally, we note that the least squares fit to the data does not intercept the origin. That is, in the limit that the Sun's polar field goes to zero, the interplanetary field remains finite. While we are not suggesting that the Sun's magnetic field will in fact drop to zero (although such a scenario is appealing to consider), it suggests the possibility that an additional component to the interplanetary field may exist. It is, of course, quite possible that this effect is due entirely to the aforementioned uncertainties and errors associated with a determination of the average polar photospheric magnetic fields. However, we also raise the possibility that it results from a residual open flux in the heliosphere due to the legs of coronal mass ejections propagating away from the Sun [*Owens and Crooker*, 2006; *Riley*, 2007].

3. Numerical Simulations

3.1. Model Description

[14] Our approach for computing 1-D solutions along open coronal hole field lines is similar to the one-fluid model

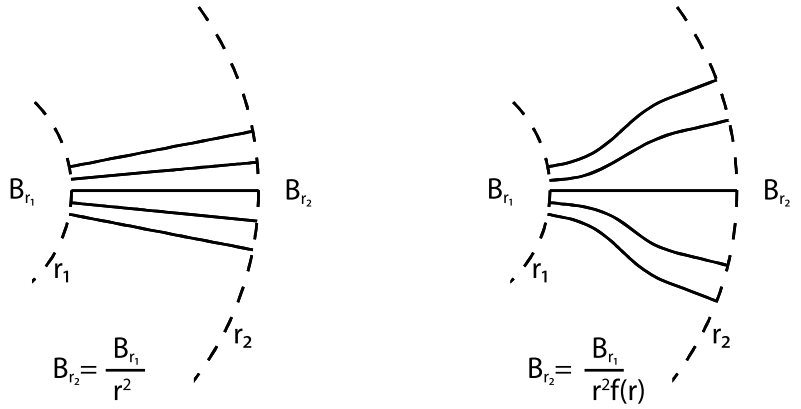

Figure 6. (left) Expansion of radial magnetic field lines. (right) Idealized superradial expansion, governed by the parameter $f(r)$.

described by *Withbroe* [1988]. Here we briefly describe that approach and point out some of the modifications we have made. As with *Withbroe* [1988], we include radiation losses, collisional and collisionless conduction (the transition occurring at $r \sim 10\ R_S$), and the effects of transport of energy via Alfvén waves. In the 1-D model, the magnetic field enters only through the momentum equation, where it appears as a nonlinear force due to Alfvén waves. The Alfvén speed is computed by invoking conservation of magnetic flux (i.e., $B_r r^2 f(r) = C$) and using values typical of the interplanetary magnetic field at 1 AU to fix the value of C. While *Withbroe* [1988] solved the time-stationary conservation equations by iteration, our method solves the time-dependent equations by allowing the solution to relax to a steady state. Thus, unlike the earlier approach, no user interaction is required to choose the appropriate supersonic solution for which $T(r) \rightarrow 0$ for large values of r.

[15] Before proceeding, it is worth clarifying the relationship between magnetic field and flux, both near to and far from the Sun. Ulysses measures the local magnetic field. During 3 orbits, it has demonstrated that the radial component, B_r, when scaled to 1 AU (by multiplying by r^2), is independent of latitude. Magnetic flux, on the other hand, is an area integral of the magnetic field crossing a particular surface. Thus, assuming B_r is independent of latitude, over sufficiently long time periods ($\tau > 1$ solar rotation, so that we can average over longitude), $\Phi_{open} = \langle B_r \rangle \times A$, where A is the area defined by a spherical shell, say, at 1 AU. Thus, at sufficiently far distances from the Sun, where the field has become completely open, the total unsigned flux is independent of heliocentric distance. Even through some elemental area, a radial field decreases by the same factor that the elemental area increases, i.e., r^2, and so the flux through that area remains constant. Near the solar surface, however, where the field expands superradially, the radial magnetic field falls off much more rapidly than $1/r^2$. Figure 6 contrasts the case of a radial expansion of the magnetic field with a case that includes a more radical change, i.e., a superradial expansion, described by the expansion factor, f. *Kopp and Holzer* [1976] developed the following analytic approximation for f, which we have implemented in our code:

$$f(r) = \frac{f_{\max} e^{(r-r_o)/\sigma} + f_1}{e^{(r-r_o)/\sigma} + 1} \tag{1}$$

where

$$f_1 = 1 - (f_{\max} - 1) e^{(R_S - r_o)/\sigma} \tag{2}$$

where $f_{\max}$ is the expansion factor amplitude, r_o is the expansion radius, and σ is the width over which it operates. Thus, the expansion factor captures by how much the magnetic field falls off from r_1 to r_2, above and beyond the $1/r^2$ due to spherical expansion. Phrased another way, the area of a flux tube at distance r from the Sun varies in the following way:

$$\frac{A(r)}{A(R_S)} = \left(\frac{r}{R_S}\right)^2 f(r) \tag{3}$$

For near-solar minimum conditions, f can be ~10 within polar coronal holes.

[16] The effects of expansion factor on the mass flux of the asymptotic solar wind can be seen by invoking conservation of mass for steady state outflow: $\rho(r)v(r)A(r) = \rho(R_S)v(R_S)A(R_S)$ and applying equation (3):

$$\rho(r)v(r) = \left(\frac{R_S}{r}\right)^2 \frac{\rho(R_S)v(R_S)}{f(r)} \tag{4}$$

[17] Thus, in the absence of other effects, a large expansion factor, which would be found near the boundary between open and closed field lines, would drive the asymptotic mass flux ($\rho(\infty)v(\infty)$) down.

[18] The model allows the user to specify a wide array of heating profiles, some of which have been described in some detail by *Lionello et al.* [2009]. In this study, we restrict ourselves to heating along open field lines assumed to lie well within coronal holes. For such cases, we adopt the following simple exponential volumetric heating rate:

$$H_{\exp} = H_o e^{\frac{-(r-R_S)}{\lambda_o}}, \tag{5}$$

where H_o is the volumetric heating rate at the base of the field line and λ_o is the heating scale length. Although neither H_o nor λ_o have yet been well constrained by observations, values of $H_o = 4.9 \times 10^{-7}$ erg/cm^3/s and $\lambda_o = 0.7\ R_S$ [*Lionello et al.*, 2009] yield the type of fast, tenuous solar wind observed by Ulysses, when it is used together with an Alfvén wave

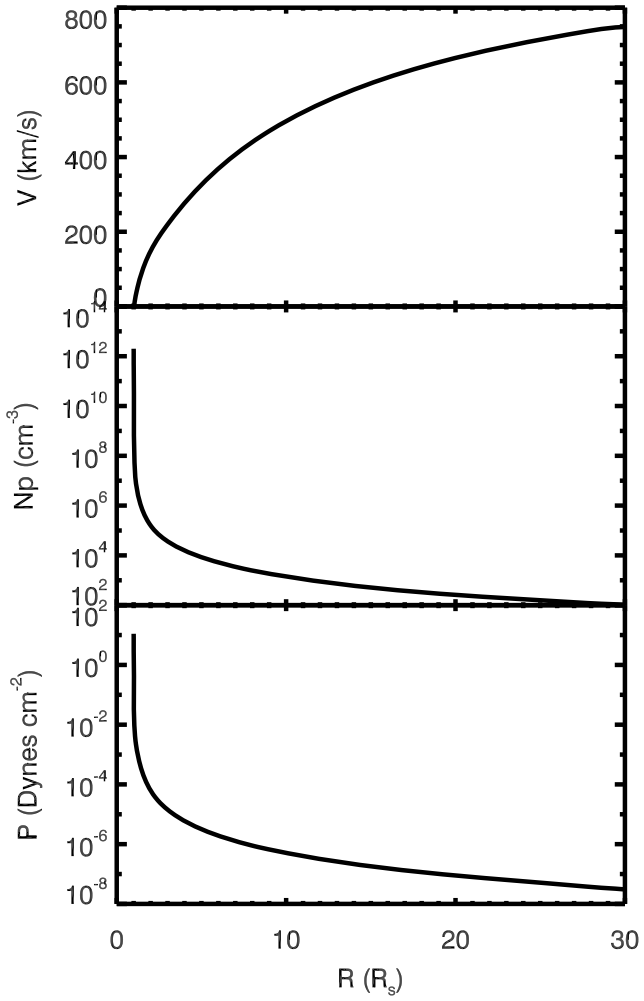

Figure 7. Variation of solar wind speed (v_r), number density (n_p), and thermal pressure (P) as a function of distance from the Sun, r, for a 1-D hydrodynamic simulation described in more detail in the text.

pressure at the base of the corona of $p_w = 8.4 \times 10^{-2}$ dyne/cm^2. The total power injected into the corona, using these parameters, is 4.9×10^{27} erg/s.

[19] Since both terms are often used, sometimes interchangeably, it is worth distinguishing between the volumetric heating rate (H) and flux (Q). The two quantities are related by:

$$H = -\nabla \cdot Q. \tag{6}$$

[20] Thus flux, which is prescribed on a spherical shell (typically the lower boundary of the calculation, $r = R_S$), is in units of ergs per square centimeter per second, while the volumetric heating rate is measured in units of energy per cubic centimeter per second. For the function given by equation (5), using equation (6), it is straightforward to show that:

$$H_o = \frac{Q_o}{\lambda_o\left(1 + \frac{2\lambda_o}{R_S} + \frac{2\lambda_o^2}{R_S^2}\right)} \tag{7}$$

which, for $\lambda_o \ll R_S$ reduces to $H_o = Q_o/\lambda_o$.

[21] Finally, it is worth noting that, while expressions developed to mimic heating in QRs and ARs depend explicitly on the magnetic field strength [*Lionello et al.*, 2009], the exponential heating function implemented for fast solar wind from within coronal holes does not. However, given the preceding discussion, it would not be unreasonable to presuppose that H_o depends on magnetic field strength, that is, $H_o = H_o(B)$.

[22] In summary, our 1-D model produces supersonic solar wind solutions for a variety of input parameters. For the current investigation, the most important are: (1) the volumetric heating rate at the base of the field line (H_o); (2) the heating scale length (λ_o); (3) the Alfvén wave pressure, specified by the average value of the IMF at 1 AU (P_{w0}); and (4) the magnetic field expansion factor ($f(r)$), which, in turn depends on expansion factor amplitude ($f_{\max}$), the expansion radius (r_o), and the width (σ) over which it operates.

3.2. Model Results

[23] Since the pioneering papers by *Kopp and Holzer* [1976] and *Withbroe* [1988], there have been many studies aimed at exploring and constraining the presumed relevant input parameters for solar wind solutions [e.g., *Leer and Holzer*, 1980; *Sandbaek and Leer*, 1995]. Our goal here is not to replicate these results, but to understand the results returned from Ulysses' first and third polar transits. To introduce the model results, we describe one specific solution in detail and summarize the main results from a selection of parametric studies.

[24] In Figure 7, solar wind density, velocity, and pressure are shown as functions of r for a solution for which: $H_o = 0.003$, $\lambda_o = 0.5$, $P_{w0} = 0.225$, $f_{\max} = 8.0$, $r_o = 1.3$, and $\sigma = 0.5$. To allow us the opportunity to perform a large number of runs, we chose the outer boundary to lie at 30 R_S. For fast solar wind, in particular, this is sufficiently far from the Sun that the plasma has reached a relatively asymptotic state, with v being essentially constant and n_p and B_r decreasing as r^{-2}. With these relationships, it is straightforward to extrapolate the plasma parameters from 30 R_S to 1 AU.

[25] The effects of different heat fluxes on the asymptotic properties of the solar wind are explored in Figure 8, which summarizes nine 1-D solutions, in which H_o was varied from 0.00033 to 0.0022, while holding all other input parameters constant ($\lambda_o = 0.7$, $P_{w0} = 0.225$, $f_{\max} = 8.0$, $r_o = 1.3$, and $\sigma = 0.5$). We note the following properties of the solutions: (1) n_p depends linearly on the heating rate; (2) solar wind speed is only modestly affected by different heating rates, and shows a tendency to asymptote to a constant value for sufficiently large values; and (3) the plasma thermal pressure also depends linearly on heat flux. Thus, temperature (not shown) is relatively independent of heat flux.

[26] We have also studied the effects of varying magnetic field expansion factors on the properties of the solar wind. Using the results of global MHD solutions (available at http://predsci.com/mhdweb/), we computed the expansion factors for four Carrington rotations, roughly coinciding with the four polar intervals indicated in Figure 2. These are summarized in Table 1. Although there is some variability within a single solution (both intrahemispheric and interhemispheric) in an average sense, we infer that the expansion factor has varied from between ~8 to ~12 during the four polar intervals. Thus, we conclude that, for a given photospheric magnetic

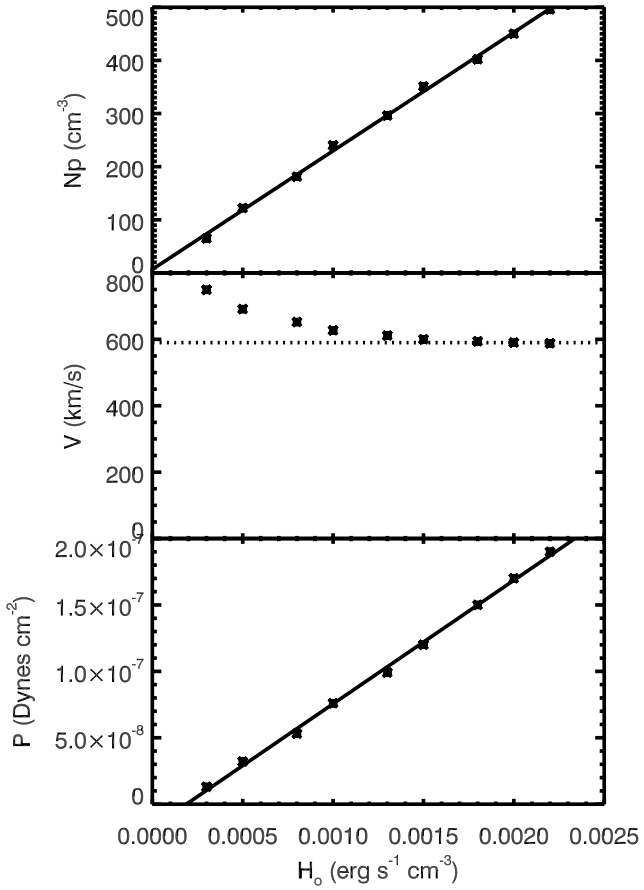

Figure 8. Variation of n_p, v_r, and P as a function of the amplitude of the volumetric heating rate, H_o for simulations described in more detail in the text. Least squares fits have been applied to the data in Figure 8 (top and bottom), while a straight, horizontal dashed line has been added to Figure 8 (middle) to draw attention to the flattening of the asymptotic speed with increasing H_o.

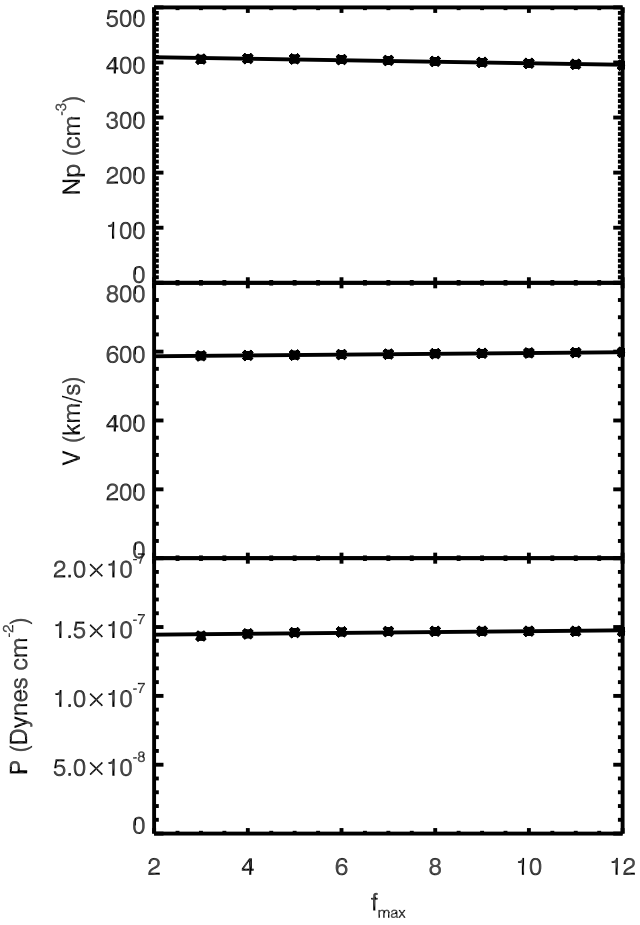

Figure 9. Variation of n_p, v_r, and P versus expansion factor amplitude, f_{max}, for simulations described in more detail in the text. Least square fits have been applied to each plot.

field strength, the expansion of the polar field lines alone cannot produce the significant differences in the interplanetary magnetic field that Ulysses observed between orbit 1 and 3. Or, phrased another way, we infer that the observed variations in the photospheric fields from one minimum to the next are propagated relatively directly to the interplanetary field. However, it is possible that these modest expansion factor differences affect the thermodynamic solutions, and, in particular, the properties of the solar wind plasma. Figure 9 shows how n_p, v_r, and P vary with expansion factor amplitude, f_{max}, when other inputs were held constant (λ_o = 0.7, P_{w0} = 0.225, r_o = 1.3, σ_{ef} = 0.5). Thus, as the expansion factor was increased from 8 to 12, the number density decreased by less than 2%, solar wind speed varied by 0.7%, and plasma pressure varied by 0.01%. We conclude, then, that, within the constraints of the model parameters, variations in expansion factor deep within coronal holes do not appreciably affect the properties of the solar wind plasma at 1 AU.

Table 1. Magnetic Expansion Factors, as Computed From Global MHD Solutions for the Carrington Rotations Indicated, Which Coincide With the Intervals S1, N1, S3, and N3[a]

CR	Date (DOY/Year)	N (Minimum/Maximum)	S (Minimum/Maximum)
1887	257/1994	6.6/8.3	9.0/9.6
1898	211/1995	7.3/9.1	8.8/9.24
2051	004/2007	7.8/9.6	10.2/11.7
2065	013/2008	8.3/9.6	7.5/9.4

[a]Expansion factors were computed by tracing from a regular grid at 30 R_S back down to the surface of the Sun. In each case, the minimum and maximum expansion factors for all latitudes above 70° are given.

4. Summary and Discussion

[27] Using Ulysses measurements, we have shown that the polar solar wind plasma density and interplanetary magnetic flux at the minimum of the solar activity cycle are linearly proportional to one another, consistent with the results of *Schwadron and McComas* [2008], *McComas et al.* [2008], and *Ebert et al.* [2009]. Using disc magnetograms from WSO, we have also shown that the solar minimum polar photospheric magnetic field correlates with the interplanetary magnetic field. And, using one-fluid simulations, we have shown that the density of the solar wind far from the Sun varies linearly with the volumetric heating rate. Taken together,

these results suggest that the heating rate within CHs scales linearly with the open, unsigned magnetic flux. These results are consistent with solar and astrophysical studies demonstrating a linear relationship between X-ray luminosity, L_x and the total unsigned magnetic flux in the low corona (Φ_{total}) [*Fisher et al.*, 1998; *Pevtsov et al.*, 2003]. In turn, they are supported by theoretical models of coronal heating and solar wind acceleration that suggest $H_o \propto B$ along open field lines [*Schwadron et al.*, 2006; *Cranmer*, 2009].

[28] We have also explored the possibility that differences in the expansion factor of the coronal magnetic field during the time from the S1 to N3 polar passes could account for the dramatic decrease in solar wind density (with little change in solar wind speed). However, even for a relatively large change in expansion factor, only a very modest change in number density was found. It is worth emphasizing that our results are not inconsistent with empirical models of Wang, Sheeley, Arge, and Suzuki [*Wang and Sheeley*, 1990; *Arge and Pizzo*, 2000; *Suzuki*, 2006]. Their negative correlation between expansion factor and solar wind speed is driven primarily by the bimodal slow and fast components of the solar wind. (See, for example, the correlation between solar wind speed and $1/f$ in Figure 1 (middle) of *Suzuki* [2006].) In this study, we have concerned ourselves exclusively with the properties of fast solar wind emanating from deep within polar coronal holes.

[29] Our model results (Figure 8) suggest that for a fixed flux of Alfvén waves (set by a parameter proportional to the strength of the IMF), solar wind speed increases as the heating is reduced. This presents a potential paradox: if we are to assume $H_o \propto B$, then, as we move deeper into a polar coronal hole and the large-scale field strengthens, the heating rate increases, and thus, we would predict slightly lower speeds. Ulysses observations, however, during its first fast latitude scan in the late declining phase of solar cycle 22 clearly, showed a small, but significant increase in speed toward each pole. This likely reflects an inconsistency in our hydrodynamic, 1-D model, in the sense that: (1) H_o is specified independently of the strength of the IMF used to drive the Alfvén waves; and (2) the results in Figure 8 relied on a fixed flux of Alfvén waves. In a more consistent approach, where $H_o \propto B$, the Alfvén wave pressure would also be coupled to B. Thus, as B increased, although H_o would also increase, the asymptotic wind speed would be boosted by a larger Alfvén wave pressure.

[30] The relationship between proton number density and the interplanetary magnetic field described here is not envisaged to hold in general for the entire solar wind. In particular, in comparing the slow and fast wind, we note that the density is approximately inversely proportional to the solar wind speed such that the mass flux is roughly constant [e.g., *Riley et al.*, 1997]. On the other hand, Ulysses measurements have also shown that the radial magnetic field is essentially independent of latitude [*Smith et al.*, 1995]. Thus, in the absence of stream interactions, B_r remains constant while n_p varies inversely with solar wind speed. Even when stream dynamics are considered, the principal effects are to modify the transverse components of the field, not the radial component. Within compression/rarefaction regions, n_p increases/decreases as does the transverse component of $\mathbf{B}$, $\mathbf{B}_t$ (and hence B), while B_r remains unchanged. Thus, we argue that the relationship between n_p and B_r described here cannot result from evolutionary processes as the plasma propagates away from the Sun. Instead, it points to a more fundamental solar origin: The strength of the solar magnetic field controls the amount by which the coronal plasma is heated, which in turn, governs the resulting density of the solar wind plasma.

[31] The present study complements and is consistent with the results of *Schwadron and McComas* [2008]. Whereas we have deduced a relationship between the average interplanetary radial magnetic field component and the solar wind number density, they showed how solar wind power correlates well with the Sun's total open flux, which is approximately B_r. Since the solar wind power (sufficiently far from the Sun that gravitational effects can be neglected) varies as $n_p V_{sw}^2$, and V_{sw} was essentially the same during Ulysses' first and third orbit polar passes [*McComas et al.*, 2008], it is not surprising that a correlation exists for both sets of parameters.

[32] **Acknowledgments.** P.R., Z.M., J.A.L., and R.L. gratefully acknowledge the support of the National Aeronautics and Space Administration and National Science Foundation. D.M. gratefully acknowledges support from NASA's ACE and Ulysses programs.

[33] Philippa Browning thanks Leonard Strachan and Roland Grappin for their assistance in evaluating this paper.

References

Arge, C. N., and V. J. Pizzo (2000), Improvement in the prediction of solar wind conditions using near-real time solar magnetic field updates, *J. Geophys. Res.*, *105*(A5), 10,465.

Cranmer, S. R. (2009), Coronal holes, *Living Rev. Sol. Phys.*, *6*, arXiv:0909.2847v1.

Cranmer, S. R., A. A. van Ballegooijen, and R. J. Edgar (2007), Self-consistent coronal heating and solar wind acceleration from anisotropic magnetohydrodynamic turbulence, *Astrophys. J. Suppl. Ser.*, *171*, 520–551, doi:10.1086/518001.

Ebert, R. W., D. J. McComas, H. A. Elliott, R. J. Forsyth, and J. T. Gosling (2009), Bulk properties of the slow and fast solar wind and interplanetary coronal mass ejections measured by Ulysses: Three polar orbits of observations, *J. Geophys. Res.*, *114*, A01109, doi:10.1029/2008JA013631.

Fisher, G. H., D. W. Longcope, T. R. Metcalf, and A. A. Pevtsov (1998), Coronal heating in active regions as a function of global magnetic variables, *Astrophys. J.*, *508*, 885–898, doi:10.1086/306435.

Fisk, L. A. (2003), Acceleration of the solar wind as a result of the reconnection of open magnetic flux with coronal loops, *J. Geophys. Res.*, *108*(A4), 1157, doi:10.1029/2002JA009284.

Fisk, L. A., and T. H. Zurbuchen (2006), Distribution and properties of open magnetic flux outside of coronal holes, *J. Geophys. Res.*, *111*, A09115, doi:10.1029/2005JA011575.

Fisk, L. A., T. H. Zurbuchen, and N. A. Schwadron (1999), On the coronal magnetic field: Consequences of large-scale motions, *Astrophys. J.*, *521*(2), 868.

Geiss, J., G. Gloeckler, and R. von Steiger (1995), Origin of the solar wind from composition data, *Space Sci. Rev.*, *72*, 49–60, doi:10.1007/BF00768753.

Holzer, T. E., and E. Leer (1980), Conductive solar wind models in rapidly diverging flow geometries, *J. Geophys. Res.*, *85*, 4665–4679, doi:10.1029/JA085iA09p04665.

Klimchuk, J. A. (2006), On solving the coronal heating problem, *Sol. Phys.*, *234*, 41–77, doi:10.1007/s11207-006-0055-z.

Kopp, R. A., and T. E. Holzer (1976), Dynamics of coronal hole regions. I - Steady polytropic flows with multiple critical points, *Sol. Phys.*, *49*, 43–56, doi:10.1007/BF00221484.

Leer, E., and T. E. Holzer (1980), Energy addition in the solar wind, *J. Geophys. Res.*, *85*, 4681–4688, doi:10.1029/JA085iA09p04681.

Leer, E., T. E. Holzer, and T. Fla (1982), Acceleration of the solar wind, *Space Sci. Rev.*, *33*, 161–200, doi:10.1007/BF00213253.

Lionello, R., J. A. Linker, and Z. Mikić (2009), Multispectral emission of the Sun during the first whole Sun month: Magnetohydrodynamic simulations, *Astrophys. J.*, *690*, 902–912, doi:10.1088/0004-637X/690/1/902.

McComas, D. J., R. W. Ebert, H. A. Elliott, B. E. Goldstein, J. T. Gosling, N. A. Schwadron, and R. M. Skoug (2008), Weaker solar wind from the polar coronal holes and the whole Sun, *Geophys. Res. Lett.*, *35*, L18103, doi:10.1029/2008GL034896.

Owens, M. J., and N. U. Crooker (2006), Coronal mass ejections and magnetic flux buildup in the heliosphere, *J. Geophys. Res.*, *111*, A10104, doi:10.1029/2006JA011641.

Parker, E. N. (1958), Dynamics of the interplanetary gas and magnetic fields, *Astrophys. J.*, *128*, 664.

Parker, E. N. (1963), *Interplanetary Dynamical Processes*, Interscience, New York.

Parker, E. N. (1965), Dynamical theory of the solar wind, *Space Sci. Rev.*, *4*, 666–708, doi:10.1007/BF00216273.

Parker, E. N. (1988), Nanoflares and the solar X-ray corona, *Astrophys. J.*, *330*, 474–479, doi:10.1086/166485.

Pevtsov, A. A., G. H. Fisher, L. W. Acton, D. W. Longcope, C. M. Johns-Krull, C. C. Kankelborg, and T. R. Metcalf (2003), The relationship between X-ray radiance and magnetic flux, *Astrophys. J.*, *598*, 1387–1391, doi:10.1086/378944.

Pinto, R., R. Grappin, Y. Wang, and J. Léorat (2009), Time-dependent hydrodynamical simulations of slow solar wind, coronal inflows, and polar plumes, *Astron. Astrophys.*, *497*, 537–543, doi:10.1051/0004-6361/200811183.

Riley, P. (2007), An alternative interpretation of the relationship between the inferred open solar flux and the interplanetary magnetic field, *Astrophys. J. Lett.*, *667*, L97–L100, doi:10.1086/522001.

Riley, P. (2010), The three-dimensional structure of the inner heliosphere, in *Proceedings of Twelfth International Solar Wind Conference*, edited by M. Maksimovic, Am. Inst. of Phys., Melville, N. Y., in press.

Riley, P., et al. (1997), Ulysses solar wind plasma observations at high latitudes, *Adv. Space Res.*, *20*, 15.

Riley, P., J. A. Linker, and Z. Mikić (2001), An empirically driven global mhd model of the corona and inner heliosphere, *J. Geophys. Res.*, *106*(A8), 15,889.

Riley, P., J. A. Linker, and Z. Mikic (2009), Global MHD modeling of the solar corona and inner heliosphere for the whole heliosphere interval, paper presented at IAU General Assembly Joint Discussion JD16, Rio de Janeiro, Brazil.

Sandbaek, O., and E. Leer (1995), Coronal heating and solar wind energy balance, *Astrophys. J.*, *454*, 486, doi:10.1086/176500.

Schwadron, N. A., and D. J. McComas (2008), The solar wind power from magnetic flux, *Astrophys. J. Lett.*, *686*, L33–L36, doi:10.1086/592877.

Schwadron, N. A., D. J. McComas, and C. DeForest (2006), Relationship between solar wind and coronal heating: Scaling laws from solar X-rays, *Astrophys. J.*, *642*, 1173–1176, doi:10.1086/501066.

Smith, E. J., M. Neugebauer, A. Balogh, S. J. Bame, R. P. Lepping, and B. T. Tsurutani (1995), ULYSSES observations of latitude gradients in the heliospheric magnetic field: Radial component and variances, *Space Sci. Rev.*, *72*, 165–170, doi:10.1007/BF00768773.

Suzuki, T. K. (2006), Forecasting solar wind speeds, *Astrophys. J. Lett.*, *640*, L75–L78, doi:10.1086/503102.

Wang, Y., Y. Ko, and R. Grappin (2009), Slow solar wind from open regions with strong low-coronal heating, *Astrophys. J.*, *691*, 760–769, doi:10.1088/0004-637X/691/1/760.

Wang, Y. M., and N. R. Sheeley Jr. (1990), Solar wind speed and coronal flux-tube expansion, *Astrophys. J.*, *355*, 726.

Withbroe, G. L. (1988), The temperature structure, mass, and energy flow in the corona and inner solar wind, *Astrophys. J.*, *325*, 442–467, doi:10.1086/166015.

J. A. Linker, R. Lionello, Z. Mikic, and P. Riley, Predictive Science, 9990 Mesa Rim Rd., Ste. 170, San Diego, CA 92121, USA. (pete@predsci.com)

D. J. McComas, Southwest Research Institute, San Antonio, TX 78228, USA.

N. A. Schwadron, Department of Astronomy, Boston University, Boston, MA 02215, USA.

Appendix D

Interpretation of the cross-correlation function of ACE and STEREO solar wind velocities using a global MHD Model

Riley, P. and Luhmann, J. and Opitz, A. and Linker, J. A. and Mikic, Z.

Published in J. Geophys. Res., 2010.

Interpretation of the cross-correlation function of ACE and STEREO solar wind velocities using a global MHD Model

Pete Riley,[1] J. Luhmann,[2] A. Opitz,[3] J. A. Linker,[1] and Z. Mikic[1]

Received 25 May 2010; revised 7 July 2010; accepted 13 August 2010; published 13 November 2010.

[1] Measurements from the ACE and STEREO A and B spacecraft are allowing an unprecedented view of the structure of the three-dimensional heliosphere. One aspect of this is the degree to which the measurements at one spacecraft correlate with those at the other. We have computed the cross-correlation functions (CCFs) for all three combinations of ACE and STEREO A and B in situ observations of the bulk solar wind velocity as the spacecraft moved progressively farther away from one another. Our results confirm previous studies that the phase lag between the signals becomes linearly larger with time. However, we have identified two intervals where this appears to break down. During these "lulls," the CCF reveals a phase lag considerably less than that which would be predicted based only on the angular separation of the spacecraft. We modeled the entire STEREO time period using a global MHD model to investigate the cause for these "lulls." We find that a combination of time-dependent evolution of the streams as well as spatial inhomogeneities, due to the latitudinal separation of the spacecraft, are sufficient to explain them.

Citation: Riley, P., J. Luhmann, A. Opitz, J. A. Linker, and Z. Mikic (2010), Interpretation of the cross-correlation function of ACE and STEREO solar wind velocities using a global MHD Model, *J. Geophys. Res.*, *115*, A11104, doi:10.1029/2010JA015717.

1. Introduction

[2] The STEREO (Solar Terrestrial RElations Observatory) spacecraft launched on 25 October 2006 on a Delta II rocket. Since early 2007, it has been continuously returning a wide range of remote solar and in situ measurements of the Sun's corona and the inner heliosphere. Charged with a number of fundamental scientific objectives, one of particular relevance to this study is to improve our understanding of the structure of the ambient solar wind. With nearly identical instrumentation, the STEREO ahead (A) and behind (B) spacecraft are separating by ~45° per year. Restricted to the ecliptic plane, in addition to the monotonically increasing longitudinal separation, the spacecraft also separate from one another in radial separation (up to a maximum of ~0.15 AU) as well as in heliographic latitude (up to a maximum separation of ~14.4°). THE ACE (Advanced Composition Explorer) spacecraft launched on 25 August 1997, and since then has provided a continuous stream of in situ measurements of the solar wind [*Stone et al.*, 1998]. The measurements from STEREO A and B, coupled with those from ACE, thus represent a unique data set from which to study the effects of spatial and temporal evolution of solar wind streams, and, in particular, to assess the degree of correlation between them.

[3] Previous studies have investigated the correlation of solar wind stream structure from one and multiple spacecraft. The first comprehensive auto-correlation analysis of in situ solar wind data was performed by *Gosling and Bame* [1972]. Using solar wind speed data from the Vela 2 and 3 missions, they assessed to what extent solar wind structure persisted from one rotation to the next. They found that the average correlation was only 0.3, suggesting that most structure did not persist from one rotation to the next; However, this coefficient varied from 0.1 to 0.7 at different times. They also noted that differential rotation affected the results, the implication being that a wide range of heliolatitudes contributed to the solar wind measured at Earth. In a more comprehensive analysis, *Gosling et al.* [1976] found that the most stable stream structure occurred during the declining phase of the solar cycle. *Richardson et al.* [1998] cross-correlated data from ISEE 3 at L1 and IMP 8 at Earth for times corresponding to near-solar maximum conditions. They found that the temporal lag between the structures observed at the two spacecraft depended on both the radial and azimuthal separation. Additionally, they found that the lag required a correction due to corotation, that is, that the stream normals are tilted away from the radial direction and toward the direction of planetary motion. In contrast, *Paularena et al.* [1998], investigating the correlation between data observed by IMP 8, Interball-1, and Wind during near-solar minimum conditions, found that the correlation depended only on the radial separation of the spacecraft and not on the azimuthal separation. Moreover, they did not find any need to correct for corotation. *Richardson et al.* [1998] suggested that the smaller angular separation of the spacecraft in the *Paularena et al.* [1998]

[1]Predictive Science, San Diego, California, USA.
[2]SSL, University of California, Berkeley, California, USA.
[3]Centre d'Etude Spatiale des Rayonnements (CNRS-UPS), University of Toulouse, Toulouse, France.

0148-0227/10/2010JA015717

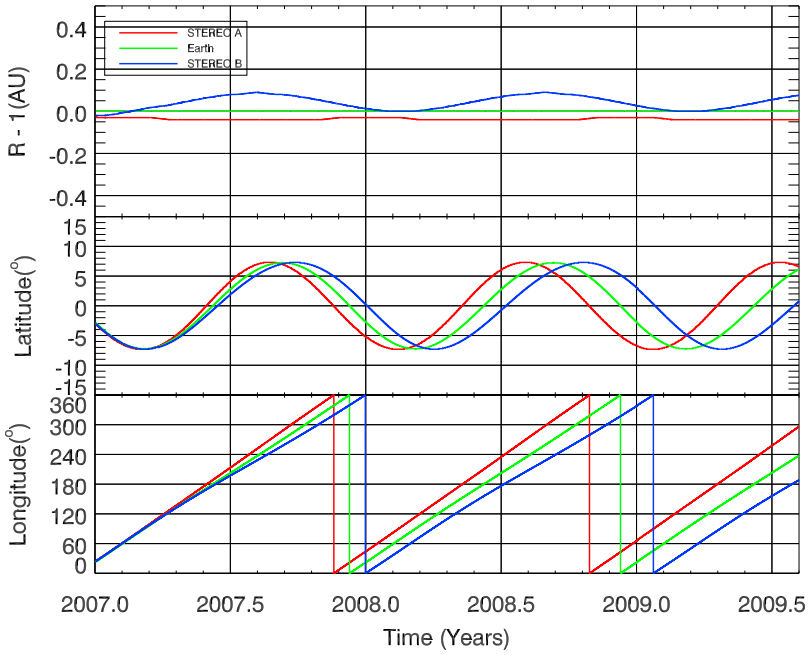

Figure 1. Ephemeris data for the ACE and STEREO spacecraft. In each frame, the red curve corresponds to the location of STEREO A, the blue curve to the location of STEREO B, and the green curve to the location of ACE. (top) The heliocentric location of the spacecraft, plotted relative to 1 AU. (middle) The heliographic latitude of the spacecraft. (bottom) The heliographic, inertial longitude of the spacecraft.

study, together with the fact that the two investigations used data from different extremes of the solar cycle could account for these apparent contradictions.

[4] *Podesta et al.* [2008] first reported on the correlation length of large-scale solar wind velocity fluctuations measured at STEREO A and B. They focused on the interval between February 2007 and August 2007, corresponding to near-solar minimum conditions. They found that the transverse correlation length was 0.25 ± 0.02 AU. *Opitz et al.* [2009] analyzed the solar wind velocity from STEREO A and B from March to August of 2007. Their study focused on the temporal evolution of the solar wind at the two spacecraft by removing spatial effects caused by the radial and angular separation of the two spacecraft. In particular, they time-shifted STEREO B, accounting for both longitudinal and radial separation and computed the correlation coefficient between it and STEREO A data. They found that the correlation decreased with increasing separation (and time). However, they noted some exceptions to the otherwise good correlations found: (1) day 142, 2007, which coincided with an ICME; (2) day 155, 2007, associated with a CIR; (3) day 201, 2007, which coincided with significant velocity gradient bisecting the ~2° latitudinal separation of the spacecraft [*Rouillard et al.*, 2009]; and (4) days 227–235, 2007. They ascribed the poor correlation during the first portion of this last interval (days 227–231) to temporal evolution of the solar wind source as it moved from under one spacecraft to the other. Since the stream structure of the second half of this interval remained intact one rotation later, they suggested that the poor correlation was due to spatial inhomogeneities.

2. Orbits of the ACE and STEREO Spacecraft

[5] The relative locations of the ACE and STEREO spacecraft obviously play an important role in understanding the large-scale correlation of solar wind parameters. Figure 1 summarizes the heliocentric distance, latitude, and longitude of the spacecraft, together with the differences between them. In Figure 1 (top), R - 1 is plotted, showing that the STEREO spacecraft oscillate about values slightly less or more than 1 AU. These oscillations are synchronous so that during mid/late 2007, 2008, and 2009 the spacecraft have a maximum radial separation of ~0.13 AU. We can estimate the maximum temporal lag between the STEREO spacecraft due to the radial separation using $\Delta t = \Delta r / v_{sw}$. Assuming v_{sw} = 600 km s^{-1}, we obtain $\Delta t \sim 9$ h. The temporal lag due to longitudinal effects obviously begins to dominate once the spacecraft are separated by $\sim \frac{1 day}{27 days} \times 360° \sim 13°$. Following launch, the two STEREO spacecraft maintained their position in the ecliptic plane, but as they moved farther away from Earth (and hence ACE), their heliographic latitudinal separation began to oscillate, the amplitude of which became progressively larger. Maximum latitudinal differences occurred at the shortly before the beginning of, and midway through each year. Finally, in Figure 1 (bottom), the inertial longitude of the three spacecraft is shown. Of particular note is that this separation is not strictly linear: Prior to, and during the early portion of each calendar year, the increase in separation is modest, whereas, for the remainder of the year, it is more pronounced.

[6] In this study, we investigate the evolving cross-correlation functions (CCFs) computed from 1 h averaged solar wind velocity measurements from the PLASTIC instruments [*Galvin et al.*, 2008] onboard STEREO A and B and the SWEPAM instrument onboard ACE [*McComas et al.*, 1998]. The three spacecraft allow us to compute three CCFs: (1) STEREO B/ACE; (2) ACE/STEREO A; and (3) STEREO B/ACE. Unlike the previous study of *Opitz et al.* [2009], which did not include near-Earth measurements, we do not assume and apply a phase lag between the measurements

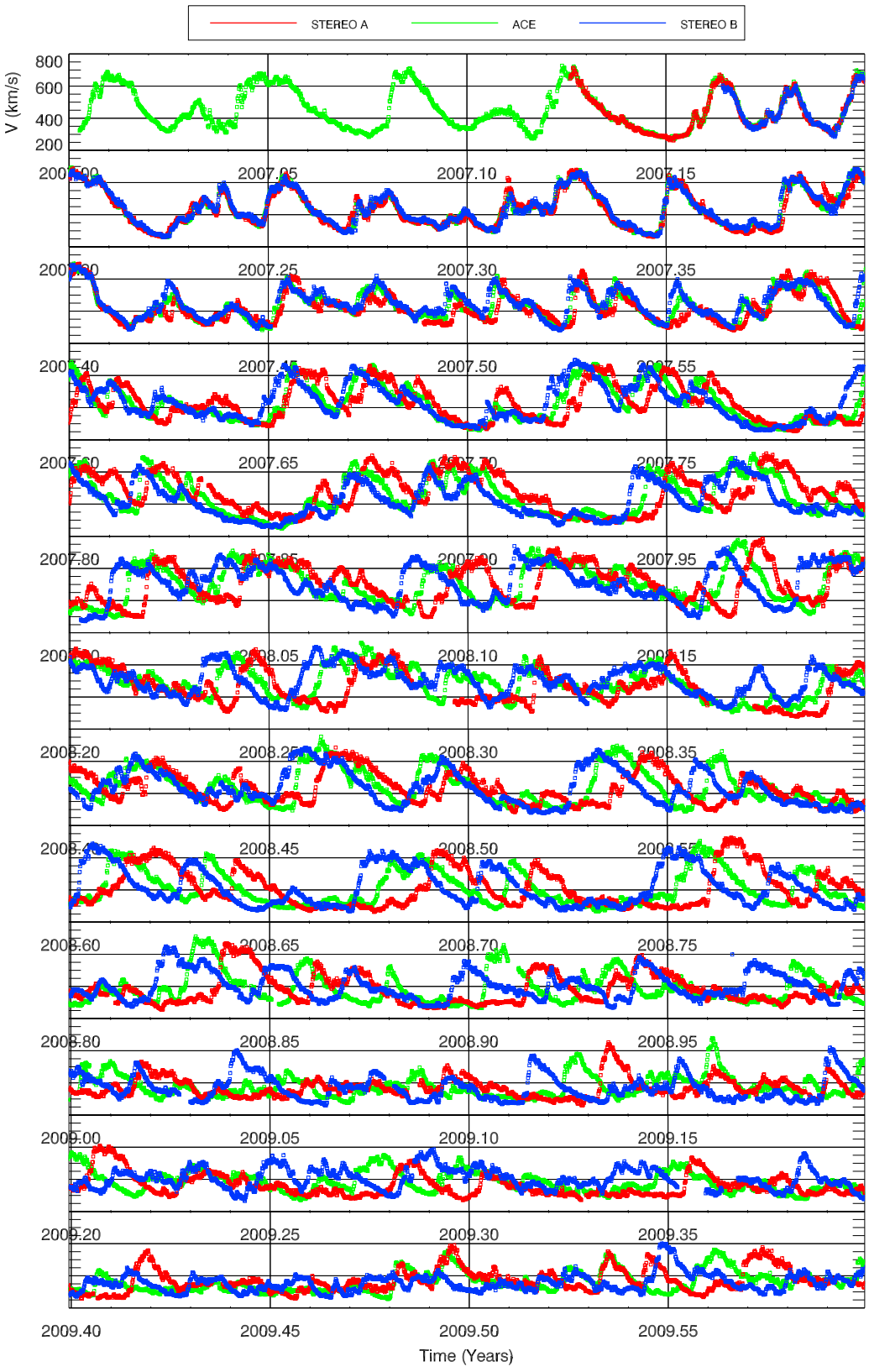

Figure 2. Bulk solar wind speed from (top) 2007.0 through (bottom) 2009.5. Green, red, and blue correspond to ACE, STEREO A, and STEREO B, respectively. A movie illustrating the evolution of these streams can be viewed/downloaded at http://www.predsci.com/stereo/movies/.

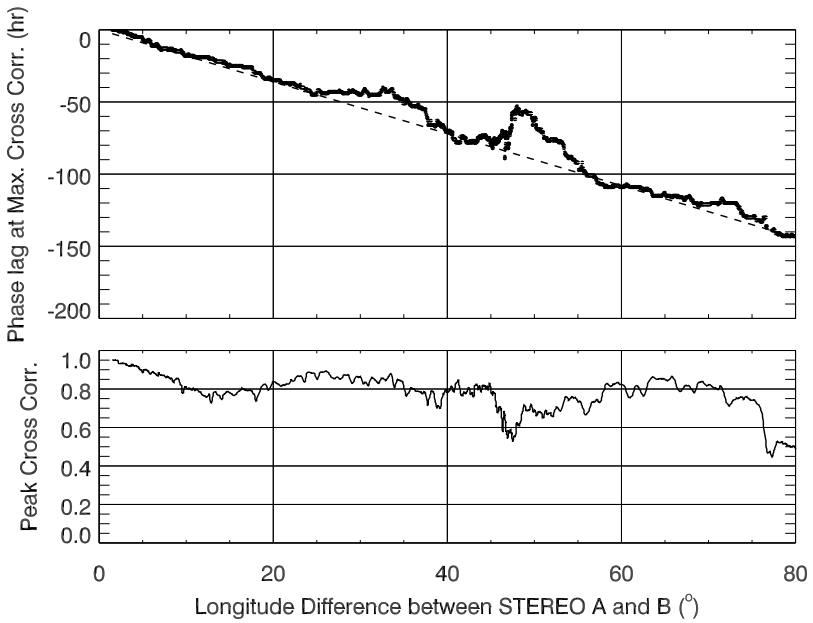

Figure 3. (top) The temporal phase lag that maximizes the cross-correlation function (CCF) between the solar wind velocities measured at STEREO B and A, plotted as a function of longitudinal separation of the spacecraft. (bottom) The correlation coefficient corresponding to the phase lag in the plot above.

from which a correlation coefficient is computed, but rather compute the temporal phase lag between each pair of spacecraft that maximizes the CCF. To a first approximation, the results match our intuition and previous studies, that the phase lag increases linearly with the angular separation of the spacecraft; However, there are two interesting intervals, in particular, where the phase lag "pauses." We use global MHD model solutions to show that these intervals are due to a combination of both temporal and spatial effects.

3. Analysis of ACE and STEREO In Situ Bulk Solar Wind Speed Observations

[7] In general, the CCF between two continuous functions is the integral of the complex conjugate of one variable and the time-shifted value of the other variable,

$$(f \text{ å } g)(\Delta t) = \int_{-\infty}^{\infty} f^{*}(\tau) g(\Delta t + \tau) d\tau. \quad (1)$$

Extending this to real-valued discrete functions of finite length, which in this study are the bulk solar wind velocities measured at the two spacecraft (v_A and v_B) over some temporal lag, Δt, we can define the CCF to be

$$(v_A \text{ å } v_B)(\Delta t) = \frac{\sum_{k=0}^{N-|\Delta t|-1} \left(v_{A,k+|\Delta t|} - \overline{v}_A\right)\left(v_{B,k} - \overline{v}_B\right)}{\sqrt{\left[\sum_{k=0}^{N-1}\left(v_{A,k} - \overline{v}_A\right)^2\right]\left[\sum_{k=0}^{N-1}\left(v_{B,k} - \overline{v}_B\right)^2\right]}} \; for L < 0$$

$$= \frac{\sum_{k=0}^{N-|\Delta t|-1} \left(v_{A,k} - \overline{v}_A\right)\left(v_{B,k+\Delta t} - \overline{v}_B\right)}{\sqrt{\left[\sum_{k=0}^{N-1}\left(v_{A,k} - \overline{v}_A\right)^2\right]\left[\sum_{k=0}^{N-1}\left(v_{B,k} - \overline{v}_B\right)^2\right]}} \; for L > 0, \quad (2)$$

where $\overline{v}_A$ and $\overline{v}_B$ are the mean values of variables between 0 and N - 1 (The algorithm used to compute this function is available as part of the Interactive Data Language (IDL) numerical package (c_correlate.pro in the main library directory)).

[8] Thus, for two real-valued functions (v_A and v_B), which differ only by a shift along the time axis, we can compute the CCF for a range of time lags (Δt). Where the functions match, the peaks and troughs become aligned, making a positive contribution to the summation, and the CCF is maximized. In the specific case of bulk solar wind velocities, which are always positive, the CCF maximum is weighted more by the fast solar wind streams, than the slow wind, since they contribute proportionately more to the summations.

[9] Figure 2 illustrates graphically how the time shift that maximizes the CCF increases as the angular separation of the spacecraft becomes larger. We can estimate how we would expect the time lag (Δt) that maximizes the CCF to increase with angular separation ($\Delta\lambda$). It is simply the fraction of a solar rotation by which the spacecraft are separated. Thus, we anticipate that the phase lag should change by

$$\Delta t = -\frac{\tau_{rot}}{360^{\circ}} \Delta\lambda, \quad (3)$$

where τ_{rot} is the rotation period of the Sun, and we have chosen a negative decrease to reflect a convention that it is the amount of time that measurements from the ahead spacecraft must be shifted back in time to align with the spacecraft located at an earlier longitude. As a concrete example, at a separation of 55.5°, the predicted absolute phase lag would be ~100 h, or a little over 4 days. It is worth noting that the synodic (τ_{rot} = 27.27 days), rather than the sidereal (τ_{rot} = 25.38 days) period is the appropriate interval to use, since the spacecraft are drifting in an Earth-based reference frame, and not some fixed inertial point in space.

[10] In Figure 3 (top), we have identified and plotted the phase lag of the peak of the computed CCF as a function of

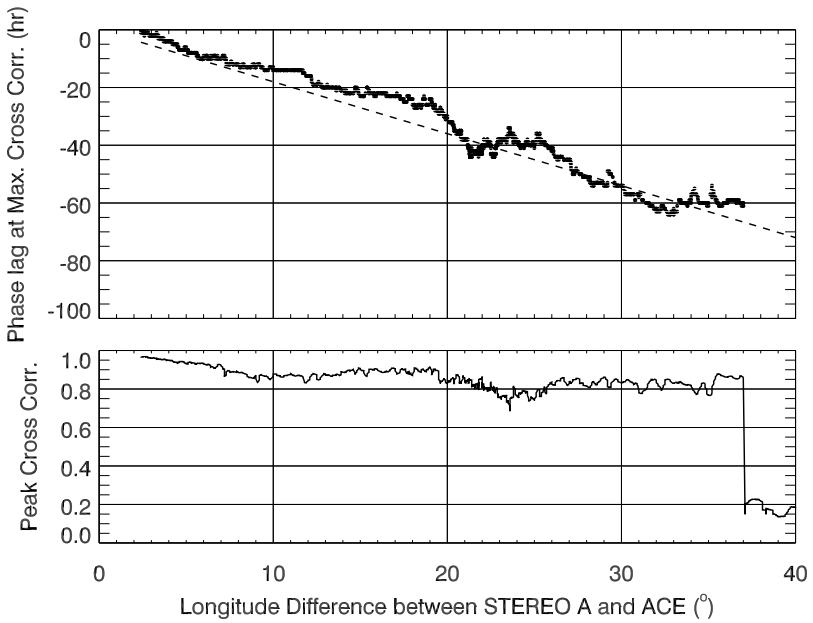

Figure 4. As in Figure 3, but for ACE and STEREO A. Note that the scales for the (top and bottom) abscissa and (top) ordinate span half the range of those in Figure 3.

the STEREO A and B spacecraft separation. A CCF was computed every 10^{-3} years and each CCF was computed using a window of 0.1 years. The phase lag was identified automatically by locating the peak in the CCF and all CCFs were visually inspected to verify that the peak represented a pronounced maximum in the distribution. The anticipated phase lag from equation (3) is shown by the dashed line. To a first approximation, then the computed phase lag matches the simple formula. That is, the phase lag increases linearly with time. However, two obvious deviations are apparent. Since they represent intervals where the phase lag appears to "pause" from its trend of increasing, we refer to them as "lulls." The first is centered on Carrington rotation (CR) 2061 (which spanned from 10 September 2007 to 8 October 2007, or days 253 through 281), while the second is centered on CR 2069 (which spanned from 16 April 2008 to 13 May 2008, or days 107 through 134). Both intervals encompass approximately the same duration in longitude, ~12.5°, corresponding to ~3.5 months or 101 days. Whereas the first has the appearance of a "pause," in the sense that the phase lag holds steady at −45 h before returning to its expected value, the second shows a significant reversal in the trend of increasing lag: Where the

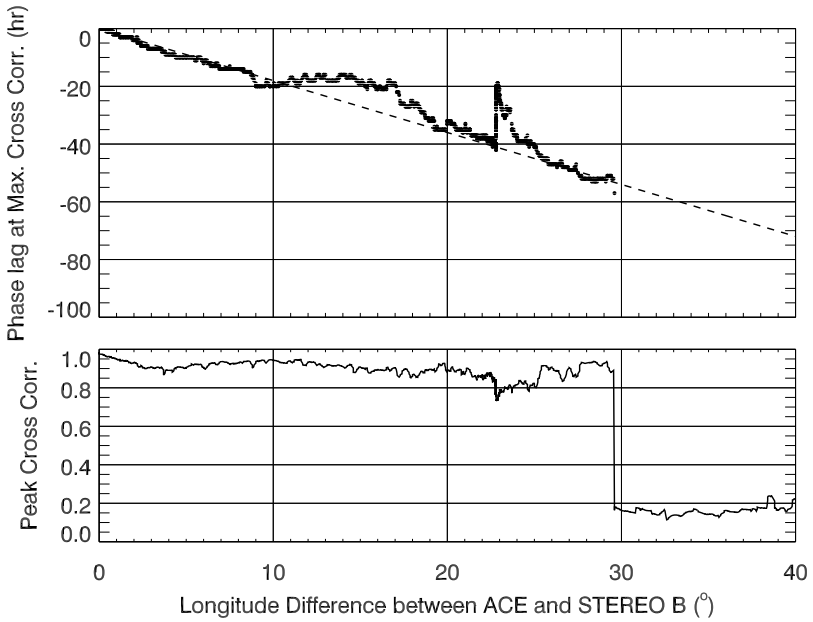

Figure 5. As in Figure 3, but for STEREO B and ACE.

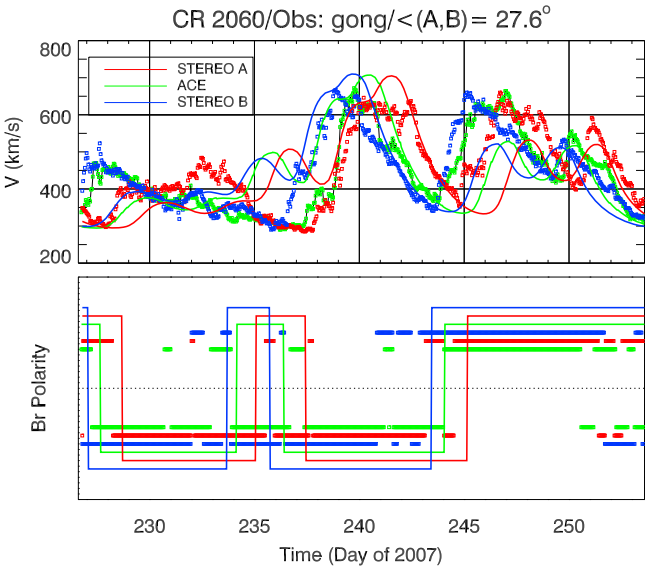

Figure 6. Comparison of model results with (top) in situ speed and (bottom) radial IMF polarity for Carrington rotation (CR) 2060. The solid lines are model results, and the symbols are in situ measurements from ACE (green), STEREO A (red), and STEREO B (blue). The amplitude of polarities have been adjusted to more easily show the variations at each spacecraft; there is no physical significance however to them.

predicted lag would have been −90 h, the computed lag was only −55 h, a difference of 35 h, or 19.4° in effective longitude.

[11] In Figure 3 (bottom), we show the value of the peak correlation coefficient at that phase lag. Thus, until the STEREO spacecraft reached a separation of ~75°, the correlation coefficient exceeded 0.6 and, for the majority of the time remained near 0.8. We note that during the first lull, the peak cross-correlation coefficient was slightly higher than the surrounding values, but during the second lull, it was markedly lower. Beyond ~75°, as the peak correlation coefficient decreased, multiple peaks appeared, and, while it would have been possible to force a local phase lag that matched our expectations based on equation (3), the low value of the correlation coefficient would cast doubt on any inferences drawn.

[12] We performed a similar analysis for ACE and STEREO A. The results are shown in Figure 4. We have scaled the plot to half the maximum values of Figure 3 so that features can be compared directly. In particular, by scaling the longitude to half the maximum value of Figure 3, the two panels span the same duration in time. In the top, we can see similar lulls centered at approximately 17° and 29°. These are roughly half the longitudinal separations for the lulls found in the analysis of STEREO A/B, and thus occur at the same time. Concerning the duration of the lulls; while the second one lasts approximately the same duration in time, the first appears to be significantly broader. We also note that the peak cross-correlation coefficient is, on average slightly larger for this pair of spacecraft; a predictable result given that the spacecraft are closer to one another.

[13] Finally, in Figure 5, we summarize the cross-correlation analysis for STEREO B and ACE. Here the first lull is approximately the same duration as in Figure 3, while the second one is slightly shorter. More strikingly, the second lull shows a steep initial rise from −40 h to less than −20 h, with a subsequent slower decay back to the predicted phase lag.

4. Global MHD Model Solutions for the STEREO Era

[14] The first MHD models of the solar corona were developed almost 40 years ago [*Endler*, 1971; *Pneuman and Kopp*, 1971]. Over the years they have become progressively more sophisticated [*Steinolfson et al.*, 1982; *Linker et al.*, 1990; *Mikić and Linker*, 1994], culminating in models that include the photospheric field as a boundary condition [*Usmanov*, 1993; *Mikic et al.*, 1996; *Riley et al.*, 2001a; *Roussev et al.*, 2003]. Complementary efforts focusing on heliospheric models, where the inner boundary was placed beyond the outermost critical point, have also been pursued [*Dryer et al.*, 1978; *Pizzo*, 1978; *Smith and Dryer*, 1990; *Detman et al.*, 1991; *Odstrcil*, 1994]. Most recently, coronal

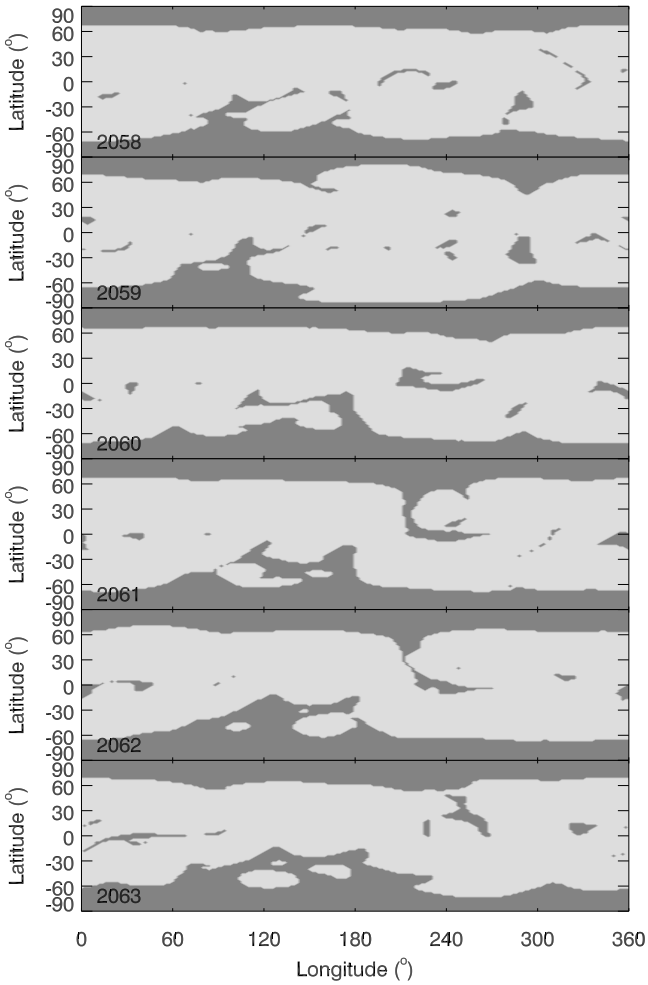

Figure 7. The computed coronal holes for CRs 2058 through 2063. These were obtained by tracing magnetic field lines outward from the photosphere and into the heliosphere. If the field line returned to the photosphere, it was labeled "closed" and shaded light gray, whereas if it reached the outer radial boundary of the simulation domain, it was labeled "open" and shaded dark gray.

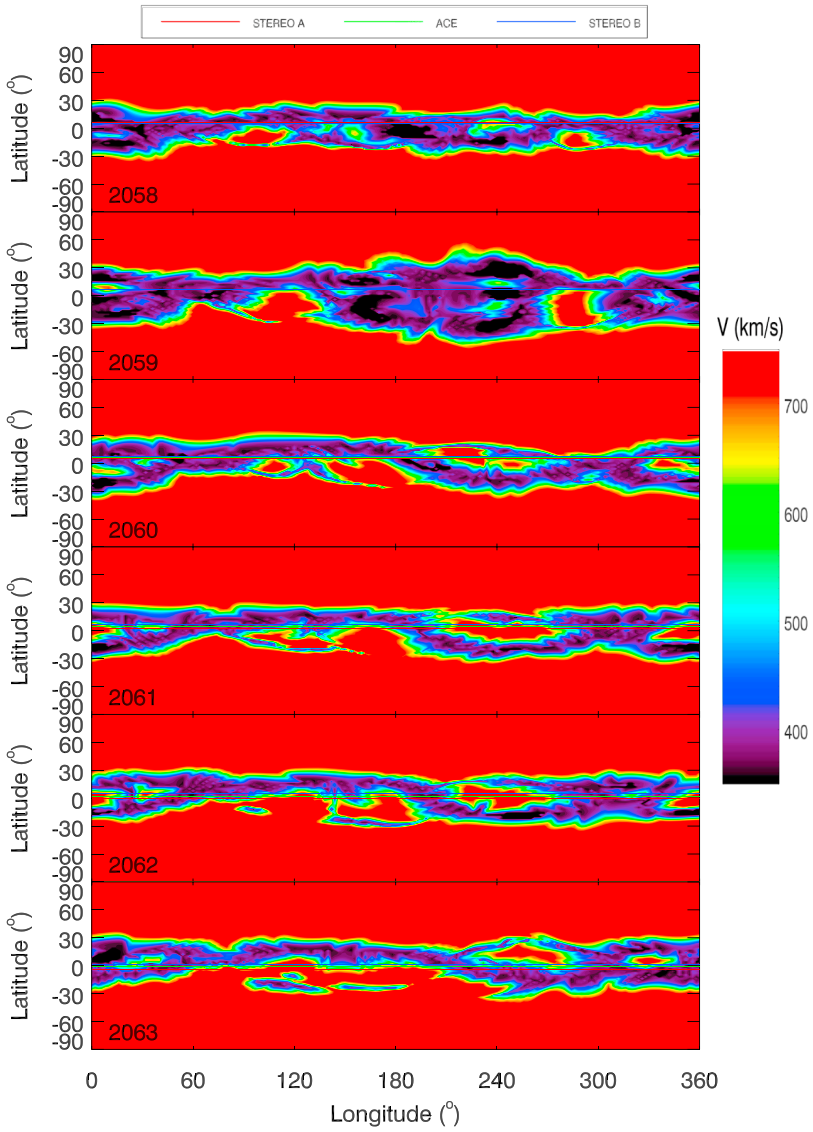

Figure 8. The computed radial solar wind velocities for CRs 2058 through 2063. These were obtained by mapping a photospheric velocity profile [see *Riley et al.*, 2001a] outward along open field lines to 30 R_S. Red corresponds to ~750 km s^{-1}, while black corresponds to ~350 km s^{-1}.

and heliospheric models have been coupled [*Riley et al.*, 2001a, 2002; *Odstrcil et al.*, 2002; *Riley et al.*, 2003; *Odstrcil et al.*, 2004; *Manchester et al.*, 2006; *Riley et al.*, 2007] and more sophisticated descriptions of energy transport processes have been included [*Lionello et al.*, 2001, 2009].

[15] We have computed global coronal and heliospheric polytropic MHD solutions spanning more than 35 years, and, in particular, for the entire STEREO mission to date (available at http://www.predsci.com/stereo/). An important feature that makes our approach unique is the use of observed photospheric magnetograms to drive the solutions. Studies comparing model results with eclipses [*Mikic et al.*, 2002; *Mikić et al.*, 2007] as well as in situ observations at Ulysses and near Earth have shown that we can reproduce the basic features of the solar corona and inner heliosphere [*Riley et al.*, 1996, 2001a, 2001b, 2002, 2003; *Riley*, 2007].

[16] In general, our three-dimensional, time-dependent algorithm solves the following form of the resistive MHD equations on a nonuniform grid in spherical coordinates:

$$\nabla \times \mathbf{B} = \frac{4\pi}{c}\mathbf{J}, \tag{4}$$

$$\nabla \times \mathbf{E} = -\frac{1}{c}\frac{\partial \mathbf{B}}{\partial t}, \tag{5}$$

$$\mathbf{E} + \frac{\mathbf{v} \times \mathbf{B}}{c} = \eta \mathbf{J}, \tag{6}$$

$$\frac{\partial \rho}{\partial t} + \nabla \cdot (\rho \mathbf{v}) = 0, \tag{7}$$

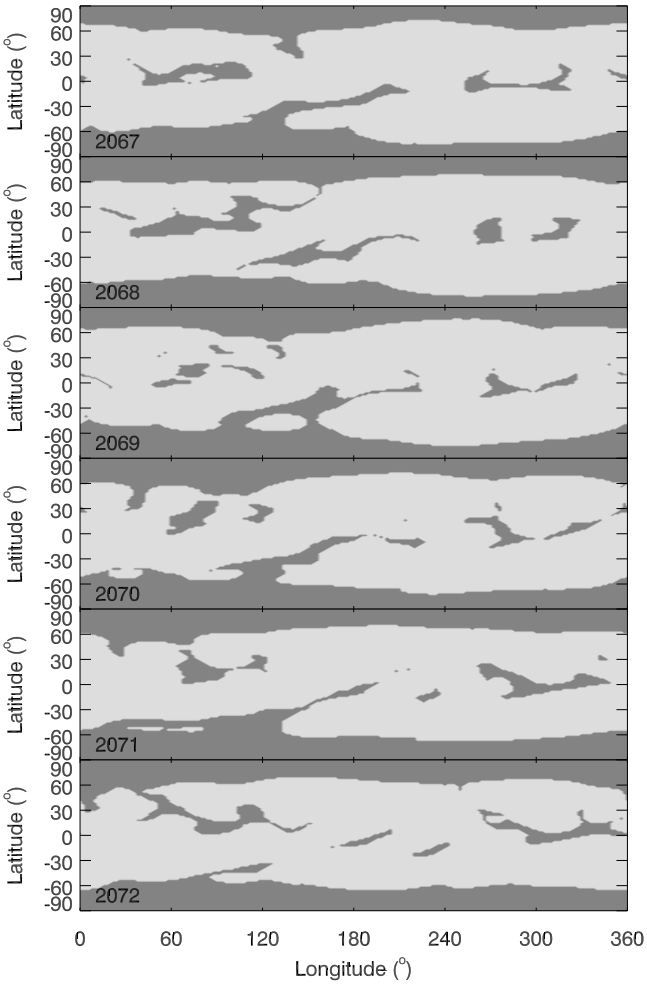

Figure 9. As in Figure 7, but for CRs 2067 through 2072.

$$\frac{1}{\gamma-1}\left(\frac{\partial T}{\partial t}+\mathbf{v}\cdot\nabla T\right)=-T\nabla\cdot\mathbf{v}+\frac{m_p}{2k\rho}S, \tag{8}$$

$$\rho\left(\frac{\partial \mathbf{v}}{\partial t}+\mathbf{v}\cdot\nabla\mathbf{v}\right)=\frac{1}{c}\mathbf{J}\times\mathbf{B}-\nabla(p+p_w)+\rho\mathbf{g}+\nabla\cdot(\nu\rho\nabla\mathbf{v}), \tag{9}$$

$$S=\left(-\nabla\cdot\mathbf{q}-n_e n_p Q(T)+H_{\mathrm{ch}}\right) \tag{10}$$

where **B** is the magnetic field, **J** is the electric current density, **E** is the electric field, ρ, **v**, p, and T are the plasma mass density, velocity, pressure, and temperature, $\mathbf{g} = -g_0 R_S^2 \hat{\mathbf{r}}/r^2$ is the gravitational acceleration, η the resistivity, and ν is the kinematic viscosity. Equation (10) contains the radiation loss function $Q(T)$, n_e and n_p are the electron and proton number density (which are equal for a hydrogen plasma), m_p is the proton mass, γ is the polytropic index, H_{ch} is the coronal heating term, and **q** is the heat flux. The wave pressure term p_w in equation (9) represents the contribution due to Alfvén waves and is evolved using the WKB approximation for time-space averaged Alfvén wave energy density ε [*Mikić et al.*, 1999]. The method of solution of equation (6) through (9), including the boundary conditions, has been described previously [*Mikić and Linker*, 1994; *Linker and Mikić*, 1997; *Lionello et al.*, 1999; *Mikić et al.*, 1999; *Linker et al.*, 2001; *Lionello et al.*, 2009]. In the work presented here, however, we simplify these equations by employing a "polytropic" energy equation, where $S = 0$ [*Usmanov*, 1993; *Mikic et al.*, 1996; *Usmanov*, 1996; *Linker et al.*, 1999; *Mikić et al.*, 1999; *Riley et al.*, 2001a, 2002, 2003; *Roussev et al.*, 2003] and employ an empirical technique for deriving the speed profile for the inner boundary of the heliospheric model. Although such an approximation is at odds with observations (it requires that we set $\gamma = 1.05$ in the coronal model, for example), we have found that that this approach for deriving solar wind speed is, at least currently, more accurate than can be obtained from the more self-consistent thermodynamic approach (P. Riley et al., A multi-observatory inter-calibration of line-of-sight diachronic solar magnetograms and implications for the open flux of the heliosphere, submitted to *Astrophysical Journal*, 2010).

[17] Figure 6 compares model results with STEREO and ACE observations for CR 2060, which occurred during one of the intervals identified as "lulls." The solid lines show model solutions, which were extracted by flying the spacecraft trajectories through the simulation domain. We note that the relative phasing of the streams at the three locations is captured in the model results. The fast stream centered on day 240, for example, is first seen at STEREO B, then ACE, and finally at STEREO A. Moreover, the general large-scale stream structure for this rotation is reproduced by the model: Generally slow and variable wind during the first half, followed by a large stream at day 240, and two smaller streams following it. The precise phasing of the modeled streams relative to the observations does not match up well, however: The first stream is predicted to arrive earlier than it actually does and the second stream is predicted to arrive later. Overall, however, these relatively typical results match sufficiently well that the model can be used to interpret the observations. The bottom summarizes the polarity of the radial component of the magnetic field. Both model and observations suggest an essentially two-sector pattern for this rotation.

[18] Figure 7 summarizes the computed coronal hole boundaries for CRs 2058 through 2063. These maps mark regions of open field lines (dark grey) and closed field lines (light grey) at the photosphere. We note that, during this time, there were well-defined polar coronal holes, together with equatorward extensions to these holes, as well as low and midlatitude holes, not obviously connected to other open field regions. The quantitative steps taken to compute the speed profiles in the model are described by *Riley et al.* [2001a]. In brief, a velocity profile at the photosphere, consisting of fast wind everywhere with slow wind localized at the boundaries between the open and closed field lines, is mapped outward along the field lines to30 R_S. Figure 8 shows the results of that mapping. Specifically, it shows the bulk radial solar wind velocity at 30 R_S for each of these six rotations. The trajectories of ACE, STEREO A, and STEREO B are overlaid. Since Carrington longitude increases from left to right in each frame, time proceeds from right to left. Thus, with increasing time, the spacecraft sample progressively earlier Carrington longitudes.

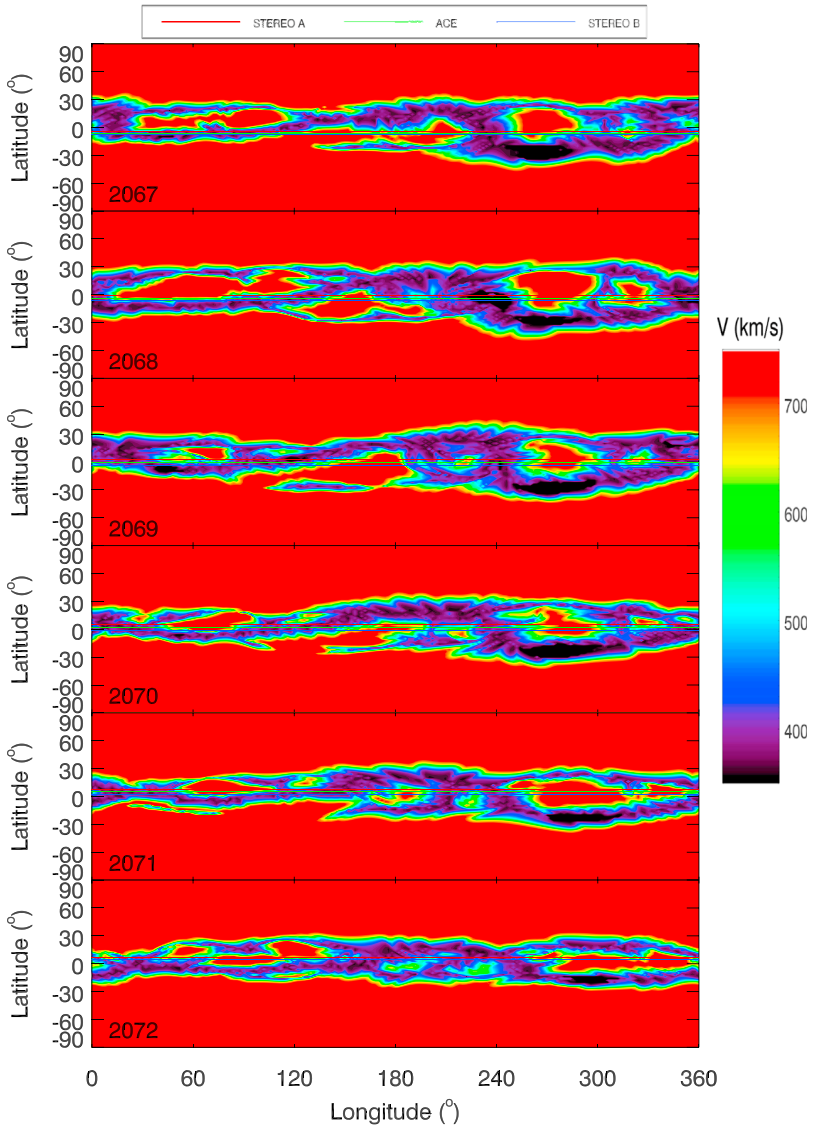

Figure 10. As in Figure 8, but for CRs 2067 through 2072.

[19] The connection between the computed coronal holes in Figure 7 and the high-speed streams within Figure 8 can, at least qualitatively, be understood; however, it is clear that the topology of the field lines between 1 R_S and 30 R_S has added a great deal of complexity to the velocity map. From Figure 8, we note the following points. First, the spacecraft were essentially located at the same heliographic latitude during this interval. Certainly, based on the quality of the match shown in Figure 6, we could not reliably ascribe any spatial inhomogeneities to these modest separations. Second, the three high-speed streams intercepted by all three spacecraft, initially at ~120° in CR 2059 and ~210° and ~340° in CR 2060 drift westward in the ensuing rotations.

[20] Figures 9 and 10 show coronal hole boundaries and speed profiles for CRs 2067 through 2072, which span the second "lull." For this interval, we note the following. First, the spacecraft were separated more substantially in heliographic latitude. Second, again, there was a westward progression of the high-speed streams that were intercepted by the spacecraft. Third, the stream boundaries tended to have a systematic tilt to them. This can be seen more clearly in the low-latitude coronal holes, which are orientated from SE to NW. The fast streams have a more complex profile, however, there is a tendency for STEREO A, which is at the highest heliographic latitude, to intercept the matching stream interface at a more westerly longitude.

5. Interpretation

[21] There are two obvious ways that the linear relationship between time lag and the increasing longitude of the ACE and STEREO spacecraft can be broken: temporal changes and/or spatial inhomogeneities. In the case of the latter, the pattern at the Sun does not change in time so that the structure of the solar wind in a frame rotating with the Sun is stationary; that is, it is strictly corotating. However, if the spacecraft are not located at exactly the same heliographic latitude, they will intercept different plasma sources. Consider, for example, an

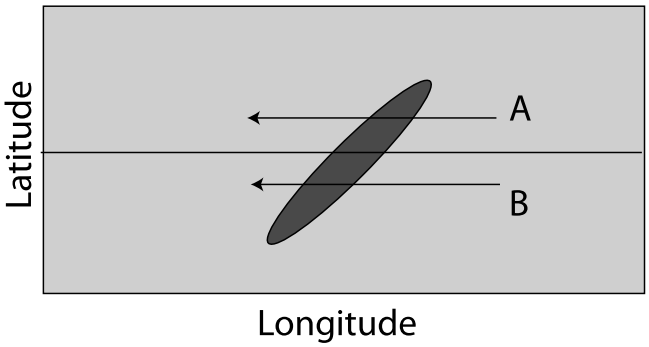

Figure 11. Schematic illustration of how the orientation of a coronal hole can affect the phase lag between two spacecraft, i.e., STEREO A and B. Their trajectory through the coronal hole are marked by horizontal arrows.

idealized, elongated low-latitude coronal hole, oriented so that one end is in the SE and the other end lies in the NW. This is shown schematically in Figure 11. If STEREO A is located at a higher heliographic latitude than either ACE or STEREO B, then the CH, and hence fast solar wind stream, will arrive slightly earlier than predicted since it is rooted in a more western source. Temporal effects can be understood in a similar way. If a low-latitude CH evolves in time so that it shifts toward the west as the structure passes from STEREO B to ACE and onto STEREO A, then the stream will arrive earlier than predicted by equation (3). Both of these examples, thus, lead to the "lulls" we have identified in the data. Clearly, in principle, it is possible for the opposite effects to take place: Structure that is oriented from the NE to SW or temporal evolution of structure that tends to precess in the Carrington frame would drive larger time lags. Our model results, however, do not provide any examples of this occurring during the STEREO timeframe. Instead, surrounding CR 2061, the general trend was for structures intercepted by the spacecraft to drift westward, while surrounding CR 2070,

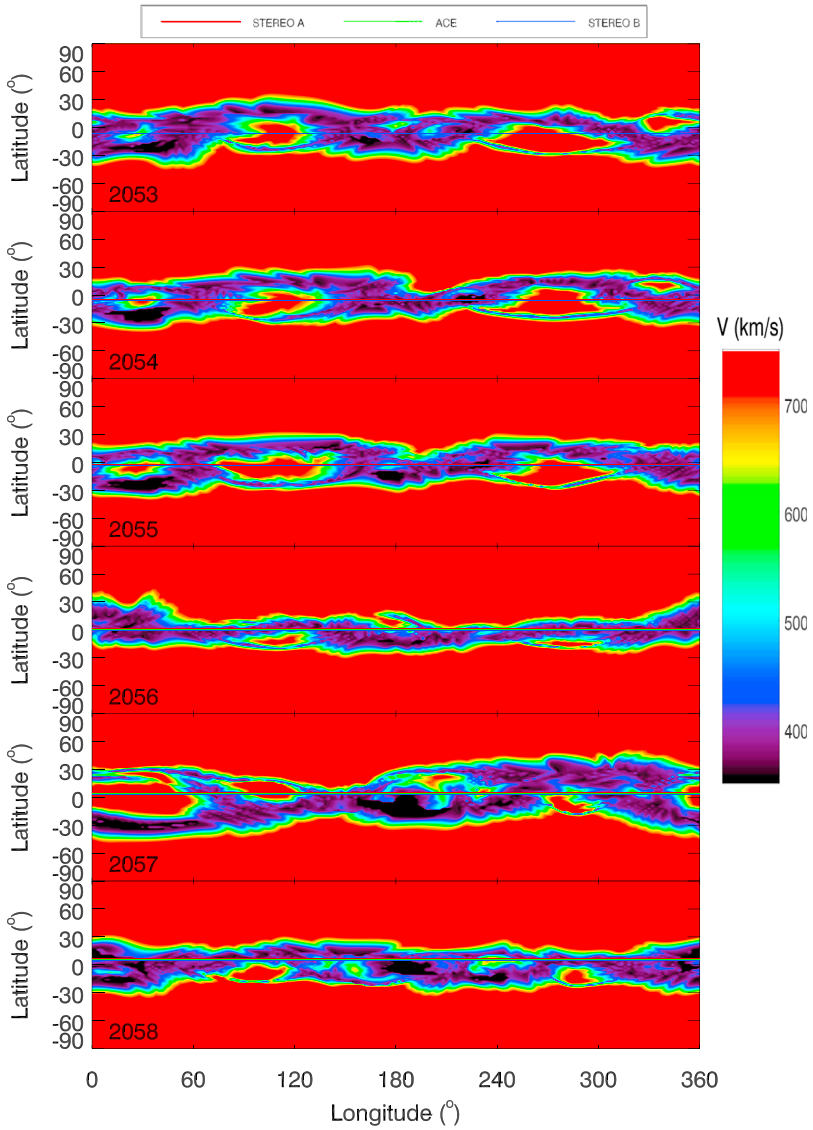

Figure 12. As in Figure 8, but for CRs 2053 through 2058.

both spatial and temporal effects likely contributed to the "lulls." In particular, the stream interfaces were oriented from the SE to NW, so that wind from the same coronal hole arrived earlier than would have been predicted, and the coronal hole structure evolved such that the fast wind streams migrated westward. The variations in the peak cross-correlation coefficient during these lulls also provide some clues as to the nature of the processes producing them. In all three cases, the peak coefficient was as large, or slightly larger than surrounding values during the first lull, but was markedly lower during the second lull. This suggests a more transient, or nonsteady component to the processes producing the second lull.

[22] As a final verification of this interpretation, we consider the first 6 Carrington rotations of the STEREO mission. During this interval, the phase lag of the signals at all three spacecraft matched the linear increase predicted by equation (3). The computed solar wind velocities at 30 R_S for this interval are shown in Figure 12. During CR 2053 through 2055 the CCFs were driven by a stable pattern involving two long-lived equatorial coronal holes (at longitudes of ~110° and ~270°). The spacecraft were not significantly separated in latitude, and thus, we would not expect spatial inhomogeneities to drive a deviation in the time lag. Moreover, there was no systematic evolution of the coronal holes during this interval. On the basis of these results, then, we would not expect any deviations in the time lag profile. During the second half of this interval, the wind sampled by the spacecraft was slow, variable, and unorganized. Again, there were no obvious systematic trends.

[23] Finally, it is worth noting that our analysis has tacitly assumed a fixed rotation period of 27.27 days. However, due to the super-radial expansion of the solar magnetic field, the plasma may originate from a range of heliographic latitudes. *Lee et al.* [2008] have shown that long-lived, high-speed streams may recur with periodicities in the range of 26.5–27.3 days. Using the Snodgrass formula for differential rotation of the photosphere [*Snodgrass*, 1983], this would suggest a source latitude lower than 43.4°, which τ_{rot} = 27.3 days would imply. Although the sense of this effect is in the same direction as the lulls we have identified, its magnitude is too small to explain them: The lulls suggest deviations of >30 h away from 27.27 days, whereas the effects described by *Lee et al.* [2008] were limited to a fraction of a day. Nevertheless, this effect may contribute to some of the smaller deviations evident in Figures 3–5.

6. Summary

[24] In this study, we have applied a cross-correlation analysis to ACE, STEREO A, and B bulk solar wind velocity measurements for the period from STEREO's launch through mid-2009. We found that, as with previous studies [*Podesta et al.*, 2008; *Opitz et al.*, 2009], there is a general trend for the phase lag between the streams to increase within increasing separation of the spacecraft. We also identified two intervals that deviated significantly from this trend. The first, centered around CR 2060, was previously identified by *Opitz et al.* [2009]. We used global MHD simulation results to understand these "lulls" in terms of both temporal evolution of the streams, as they swept first past STEREO B, then ACE, and finally past STEREO A, as well as spatial inhomogeneities, such that the spacecraft, separated in latitude by up to ~14° sampled different portions of the streams. Finally, beyond a separation of ~77/36/30°, between STEREO A-B/STEREO A-ACE/ACE-STEREO-B, corresponding to an interval of approximately ~1.6 years, the CCF peaked at values <0.5, suggesting that from this point, correlation analysis must be applied and interpreted with considerably more caution.

[25] **Acknowledgments.** PR, ZM, and JAL gratefully acknowledge the support of the LWS Strategic Capabilities Program (NASA, NSF, and AFOSR), the NSF Center for Integrated Space Weather Modeling (CISM), NASA's Heliophysics Theory Program (HTP), and the NASA STEREO IMPACT and SECCHI teams. We thank the SWEPAM/ACE and PLASTIC/STEREO teams for providing data.

References

Detman, T. R., M. Dryer, T. Yeh, S. M. Han, and S. T. Wu (1991), A time-dependent, three-dimensional MHD numerical study of interplanetary magnetic draping around plasmoids in the solar wind, *J. Geophys. Res.*, *96*(A6), 9531–9540, doi:10.1029/91JA00443.

Dryer, M., Z. K. Smith, E. J. Smith, J. D. Mihalov, J. H. Wolfe, R. S. Steinolfson, and S. T. Wu (1978), Dynamic MHD modeling of solar wind corotating stream interaction regions observed by Pioneer 10 and 11, *J. Geophys. Res.*, *83*(A9), 4347–4352, doi:10.1029/JA083iA09p04347.

Endler, F. (1971), Wechselwirkung zwischen Sonnenwind und koronalen Magnetfeldern, *Mitteilungen Astron. Gesellschaft Hamburg*, *30*, 136.

Galvin, A. B., et al. (2008), The Plasma and Suprathermal Ion Composition (PLASTIC) investigation on the STEREO observatories, *Space Sci. Rev.*, *136*, 437–486, doi:10.1007/s11214-007-9296-x.

Gosling, J. T., and S. J. Bame (1972), Solar-wind speed variations 1964–1967: An autocorrelation analysis, *J. Geophys. Res.*, *77*(1), 12–26, doi:10.1029/JA077i001p00012.

Gosling, J. T., J. R. Asbridge, S. J. Bame, and W. C. Feldman (1976), Solar wind speed variations: 1962–1974, *J. Geophys. Res.*, *81*(28), 5061–5070, doi:10.1029/JA081i028p05061.

Lee, C. O., et al. (2008), Manifestations of solar differential rotation in the solar wind: An update, *Eos Trans. AGU*, *89*, Spring Meet. Suppl., Abstract SH31A-02.

Linker, J. A., and Z. Mikić (1997), Extending coronal models to earth orbit, in *Coronal Mass Ejections*, edited by N. Crooker, J. Joselyn, and J. Feynmann, p. 269, AGU, Washington, D. C.

Linker, J. A., G. van Hoven, and D. D. Schnack (1990), A three-dimensional simulation of a coronal streamer, *Geophys. Res. Lett.*, *17*(13), 2281–2284, doi:10.1029/GL017i013p02281.

Linker, J. A., et al. (1999), Magnetohydrodynamic modeling of the solar corona during whole Sun month, *J. Geophys. Res.*, *104*(A5), 9809–9830, doi:10.1029/1998JA900159.

Linker, J. A., R. Lionello, Z. Mikić, and T. Amari (2001), Magnetohydrodynamic modeling of prominence formation within a helmet streamer, *J. Geophys. Res.*, *106*(A11), 25,165–25,175, doi:10.1029/2000JA004020.

Lionello, R., Z. Mikić, and J. A. Linker (1999), Stability of algorithms for waves with large flows, *J. Comput. Phys.*, *152*(1), 346–358.

Lionello, R., J. A. Linker, and Z. Mikić (2001), Including the transition region in models of the large-scale solar corona, *Astrophys. J.*, *546*(1), 542–551.

Lionello, R., J. A. Linker, and Z. Mikić (2009), Multispectral emission of the sun during the first whole Sun month: Magnetohydrodynamic simulations, *Astrophys. J.*, *690*, 902–912, doi:10.1088/0004-637X/690/1/902.

Manchester, W. B., A. J. Ridley, T. I. Gombosi, and D. L. Dezeeuw (2006), Modeling the Sun-to-Earth propagation of a very fast CME, *Adv. Space Res.*, *38*, 253–262, doi:10.1016/j.asr.2005.09.044.

McComas, D. J., S. J. Bame, P. Barker, W. C. Feldman, J. L. Phillips, P. Riley, and J. W. Griffee (1998), Solar wind electron proton alpha monitor (swepam) for the advanced composition explorer, *Space Sci. Rev.*, *86*(1–4), 563–612.

Mikić, Z., and J. A. Linker (1994), Disruption of coronal magnetic field arcades, *Astrophys. J.*, *430*, 898–912.

Mikic, Z., J. A. Linker, and J. A. Colborn (1996), An MHD Model of the solar corona and solar wind, *BAAS*, *28*, 868.

Mikić, Z., J. A. Linker, D. D. Schnack, R. Lionello, and A. Tarditi (1999), Magnetohydrodynamic modeling of the global solar corona, *Phys. Plasmas*, *6*(5), 2217–2224.

Mikic, Z., J. A. Linker, R. Lionello, and P. Riley (2002), Predicting the structure of the solar corona during the December 4, 2002 total solar eclipse, *Eos Trans AGU*, *83*(47), Fall Meet. Abstract SH52A-0468.

Mikić, Z., J. A. Linker, R. Lionello, P. Riley, and V. Titov (2007), Predicting the structure of the solar corona for the total solar eclipse of March 29, 2006, in *Solar and Stellar Physics Through Eclipses*, *Astron. Soc. Pac. Conf. Ser.*, vol. 370, edited by O. Demircan, S. O. Selam, and B. Albayrak, pp. 299, Side, Turkey.

Odstrcil, D. (1994), Interactions of solar wind streams and related small structures, *J. Geophys. Res.*, *99*(A9), 17,653–17,671, doi:10.1029/94JA01225.

Odstrcil, D., J. A. Linker, R. Lionello, Z. Mikić, P. Riley, V. J. Pizzo, and J. G. Luhmann (2002), Merging of coronal and heliospheric numerical 2-d mhd models, *J. Geophys. Res.*, *107*(A12), 1493, doi:10.1029/2002JA009334.

Odstrcil, D., V. J. Pizzo, J. A. Linker, P. Riley, R. Lionello, and Z. Mikic (2004), Initial coupling of coronal and heliospheric numerical magnetohydrodynamic codes, *J. Atmos. Sol. -Terr. Phys.*, *66*, 1311–1320.

Opitz, A., et al. (2009), Temporal evolution of the solar wind bulk velocity at solar minimum by correlating the STEREO A and B PLASTIC measurements, *Sol. Phys.*, *256*, 365–377, doi:10.1007/s11207-008-9304-7.

Paularena, K. I., G. N. Zastenker, A. J. Lazarus, and P. A. Dalin (1998), Solar wind plasma correlations between IMP 8, INTERBALL-1, and WIND, *J. Geophys. Res.*, *103*(A7), 14,601–14,618, doi:10.1029/98JA00660.

Pizzo, V. (1978), A three-dimensional model of corotating streams in the solar wind: I. Theoretical foundations, *J. Geophys. Res.*, *83*(A12), 5563–5572, doi:10.1029/JA083iA12p05563.

Pneuman, G. W., and R. A. Kopp (1971), Gas-magnetic field interactions in the solar corona, *Sol. Phys.*, *18*, 258–270.

Podesta, J. J., A. B. Galvin, and C. J. Farrugia (2008), Correlation length of large-scale solar wind velocity fluctuations measured tangent to the Earth's orbit: First results from Stereo, *J. Geophys. Res.*, *113*, A09104, doi:10.1029/2007JA012865.

Richardson, J. D., F. Dashevskiy, and K. I. Paularena (1998), Solar wind plasma correlations between L1 and Earth, *J. Geophys. Res.*, *103*(A7), 14,619–14,630, doi:10.1029/98JA00675.

Riley, P. (2007), Modeling corotating interaction regions: From the Sun to 1 AU, *J. Atmos. Sol. -Terr. Phys.*, *69*, 32–42, doi:10.1016/j.jastp.2006.06.008.

Riley, P., J. T. Gosling, L. A. Weiss, and V. J. Pizzo (1996), The tilts of corotating interaction regions at midheliographic latitudes, *J. Geophys. Res.*, *101*(A11), 24,349–24,357, doi:10.1029/96JA02447.

Riley, P., J. A. Linker, and Z. Mikić (2001a), An empirically driven global MHD model of the corona and inner heliosphere, *J. Geophys. Res.*, *106*(A8), 15,889–15,901, doi:10.1029/2000JA000121.

Riley, P., J. A. Linker, Z. Mikić, and R. Lionello (2001b), Mhd modeling of the solar corona and inner heliosphere: Comparison with observations, in *Space Weather*, *Geophys. Monogr. Ser.*, vol. 125, edited by P. Song, H. J. Singer, and G. L. Siscoe, p. 159, AGU, Washington, D. C.

Riley, P., J. A. Linker, and Z. Mikić (2002), Modeling the heliospheric current sheet: Solar cycle variations, *J. Geophys. Res.*, *107*(A7), 1136, doi:10.1029/2001JA000299.

Riley, P., Z. Mikić, and J. A. Linker (2003), Dynamical evolution of the inner heliosphere approaching solar activity maximum: Interpreting ulysses observations using a global mhd model, *Ann. Geophys.*, *21*(6), 1347–1357.

Riley, P., R. Lionello, Z. Mikić, J. Linker, E. Clark, J. Lin, and Y.-K. Ko (2007), "Bursty" reconnection following solar eruptions: MHD simulations and comparison with observations, *Astrophys. J.*, *655*, 591–597, doi:10.1086/509913.

Rouillard, A. P., et al. (2009), A multispacecraft analysis of a small-scale transient entrained by solar wind streams, *Sol. Phys.*, *256*, 307–326, doi:10.1007/s11207-009-9329-6.

Roussev, I. I., T. I. Gombosi, I. V. Sokolov, M. Velli, W. Manchester, D. L. DeZeeuw, P. Liewer, G. Tóth, and J. Luhmann (2003), A three-dimensional model of the solar wind incorporating solar magnetogram observations, *Astrophys. J. Lett.*, *595*(1), L57–L61.

Smith, Z., and M. Dryer (1990), Mhd study of temporal and spatial evolution of simulated interplanetary shocks in the ecliptic-plane within 1 au, *Sol. Phys.*, *129*, 387–405.

Snodgrass, H. B. (1983), Magnetic rotation of the solar photosphere, *Astrophys. J.*, *270*, 288–299, doi:10.1086/161121.

Steinolfson, R. S., S. T. Suess, and S. T. Wu (1982), The steady global corona, *Astrophys. J.*, *255*, 730–742, doi:10.1086/159872.

Stone, E. C., A. M. Frandsen, R. A. Mewaldt, E. R. Christian, D. Margolies, J. F. Ormes, and F. Snow (1998), The advanced composition explorer, *Space Sci. Rev.*, *86*, 1–22, doi:10.1023/A:1005082526237.

Usmanov, A. V. (1993), A global numerical 3-D MHD model of the solar wind, *Sol. Phys.*, *146*, 377–396, doi:10.1007/BF00662021.

Usmanov, A. V. (1996), A global 3-d mhd solar wind model with Alfven waves, *Int. Solar Wind Conf.*, *382*, 141–144.

J. A. Linker, Z. Mikic, and P. Riley, Predictive Science, San Diego, CA 92121, USA.

J. Luhmann, SSL, University of California, Berkeley, CA 94720, USA.

A. Opitz, Centre d'Etude Spatiale des Rayonnements (CNRS-UPS), University of Toulouse, F- 31028 Toulouse, France.

Appendix E

Mapping Solar Wind Streams from the Sun to 1 AU: A Comparison of Techniques

Riley, P. and Lionello, R.

Published in Solar Physics, 2011.

Solar Phys (2011) 270:575–592
DOI 10.1007/s11207-011-9766-x

Mapping Solar Wind Streams from the Sun to 1 AU: A Comparison of Techniques

P. Riley · R. Lionello

Received: 3 December 2010 / Accepted: 31 March 2011 / Published online: 11 May 2011

Abstract A variety of techniques exist for mapping solar wind plasma and magnetic field measurements from one location to another in the heliosphere. Such methods are either applied to extrapolate solar data or coronal model results from near the Sun to 1 AU (or elsewhere), or to map *in-situ* observations back to the Sun. In this study, we estimate the sensitivity of four models for evolving solar wind streams from the Sun to 1 AU. In order of increasing complexity, these are: *i*) ballistic extrapolation; *ii*) *ad hoc* kinematic mapping; *iii*) 1-D upwinding propagation; and *iv*) global heliospheric MHD modeling. We also consider the effects of the interplanetary magnetic field on the evolution of the stream structure. The upwinding technique is a new, simplified method that bridges the extremes of ballistic extrapolation and global heliospheric MHD modeling. It can match the dynamical evolution captured by global models, but is almost as simple to implement and as fast to run as the ballistic approximation.

Keywords Corona · Evolution · Interplanetary medium · Magnetic fields · Solar wind

1. Introduction

The structure of the solar wind plasma populating the heliosphere is rich and complex. It is convenient to separate what we believe are intrinsically time-stationary processes (giving rise to corotating interaction regions) from temporal processes (typified by coronal mass ejections (CMEs)), although we realize, in practice that this distinction may not hold. That is, even those processes that we believe to be "steady-state" may be driven by inherently time-dependent phenomena, such as interchange reconnection. However, for simplicity, in this study, we adopt a pragmatic view that at least some of the structure we observe in the solar wind is driven by spatially varying, but time-stationary sources at the Sun. This is

P. Riley (✉) · R. Lionello
Predictive Science, 9990 Mesa Rim Road, Suite 170, San Diego, CA, USA
e-mail: pete@predsci.com

R. Lionello
e-mail: lionel@predsci.com

borne out by comparisons between models and *in-situ* observations that suggest that, in the absence of obviously transient phenomena, appropriate boundary conditions derived from the observed photospheric magnetic field produce model solutions that reasonably match *in-situ* observations (see, *e.g.*, Riley, Linker, and Mikić, 2001).

The time-stationary structure in the heliosphere can be conveniently described by the combination of two basic effects. The first is that, beyond $\approx 10 R_\odot$, solar material streams away from the Sun along roughly radial trajectories with a range of speeds. The second is that as the Sun rotates, it places plasma on the same radial trajectory with faster or slower wind. Faster wind overtaking slower wind leads to a compression front, while slower material being outrun by faster material leads to a rarefaction region, or expansion wave (Sarabhai, 1963). The boundary within the compression region, separating the slow and fast wind, is known as a stream interface (SI) (Gosling *et al.*, 1978). In the simplest possible scenario, where speed variations depend only on their source location at the Sun, that is, the flow pattern does not vary significantly on the timescale of a solar rotation, the large-scale compressive structures created by the interaction of these streams are fixed in a frame corotating with the Sun, and they are known as corotating interaction regions (CIRs) (Smith and Wolfe, 1976). If the speed difference is sufficiently large, and typically beyond about 2 AU, a pair of shocks form bounding the CIR (see, *e.g.* Pizzo, 1985).

Modeling the structure of the solar wind for specific time periods of interest is a challenging task. In the chain connecting observations of the photosphere to predictions of magnetic field (**B**), velocity (**v**), number density (n), and plasma temperature (T) at Earth there are a number of poorly known parameters, associated with both the observations used to drive the models, and the models themselves, that can have a substantial impact. These include: *i*) the photospheric magnetogram used to drive the model; *ii*) the processing of the magnetogram, including smoothing and filtering, as well as extrapolation of data to poorly observed or even unseen poles; *iii*) the coronal model used; *iv*) the approximations used to derive the boundary conditions for the heliospheric model; and *v*) the heliospheric model used to map the solar wind from, say, $30 R_\odot$ to 1 AU. In a series of papers, we investigate the sensitivity of this modeling chain within each major area, with the objective of quantifying to what degree the predictions depend on each parameter. Ultimately, we hope that such studies will sufficiently constrain these parameters and improve our predictive capabilities. In this study, we focus on the question of mapping solar wind streams from $30 R_\odot$ to 1 AU. Although accuracy is obviously the most important criteria for assessing a particular technique, given the value of being able to run many cases with different inputs to test other portions of the chain, both speed of execution and ease of use are also valuable assets for any mapping technique.

Models developed to capture the basic phenomenon of corotating structure have grown in sophistication since the first 1-D fluid models were applied in the late 1960s (Hundhausen and Gentry, 1968). In a series of successively more sophisticated treatments, V. Pizzo described the effects of, and differences between 1-D, 2-D, and 3-D models as well as the differences between hydrodynamic and MHD solutions under idealized configurations (Pizzo 1978, 1980, 1982).

Heliospheric models, which simulate only the region of space beyond perhaps $30 R_\odot$ are simpler than their coronal counterparts for several reasons. Because the solar wind is supercritical with respect to all the characteristic wave mode speeds, the boundary conditions are simpler to implement and the physics too is more straightforward. Complex energy transport processes (see, *e.g.* Lionello, Linker, and Mikić, 2001), such as radiative losses, anisotropic thermal conduction, and coronal heating, for example, can, for the most part, be neglected. However, the value of these models for understanding basic physical processes is also limited because of the location of the inner boundary. The boundary conditions at $30 R_\odot$ are

essentially free parameters: Little reliable information about the speed, density, or magnetic field can be derived from current observations. Instead, heliospheric models are typically coupled with coronal models; the latter driving the former. In many applications then, heliospheric models can be considered to be mapping routines, taking the output of the coronal models and mapping it to the vicinity of Earth, or elsewhere. Given perfect inner boundary conditions, heliospheric models are usually presumed to give perfect output. In reality, of course, the models probably do not include all the relevant physics, such as pickup ions, or the necessary numerical fidelity to justify this supposition.

A number of techniques exist for mapping solar wind streams from one point in the heliosphere to another, the simplest of which is the so-called "ballistic" approximation. Here, it is assumed that each parcel of plasma maintains a constant speed as it travels through the heliosphere. The technique can be used to map *in-situ* observations at 1 AU back toward the Sun (Snyder and Neugebauer, 1966) or to map modeled plasma profiles from near the Sun to 1 AU. While simple to implement, the technique can generate substantial errors, particularly at compression regions, where dynamical interactions between adjacent plasma results in slower plasma ahead being accelerated and the faster plasma itself being decelerated. Similarly, in rarefaction regions, slower plasma following faster plasma is accelerated into the vacuum created by the fast plasma. The net effect of these interactions is that peaks in speed are eroded and troughs are filled in. At the leading edge of high-speed streams (*i.e.*, compression regions), this interaction is dynamic whereas at the trailing edge (*i.e.*, rarefaction regions) it is more kinematic. We anticipate, then, that rarefactions will map reasonably well, whereas mapping of compression regions will introduce more significant errors. Moreover, when applied to the inward mapping of rarefaction regions, non-physical results can be produced, where a parcel of plasma observed at a later time in the solar wind maps back to an earlier launch time from the Sun. These are the so-called "dwells" (Nolte and Roelof, 1973).

At the other end of the modeling spectrum, time-dependent, global heliospheric MHD models attempt to avoid the limitations of ballistic mappings by including the relevant dynamical processes. Models today are capable of running with grid sizes of 300^3 in the radial, meridional, and azimuthal directions (see, *e.g.* Riley *et al.*, 2011). They include shock capture algorithms (see, *e.g.*, Odstrcil *et al.*, 2002) and have been shown to match *in-situ* observations (see, *e.g.*, Riley, Linker, and Mikić, 2001). However, they are complex and difficult for the non-expert user to run on a regular basis. To address this, efforts such as NASA's Community Coordinated Modeling Center (CCMC) have been undertaken, which allow general members of the scientific community to run sophisticated heliospheric models, such as *Enlil*. Simpler time-stationary MHD models were also developed in the past that constructed corotating solutions by marching radially outward (Pizzo, 1978; Usmanov *et al.*, 2000).

There have been several attempts to bridge the gap between the simple ballistic mapping and global heliospheric MHD model. In the Hakamada–Akasofu–Fry (HAF) model (Hakamada and Akasofu, 1982; Fry *et al.*, 2001), for example, developed a kinematic technique for at least qualitatively accounting for the interaction of slow and fast streams leading to the formation of a shock pair. Arge and Pizzo (2000) also proposed an *ad hoc* scheme whereby each element of plasma at some radius is kinematically accelerated or decelerated based on the speed of the surrounding plasma. Others have proposed various 1-D fluid and quasi-MHD routines driven by *in-situ* data at some location in the heliosphere and mapped either farther out (Pizzo, Intriligator, and Siscoe, 1995; Wang, Richardson, and Gosling, 2000) or back to the Sun (Pizzo, 1981; Riley *et al.*, 2003).

In this study, we assess how sensitive the mappings of solar wind streams near the Sun are on the technique used. We also assess the role and importance of the interplanetary field on

the resulting stream structure. We derive a new technique for mapping streams from the Sun to 1 AU that is more accurate than the ballistic approximation, yet is considerably simpler to implement than an MHD model.

2. The Models

2.1. The Ballistic Model

The ballistic model for mapping solar wind streams to different locations in the heliosphere is the simplest possible approximation. It assumes that each parcel of plasma continues at a constant speed through the heliosphere. Thus, mapping data from an inner boundary at $30R_{\odot}$ requires only a shift in the longitudinal position of $\Delta\phi = -\Omega_{\rm rot}\Delta t = -\Omega_{\rm rot}\Delta r/v_{ro}$. For example, with $\Omega_{\rm rot} = 25.38$ days, and $\Delta r = (215-30)R_{\odot}$, solar wind traveling at 400 km s^{-1} would shift in Carrington longitude by 0.92 radians, or 52.8°.

The direction of the ballistic mapping (that is, either outward from the Sun or backward to the Sun) introduces different errors because of the non-linear nature of dynamic interactions. Streams close to the Sun that are mapped to 1 AU will suffer greater errors if each parcel of plasma is mapped at its own speed because the speed differences between the high- and low-speed streams are greater than the differences in speed of dynamically evolved streams at 1 AU that would be kinematically mapped back to the Sun. Moreover, radial gradients in speed will be reduced more quickly closer to the Sun, that is, plasma is accelerated or decelerated exponentially. Thus, the speed at 1 AU is likely to be a better average of the speed during its propagation from $30R_{\odot}$ to 1 AU, than its initial speed at $30R_{\odot}$.

2.2. The Arge–Pizzo Kinematic Evolution Model

Arge and Pizzo (2000) proposed an *ad hoc* kinematic scheme to modify the speed of solar wind streams based on whether they were traveling faster or slower than the adjacent plasma. It was intended to provide a better mapping than the ballistic approximation, while not requiring the complication of using a fluid or MHD algorithm. In their approach, each element of plasma at some radius, r_i, is modified according to the following prescription:

$$v_{i+1,j} = \sqrt{\frac{2}{(1/v_{i,j})^2 + (1/v_{i,j+1})^2}} \tag{1}$$

where $v_{i+1,j}$ is the speed at r_{i+1} for longitude j. Given the relatively low resolution of their potential-field source-surface (PFSS) model solutions, from which the velocity map at $30R_{\odot}$ was computed (5°), Arge and Pizzo (2000) applied Equation (1) each time after the plasma had been allowed to travel 1/8 AU at constant speed. The essence of this formula is that, if $v_{i,j} < v_{i,j+1}$, then the updated $v_{i+1,j}$ is increased, that is, the parcel of plasma is accelerated, while if $v_{i,j} > v_{i,j+1}$, it is decelerated.

2.3. The Heliospheric MHD Model

Predictive Science's MAS model solves the usual set of resistive MHD equations in three dimensions. Although the algorithm includes a range of energy transport processes, these are not believe to be important in the heliosphere. Thus, we use the polytropic approximation, setting the ratio of specific heats, $\gamma = 5/3$. The inner boundary is set to $R = 30R_{\odot}$, where the

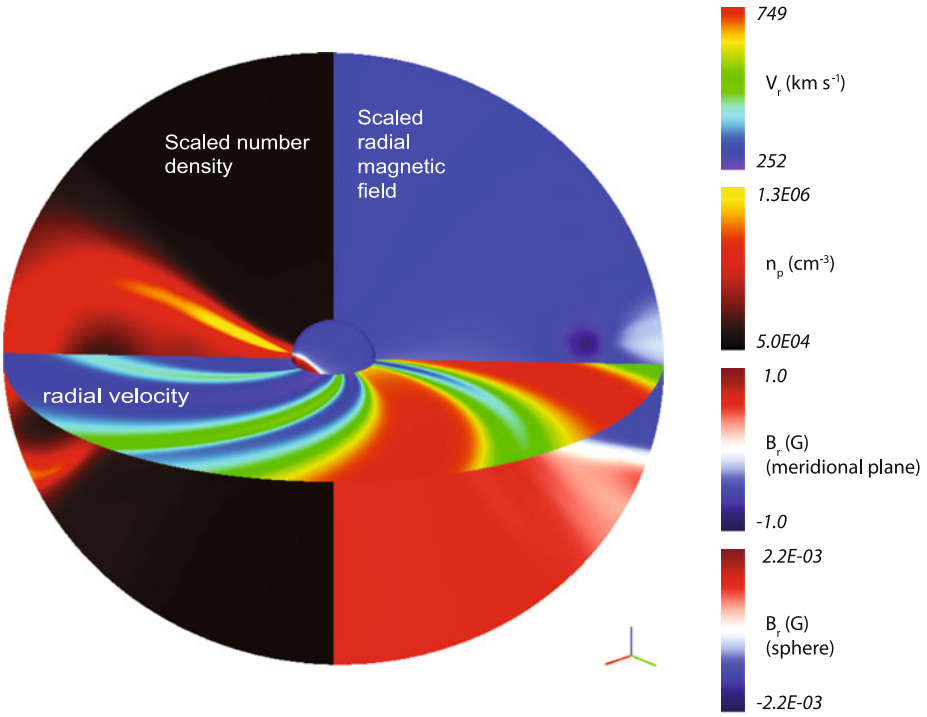

Figure 1 Global picture of the inner heliosphere (out to 1 AU) for CR 2068. The equatorial slice shows radial speed, while the two meridional slices show (left) scaled number density and (right) scaled radial magnetic field. The central sphere is located at the inner boundary of the calculation ($30R_{\odot}$) and also shows the strength of the radial component of the magnetic field.

flow is supercritical with respect to all wave modes, and the outer boundary is set to 1 AU. The entire volume within these bounds, *i.e.*, from pole to pole, is modeled. The basic features of MAS as applied to the heliospheric environment (MAS-H) have been described by Riley, Linker, and Mikić (2001). However, since its initial development, we have made a number of significant improvements. First, the algorithm uses finite difference and is fully parallelized in all three dimensions. This allows us to run cases at resolutions significantly higher than were possible in the past. The results we present here, for example, were computed on grids with $281 \times 181 \times 361$ points in radius (r), colatitude (θ), and azimuth (ϕ), respectively. Second, the solutions can be computed in either the corotating frame of reference or in an inertial frame. Third, boundary conditions are specified at some inner radial sphere as a function of time. For this particular study, because we are interested in time-stationary phenomena, we supplied an ambient coronal solution that is rotated at the solar rotation rate and the model is run forward in time until a steady state is achieved.

In this study, we consider the structure of the heliosphere for Carrington rotation (CR) 2068, which coincided with the interval known as "Whole Heliosphere Interval" and has been the topic for a coordinated campaign study (see, *e.g.*, Riley, Linker, and Mikic, 2009; Riley *et al.*, 2011). Figure 1 illustrates the large-scale features during this interval. The equatorial plane shows the spiral structure created by the rotation of the Sun in the form of bulk solar wind speed. The two high-speed streams seen here will be analyzed in more detail later. The meridional slice on the left shows number density, scaled by $1/r(\mathrm{AU})^2$, illustrating the

variable nature of the solar wind surrounding the solar equator. The meridional slice on the right shows the radial component of the magnetic field, again scaled by $1/r^2$. The location of the heliospheric current sheet (HCS) can be seen by the white trace separating the outward (red) and inward (blue) polarity fields, roughly organized by hemisphere. During the most recent minimum, the large-scale magnetic field was outward in the southern hemisphere and inward in the northern hemisphere. The details of the large-scale, three-dimensional structure of the inner heliosphere have been described by Riley *et al.* (2011).

2.4. 1-D Upwind Model

To bridge the gap between the ballistic approximation and the global heliospheric MHD model, we develop a simple numerical algorithm that simplifies the MHD equations as much as possible, by neglecting magnetic field, gravity, and pressure gradient effects. Following Pizzo (1978), we can write the fluid momentum equation in a corotating frame of reference as

$$-\Omega_{\rm rot}\frac{\partial \mathbf{v}}{\partial \phi} + (\mathbf{v}\cdot\nabla)\mathbf{v} = \frac{1}{\rho}\nabla P - \frac{GM_{\rm S}}{r^2}\mathbf{e}_r \tag{2}$$

where ρ is the proton mass density, $\mathbf{v}$ is the velocity, P is the thermal pressure, G is the gravitational constant, $M_{\rm S}$ is the mass of the Sun, and γ is the polytropic index. This differs from the more usual form of the momentum equation in that the time derivative, $\partial/\partial t$, has been replaced by the term $-\Omega_{\rm rot}\partial/\partial\phi$, which is exact for time-stationary flows in the corotating frame of reference.

In one dimension, neglecting the pressure gradient and gravity terms, this reduces to:

$$-\Omega_{\rm rot}\frac{\partial v_r}{\partial \phi} + v_r\frac{\partial v_r}{\partial r} = 0, \tag{3}$$

which is the inviscid Burgers' equation. Following Press *et al.* (2002), we can recast this expression as an upwind difference algorithm:

$$v_{i+1,j} = v_{i,j} - \Delta r\left(a^+\Delta^- + a^-\Delta^+\right) \tag{4}$$

where for simplicity, we have omitted the subscript r on the radial velocity. The indices i and j refer to the r and ϕ grids, respectively, so that this expression gives the speed of the solar wind at $i+1$ for each point in ϕ for known values at i in r. As usual, the step size Δr should be limited by the Courant condition. The remaining terms are given by

$$a^+ = \max\left(-\frac{\Omega_{\rm rot}}{v_{i,j}}, 0\right); \tag{5}$$

$$a^- = \min\left(-\frac{\Omega_{\rm rot}}{v_{i,j}}, 0\right); \tag{6}$$

$$\Delta^- = \frac{v_{i,j} - v_{i,j-1}}{\Delta\phi}; \tag{7}$$

$$\Delta^+ = \frac{v_{i,j+1} - v_{i,j}}{\Delta\phi}. \tag{8}$$

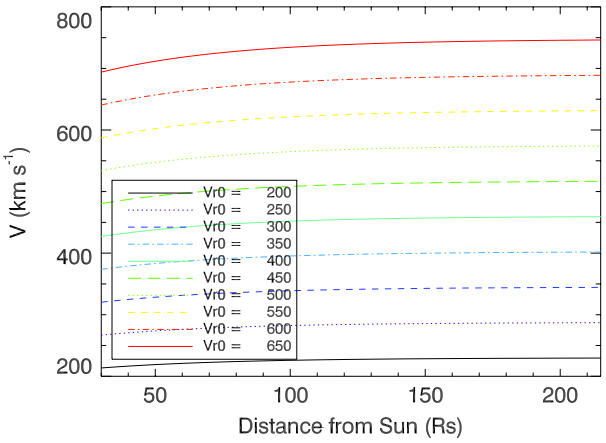

Figure 2 Velocity profiles for different initial speeds (v_{ro}) as a function of distance from the Sun (r) based on Equation (10).

Since $\frac{-\Omega_{\rm rot}}{v_{i,j}}$ is always less than zero for the solar wind, then $a^+ = 0$ and Equation (4) simplifies to

$$v_{i+1,j} = v_{i,j} + \frac{\Delta r \Omega_{\rm rot}}{v_{i,j}} \left(\frac{v_{i,j+1} - v_{i,j}}{\Delta \phi} \right). \tag{9}$$

In summary, Equation (9) allows us to map a velocity stream from $30R_\odot$ to 1 AU in steps of Δr. We verified that the solution was not sensitive to the choice of CFL number by repeating mappings using between 100 and 10 000 steps in r.

2.5. Effect of Acceleration

Although by $30R_\odot$ the solar wind plasma has accelerated significantly toward its final, asymptotic speed, a residual acceleration is expected (Schwenn, 1990). Based on previous simulations (see, *e.g.*, Riley and Gosling, 1998; Riley, 1999; Riley, Linker, and Mikić, 2001; Riley, 2010) we have derived a simple expression to mimic this residual acceleration from $30R_\odot$ to 1 AU:

$$v_{\rm acc}(r) = \alpha v_{ro} \left(1 - {\rm e}^{-r/r_{\rm h}}\right) \tag{10}$$

where v_{ro} is the speed at the inner boundary ($r_{\rm o}$), α is some factor by which the initial speed is increases, and $r_{\rm h}$ is the scale length over which the acceleration spans. Therefore, the total solar wind speed, as a function of radius is $v(r) = v_{ro} + v_{\rm acc}(r)$. Figure 2 illustrates the evolution of $v(r)$ with distance from the Sun for $r_{\rm h} = 50R_\odot$ and $\alpha = 0.15$. Thus, wind initially traveling at 650 km s^{-1} will accelerate by a further $\approx$ 100 km s^{-1}, whereas 300 km s^{-1} wind will accelerate by a more modest $\approx$ 45 km s^{-1}. Since we are primarily interested in mapping the streams from one point ($30R_\odot$) to another (1 AU), the value of $r_{\rm h}$ and the profile of the curve between the end-points is not crucial here. In reality, it is likely that the slow wind will asymptote to its final speed over a longer distance than fast wind (Schwenn, 1990). The parameter α, however, acts to accelerate the wind in proportion to its initial speed. As we will show below, these values lead to reasonable accelerations for both slow and fast solar wind.

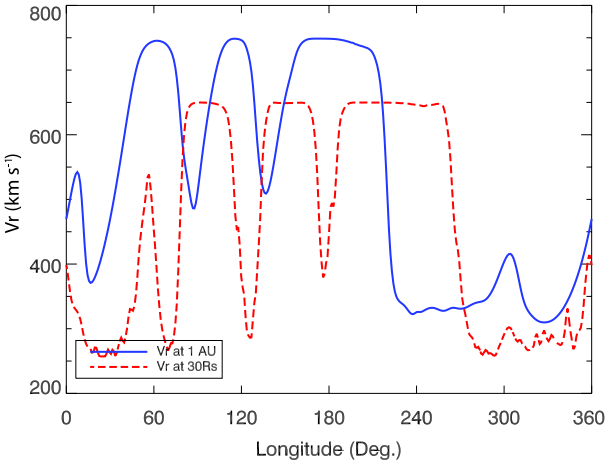

Figure 3 Comparison of radial velocity for CR 2068 at the inner boundary of the heliospheric MHD model at $30R_{\odot}$ (red) and at 1 AU (blue) as a function of Carrington longitude.

3. Results

3.1. Evolution of the Solar Wind in the MHD Model

Using the heliospheric MHD solution as the *a priori* correct answer, we have applied these mappings to test the different approaches for determining the speed of the solar wind at 1 AU. In principle, a generalization of this approach could be developed for mapping the remaining magnetofluid parameters. We have also considered the effects of the strength of the interplanetary magnetic field on the resulting stream structure at 1 AU.

To appreciate how much the solar wind evolves in its journey from $30R_{\odot}$ to 1 AU, we begin by comparing the equatorial speed profile at $30R_{\odot}$ with its evolved profile at 1 AU. (For simplicity, we have chosen a hypothetical spacecraft trajectory along the heliographic equator. In reality, the heliographic latitude of the center of the disk, $B_0 = -6.5^{\circ}$ for CR 2068. Thus, an Earth-based spacecraft such as ACE or Wind would have traced a latitude of $\approx -6.5^{\circ}$). Figure 3 shows both for CR 2068. We note several points. First, there is a net acceleration of all plasma as it moves away from the Sun, as discussed above. Second, the high-speed streams (*i.e.*, regions where $v > 500$ km s^{-1}) have drifted to the left, that is, to earlier longitudes. This is the result of corotation on the solution. The profiles are plotted as a function of Carrington longitude, thus, the same feature (*e.g.*, a high-speed stream) will map to earlier longitudes as it is traced back along a Parker spiral field line. Third, the edges of the high-speed streams have been eroded, while local speed minima in between these streams have been accelerated. This is due to a combination of compression regions bounded by pressure waves accelerating slower wind ahead and decelerating faster wind behind, as well as expansion waves connecting and accelerating slower wind behind, and decelerating faster wind ahead. Fourth, gradients on the eastward side of high-speed streams are reduced (the expansion wave, or rarefaction region) but steepened on the westward edge (at the center of the compression region). At 1 AU, the streams interfaces have not steepened enough to shock. Typically this is true for interaction regions at 1 AU, but could also be a consequence of the diffusive nature of the code, which uses a first-order upwinding scheme. Fifth, smaller-scale structure at the inner boundary is smoothed out by 1 AU. In general, the solar wind is known to act as a low-pass filter; however, our algorithm could also be numerically diffusing some smaller-scale structure as well.

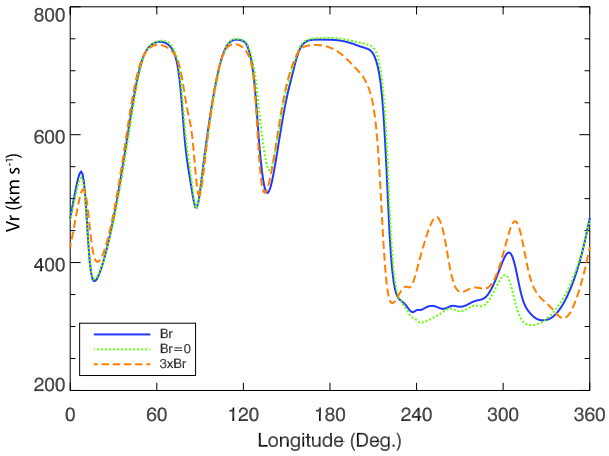

Figure 4 Comparison of radial velocity for CR 2068 at the outer boundary at 1 AU as a function of Carrington longitude. The three curves correspond to an MHD model using: *i*) the field computed in the coronal solution (blue); *ii*) zero field, that is, a hydrodynamic solution (green); and *iii*) a field three times that of the solution from the coronal solution (orange).

3.2. Effects of the Interplanetary Magnetic Field

We next investigate the effects of the interplanetary magnetic field on the structure of solar wind streams at 1 AU. In general, the dynamic, or ram pressure associated with the outward propagation of the solar wind plasma dominates over the plasma's thermal pressure ($P_{\rm th}$) or magnetic pressure ($P_{\rm mag}$). This can be demonstrated by comparing their relative contributions to the total momentum flux at 1 AU. Assuming typical solar wind values at 1 AU for number density ($n = 5$ cm^{-3}), speed ($v = 500$ km s^{-1}), we can derive a dynamic pressure, ρv^2 of $\approx 2 \times 10^{-9}$ Pa. Assuming a typical transverse magnetic field value of $B \approx 5$ nT yields a magnetic pressure of $\approx 10^{-11}$ Pa. Finally, assuming a typical proton temperature, $T_{\rm p} \approx 5 \times 10^4$ K, yields a thermal pressure of $\approx 3.5 \times 10^{-12}$ Pa. Thus the ratio of the dynamic pressure to magnetic pressure is $\approx 10^2$ and the ratio of the dynamic pressure to thermal pressure is ≈ 600.

To assess the effects of the IMF then, we can repeat model runs where we set the radial component of the magnetic field to zero, and the solution is effectively hydrodynamic. This sensitivity experiment of course presumes that the modeled field is a good match with observations. However, during the recent solar minimum (of which CR 2068 was a part) global heliospheric MHD models underestimated the magnitude of the interplanetary field (Svalgaard and Cliver, 2007). Although the reasons are not yet known, one possible explanation could be that the models magnetic field boundary conditions may be low by a factor of up to three. Thus, to more fully assess the possible effects of the interplanetary magnetic field, we also consider the case where the inner radial field is three times the value computed in the coronal solution.

Figure 4 compares these cases as a function of longitude for CR 2068. The baseline result is shown in blue, while the hydrodynamic solution (*i.e.*, $B_r = 0$) is shown in green, and the effects of multiplying the baseline field by a factor of three is shown in red. We can see that the baseline field does not substantially alter the stream structure over the hydrodynamic solution. This is particularly true at higher speeds, where, because the ram pressure scales as v^2, the relative contribution is larger than either the thermal or magnetic pressures, which are independent of solar wind speed. The effects of the magnetic field become apparent at lower speeds, in this case, between $240° - 330°$, where the phasing and amplitude of the local speed enhancement is different between the two solutions. Comparing the baseline solution with the $3 \times B_r$ solution reveals more fundamental differences. Here, even at high

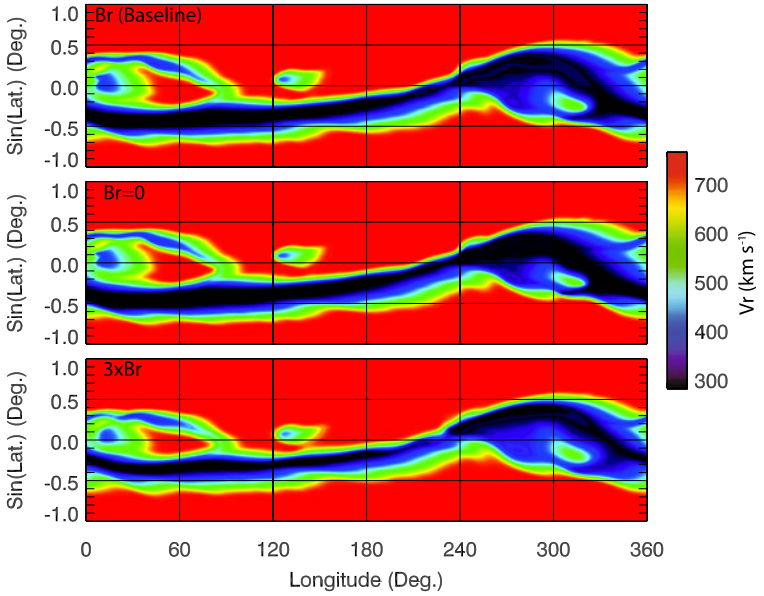

Figure 5 Comparison of radial velocity profiles for CR 2068 at 1 AU as a function of Sin (heliographic latitude) and Carrington longitude for the 3 MHD solutions: *i*) Using the baseline B_r values; *ii*) Setting $B_r = 0$; and *iii*) multiplying B_r by a factor of three. The solid white line traces a hypothetical spacecraft's trajectory at the heliographic equator to highlight the global context of the traces shown in Figure 4.

speeds, the general shape of the third (from the left) high-speed stream is notably different. Moreover, during the right-most third of the interval, the original single, modest stream is significantly larger and shifted in longitude, and a second stream, which was not even present in the baseline solution, appears at $\approx 250°$.

The differences in the profiles shown in Figure 4 can be better appreciated by considering the global velocity structure at 1 AU. In Figure 5 we show velocity profiles as a function of longitude and latitude for these three cases. Focusing first on the baseline solution, we can now interpret the three high-speed streams as coming from a single equatorial coronal hole followed by immersion into the northern polar coronal hole. In fact, the second two streams are really a single high-speed wind source, interrupted by an island of slower wind. The slow wind from 240° to 360° is due to the hypothetical spacecraft's entry into the "band of solar wind variability" that surrounds the heliospheric current sheet. A small equatorial coronal hole interrupts the slow flow at $\approx 310°$ longitude. Note how this feature broadens from zero field, to baseline field, to $\times 3$ field. Additionally, note how the southern polar coronal hole's northern-most extension, at $\approx 250°$ reaches farther north with increasing field. This is the cause of the second modest speed bump in the red curve of Figure 4, also at $\approx 250°$.

3.3. Outward Mapping Using the Ballistic Approximation

Next we consider the simplest possible mapping technique: the ballistic approximation. Typically this is applied to *in-situ* observations at 1 AU (or elsewhere) as a technique for inferring their source longitude back at the Sun. However, *ad hoc* models, such as the initial implementation of the Wang–Sheeley model (Wang and Sheeley, 1990) at NOAA's Space Weather Prediction Center (SWPC) have used it to propagate coronal model solutions from

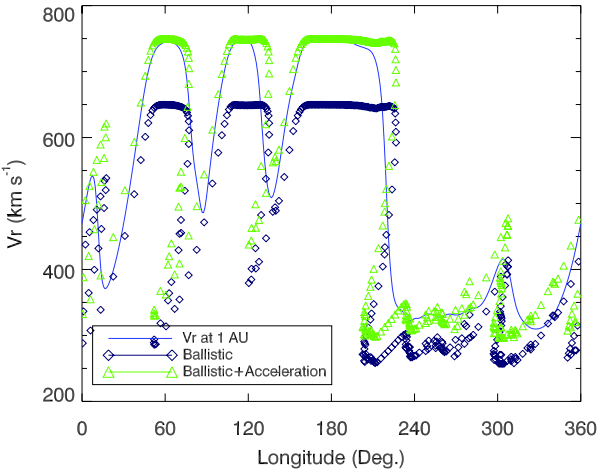

Figure 6 Comparison of radial velocity for CR 2068 at 1 AU with multiple-speed, ballistically mapped (and enhanced) speed from $30R_{\odot}$ to 1 AU as a function of Carrington longitude.

near the Sun to 1 AU. Figure 6 compares the MHD solution at 1 AU in the equator (blue) with ballistically mapped solutions where an acceleration correction was (green) and was not (purple) applied to the mapping. Comparison between the purple and green mappings shows that the acceleration correction has boosted both the slow and fast streams to approximately correct values. Comparison between the blue and green profiles demonstrates the limitation of the ballistic approximation. Most notably we see that the leading edge of high-speed streams (the right-hand side of each stream) has outrun the slower wind to the west, leading to multiple values at the interface. This makes sense because, in the ballistic approximation, slower wind does not impede the constant-moving fast wind and it overtakes it. Additionally, the difference could be quite substantial. Consider solar wind traveling at $v_{\rm sw}$ km s^{-1}. It would be shifted in longitude by

$$\phi_{\rm shift} = \frac{2\pi}{25.38 \text{ days}} \frac{\Delta r}{v_{\rm sw}}. \tag{11}$$

Therefore, mapping from $30R_{\odot}$ to 1 AU would lead to a shift of 77.3° for wind traveling at 275 km s^{-1} and 32.1° for wind traveling at 650 km s^{-1}. This would move the low-speed wind initially located at ≈280° to an earlier longitude than the fast wind initially at ≈260° (see also ≈210° in Figure 3), which, assuming the flow is radial, is clearly unphysical.

To avoid this problem, then, a better approximation might be to assume that the wind as a whole is propagating at some constant speed. To determine the appropriate speed to apply to the data at $30R_{\odot}$, we computed the Pearson correlation coefficient between this speed profile and the MHD solution at 1 AU for a range of phase shifts, choosing the one that maximized the correlation. While this aligns the streams up fairly well, the speeds are systematically too low. To address this, we applied Equation (10) to each parcel of plasma. The results of these operations are compared with the MHD solution in Figure 7. A phase shift of ≈44° maximized the correlation.

Although the stream structure matches reasonably well, there are some notable differences. First, the widths of the MHD-evolved streams at 1 AU are narrower. This is a consequence of both the steepening of the leading edge, and the erosion of the trailing edge. Second, for the same reasons, the stream gradients are higher at the leading edge and lower at the trailing edge of the MHD solutions. In contrast, the ballistically mapped streams remain symmetric. Third, the slow wind between the streams is substantially lower in the

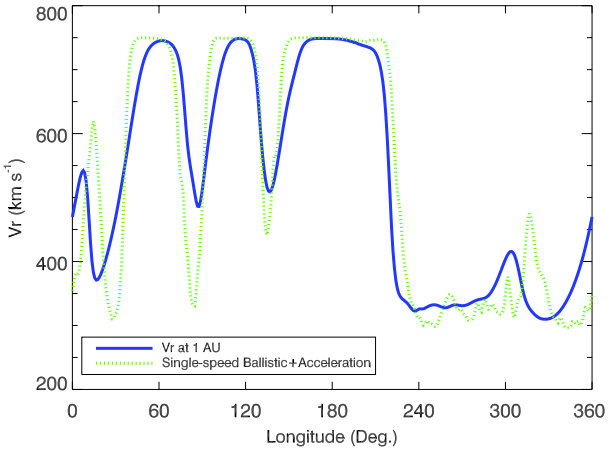

Figure 7 Comparison of radial velocity for CR 2068 at 1 AU with single-speed, ballistically mapped (and enhanced) speed from $30R_{\odot}$ to 1 AU as a function of Carrington longitude.

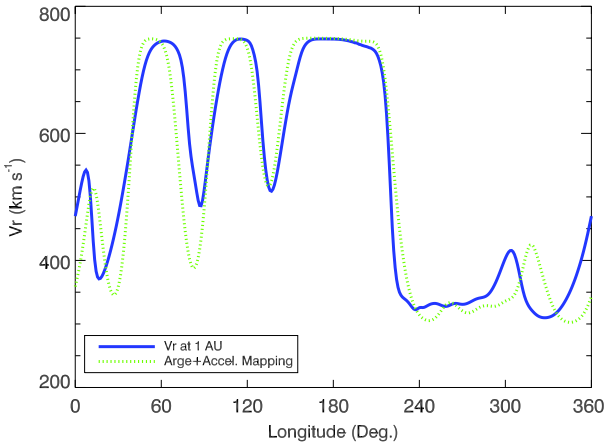

Figure 8 Comparison of radial velocity for CR 2068 at 1 AU with the Arge–Pizzo-evolved speed from $30R_{\odot}$ to 1 AU as a function of Carrington longitude.

ballistically mapped data because there is no accounting for the acceleration by neighboring faster wind. Fourth, all of the small-scale structure present at $30R_{\odot}$ is directly mapped to 1 AU, that is, there is no low-pass filtering of the structure in the simpler technique. This is particularly noticeable during the extended interval of slow wind between 240° and 360°. Fifth, the accuracy of the phasing of the high-speed streams changes from one stream to another. The phase shift of 46.5° that maximized the correlation coefficient was weighted by the stream of the longest duration, since it contributed most to the least-squares error estimate. Therefore, the phasing is best surrounding the structure at 180° longitude and becomes worse away from that location. The stream centered at $\approx 50°$, for example, is offset from the MHD solution by $\approx 15°$. In spite of these differences, the combination of a phase shift, together with an enhancement to velocity given by Equation (10) produced a profile with a correlation coefficient of 0.91.

3.4. Outward Mapping Using the Arge–Pizzo Kinematic Method

Arge and Pizzo (2000) developed a simple *ad hoc* technique for kinematically accounting for the steepening of solar wind streams at their leading edges and the complementary stretch-

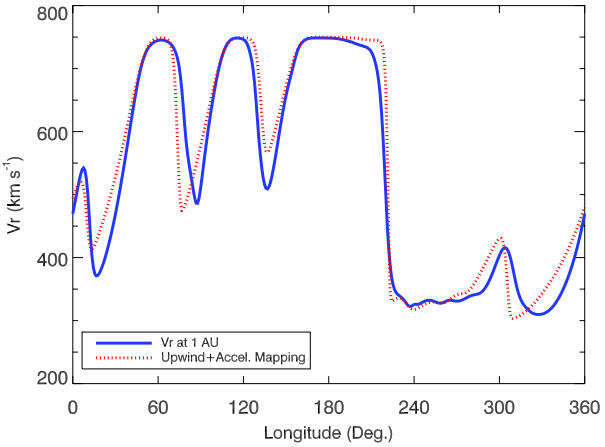

Figure 9 Comparison of radial velocity for CR 2068 at 1 AU with 1-D, upwind-evolved speed from $30R_{\odot}$ to 1 AU as a function of Carrington longitude.

ing at their trailing edges. In Figure 8 we compare the MHD model results with the initial stream mapped using this technique. The number of iterations that must be applied between $30R_{\odot}$ and 1 AU depends on the azimuthal separation of the data. Arge and Pizzo (2000) applied this technique ≈ 8 times to map speed profiles separated by 5° in longitude. Rather than impose a specific number of iterations, we computed correlation coefficients for a range of iterations from zero to 100, finding that a peak correlation coefficient of 0.93 occurred when 94 iterations of Equation (1) were applied. In comparison with the ballistic approximation (Figure 7), we note that several discrepancies have been removed: *i*) the widths of the streams now match better; *ii*) the higher-frequency variability has been reduced; and *iii*) the minima of the inter-stream slow wind has been elevated to better match the 1 AU results. However, several incongruities remain: *i*) the modest speed enhancement at $\approx 300°$ is misaligned, as is the one at $\approx 5°$; and *ii*) the fast streams do not show the same degree of asymmetry with the leading edges being steeper than the trailing edges.

3.5. Outward Mapping Using the Upwind + acceleration Method

Here, we consider the mapping of the solar wind stream using the newly developed upwind scheme defined by Equation (9). Since this method does not address acceleration by the $-\nabla P$ term, the general acceleration of the plasma that would be present in a full solution is not included, and we must again apply Equation (10) to boost the velocities. The results are shown in Figure 9. Comparing the two solutions, we see that the majority of the discrepancies noted for the ballistic comparison have, to a large extent, disappeared. First, the widths of the streams are now approximately the same, although the broadest stream lasts longer in the upwind solution. Second, the gradients on both edges of the streams match better, with the leading edge being steepened and the trailing edge being shallower. Third, the local speed minima between the high-speed streams match well. Fourth, the small-scale structure has disappeared in both solutions. Fifth, the phasing of the high-speed streams is generally better. One notable exception is the middle stream, where the upwind solution leads the heliospheric MHD solution. The correlation coefficient for these profiles was 0.98.

To understand the differences between the ballistic + acceleration and upwind + acceleration results, we computed Pearson correlation coefficients for a weighted upwind scheme, that is, we added a weighting function g_{up} to the right-hand sides of Equations (7) and (8), ranging from zero to one. To factor in the necessary phase shift that this would eliminate,

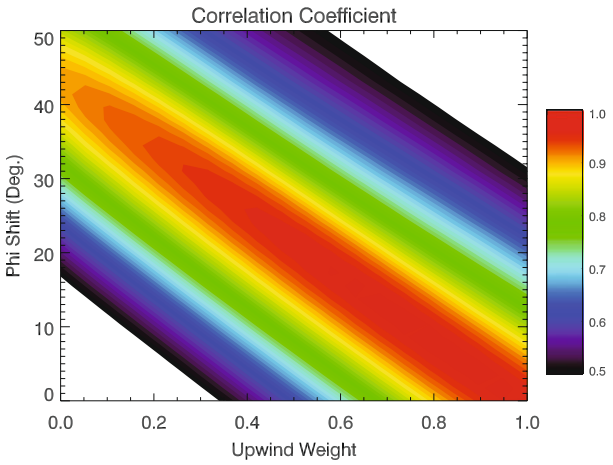

Figure 10 Color contour of Pearson correlation coefficient as a function upwind weighting function and longitudinal shift.

we also subtracted an arbitrary phase shift in longitude. The resulting 2-D correlation map is shown in Figure 10. In this view, the full upwind + acceleration scheme is on the far right and the pure ballistic + acceleration scheme is on the far left. The results make intuitive sense in that the correlation improves as we rely more and more on the upwind method, which does not require any longitudinal correction.

3.6. Inward Mapping of Solar Wind Streams

The ballistic approximation is usually applied to map stream structure observed at 1 AU by *in-situ* spacecraft back to the Sun. Since we have a complete MHD solution bounding the entire region from $30R_\odot$ to 1 AU, we can test the ability of this and the new upwind + acceleration technique for reconstructing the stream structure near the Sun. In Figure 11 we compare the MHD solution at $30R_\odot$ with the ballistically mapped 1 AU data. In addition to ballistically mapping the data back (purple), we have also reduced the velocities based on Equation (10) (green). We note the following points, which have been alluded to in the previous discussions of the various outward mapping techniques. First, the ballistic mapping fails to reproduce the steep gradient in velocity at the leading edge of the high-speed streams. Second, the leading edge remains 'eroded.' Third, the high-frequency perturbations are not recovered. Fourth, the minima in the inter-stream slow wind is not produced. Fifth, the phase of the high-speed streams does not match the model solution at $30R_\odot$: High-speed streams appear at earlier longitudes, and the troughs associated with inter-stream wind appears at later longitudes. All of these effects can be understood simply either by the fact that either: *i*) the dynamical evolution of the streams is wound up into the solution at 1 AU and is not unraveled by the ballistic mapping; and/or *ii*) the speed used to map the data back to $30R_\odot$ does not represent the average speed of that parcel of plasma. In particular, for the high-speed streams, the mapped speed is an overestimate, while for the slow speed and inter-streams, it is an underestimate.

We had anticipated that the upwind + acceleration method would resolve the problems associated with the ballistic mapping. However, it turns out that Equation (4) is unstable when $r \rightarrow -r$. When run in reverse, the mapping typically worked for some fraction of an AU before small perturbations amplify and propagate outward in longitude, eventually destroying the entire solution. It is likely that, in this direction, the characteristics intersect and no valid solution exists; that is, it is fundamentally unstable. It is possible that

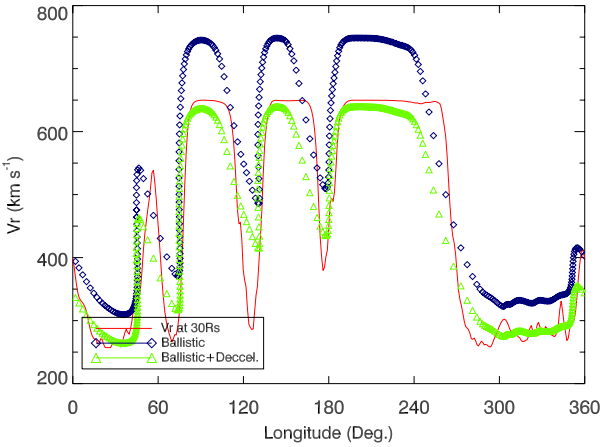

Figure 11 Comparison of radial velocity for CR 2068 at $30R_{\odot}$ with ballistically mapped back data, with and without a deceleration term, as a function of Carrington longitude.

the addition of a diffusion term mimicking viscosity would rectify this; however, by introducing this, the appeal of the simplicity of the approach would have been lost, and 1-D hydrodynamic and MHD techniques should probably be considered (see, *e.g.*, Pizzo, 1981; Riley *et al.*, 2003).

4. Summary and Discussion

In this report, we have explored the evolution of solar wind streams from near the Sun to 1 AU. We investigated the role played by the interplanetary magnetic field on the solution, finding that, in general, the IMF's effect is quantitative, not qualitative. However, if the computed coronal fields are lower than observations at 1 AU suggest, particularly during the recent solar minimum, then their neglect could be important. We then explored a range of techniques for mapping solar wind streams from the Sun to 1 AU and from 1 AU back to the Sun. We found that the transition from ballistic to kinematic to simple upwind techniques resulted in increasingly more accurate matches with the heliospheric MHD solution (correlation coefficients: 0.91, 0.93, and 0.98, respectively).

Our results suggest that the upwind + acceleration technique can be a powerful tool for exploring the relationship between the Sun and the near-Earth environment, particularly, in space weather applications. Although global heliospheric MHD models are regularly applied to model specific intervals (see, *e.g.*, Riley *et al.*, 2011), and can be used to create long-term databases of solutions (*e.g.*, http://www.predsci.com/mhdweb/), they are sufficiently complex that non-expert users may avoid them. Moreover, even at the lowest meaningful resolutions, solutions can take several hours on many processors to complete. This makes it difficult, if not impossible, to perform parametric or sensitivity studies where model results for a range of input parameters are compared with *in-situ* observations. For example, for the Wang–Sheeley model, there are arguably three free parameters needed to specify the solar wind speed from the areal expansion factor (Wang and Sheeley, 1990), while for the PSI model (which is based on perpendicular distance from the current sheet), there are four parameters (Riley, Linker, and Mikić, 2001), and for the Wang–Sheeley–Arge approach, there are seven (Arge *et al.*, 2003). Thus, to compare ten Carrington rotations, using magnetograms from 6 solar observatories, where the speed-profile free parameters are varied over say ten values each would require 180 000, 240 000, or 42 000 runs, for the WS, PSI, and WSA models,

respectively. Runs utilizing 64 processor runs and taking 4 h to complete would require 10 million processor hours to complete. On the other hand, the upwind + acceleration technique completes in seconds on a desktop computer. Thus, provided the errors introduced are tolerable, the upwind + acceleration provides a tractable means for exploring a wide range of parameters, which should ultimately, allow us to constrain many of the free parameters in the system. Once localized, global simulations can be used to 'spot' test several cases to verify that the results are robust.

Although the heliospheric MHD solutions with various magnetic field strengths resulted in speed profiles that, in a global sense, were very similar (Figure 5), direct comparisons of time series at the heliographic equator (Figure 4) showed significant differences; Differences that could be substantial from a space weather perspective. This illustrates a phenomenon that has been known for many years, and certainly since the launch of Ulysses, that, from a predictive point of view, Earth is located in an unfortunate location. The difficulty in reproducing observations lies in the fact that the band of solar wind variability, that is, where the slow and more variable wind flows, is roughly aligned with the magnetic equator. During the declining phase and at solar minimum, which is when modeling of the quiescent solar wind is most applicable, this tilt is modest and iso-contours of speed are not significantly inclined. What this means is that most spacecraft trajectories, which are approximately horizontal lines running from right to left in plots such as Figure 5, result in grazing encounters with slow–fast boundaries. Therefore, small changes in the boundary conditions, such as a larger or smaller magnetic field, can result in modest shifts in the boundaries, which, in turn, can make the difference between whether a spacecraft intercepts a stream or not. We might further infer that the phase of the solar cycle that allows for the most accurate model solutions is when: *i*) stream boundaries are significantly inclined to the equatorial plane; and *ii*) the rate of CMEs is the lowest. Typically, the tilt of the heliospheric current sheet increases sharply during the rising phase, peaking at solar maximum, and declining more slowly thereafter. Unfortunately, the rate of CMEs shows a similar profile, and there is no obvious interval where both scenarios are optimal. Nevertheless, it may be possible to derive a solar-cycle dependent measure of the potential accuracy of the solution based on the inclination of the HCS and the presence or absence of CMEs.

In assessing why the upwind and heliospheric MHD solutions differ, there are several potential contributions. First, and most significant is that the former is a 1-D solution. As such, there is no way for the plasma to relieve pressure in the plane perpendicular to the radial direction. In 3-D, on the other hand, shear flows can be generated, manifested by non-radial velocities that will generally act to retard the steepening of high-speed streams. This is why the leading edge of the broadest peak at $\approx 180^\circ$ in Figure 9 is steeper in the upwind solution. A second major contribution to the differences is that the upwind approximation neglects forces associated with the thermal pressure of the plasma as well as the interplanetary magnetic field. As we have seen from Figure 4, at least for the field, this can introduce non-negligible effects. We infer that neglecting $-\nabla P$ can produce similar disparities. In particular, its presence at the inner boundary provides a mechanism to accelerate the plasma to speeds that are measured at 1 AU. Our *ad hoc* procedure for accomplishing this using Equation (10), while reasonable, has not captured the full functional relationship that is contained within the MHD solution, or even the Parker solution (Parker, 1958). The value of this simple approach, however, is that it does not rely on other parameters such as P and T, which may not be well determined from coronal solutions.

In closing, the main point of this study was to introduce a new mapping technique (upwind + acceleration) and compare it with several approaches. We used global heliospheric MHD solutions as the 'ground truth' answer with which to assess their accuracy.

We found that the upwind + acceleration method, which is as simple to implement as the other techniques, produced a highly correlated result. The quality of the mapping, however, relies on the relative contribution of the IMF to the overall dynamics. By manipulating the input field to the MHD solution we showed that, if the current magnetic field strengths used in the models are reasonable, then the neglect of the IMF is justified. However, and particularly, for the recent minimum, if there is a 'missing magnetic flux' that is not being accounted for by the models, then its omission could be significant. Even then, however, since the alternative *ad hoc* approaches do not even account for the dynamical evolution of the solar wind to the extent that the new technique does, the upwind + acceleration should still perform better.

Acknowledgements The authors gratefully acknowledge the support of the LWS Strategic Capabilities Program (NASA, NSF, and AFOSR), the NSF Center for Integrated Space Weather Modeling (CISM), NASA's Heliophysics Theory Program (HTP), the Causes and Consequences of the Minimum of Solar Cycle 24 program, and the STEREO (IMPACT and SECCHI) teams.

References

Arge, C.N., Pizzo, V.J.: 2000, Improvement in the prediction of solar wind conditions using near-real time solar magnetic field updates. *J. Geophys. Res.* **105**, 10465.

Arge, C.N., Odstrcil, D., Pizzo, V.J., Mayer, L.R.: 2003, Improved method for specifying solar wind speed near the sun. In: Velli, M., Bruno, R., Malara, F., Bucci, B. (eds.) *Solar Wind Ten*, *AIP. Conf. Proc.* **679**, 190.

Fry, C.D., Sun, W., Deehr, C.S., Dryer, M., Smith, Z., Akasofu, S., Tokumaru, M., Kojima, M.: 2001, Improvements to the HAF solar wind model for space weather predictions. *J. Geophys. Res.* **106**, 20985.

Gosling, J.T., Asbridge, J.R., Bame, S.J., Feldman, W.C.: 1978, Solar wind stream interfaces. *J. Geophys. Res.* **83**, 1401.

Hakamada, K., Akasofu, S.: 1982, Simulation of three-dimensional solar wind disturbances and resulting geomagnetic storms. *Space Sci. Rev.* **31**, 3.

Hundhausen, A.J., Gentry, R.A.: 1968, The propagation of blast waves in the solar wind. *Astron. J.* **73**, 63.

Lionello, R., Linker, J.A., Mikić, Z.: 2001, Including the transition region in models of the large-scale solar corona. *Astrophys. J.* **546**, 542.

Nolte, J.T., Roelof, E.C.: 1973, Large-scale structure of the interplanetary medium, I: High coronal source longitude of the quiet-time solar wind. *Solar Phys.* **33**, 241.

Odstrcil, D., Linker, J.A., Lionello, R., Mikić, Z., Riley, P., Pizzo, V.J., Luhmann, J.G.: 2002, Merging of coronal and heliospheric numerical 2-D MHD models. *J. Geophys. Res.* **107**, 1493.

Parker, E.N.: 1958, Dynamics of the interplanetary gas and magnetic fields. *Astrophys. J.* **128**, 664.

Pizzo, V.: 1978, A three-dimensional model of corotating streams in the solar wind. I – Theoretical foundations. *J. Geophys. Res.* **83**, 5563.

Pizzo, V.J.: 1980, A three-dimensional model of corotating streams in the solar wind. II – Hydrodynamic streams. *J. Geophys. Res.* **85**, 727.

Pizzo, V.J.: 1981, On the application of numerical models to the inverse mapping of solar wind flow structures. *J. Geophys. Res.* **86**, 6685.

Pizzo, V.J.: 1982, A three-dimensional model of corotating streams in the solar wind. III – Magnetohydrodynamic streams. *J. Geophys. Res.* **87**, 4374.

Pizzo, V.J.: 1985, Interplanetary shocks on the large scale: A retrospective on the last decade's theoretical efforts. In: Tsurutani, B.T., Stone, R.G. (eds.) *Collisionless Shocks in the Heliosphere: Reviews of Current Research*, *AGU Geophys. Monogr.* **35**, 51.

Pizzo, V.J., Intriligator, D.S., Siscoe, G.L.: 1995, Radial alignment simulation of solar wind streams observed by Pioneers 10 and 11 in 1974. *J. Geophys. Res.* **100**, 12251.

Press, W.H., Teukolsky, S.A., Vetterling, W.T., Flannery, B.P.: 2002, *Numerical Recipes in C++: The Art of Scientific Computing*, Cambridge University Press, Cambridge, 832.

Riley, P.: 1999, CME dynamics in a structured solar wind. In: Habbal, S.R., Esser, R., Hollweg, V., Isenberg, P.A. (eds.) *Solar Wind Nine*, *AIP Conf. Proc.* **471**, 131.

Riley, P.: 2010, The three-dimensional structure of the inner heliosphere. In: Maksimovic, M., Issautier, K., Meyer-Vernet, N., Moncuquet, M., Pantellini, F. (eds.) *Twelfth International Solar Wind Conference*, *AIP Conf. Proc.* **1216**, 323.

Riley, P., Gosling, J.T.: 1998, Do coronal mass ejections implode in the solar wind? *Geophys. Res. Lett.* **25**, 1529.
Riley, P., Linker, J.A., Mikić, Z.: 2001, An empirically-driven global MHD model of the corona and inner heliosphere. *J. Geophys. Res.* **106**, 15889.
Riley, P., Linker, J.A., Mikic, Z.: 2009, Global MHD modeling of the solar corona and inner heliosphere for the whole heliosphere interval. IAU General Assembly Joint Discussion JD16, in press.
Riley, P., Mikic, Z., Linker, J., Zurbuchen, T.H.: 2003, Understanding the solar sources of in situ observations. In: Velli, M., Bruno, R., Malara, F., Bucci, B. (eds.) *Solar Wind Ten*, *AIP Conf. Proc.* 79.
Riley, P., Lionello, R., Linker, J.A., Mikic, Z., Luhmann, J., Wijaya, J.: 2011, Global MHD modeling of the solar corona and inner heliosphere for the whole heliosphere interval. Solar Phys., in press.
Sarabhai, V.: 1963, Some consequences of nonuniformity of solar wind velocity. *J. Geophys. Res.* **68**, 1555.
Schwenn, R.: 1990, Large-scale structure of the interplanetary medium. In: Schwenn, R., Marsch, E. (eds.) *Physics of the Inner Heliosphere I. Large-Scale Phenomena*, Springer, Berlin, 99.
Smith, E.J., Wolfe, J.H.: 1976, Observations of interaction regions and corotating shocks between one and five AU: Pioneers 10 and 11. *Geophys. Res. Lett.* **3**, 137.
Snyder, C.W., Neugebauer, M.: 1966, The relation of Mariner-2 plasma data to solar phenomena. In: Mackin, R.J., Neugebauer, M. (eds.) *The Solar Wind*, Pergamon Press, Oxford, 25.
Svalgaard, L., Cliver, E.W.: 2007, A floor in the solar wind magnetic field. *Astrophys. J. Lett.* **661**, 203.
Usmanov, A.V., Goldstein, M.L., Besser, B.P., Fritzer, J.M.: 2000, A global MHD solar wind model with WKB Alfvén waves: Comparison with Ulysses data. *J. Geophys. Res.* **105**, 12675.
Wang, C., Richardson, J.D., Gosling, J.T.: 2000, A numerical study of the evolution of the solar wind from Ulysses to Voyager 2. *J. Geophys. Res.* **105**, 2337.
Wang, Y.M., Sheeley, N.R. Jr.: 1990, Solar wind speed and coronal flux-tube expansion. *Astrophys. J.* **355**, 726.

Appendix F

Global MHD modeling of the solar corona and inner heliosphere for the whole heliosphere interval

Riley, P. and Lionello, R. and Linker, J. A. and Mikic, Z. and Luhmann, J. and Wijaya, J.

Published in Solar Physics, 2011.

Solar Phys (2011) 274:361–377
DOI 10.1007/s11207-010-9698-x

Global MHD Modeling of the Solar Corona and Inner Heliosphere for the Whole Heliosphere Interval

P. Riley · R. Lionello · J.A. Linker · Z. Mikic · J. Luhmann · J. Wijaya

Received: 14 October 2010 / Accepted: 3 December 2010 / Published online: 5 February 2011

Abstract In an effort to understand the three-dimensional structure of the solar corona and inner heliosphere during the Whole Heliosphere Interval (WHI), we have developed a global magnetohydrodynamics (MHD) solution for Carrington rotation (CR) 2068. Our model, which includes energy-transport processes, such as coronal heating, conduction of heat parallel to the magnetic field, radiative losses, and the effects of Alfvén waves, is capable of producing significantly better estimates of the plasma temperature and density in the corona than have been possible in the past. With such a model, we can compute emission in extreme ultraviolet (EUV) and X-ray wavelengths, as well as scattering in polarized white light. Additionally, from our heliospheric solutions, we can deduce magnetic-field and plasma parameters along specific spacecraft trajectories. In this paper, we present a general analysis of the large-scale structure of the solar corona and inner heliosphere during WHI, focusing, in particular, on *i*) helmet-streamer structure; *ii*) the location of the heliospheric current sheet; and *iii*) the geometry of corotating interaction regions. We also compare model results with *i*) EUV observations from the EIT instrument onboard SOHO; and *ii*) *in-situ* measurements

The Sun – Earth Connection near Solar Minimum
Guest Editors: M.M. Bisi, B.A. Emery, and B.J. Thompson

P. Riley (✉) · R. Lionello · J.A. Linker · Z. Mikic · J. Wijaya
Predictive Science, Inc., 9990 Mesa Rim Road, Suite 170, San Diego, CA 92121, USA
e-mail: pete@predsci.com

R. Lionello
e-mail: lionel@predsci.com

J.A. Linker
e-mail: linkerj@predsci.com

Z. Mikic
e-mail: mikicz@predsci.com

J. Wijaya
e-mail: wijayaj@predsci.com

J. Luhmann
Space Sciences Laboratory, University of California, Berkeley, CA 94720, USA
e-mail: jgluhman@ssl.berkeley.edu

made by the STEREO-A and B spacecraft. Finally, we contrast the global structure of the corona and inner heliosphere during WHI with its structure during the Whole Sun Month (WSM) interval. Overall, our model reproduces the essential features of the observations; however, many discrepancies are present. We discuss several likely causes for them and suggest how model predictions may be improved in the future.

Keywords Sun · Corona · Corotating interaction regions · Magnetic fields · Solar wind · Interplanetary medium

1. Introduction

The Whole Heliosphere Interval (WHI), which ran from 20 March through 16 April 2008, and coincided with Carrington rotation (CR) 2068, is providing a unique opportunity for both observers and modelers to collaborate in an effort to understand the three-dimensional (3D) structure and evolution of the solar corona and inner heliosphere. It builds on the previous Whole Sun Month (WSM) interval, which proved to be exceptionally successful (*e.g.*, Gibson *et al.*, 1999; Linker *et al.*, 1999; Riley *et al.*, 1999). The WHI occurred on the way to the most recent solar minimum (December 2008), which has, thus far, been unique in a number of ways. For example, in 2009 260 days (71%) were spotless. Moreover, from 1 January 2004 through 8 October 2010, 812 days have been spotless (see http://spaceweather.com), making the current solar minimum the most prolonged and quiet in a century (Phillips, 2009). The polar photospheric flux has decreased by $\approx$40% (Svalgaard and Cliver, 2007) and the coronal holes are noticeably smaller (Kirk *et al.*, 2009). Measurements by *in-situ* spacecraft show substantial differences between the recent minimum and the previous three. *Ulysses* polar observations through late 2008, in particular, suggest that *i*) the interplanetary magnetic field (IMF) was $\approx$36% lower than the previous minimum (Smith and Balogh, 2008); *ii*) the scaled number density was $\approx$17% lower (Issautier *et al.*, 2008; McComas *et al.*, 2008); and *iii*) the scaled temperature was $\approx$14% lower (McComas *et al.*, 2008). It was also determined that the bulk solar-wind speed was $\approx$3% lower, although this may not be a statistically significant change. From these measurements it was inferred that *i*) the dynamic pressure decreased by $\approx$22%; *ii*) the proton thermal pressure decreased by $\approx$25%; and *iii*) the magnetic pressure decreased by $\approx$87% (McComas *et al.*, 2008). The profiles of high-speed streams upstream of Earth also seem to be unique, being stronger, longer in duration, and more recurrent than during the previous minimum (Gibson *et al.*, 2009). Strong periodicities were also found in early-mid 2008, with periods of 9, 13.5, and 27 days (Emery *et al.*, 2008), with no comparable patterns found during the previous minimum. It appears that the solar wind at Earth during this minimum was 47% less dense and 13% faster, and the IMF is reduced by 11% (Gibson *et al.*, 2009). However, given the complexity of in-Ecliptic measurements, including the contribution from multiple sources of solar wind and the formation and evolution of compression and rarefaction regions, the causes of such changes are more difficult to interpret than the *Ulysses* polar counterparts. However, their consequences could be readily seen within the Earth's magnetosphere, particularly in the form of enhanced auroral power and an elevated radiation environment (Gibson *et al.*, 2009).

To understand the properties and structure of the corona and inner heliosphere during WHI, we can analyze a range of phenomena in remote-sensing observations and *in-situ* measurements and compare with model results. Previously, we have compared high-latitude, quiescent observations by *Ulysses* with 1D, thermodynamic solutions to understand the

acceleration characteristics of the solar wind and the relationship between magnetic-field strength within coronal holes and heating of the solar wind plasma (Riley *et al.*, 2010b). In this study, we provide a broad overview of the 3D structure of the inner heliosphere during WHI. We compare the state of the corona and heliosphere during WHI and WSM. We also directly compare model results with emission observations and *in-situ* measurements to illustrate where the model performs well and where it performs poorly. Finally, we discuss the current limitations of global magnetohydrodynamic (MHD) models and suggest from where future improvements may come.

From a global perspective of the heliosphere, two particularly useful structures are *i*) helmet streamers and *ii*) the heliospheric current sheet (HCS). Helmet streamers are arch-like, bright features seen in white-light observations. They extend outward several solar radii from the Sun and are drawn into a cusp-like structure. They are composed of closed magnetic loops that sometimes overlay sunspots and active regions (ARs). Often a prominence (or filament) is embedded at the bottom of the streamer. A necessary requirement for such loops is a neutral line (that is, the location where B_r changes sign), and the footpoints of the helmet streamer field lines lie in regions of opposite polarity. From this, we can understand the association of streamers with ARs, which contain a strong, localized neutral line, as well as their interplanetary extension in the form of stalks and association with the HCS. At solar minimum, even in the absence of any ARs, helmet streamers are produced from the large-scale solar dipole. In this case, the neutral line is a simple curve, circumscribing the Sun and confined to low heliographic latitudes. Whereas helmet streamers separate open field lines of opposite polarity, a second class of "pseudostreamers" separate field lines of the same polarity (Wang, Sheeley, and Rich, 2007). Stated another way, while helmet streamers separate coronal holes of opposite polarity, pseudostreamers separate holes of the same polarity. Wang, Sheeley, and Rich (2007) showed that although pseudostreamers also have plasma-sheet extensions, they are not associated with the HCS. As we will show, their presence during the recent minimum led to the disappearance of the more usual quiescent equatorial streamer belt.

The HCS, a surface separating regions of opposite magnetic polarity, is a fundamental feature of the heliosphere, and is intimately related to the large-scale dynamic flow of the solar wind. As the largest coherent structure within the heliosphere, the HCS acts as a "frame" about which corotating interaction regions (CIRs) are organized (Pizzo and Gosling, 1994). This makes it a particularly attractive entity to study with global MHD models (Riley, Linker, and Mikić, 2002). Its shape also plays an important role in the modulation of galactic cosmic rays (*e.g.*, Jokipii, Sonett, and Giampapa, 1997). The tilt of the HCS (that is, its maximum latitudinal extent) has displayed some unusual properties during the recent solar minimum. At the end of Cycles 21 (1986) and 22 (1996), the tilt in both hemispheres declined relatively monotonically, reaching near-zero values at approximately the same time as the sunspot number. Applying a similar relationship during the declining phase of Cycle 23, one might have predicted that the tilt of the HCS would reach zero in late 2007. However, since mid-2006 and through 2008 it remained steady at $\approx 15^\circ$ (see Figure 1).

2. Observations During WHI

Observations during WHI are discussed in several complementary companion studies (Bisi, Emery, and Thompson, 2011). Here we limit ourselves to brief remarks that will be relevant for our discussion of the model results later. To orient ourselves, in Figure 1 we summarize several solar-related time-series parameters over a period of more than three decades.

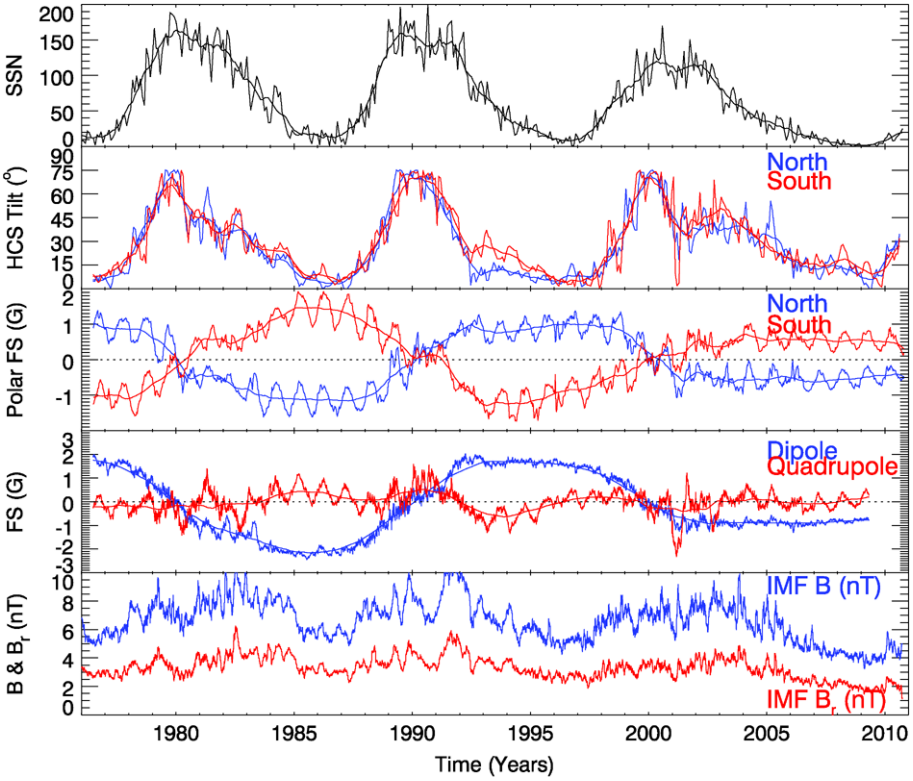

Figure 1 Time series of (a) sunspot number (SSN); (b) HCS tilt, as inferred from potential field source surface (PFSS) solutions driven by Wilcox Solar Observatory (WSO) data; (c) northern and southern polar field strengths (FS); (d) axial dipole and zonal quadrupole contributions to the field strength; and (e) total and radial IMF, as measured by the many spacecraft contributing to the OMNI dataset. Data for panels two through four were provided by J.T. Hoeksema.

We note the following points. First, the last full solar cycle (23), which spanned from August/September 1996 through December 2008 (as determined from a 12-month smoothed sunspot number (SSN): *i*) contained a more modest peak than the previous two cycles; and *ii*) lasted $\approx$2.5 years longer. Second, following the peak, the tilt (or maximum extent) of the HCS remained elevated ($\approx 45°$) for $\approx$three years, falling lower to $\approx 15°$ and again holding steady before dropping to nearly zero in 2009. Third, the polar fields have remained steady and reasonably symmetric since 2003, but at approximately half their values of the previous cycle. Fourth, following solar maximum in 2001, the quadrupolar component of the field has remained zero, while the axial-dipole component has remained relatively steady (again at half the amplitude of the previous cycles). Fifth, both the total magnitude and radial component of the IMF decreased relatively monotonically from 2003 onwards, reaching a minimum in 2009. Based on data available for 2010, activity appears to be returning: SSN is increasing, the tilt of the HCS is becoming larger, and the strength of the IMF is growing.

3. MHD Modeling of the Corona and Inner Heliosphere

MHD models have proven very successful in interpreting and comprehending a wide array of solar and heliospheric phenomena. They provide a global context for connecting diverse datasets and understanding the physical interrelationship between often dissimilar phenomena.

The first MHD models of the solar corona were developed almost 40 years ago (Endler, 1971; Pneuman and Kopp, 1971). Over the years they have become progressively more sophisticated (*e.g.*, Mikić and Linker, 1994), culminating in models that include the photospheric field as a boundary condition (*e.g.*, Riley, Linker, and Mikić, 2001; Roussev *et al.*, 2003). Complementary efforts focusing on heliospheric models, where the inner boundary was placed beyond the outermost critical point, were also pursued (*e.g.*, Pizzo, 1978; Odstrcil, 1994). Most recently, coronal and heliospheric models have been coupled (*e.g.*, Riley, Mikić, and Linker, 2003; Odstrcil *et al.*, 2004; Manchester *et al.*, 2006; Riley *et al.*, 2007), and more sophisticated descriptions of energy-transport processes have been included (*e.g.*, Lionello, Linker, and Mikić, 2009).

Our group has studied the properties of the ambient solar wind for a number of years (Riley *et al.*, 1996, 2001; Riley, Linker, and Mikić, 2001, 2002; Riley, Mikić, and Linker, 2003; Riley, 2007b), finding that, in general, our models can reproduce the essential large-scale features of the solar wind. We say "models" and not "model" because we have found that different approaches are required depending on the specific scientific question being addressed. In the simulations described here, the two primary models are *i*) the thermodynamic coronal model and *ii*) the polytropic heliospheric model. For the latter, we drive the inner radial boundary using one of two approaches: (a) directly using output from the thermodynamic coronal solution, or (b) using empirically based boundary conditions derived from the structure of the coronal magnetic field (Riley, Linker, and Mikić, 2001). In the following sections, we summarize how these models differ and justify when and how each should be applied.

3.1. The General MHD Model

In general, our 3D, time-dependent algorithm (Magnetohydrodynamics Around a Sphere: MAS) solves the following form of the resistive MHD equations on a nonuniform grid in spherical coordinates:

$$\nabla \times \mathbf{B} = \frac{4\pi}{c}\mathbf{J}, \tag{1}$$

$$\nabla \times \mathbf{E} = -\frac{1}{c}\frac{\partial \mathbf{B}}{\partial t}, \tag{2}$$

$$\mathbf{E} + \frac{\mathbf{v} \times \mathbf{B}}{c} = \eta \mathbf{J}, \tag{3}$$

$$\frac{\partial \rho}{\partial t} + \nabla \cdot (\rho \mathbf{v}) = 0, \tag{4}$$

$$\frac{1}{\gamma - 1}\left(\frac{\partial T}{\partial t} + \mathbf{v} \cdot \nabla T\right) = -T \nabla \cdot \mathbf{v} + \frac{m_{\mathrm{p}}}{2k\rho} S, \tag{5}$$

$$\rho\left(\frac{\partial \mathbf{v}}{\partial t} + \mathbf{v} \cdot \nabla \mathbf{v}\right) = \frac{1}{c}\mathbf{J} \times \mathbf{B} - \nabla(p + p_{\mathrm{w}}) + \rho \mathbf{g} + \nabla \cdot (\nu \rho \nabla \mathbf{v}), \tag{6}$$

$$S = \left(-\nabla \cdot \mathbf{q} - n_{\mathrm{e}} n_{\mathrm{p}} Q(T) + H_{\mathrm{ch}}\right); \tag{7}$$

where **B** is the magnetic field, **J** is the electric-current density, **E** is the electric field, ρ, **v**, p, and T are the plasma mass density, velocity, pressure, and temperature, respectively, $\mathbf{g} = -g_0 R_\odot^2 \hat{\mathbf{r}}/r^2$ is the gravitational acceleration, η the resistivity, and ν is the kinematic viscosity. Equation (7) contains the radiation loss function $[Q(T)]$ as in Athay (1986), n_e and n_p are the electron and proton number density (which are equal for a hydrogen plasma), m_p is the proton mass, $\gamma = 5/3$ is the polytropic index, H_{ch} is the coronal heating term, and **q** is the heat flux. A combination of Spitzer collisional ($r < 10R_\odot$) and collisionless ($r > 10R_\odot$, Hollweg, 1978) heat fluxes is used to prescribe **q**. The wave pressure term $[p_w]$ in Equation (6) represents the contribution due to Alfvén waves (Jacques, 1977) and is evolved using the Wentzel – Kramers – Brillouin (WKB) approximation for time – space averaged Alfvén wave energy density $[\epsilon]$ (Mikić *et al.*, 1999). The method of solution of Equations (1) through (6), including the boundary conditions, has been described previously (see Lionello, Linker, and Mikić, 2009 and references therein).

In the energy Equation (7), S includes radiation, thermal conduction, coronal heating, and resistive and viscous diffusion. Lionello, Linker, and Mikić (2001) describe how we incorporate these processes so as to include the upper chromosphere and transition region in the domain of the calculation. Although we simplify these equations for the heliospheric solutions by employing a "polytropic" energy equation, where $S = 0$, (*e.g.*, Linker *et al.*, 1999; Mikić *et al.*, 1999; Riley, Linker, and Mikić, 2001; Roussev *et al.*, 2003), to more accurately compute densities and temperatures in the corona (and hence the heliosphere), we prescribe a functional form for S, allowing us to set γ to a realistic value of 5/3. We refer to this model as the "thermodynamic" model, because it incorporates energy-transport processes. With such a model we can make meaningful comparisons between simulated emission (EUV and soft X-ray) and observations, which provide strong constraints on the free parameters in the heating model (Lionello, Linker, and Mikić, 2009).

Finally, an important feature that makes our approach unique is the use of observed photospheric magnetograms to drive the model. This allows us to model the specific properties of time periods of interest, including WHI and WSM.

3.2. The Heliospheric MHD Model

For computing heliospheric solutions, we have developed two complementary approaches. In the simpler empirically based technique, we use the structure of the coronal magnetic field to derive the radial velocity boundary condition at the inner edge of the heliospheric model (Riley, Linker, and Mikić, 2001). The heliospheric solutions are molded by dynamic forces so that the profile of the radial velocity at the inner boundary is believed to have the largest effect on the resulting solutions (Riley and McComas, 2009). The technique is based on the idea, supported by both the "interchange reconnection" model of L. Fisk and colleagues (Fisk, 1996; Fisk, Schwadron, and Zurbuchen, 1998) as well as the "expansion factor" models of Y.-M. Wang and colleagues (Wang and Sheeley, 1990; Cranmer, van Ballegooijen, and Edgar, 2007; Cranmer *et al.*, 2010), that the slow solar wind originates at the boundary between open and closed field lines, and the fast solar wind originates from everywhere else (that is, from deeper within coronal holes). We also use the computed magnetic field from the coronal solution directly, and infer the remaining plasma quantities (density and temperature) by assuming momentum-flux conservation and thermal-pressure balance over the sphere defining the inner boundary of the heliospheric model at $30R_\odot$.

The second, more self-consistent, approach is to drive the heliospheric model directly using all of the magnetic and plasma variables computed in the coronal solution. While this

should, in principle, be more accurate, we have found that the empirically based solutions tend to more closely match *in-situ* measurements (speed, density, temperature, and polarity of the IMF) at Earth and *Ulysses*. Ultimately, of course, we expect that as the physics contained within the coronal model improves, and the remaining free parameters become better constrained, the quality of the self-consistently derived heliospheric solutions will surpass the empirically based results. In this study, we present results using both approaches.

4. Model Results

4.1. Introduction

We computed preliminary thermodynamic solutions for both WSM and WHI. Figure 2 summarizes the large-scale structure of the inner heliosphere during these two periods. The two panels show meridional slices of the radial velocity and radial magnetic-field strength (scaled to 1 AU) in arbitrary planes, as well as an equatorial slice of the plasma density, again scaled by $1/r^2$ to values at 1 AU. Contrasting the two solutions, we note several points. First, the unipolar fields between WSM and WHI have reversed. The large-scale dipolar component of the solar field during the previous minimum (WSM) was outward over the poles of the northern hemisphere and inward over the southern poles. During WHI, which represents the minimum of the most recent cycle, it is reversed. Second, the "band of solar-wind variability," that is, the volume of the heliosphere that is defined by slower, but more variable solar wind, is narrower during WSM than during WHI. Third, this band contained several near-equatorial coronal holes that were the source of higher-speed solar wind, making the solar wind speed measured in the ecliptic plane by the *Advanced Composition Explorer* (ACE) and *Wind* more variable and complex during WHI (Gibson *et al.*, 2009). Fourth, the average number density of the solar wind during WHI was less than during WSM, yet the

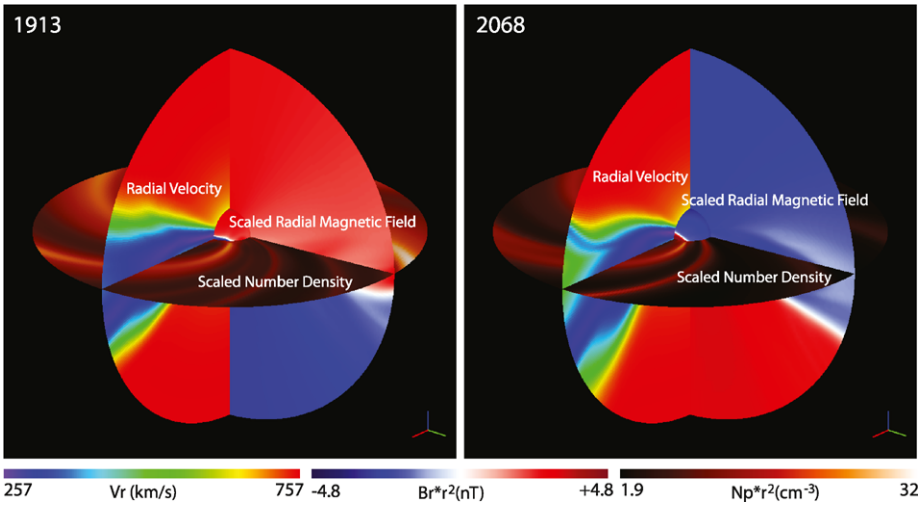

Figure 2 Illustration of the large-scale properties of the inner heliosphere (out to 1 AU) for (left) WSM and (right) WHI time periods. The two meridional slices in each panel show the radial velocity and radial magnetic-field strength, scaled to 1 AU. The slice in the equatorial plane shows the scaled number density. The sphere at $30R_{\odot}$ shows the scaled radial magnetic-field strength.

stream structure was more complex, with more interaction regions (see Gibson *et al.*, 2009, Figure 3a).

4.2. Helmet Streamer Structure

The current solar minimum, unlike the previous one, appears to have a rather unique streamer structure. Instead of the (apparently) more usual single equatorial streamer belt (that is, in coronagraph images, two streamers – one emanating from the eastern equatorial limb of the Sun and the other from the West), the streamer structure is more complex. Figure 3 shows simulation results for the WSM and WHI time periods. The model results allow us to probe the underlying magnetic structure giving rise to the observed density features in coronagraph observations.

Focusing first on CR1913, we infer that all three streamers (one on the east limb and two on the west limb) can be classified as the usual helmet streamers, where the streamer stalk marks the boundary between oppositely directed field lines, and a current sheet is associated with the interplanetary extension of this structure. However, for CR2068 we infer that, while the two streamers in the southern hemisphere, off the east and west limbs, are also helmet streamers, the two in the North are both pseudostreamers, where the field lines on either side of the streamer stalk are of the same polarity. This is further substantiated by considering the polarity of the photospheric field under the streamers. For the usual helmet streamer, one half is of one polarity and the other half is of the opposite polarity (this is clearest for the NW streamer in CR1913 and the SW streamer in CR2068), indicating that a neutral line runs through it. Finally, and most obviously, the pseudostreamers can be identified by the double-loop structure within them, which must occur if the over-arching field lines on either side have the same polarity. Wang, Sheeley, and Rich (2007) have argued that pseudostreamers are sources of fast solar wind, but our simulation results indicate that the speeds are lower in the vicinity of the pseudostreamer.

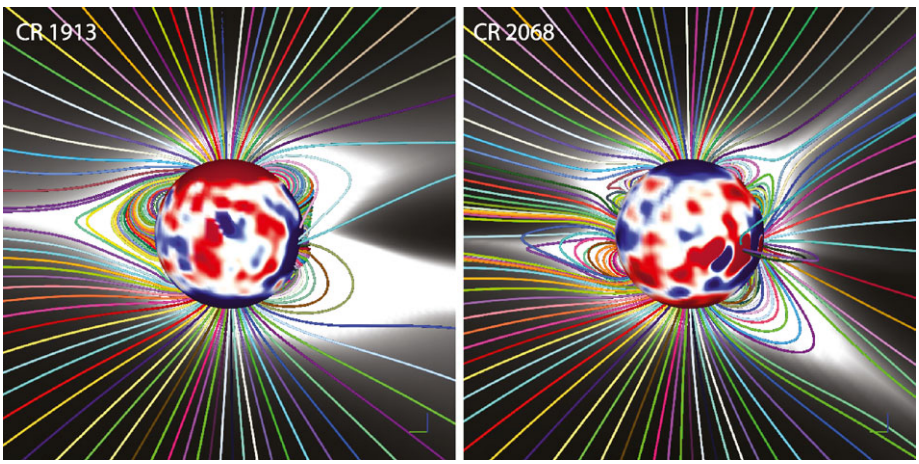

Figure 3 Composite images of the photospheric magnetic field at the solar surface (saturated at ± 1 G), with a selection of magnetic-field lines originating in the plane of the paper, and a color contour of the coronal density (scaled by r^2) for CR1913 (left) and CR2068 (right).

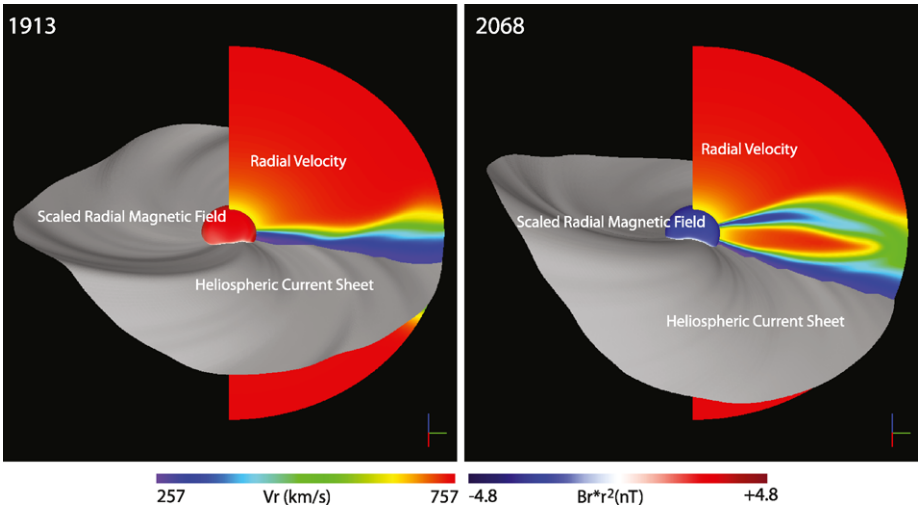

Figure 4 Illustration of the large-scale properties of the inner heliosphere (out to 1 AU) for (left) WSM and (right) WHI time periods. The isosurface marks the location of $B_r = 0$ and is the location of the HCS. The meridional slice shows radial velocity, and the sphere at $30R_\odot$ shows the radial magnetic field strength.

4.3. The Heliospheric Current Sheet

Figure 4 summarizes the shape of the HCS during the WSM and WHI time periods. Contrasting the two solutions, we note several points. First, the HCS, as well as the "band of solar wind variability," extend to higher heliographic latitudes during WHI, consistent with the results in Figure 1. Second, the polar speeds are essentially the same for the two minima. This is significant as the "self-consistent" heliospheric model was used to compute these solutions, and not the empirically based model, in which case the polar speeds would be identical by design. Instead, the similar speeds are consistent with the *Ulysses* results that while the density dropped between WSM and WHI, the speed remained constant (McComas *et al.*, 2008). Third, a significant source of fast solar wind in the ecliptic plane during WHI derives from equatorial coronal holes, whereas during WSM, the high-speed wind originated in the polar coronal holes, and, to a limited extent, from the equatorial extension of the northern polar coronal hole, known as the "elephant's trunk."

4.4. Corotating Interaction Regions

The global solar-wind structure in the heliosphere can be conveniently described by the combination of two effects. The first is that, beyond $\approx 10R_\odot$, solar material streams away from the Sun along roughly radial trajectories with a range of speeds. The second is simply that the Sun rotates: solar rotation acts to place plasma on the same radial trajectory with faster or slower wind. Faster wind overtaking slower wind leads to a compression front, while slower material being outrun by faster material leads to a rarefaction region, or expansion wave (Sarabhai, 1963). The boundary within the compression region, separating the slow and fast wind, is known as a stream interface (SI) (Gosling *et al.*, 1978). In the simplest possible scenario, where speed variations depend only on their source location at the Sun, that is, the flow pattern does not vary significantly on the time scale of a solar rotation (such as at solar minimum), the large-scale compressive structures created by the interactions of

these streams are fixed in a frame corotating with the Sun, and they are known as corotating interaction regions (CIRs, Smith and Wolfe, 1976). If the speed difference is sufficiently large, and typically beyond about 2 AU, a pair of shocks may form, bounding the CIR (*e.g.*, Pizzo, 1985).

The *Ulysses* mission revolutionized our understanding of stream structure in three dimensions. Much of the basic structure had been predicted by global MHD simulations performed by Pizzo (1991). However, it was not until *Ulysses* measurements began to uncover a systematic picture of the properties of CIRs at mid latitudes during the declining phase of Solar Cycle 22, that these earlier numerical results began to be appreciated (Pizzo and Gosling, 1994). Gosling *et al.* (1995), for example, found that CIR-associated forward shocks disappeared at helio-latitudes in excess of $\approx 26°$, which corresponded roughly to the tilt of the solar magnetic dipole. Additionally, reverse shocks continued to be observed frequently, up to latitudes of $\approx 42°$, after which their presence became rarer. Further confirmation of the model predictions came from the flow deflections observed at the shocks, suggesting that the forward shocks were oriented such that their outward normals were tilted toward the Equator, and hence were propagating equatorward, while the reverse-shock normals were tilted poleward (Riley *et al.*, 1996). These orientations can be understood heuristically based on simple geometric ideas (*e.g.*, Riley, 2010).

Figure 5 summarizes the large-scale structure of the inner heliosphere during WSM and WHI. The top panels show the three components of solar-wind velocity (in a heliocentric spherical coordinate system: r, θ, ϕ), while the bottom panels show the radial component of the magnetic field, the number density, and the plasma thermal pressure at 2.6 AU. Contrasting the two solutions, we note several points. First, the differences noted above are also present here: the "band of solar wind variability" extended to higher heliographic latitudes during CR2068; the polar speeds are essentially the same for the two minima; a significant source of fast solar wind in the ecliptic plane during CR2068 derives from equatorial coronal holes; and the computed tilt (maximum extent) of the HCS (the centroid of the white traces in the plots of radial magnetic field) matches the values shown in Figure 1. Additionally, we note that *i*) the decreases in B and B_r between CR1913 and CR2068 roughly match the changes as observed in NASA's OMNI dataset (*i.e.*, ACE and *Wind*), although the modeled values are lower than were observed (a result that is currently not understood); *ii*) the tilts of the interaction regions are much less distinct, or systematic, for CR2068 than for CR1913, although they are still present; and *iii*) during CR2068, the interaction regions are more localized and have the "U"-shaped profiles consistent with the heuristic ideas discussed by Riley, Mikić, and Linker (2003), that is, due to localized equatorial (and mid-latitude) coronal holes, "punching" through the otherwise slower wind.

5. Comparison with Observations

5.1. Extreme Ultraviolet Comparisons

As we have noted, emission images computed from the model results are quite sensitive to the form of the coronal-heating function $[H]$ used in the model. Thus, although H was not derived self-consistently from any theory of coronal heating (although it was "guided" by them), if our simulated emission matches well with observations, it suggests that our form of heating is likely a reasonable approximation to reality. In turn, it may provide a useful constraint for theories of coronal heating.

Using the densities and temperatures obtained from the global MHD models, we computed synthetic emission images in the *Extreme Ultraviolet Imaging Telescope* (EIT) bands

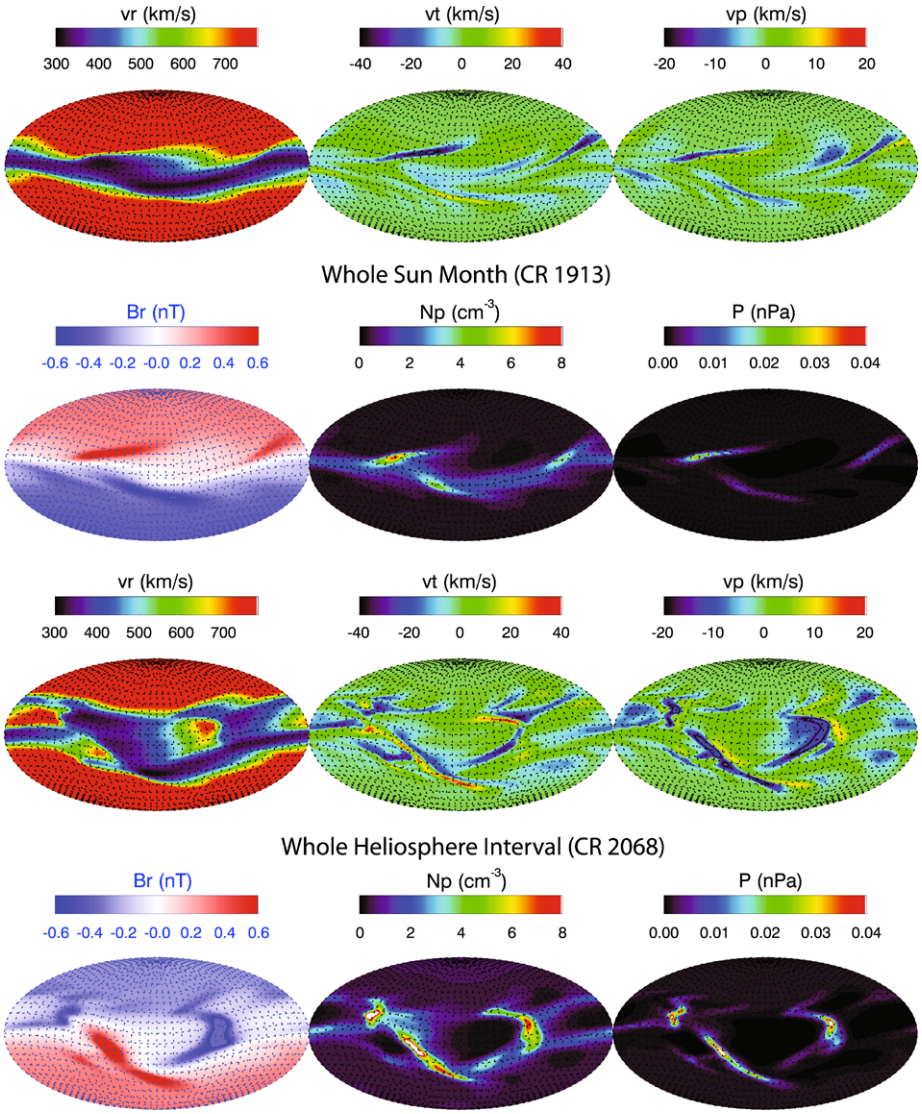

Figure 5 Mollweide projection maps of radial speed [v_r], meridional speed [v_t], azimuthal speed [v_p], radial magnetic field [B_r], scaled number density [N_p], and thermal pressure [P] for Carrington rotation 1913 (top), corresponding approximately to the Whole Sun Month (WSM) period, and 2068 (bottom), corresponding to the Whole Heliosphere Interval (WHI).

of 171, 195, and 284 Å. In Figure 6 they are compared with *Solar and Heliospheric Observatory* (SOHO)/EIT observations for CR1913. We emphasize that these are quantitative comparisons, that is, values of DN s^{-1} $pixel^{-1}$ are directly compared. We note several positive aspects of the comparison, as well as some notable discrepancies. For example, the equatorial extension of the northern polar coronal hole (the "elephant's trunk") is well reproduced in the model. Additionally, the complex AR to the East of the tip of the elephant's trunk is also captured, albeit significantly brighter than observations would suggest. Smaller

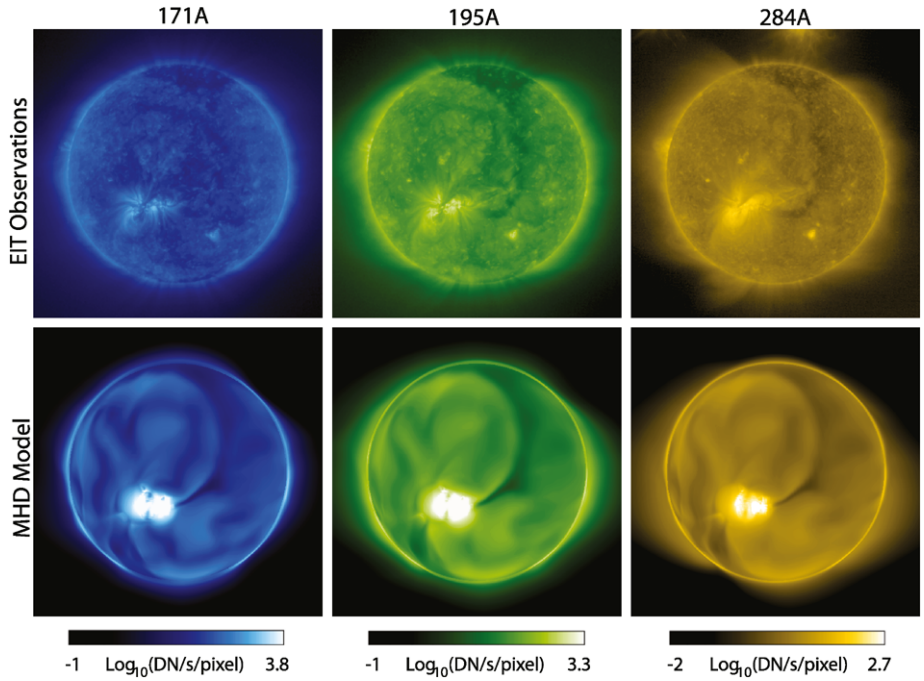

Figure 6 Comparison of SOHO/EIT emission observations at 171 Å, 195 Å, and 284 Å for Carrington rotation 1913 (top) with model results (bottom).

coronal holes, such as the one that arcs North of the AR and over to the East are also reproduced, as is the smaller one that runs away from the AR to the Southwest. Perhaps the most underappreciated match is that the overall brightness of the images, due to emission from the quiet Sun, compares favorably. The model results tend to be slightly brighter than the observations, but, overall, the close match suggests that our parameterization of the quiet-Sun heating is reasonably accurate. In identifying discrepancies, we note that some of the smaller-scale coronal hole structures in the models do not appear to have counterparts in the observations. Additionally, and not surprisingly, the model fails to pick up smaller-scale features such as the small ARs and bright points. It also does not reproduce the ray-like features emanating from the northern and southern polar coronal holes.

A comparison between simulated EIT images and observations for CR2068, using the same heating profile as for CR1913, is shown in Figure 7, and similar remarks can be made about the matches and discrepancies between the two. Unfortunately, no EIT observations at 284 Å were available at this time. One notable mismatch is that the model fails to reproduce the easternmost of the triplet of ARs. The reason may simply be that the modeled field strengths there were too low to be "lit up" by the heating function, but may also imply that our model may not be capturing important structure in the corona, which could, in turn, propagate out into significant errors in the solar wind.

5.2. *In-situ* Comparisons

While the emission image comparisons provide important information about the parameterization of the heating model, direct comparisons of model results with *in-situ* measurements

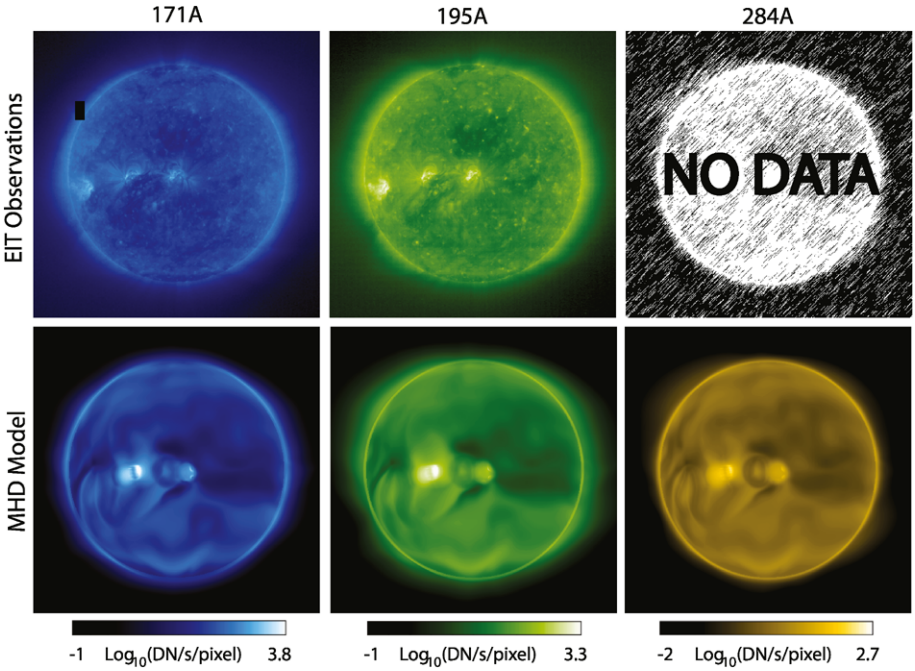

Figure 7 Comparison of SOHO/EIT emission observations at 171 Å, 195 Å, and 284 Å for Carrington rotation 2068 (top) with model results (bottom). Unfortunately, there were no data from EIT at 284 Å at this time.

provide crucial, but more difficult to interpret, feedback on a variety of model assumptions. Principally, we believe the modeled structure is most sensitive to the inner radial boundary condition for the radial component of the magnetic field: Results obtained using magnetograms from different observatories can be substantially different (*e.g.*, Riley, 2007a).

In Figure 8 we compare model results (obtained by flying the trajectory of the spacecraft through the modeling region) with observations made by the two *Solar Terrestrial Relations Observatory* (STEREO) spacecraft. We have used our simpler empirically based model (the results of which are available at http://www.predsci.com/stereo/) to illustrate how "typical" model solutions compare. Had we wanted to show the most impressive comparisons, we could have chosen to manually produce the magnetogram, and/or used magnetograms from more than six solar observatories to produce a solution that best approximates the observations. There are also several free parameters in the empirically based model used here, which, if varied, could have improved the comparison. However, our point here is to show that *i*) there is a reasonable agreement between the large-scale features in the model and observations, and *ii*) there are some noteworthy disagreements. Adjusting inputs and free parameters without understanding their role and the systematic effects on the solutions amounts to little more than "tweaking" and serves no scientific purpose, although it may be a valuable exercise in the operational environment. For more examples of comparisons, please see http://www.predsci.com/stereo/. The main points to note from Figure 8 are as follows: *i*) Overall, the model captures the two-stream flow during this time period, matching the minimum and maximum velocities. *ii*) The phasing of the fast streams between the model and observations may be offset by a day or more from one another. *iii*) The model fails to capture the sector structure of the IMF. While the sector boundary on 31 March 2008 matches

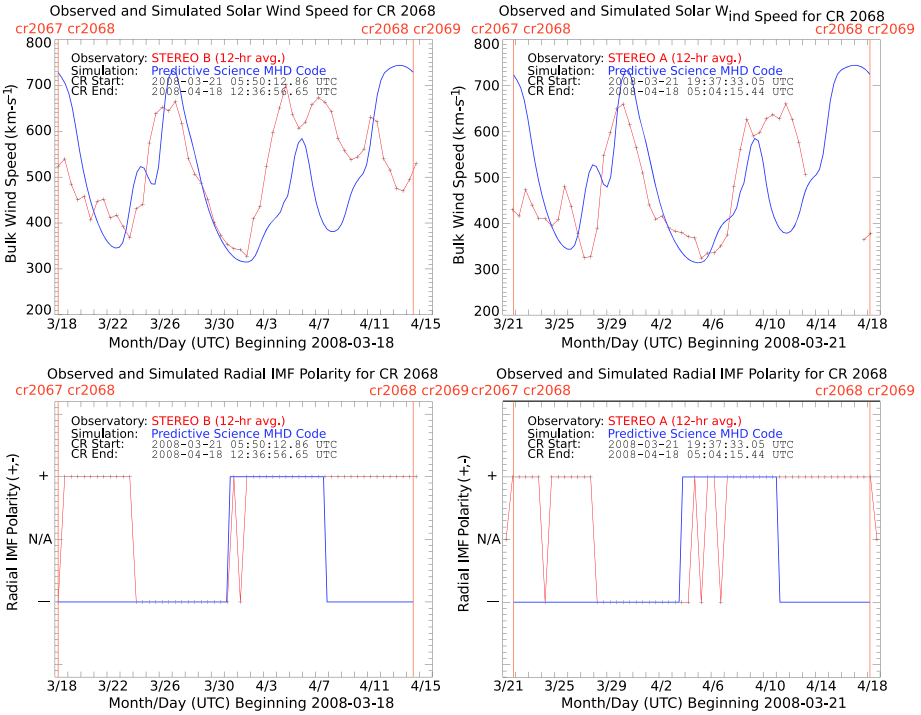

Figure 8 Time series of (top) bulk solar-wind velocity and (bottom) polarity of the radial component of the IMF. Results from STEREO-B (behind) are shown on the left and from STEREO-A (ahead) are shown on the right. Model results are colored blue, while measurements are red. The boundary of the Carrington rotation is marked by the vertical red lines.

well, the model erroneously predicts a return to negative polarity on April 2008, whereas the measurements show that this return does not occur until 24 March 2008 (since we assume that longitude [ϕ] is periodic – the solutions are in steady-state equilibrium – structures are also periodic in time).

6. Discussion and Future Directions

In this article, we have summarized our efforts to model the global structure of the solar corona and inner heliosphere during WHI. In addition to comparing the results with remote-sensing observations and *in-situ* measurements, we have contrasted the structure of the corona and heliosphere during a period approaching the recent minimum (as captured by WHI) and the previous minimum (as captured by WSM).

Overall, our modeling results have reproduced the main features of the observations, and the global picture suggested by the model has been useful in interpreting *in-situ* measurements. However, there are several significant discrepancies.

First, our *in-situ* predictions, while often reasonably accurate, are often likely to perform poorly. We are currently investigating several possible causes for this. It turns out that the model solutions are extremely sensitive to which solar observatory's magnetogram we use to drive the model (Riley *et al.*, 2011). Unfortunately, no single observatory systematically

performs better than another. Our models also contain a number of "free" parameters, the effects of which are (to varying degrees) not well known. Additionally, an intrinsic assumption of the models is that the Sun does not vary in time over the course of a solar rotation. This is clearly not the case, even during solar-minimum conditions. However, the effects of incorporating time-dependent flux evolution into these models are currently unknown.

Second, although our simulated emission images qualitatively match observations reasonably well, there are noteworthy differences. Our heating model contains a number of free (that is, not well-constrained) parameters that markedly affect the solutions. However, constructing a good set is difficult because "tuning" one parameter to affect one region on the Sun may adversely affect other regions. For example, improving emission in ARs may negatively affect the plasma properties of the resulting solar wind and/or emission in quiet-Sun regions.

In spite of these issues, we have seen significant advances in our abilities to model the corona and inner heliosphere during the nearly dozen years between WSM and WHI. Over the next decade, we anticipate commensurate advances. For example, the production of reliable chromospheric magnetograms may replace, or at least complement, the current use of photospheric magnetograms. Additionally, the incorporation of self-consistent treatments for the heating of the corona and acceleration of the solar wind (Cranmer, 2010; Rappazzo *et al.*, 2007; Buchlin and Velli, 2007; Verdini and Velli, 2007) should provide more accurate global solutions, as well as a basic test for the physics underlying these ideas. Finally, from an observational perspective, studies of STEREO remote-sensing observations and *in-situ* measurements are continuing to reveal new insights into the global properties of the inner heliosphere (*e.g.*, Riley *et al.*, 2010a). The recent launch of the *Solar Dynamics Observatory* (SDO) and the high spatial and temporal resolution of the measurements by the *Atmospheric Imaging Assembly* (AIA) and the *Helioseismic and Magnetic Imager* (HMI) will provide further, vital constraints for global models.

Acknowledgements The authors gratefully acknowledge the support of the LWS Strategic Capabilities Program (NASA, NSF, and AFOSR), the NSF Center for Integrated Space Weather Modeling (CISM), NASA's Heliophysics Theory Program (HTP), the Causes and Consequences of the Minimum of Solar Cycle 24 program, and the STEREO (IMPACT and SECCHI) teams. Data at L1 was obtained from NASA's NSSDC OMNIWEB interface. We thank J.T. Hoeksema for providing several of the parameters used to generate Figure 1. Sunspot measurements were obtained from NOAA's Space Weather Prediction Center. Simulated emission images were computed using the CHIANTI database (Dere *et al.*, 1997). Finally, we would like to thank the reviewer for useful suggestions in improving the clarity of the manuscript.

References

Athay, R.G.: 1986, Radiation loss rates in Lyman-alpha for solar conditions. *Astrophys. J.* **308**, 975 – 981. doi:10.1086/164565.

Buchlin, E., Velli, M.: 2007, Shell models of RMHD turbulence and the heating of solar coronal loops. *Astrophys. J.* **662**, 701 – 714. doi:10.1086/512765.

Cranmer, S.R.: 2010, An efficient approximation of the coronal heating rate for use in global Sun-heliosphere simulations. *Astrophys. J. Lett.* **710**, L676 – L688. doi:10.1088/0004-637X/710/1/676.

Cranmer, S.R., van Ballegooijen, A.A., Edgar, R.J.: 2007, Self-consistent coronal heating and solar wind acceleration from anisotropic magnetohydrodynamic turbulence. *Astrophys. J. Suppl. Ser.* **171**, 520 – 551. doi:10.1086/518001.

Cranmer, S.R., Kohl, J.L., Miralles, M.P., van Ballegooijen, A.A.: 2010, Extended coronal heating and solar wind acceleration over the solar cycle. In: Cranmer, S.R., Hoeksema, J.T., Kohl, J.L. (eds.) *SOHO-23: Understanding a Peculiar Solar Minimum* **CS-428**, Astron. Soc. Pacific, San Francisco, 209.

Dere, K.P., Landi, E., Mason, H.E., Monsignori Fossi, B.C., Young, P.R.: 1997, CHIANTI – an atomic database for emission lines. *Astron. Astrophys. Suppl. Ser.* **125**, 149 – 173. doi:10.1051/aas:1997368.

Emery, B.A., Richardson, I.G., Evans, D.S., Rich, F.J., Wilson, G.: 2008, Solar wind and global electron hemispheric power in solar minimum intervals. *AGU Fall Meeting Abstracts*, B1640.

Endler, F.: 1971, Wechselwirkung zwischen Sonnenwind und koronalen Magnetfeldern. *Mitt. Astron. Ges. Hamb.* **30**, 136.

Fisk, L.: 1996, Motion of the footpoints of heliospheric magnetic field lines at the sun: Implications for recurrent energetic particle events at high heliographic latitudes. *J. Geophys. Res.* **101**(A7), 15547.

Fisk, L.A., Schwadron, N.A., Zurbuchen, T.H.: 1998, On the slow solar wind. *Space Sci. Rev.* **86**, 51 – 60.

Gibson, S.E., Fludra, A., Bagenal, F., Biesecker, D., Zanna, G.D., Bromage, B.: 1999, Solar minimum streamer densities and temperatures using Whole Sun Month coordinated data sets. *J. Geophys. Res.* **104**, 9691 – 9700. doi:10.1029/98JA02681.

Gibson, S.E., Kozyra, J.U., de Toma, G., Emery, B.A., Onsager, T., Thompson, B.J.: 2009, If the Sun is so quiet, why is the Earth ringing? A comparison of two solar minimum intervals. *J. Geophys. Res.* **114**, 9105. doi:10.1029/2009JA014342.

Gosling, J.T., Asbridge, J.R., Bame, S.J., Feldman, W.C.: 1978, Solar wind stream interfaces. *J. Geophys. Res.* **83**, 1401 – 1412.

Gosling, J.T., Feldman, W.C., McComas, D.J., Phillips, J.L., Pizzo, V.J., Forsyth, R.J.: 1995, Ulysses observations of opposed tilts of solar wind corotating interaction regions in the northern and southern solar hemispheres. *Geophys. Res. Lett.* **22**(23), 3333.

Hollweg, J.V.: 1978, Some physical processes in the solar wind. *Rev. Geophys. Space Phys.* **16**, 689 – 720.

Issautier, K., Le Chat, G., Meyer-Vernet, N., Moncuquet, M., Hoang, S., MacDowall, R.J., McComas, D.J.: 2008, Electron properties of high-speed solar wind from polar coronal holes obtained by Ulysses thermal noise spectroscopy: Not so dense, not so hot. *Geophys. Res. Lett.* **35**, 19101. doi:10.1029/2008GL034912.

Jacques, S.A.: 1977, Momentum and energy transport by waves in the solar atmosphere and solar wind. *Astrophys. J.* **215**, 942 – 951. doi:10.1086/155430.

Jokipii, J.R., Sonett, C.P., Giampapa, M.S. (eds.): 1997, *Cosmic Winds and the Heliosphere*, University of Arizona, Tucson.

Kirk, M.S., Pesnell, W.D., Young, C.A., Hess Webber, S.A.: 2009, Automated detection of EUV polar coronal holes during solar cycle 23. *Solar Phys.* **257**, 99 – 112. doi:10.1007/s11207-009-9369-y.

Linker, J.A., Mikić, Z., Bisecker, D.A., Forsyth, R.J., Gibson, S.E., Lazarus, A.J., Lecinski, A., Riley, P., Szabo, A., Thompson, B.J.: 1999, Magnetohydrodynamic modeling of the solar corona during whole sun month. *J. Geophys. Res.* **104**(A5), 9809.

Lionello, R., Linker, J.A., Mikić, Z.: 2001, Including the transition region in models of the large-scale solar corona. *Astrophys. J.* **546**, 542.

Lionello, R., Linker, J.A., Mikić, Z.: 2009, Multispectral emission of the Sun during the first whole Sun month: Magnetohydrodynamic simulations. *Astrophys. J.* **690**, 902 – 912. doi:10.1088/0004-637X/690/1/902.

Manchester, W.B., Ridley, A.J., Gombosi, T.I., Dezeeuw, D.L.: 2006, Modeling the Sun-to-Earth propagation of a very fast CME. *Adv. Space Res.* **38**, 253 – 262. doi:10.1016/j.asr.2005.09.044.

McComas, D.J., Ebert, R.W., Elliott, H.A., Goldstein, B.E., Gosling, J.T., Schwadron, N.A., Skoug, R.M.: 2008, Weaker solar wind from the polar coronal holes and the whole Sun. *Geophys. Res. Lett.* **35**, 18103. doi:10.1029/2008GL034896.

Mikić, Z., Linker, J.A.: 1994, Disruption of coronal magnetic field arcades. *Astrophys. J.* **430**, 898.

Mikić, Z., Linker, J.A., Schnack, D.D., Lionello, R., Tarditi, A.: 1999, Magnetohydrodynamic modeling of the global solar corona. *Phys. Plasmas* **6**(5), 2217.

Odstrcil, D.: 1994, Interactions of solar wind streams and related small structures. *J. Geophys. Res.* **99**(A9), 17653.

Odstrcil, D., Pizzo, V.J., Linker, J.A., Riley, P., Lionello, R., Mikic, Z.: 2004, Initial coupling of coronal and heliospheric numerical magnetohydrodynamic codes. *J. Atmos. Solar-Terr. Phys.* **66**, 1311 – 1320.

Phillips, T.: 2009, Science at NASA: Deep solar minimum. http://science.nasa.gov/science-news/science-at-nasa/2009/01apr_deepsolarminimum/.

Pizzo, V.: 1978, A three-dimensional model of corotating streams in the solar wind. I – Theoretical foundations. *J. Geophys. Res.* **83**, 5563 – 5572.

Pizzo, V.J.: 1985, Interplanetary shocks on the large scale: A retrospective on the last decade's theoretical efforts. *Collisionless Shocks in the Heliosphere: Rev. Curr. Res.* **35**(A87-25331 09-92), 51.

Pizzo, V.J.: 1991, The evolution of corotating stream fronts near the ecliptic plane in the inner solar system. II – Three-dimensional tilted-dipole fronts. *J. Geophys. Res.* **96**, 5405 – 5420.
Pizzo, V.J., Gosling, J.T.: 1994, 3-D simulation of high-latitude interaction regions: Comparison with Ulysses results. *Geophys. Res. Lett.* **21**(18), 2063.
Pneuman, G.W., Kopp, R.A.: 1971, Gas-magnetic field interactions in the solar corona. *Solar Phys.* **18**, 258.
Rappazzo, A.F., Velli, M., Einaudi, G., Dahlburg, R.B.: 2007, Coronal heating, weak MHD turbulence, and scaling laws. *Astrophys. J. Lett.* **657**, L47 – L51. doi:10.1086/512975.
Riley, P.: 2007a, An alternative interpretation of the relationship between the inferred open solar flux and the interplanetary magnetic field. *Astrophys. J. Lett.* **667**, L97 – L100. doi:10.1086/522001.
Riley, P.: 2007b, Modeling corotating interaction regions: From the Sun to 1 AU. *J. Atmos. Solar-Terr. Phys.* **69**, 32 – 42. doi:10.1016/j.jastp.2006.06.008.
Riley, P.: 2010, The three-dimensional structure of the inner heliosphere. In: Maksimovic, M., Meyer-Vernet, N., Moncuquet, M., Pantellini, F. (eds.) *Twelfth International Solar Wind Conference AIP* **CS-1216**, 323 – 328. doi:10.1063/1.3395865.
Riley, P., McComas, D.J.: 2009, Derivation of fluid conservation relations to infer near-Sun properties of coronal mass ejections from in situ measurements. *J. Geophys. Res.* **114**, 9102. doi:10.1029/2009JA014436.
Riley, P., Linker, J.A., Mikić, Z.: 2001, An empirically-driven global MHD model of the corona and inner heliosphere. *J. Geophys. Res.* **106**(A8), 15889.
Riley, P., Linker, J.A., Mikić, Z.: 2002, Modeling the heliospheric current sheet: Solar cycle variations. *J. Geophys. Res.* **107**(A7). doi:1010292001JA000299.
Riley, P., Mikić, Z., Linker, J.A.: 2003, Dynamical evolution of the inner heliosphere approaching solar activity maximum: Interpreting Ulysses observations using a global MHD model. *Ann. Geophys.* **21**, 1347.
Riley, P., Gosling, J.T., Weiss, L.A., Pizzo, V.J.: 1996, The tilts of corotating interaction regions at midheliographic latitudes. *J. Geophys. Res.* **101**(A11), 24349.
Riley, P., Gosling, J.T., McComas, D.J., Pizzo, V.J., Luhmann, J.G., Biesecker, D., Forsyth, R.J., Hoeksema, J.T., Lecinski, A., Thompson, B.J.: 1999, Relationship between Ulysses plasma observations and solar observations during the whole Sun month campaign. *J. Geophys. Res.* **104**(A5), 9871.
Riley, P., Linker, J.A., Mikić, Z., Lionello, R.: 2001, MHD modeling of the solar corona and inner heliosphere: Comparison with observations. In: Song, P., Singer, H.J., Siscoe, G.L. (eds.) *Space Weather, Geophysical Monograph Series* **125**, AGU, Washington, 159.
Riley, P., Lionello, R., Mikić, Z., Linker, J., Clark, E., Lin, J., Ko, Y.K.: 2007, "Bursty" reconnection following solar eruptions: MHD simulations and comparison with observations. *Astrophys. J.* **655**, 591 – 597. doi:10.1086/509913.
Riley, P., Luhmann, J., Opitz, A., Linker, J.A., Mikic, Z.: 2010a, Interpretation of the cross-correlation function of ACE and STEREO solar wind velocities using a global MHD model. *J. Geophys. Res. (Space Phys.)* **115**, 11104. doi:10.1029/2010JA015717.
Riley, P., Mikic, Z., Lionello, R., Linker, J.A., Schwadron, N.A., McComas, D.J.: 2010b, On the relationship between coronal heating, magnetic flux, and the density of the solar wind. *J. Geophys. Res.* **115**, 6104. doi:10.1029/2009JA015131.
Riley, P., Mikic, Z., Linker, J.A., Harvey, J., Hoeksema, T., Liu, Y., Ulrich, R., Bertello, L.: 2011, A multi-observatory inter-calibration of line-of-sight diachronic solar magnetograms and implications for the open flux of the heliosphere. *Astrophys. J.*, submitted.
Roussev, I.I., Gombosi, T.I., Sokolov, I.V., Velli, M., Manchester, W., DeZeeuw, D.L., Liewer, P., Tóth, G., Luhmann, J.: 2003, A three-dimensional model of the solar wind incorporating solar magnetogram observations. *Astrophys. J. Lett.* **595**, L57 – L61.
Sarabhai, V.: 1963, Some consequences of nonuniformity of solar wind velocity. *J. Geophys. Res.* **68**, 1555.
Smith, E.J., Balogh, A.: 2008, Decrease in heliospheric magnetic flux in this solar minimum: Recent Ulysses magnetic field observations. *Geophys. Res. Lett.* **35**, 22103. doi:10.1029/2008GL035345.
Smith, E.J., Wolfe, J.H.: 1976, Observations of interaction regions and corotating shocks between one and five AU: Pioneers 10 and 11. *Geophys. Res. Lett.* **3**, 137.
Svalgaard, L., Cliver, E.W.: 2007, A floor in the solar wind magnetic field. *Astrophys. J. Lett.* **661**, L203 – L206. doi:10.1086/518786.
Verdini, A., Velli, M.: 2007, Alfvén waves and turbulence in the solar atmosphere and solar wind. *Astrophys. J.* **662**, 669 – 676. doi:10.1086/510710.
Wang, Y.M., Sheeley, N.R. Jr.: 1990, Solar wind speed and coronal flux-tube expansion. *Astrophys. J.* **355**, 726.
Wang, Y.M., Sheeley, N.R. Jr., Rich, N.B.: 2007, Coronal pseudostreamers. *Astrophys. J.* **658**, 1340 – 1348. doi:10.1086/511416.

Appendix G

Modeling the global structure of the heliosphere during the recent solar minimum: Model improvements and unipolar streamers

Riley, P. and Stevens, M. and Linker, J. A. and Lionello, R. and Mikic, Z. and Luhmann, J. G.

Published in American Institute of Physics Conference Series, 2012.

Modeling the Global Structure of the Heliosphere during the Recent Solar Minimum: Model Improvements and Unipolar Streamers

Pete Riley*, Michael Stevens†, Jon A. Linker*, Roberto Lionello*, Zoran Mikic* and Janet G. Luhmann**

*Predictive Science, San Diego, California.
†Harvard-Smithsonian Center For Astrophysics, Cambridge, Massachusetts.
**Space Science Laboratory, University of California at Berkeley, Berkeley, California.

Abstract. The recent solar minimum, marking the end of solar cycle 23, has been unique in a number of ways. In particular, the polar photospheric flux was substantially weaker, coronal holes were notably smaller, and unipolar streamers were considerably more prevalent than previous minima. To understand the origins of some of these phenomena, we have computed global solutions using a three-dimensional, time-dependent MHD model of the solar corona and heliosphere. In this report, we present a brief overview of a selection of model results, illustrating: (1) how observations are being used to better constrain model properties; and (2) how the model results can be applied to understanding complex coronal and interplanetary phenomena, and, specifically, unipolar streamers.

Keywords: Unipolar streamers, pseudostreamers, coronal holes, MHD modeling, solar cycle
PACS: 96.60.P-, 96.60.pc, 96.60.pf, 96.50.Bh, 96.50.Ci, 96.50.Wx

INTRODUCTION

The recent solar activity minimum, occurring sometime in 2008-2009, depending on its definition, has proved to be unique, at least within the context of solar cycles monitored during the space era, and likely, even on the scale of a century or more [1]. We have studied the interval from the launch of STEREO in October 2006 through the present using a global resistive MHD model of the solar corona and inner heliosphere [2] in an effort to interpret some of the unique features of this interval. In this brief report, we summarize a selection of these investigations that have, thus far, not been reported. Detailed studies are, or will be presented elsewhere (e.g., [3, 4, 5, 6, 7, 8, 9]). Specifically, we present: (1) two examples where comparisons with remote solar and *in-situ* measurements are providing important feedback for improving the quality of the solutions; and (2) an investigation of the interplanetary signatures of unipolar (also known as pseudo) streamers.

MHD MODELING APPROACH

Our numerical model solves the usual set of resistive MHD equations on a non-uniform grid, in spherical coordinates [10]. Energy transport processes are either included explicitly using the so-called thermodynamic model [11], or conveniently neglected by

Physics of the Heliosphere: A 10 Year Retrospective
AIP Conf. Proc. 1436, 337-343 (2012); doi: 10.1063/1.4723628

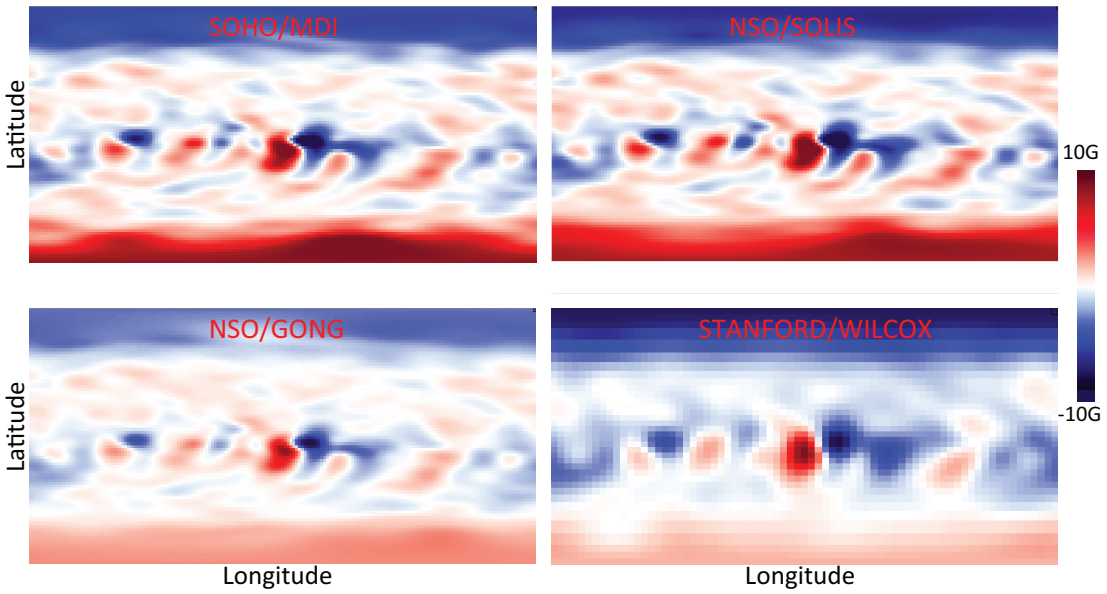

FIGURE 1. Comparison of synoptic magnetograms from four solar observatories for CR 2060. The data have been converted to a radial field, smoothed (by diffusing and filtering the measurements), and, at the highest latitudes, filled, by extrapolating mid-latitude fields poleward.

invoking a polytropic approximation with $\gamma = 1.05$ in the corona and $\gamma = 1.5$ in the solar wind [2]. Here we limit ourselves to the polytropic formalism, which allows us to compute solutions more rapidly and hence perform parametric studies of the model inputs.

For the polytropic model, three inputs variables that can be specified at the lower radial boundary are: (1) the magnetic field vector; (2) the temperature; and (3) the density. Here, we explore the effects of varying the magnetic field and temperature on the resultant solutions. Several processing steps are taken to generate maps that are suitable for the code, which may alter the maps. However, a more fundamental problem exists: We do not have a "ground truth" estimate of the photospheric magnetic field [9]. Figure 1 compares synoptic maps from four solar observatories for Carrington rotation (CR) 2060. While there is a general qualitative agreement, detailed pixel-by-pixel comparisons reveal significant quantitative differences [9]. Additionally, because the Earth's position is limited in heliographic latitude to $\pm 7.25°$, fields beyond $\sim 65 - 70°$ are poorly resolved, if at all. And finally, synoptic maps are constructed from Earth-based observations: We have no direct observations of the far-side of the Sun and must assume that the Sun does not evolve appreciably over 14-21 days, which is clearly not true. As we will show, these errors propagate through the solution: Speed profiles, for example, computed from different maps show substantial differences, and even the computed total open flux in the heliosphere is significantly affected [12].

A second boundary condition that must be specified in the polytropic model is the temperature at the base, T_o. In reality, thermal processes through the photosphere, chromosphere, and corona will likely produce a complex map of temperatures; however, in our idealization, we assume a constant value for all longitudes and latitudes. Moreover,

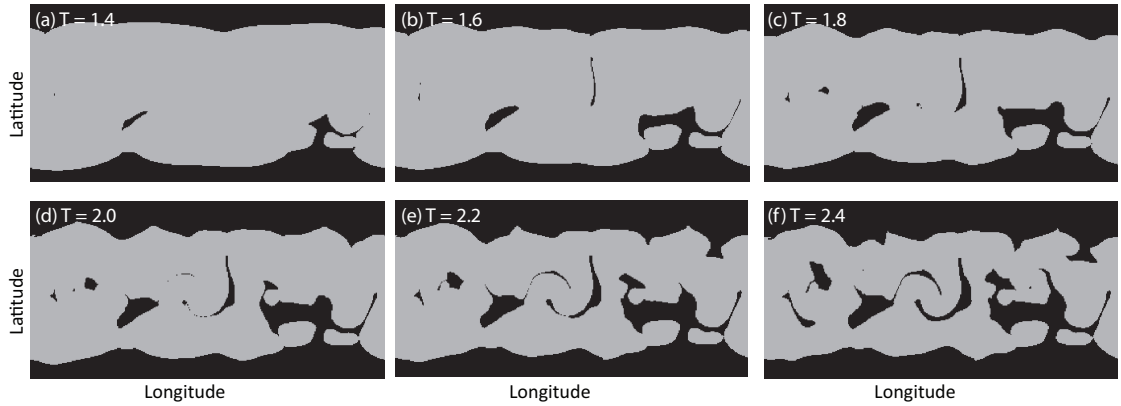

FIGURE 2. Coronal hole boundaries for a sequence of model solutions at different temperatures for CR 2051. The labels give the plasma temperature in units of $\times 10^6$K. Grey regions represent closed field lines while black indicates field lines that open into the heliosphere.

to maintain a near isothermal corona, consistent with observations, we must reduce γ to a value just slightly above one.

Recently, in a sequence of numerical experiments to investigate the impact of T_o (and the density at the base of the calculation, not considered here), we computed coronal hole boundaries for solutions of CR 2051 for model solutions run with T_o ranging from 1.4×10^6K to 2.4×10^6K [3]. These are shown in Figure 2. The trends from one panel to the next make intuitive sense. As the base temperature is increased, the thermal pressure also increases as well as the flow speed. More field lines are opened up and the coronal holes grow larger. But which map is correct? Because we are using a polytropic approximation, we cannot constrain T_o directly by observations; it is essentially a free parameter in the model. Instead, we must look to observations that contain structure, such as the coronal hole boundary.

Figure 3 shows SOHO EIT observations at 195 Å. Coronal holes are readily apparent as dark regions. Superimposed are the computed coronal hole boundaries from four of the model solutions. Based on these comparisons, a temperature, $T_o = 1.8 \times 10^6$K seems to match the observations best. Of course there are caveats: EIT observations are a measure of emission, not field-line connectivity. Overlying bright structure, for example, may tend to occlude otherwise dark regions, and EIT observations themselves may underestimate coronal hole size.

The effects of using input synoptic magnetograms from different observatories is explored in Figure 4. From top to bottom, the panels compare solar wind bulk speed at ACE with model solutions driven by data from SOLIS, MDI, GONG, and WSO solar observatories. The implication is clear: different magnetograms can have a profound effect on the quality of the solution [3, 9]. Therefore, care must be taken in choosing the boundary conditions and interpreting the results.

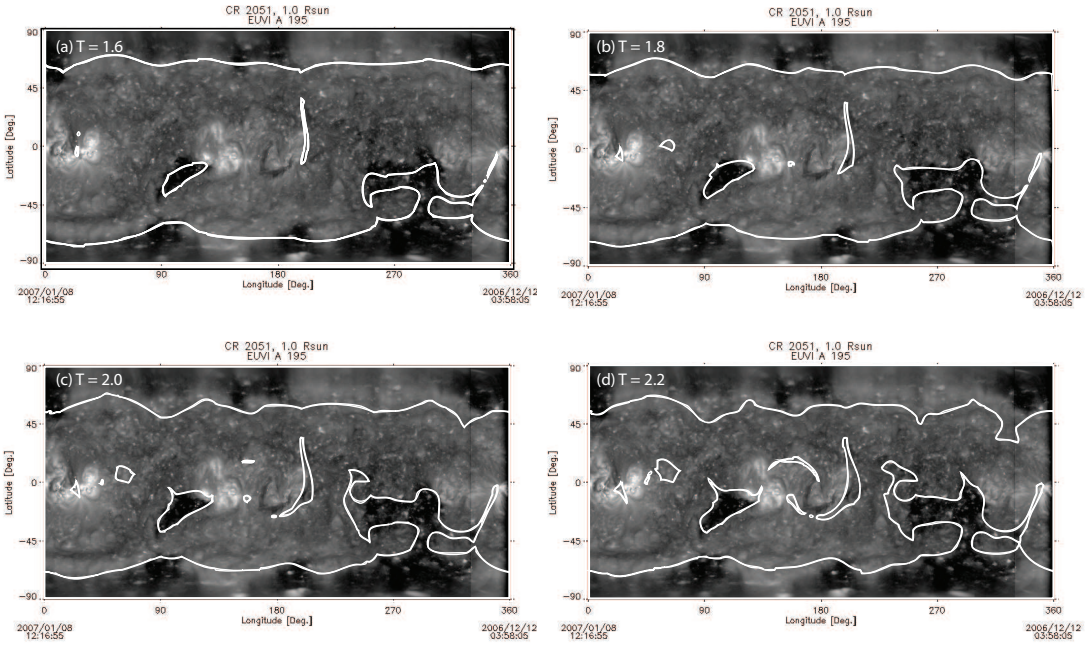

FIGURE 3. SOHO/EIT observations at 195 Å during CR 2051. Panels (a) through (d) differ only in the MHD solution used to produce the computed coronal hole boundaries (red curves).

AN APPLICATION OF THE MODEL: UNIPOLAR STREAMERS

Unipolar streamers are structures in the corona that are often indistinguishable in white light observations from the more typical dipolar streamers. However, MHD and potential field source surface models reveal a distinct loop structure within them. Dipolar streamers separate coronal holes of opposite polarity, and so must be composed of a single (or, in principle, triple) loop structure, while unipolar streamers separate holes of the same polarity, and hence contain a double loop structure. Thus, the interplanetary extension of dipolar streamers contains the heliospheric current sheet (HCS), whereas no HCS is associated with unipolar streamers.

Models of the slow solar wind predict distinct properties for wind emanating from unipolar streamers. The "expansion factor" model (e.g., [13, 14]), which relies on the super-radial expansion of coronal magnetic flux tubes, predicts a source of very fast wind from unipolar streamers, since the expansion factor associated with these field lines is very low, often close to one. In contrast, models based on the concept of a "boundary layer" between open and closed fields (the interchange reconnection idea (e.g., [15, 16]) being one example) predict slow solar wind from both unipolar and dipolar streamers. We have mapped streamer structure out into the solar wind and *in-situ* measurements back to the Sun in an effort to assess both theories. We found that unipolar sources of solar wind are associated with slow wind [17]. Figure 5 illustrates one of these mapping exercises for CR 2060, during which time there was a clear connection between unipolar structure and measurements at 1 AU in the ecliptic plane.

We also studied earlier time periods analyzed by Neugebauer et al. [18], who wanted

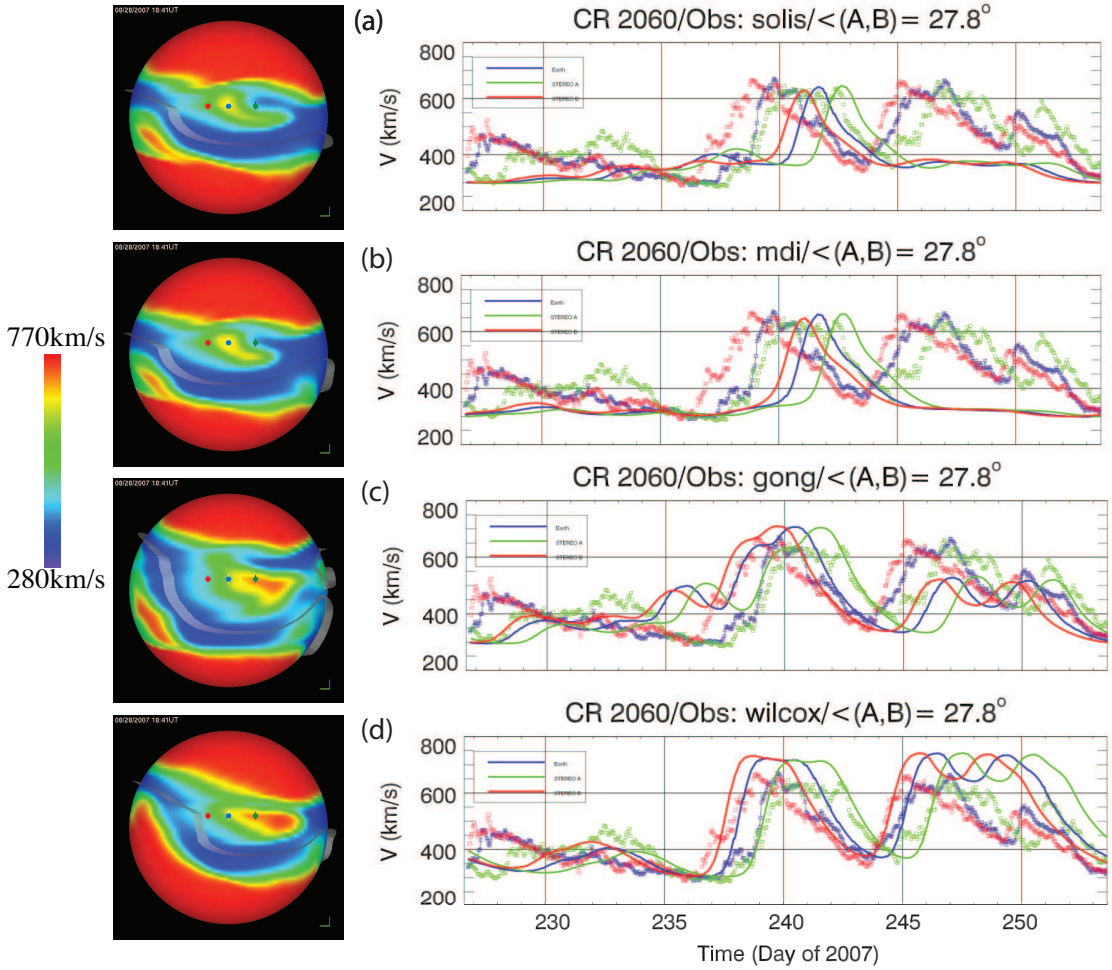

FIGURE 4. (Left) Model solar wind speed at $30R_{\odot}$, together with the location of STEREO A (green), B (red), and ACE (Earth, blue). The HCS is shown by the grey curve. The four panels show results from models driven by data from the following observatories: (a) SOLIS; (b) MDI; (c) GONG; and (d) WSO. (Right) Time series of solar wind speed for the 4 model solutions are compared with data from ACE and STEREO A/B.

to understand the properties and origin of non-HCS interaction regions. Obviously, one might suspect these events to be the interplanetary counterpart of unipolar streamers. They found that non-HCS associated slow solar wind showed properties similar to HCS-associated wind, with the exception that: (1) they were shorter induration; (2) they had a greater minimum speed; and (3) lower peak and average densities. However, no obvious connection with corona streamers was found. Using our MHD results, we were able to show that unipolar streamers did exist during these intervals. Moreover, the model results were broadly consistent with the observed differences between HCS and non-HCS events.

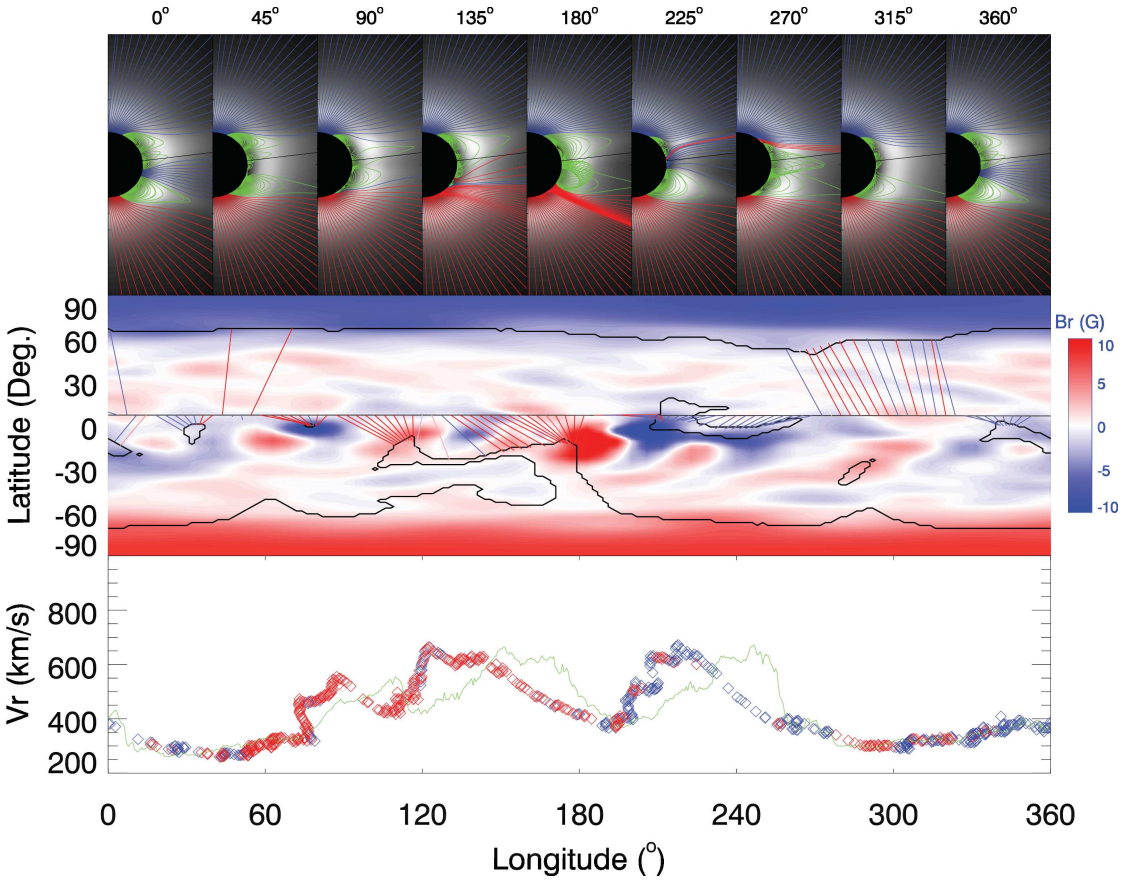

FIGURE 5. (Top) Selection of meridional slices of *pB* with field lines superimposed. Field lines colored blue (red) open into the heliosphere and are inward (outward). Field lines colored green are closed.The heliographic latitude of ACE is indicated by the solid black line. (Middle) The photospheric magnetic field used to compute the MHD solution. The boundaries of coronal holes are indicated by the black curve and the trajectory of the ACE spacecraft (from right to left as time increases) is shown by the straight black line. Measurements by ACE are mapped back to their inferred source location via the lines branching off the trajectory, color-coded according to the measured *in-situ* polarity. (Bottom) Solar wind speed measured by ACE, mapped back to $30R_{\odot}$, and color-coded with the polarity of the field is shown, together with the mapped plasma density as a function of longitude.

SUMMARY AND DISCUSSION

In this report, we have briefly summarized a few studies undertaken to: (1) improve our MHD solutions by comparing with remote solar observations and *in-situ* measurements; and (2) understand some of the unique features of the recent solar minimum. Our analysis has led us to the conclusion that unipolar streamers, when present, can be a significant source of the slow solar wind. Our results also suggest that the "expansion factor" model for the origin of the slow solar wind requires modification to account for slow wind originating from unipolar streamers.

All of the model results presented here are available on the web (www.predsci.com/stereo/). Additionally, NASA's Community Coordinated Modeling Center (ccmc.gsfc.nasa.gov)

provides a web interface for running our model suite (CORHEL) on demand.

ACKNOWLEDGMENTS

We gratefully acknowledge the support of the LWS Strategic Capabilities Program (NASA, NSF, and AFOSR), the NSF Center for Integrated Space Weather Modeling (CISM), NASA's Heliophysics Theory Program (HTP), the Causes and Consequences of the Minimum of Solar Cycle 24 program, and the STEREO (IMPACT and SECCHI) teams.

REFERENCES

1. T. Phillips, *http://science.nasa.gov/http://science.nasa.gov/* (2009).
2. P. Riley, J. A. Linker, and Z. Mikić, *J. Geophys. Res.* **106**, 15889 (2001).
3. M. Stevens, J. A. Linker, and R. P., *Submitted to JASTP* (2011).
4. P. Riley, Z. Mikic, J. A. Linker, J. Harvey, T. Hoeksema, Y. Liu, R. Ulrich, and L. Bertello, *Submitted to Ap. J.* (2010).
5. P. Riley, R. Lionello, J. A. Linker, Z. Mikic, J. Luhmann, and J. Wijaya, *Solar Phys.,* in press (2011).
6. P. Riley, R. Lionello, J. A. Linker, Z. Mikic, J. Luhmann, and J. Wijaya, *Sol. Phys.* pp. 13–+ (2011).
7. P. Riley, and R. Lionello, *Sol. Phys.* pp. 93–+ (2011).
8. P. Riley, J. Luhmann, A. Opitz, J. A. Linker, and Z. Mikic, *J. Geophys. Res. (Space Physics)* **115**, 11104–+ (2010).
9. P. Riley, Z. Mikic, J. A. Linker, J. Harvey, T. Hoeksema, Y. Liu, R. Ulrich, and L. Bertello, *Submitted to Ap. J.* (2011).
10. Z. Mikić, J. A. Linker, D. D. Schnack, R. Lionello, and A. Tarditi, *Phys. Plasmas* **6**, 2217 (1999).
11. R. Lionello, J. A. Linker, and Z. Mikić, *Astrophys. J.* **546**, 542 (2001).
12. P. Riley, *Astrophys. J. Lett.* **667**, L97–L100 (2007).
13. Y. Wang, Y. Ko, and R. Grappin, *Ap. J.* **691**, 760–769 (2009).
14. S. R. Cranmer, *Astrophys. J. Lett.* **710**, 676–688 (2010), `0912.5333`.
15. L. A. Fisk, N. A. Schwadron, and T. H. Zurbuchen, *Space Sci. Rev.* **86**, 51–60 (1998).
16. S. K. Antiochos, Z. Mikić, V. S. Titov, R. Lionello, and J. A. Linker, *The Astrophysical Journal* **731**, 112 (2011), URL `http://stacks.iop.org/0004-637X/731/i=2/a=112`.
17. P. Riley, and J. Luhmann, *Submitted to Sol. Phys.* (2011).
18. M. Neugebauer, P. C. Liewer, B. E. Goldstein, X. Zhou, and J. T. Steinberg, *J. Geophys. Res.* **109**, 10102–+ (2004).

Appendix H

Interpreting some properties of CIRs and their associated shocks during the last two solar minima using global MHD simulations

Riley, P. and Linker, J. A. and Americo Gonzalez Esparza, J. and Jian, L. K. and Russell, C. T. and Luhmann, J. G

Published in Journal of Atmospheric and Solar-Terrestrial Physics, 2012.

Journal of Atmospheric and Solar-Terrestrial Physics 83 (2012) 11–21

Contents lists available at SciVerse ScienceDirect

Journal of Atmospheric and Solar-Terrestrial Physics

journal homepage: www.elsevier.com/locate/jastp

Interpreting some properties of CIRs and their associated shocks during the last two solar minima using global MHD simulations

Pete Riley [a,*], Jon A. Linker [a], J. Americo Gonzalez Esparza [b], L.K. Jian [c], C.T. Russell [c], J.G. Luhmann [d]

[a] Predictive Science, Inc., 9990 Mesa Rim Road, San Diego, California, United States
[b] Unidad Michoacán, Instituto de Geofisica Universidad Nacional Autonoma de Mexico, Mexico
[c] UCLA, Los Angeles, California, United States
[d] UCB, Berkeley, California, United States

ARTICLE INFO

Article history:
Received 1 September 2011
Received in revised form
28 January 2012
Accepted 31 January 2012
Available online 9 February 2012

Keywords:
Corona
Solar wind
Corotating interaction regions
Magnetohydrodynamics
Space weather

ABSTRACT

In this study, we investigate some properties of corotating interaction regions (CIRs) during the recent solar minimum (December 2008), and compare them to CIRs observed during the previous minimum (September 1996). In particular, we focus on the orientation of stream interfaces (SIs), which separate wind that was originally slow and dense from wind that was originally fast and tenuous. We find that while the east–west flow deflections imply a systematic tilt of CIRs such that they are aligned with the nominal Parker spiral direction, the north–south flow deflections are much more irregular and show no discernible patterns. Comparison with global MHD model results suggest that this is a consequence of the spacecraft intercepting the equatorward flanks of the CIRs. We also study the solar-cycle variations of CIR-associated shocks over the last cycle, finding that forward (F) shocks tended to occur approximately three times more frequently than reverse (R) shocks, and, moreover, during the recent minimum, there were approximately 3–4 times more R shocks than during the previous minimum. We show that this too is likely due to the orientation of CIRs and Earth's limited vantage point in the ecliptic plane.

1. Introduction

Corotating interaction regions (CIRs) are large-scale structures in the solar wind produced primarily by the rotation of the Sun. Interaction regions, in general, occur where parcels of plasma traveling radially out from the Sun at different speeds interact (Sarabhai, 1963). Where slower wind is caught by faster wind, a compression region forms, bound by forward (F) and reverse (R) waves. Conversely, where faster wind outruns slower wind, a rarefaction or expansion wave forms. Usually, the term "interaction region" refers to the compression region, although strictly speaking, rarefaction regions are also sites of interaction. The boundary that separates what was originally slow and dense wind from what was originally fast and tenuous within a compression region is referred to as the stream interface (SI) (Burlaga, 1974). SIs also occur within rarefactions/expansion waves, but typically can only be discerned through composition signatures (Wimmer-Schweingruber et al., 1997).

The properties of CIRs have been investigated for more than 45 years, since the bimodal speed structure of the solar wind was first reported (Neugebauer and Snyder, 1966; Belcher and Davis, 1971). In a landmark paper, Gosling et al. (1978) comprehensively described the plasma properties of abrupt SIs using a superposed epoch analysis. Amongst their results, they found: (1) SIs separate wind that was originally dense and slow from wind that was originally fast and tenuous; (2) the SI is a location of shear flow; (3) SI speeds tend to be <450 km s^{-1}; and (4) a discontinuous rise in the α abundance ratio occurs at the interface, suggesting distinct origins for the flows on either side of the SI. Later, Gosling (1995) and Riley et al. (1996) studied the tilts of CIRs at mid heliographic latitudes, during the declining phase of solar cycle 22 using measurements from the Ulysses mission. Riley et al. (1996), in particular, studied the properties of the F and R shocks bounding the CIRs, finding that shock strength appeared to be modulated by the tilt of the solar dipole, peaking at latitudes roughly equivalent to the maximum extent of the heliospheric current sheet (HCS). Additionally, they found that F shocks were oriented such that they propagated equatorward and westward, while R shocks propagated poleward and eastward, suggesting that the CIRs were systematically tilted in the heliosphere. These results were confirmed by looking at the global flow deflections through the CIR.

The F and R shocks associated with CIRs have also been studied for many decades both from analysis of *in situ* measurements

* Corresponding author. Tel.: +1 8582175868; fax: +1 8584501953.
E-mail address: pete@predsci.com (P. Riley).

1364-6826/$ - see front matter © 2012 Elsevier Ltd. All rights reserved.
doi:10.1016/j.jastp.2012.01.019

(Sonett and Colburn, 1965) and inferences from 1-D (Hundhausen, 1973), 2-D (Pizzo, 1981), and 3-D (Pizzo, 1982) numerical models. Early 1-D simulations suggested that F and R shocks formed at approximately the same time, thus implying that, since the F shock was farther away from the Sun than the R shock, that R shocks would be preferentially observed at a given distance from the Sun, at least until a few AU, by which time both would presumably have fully developed.

In this study, we focus on two specific properties of CIRs and their associated shocks. In a previous investigation, Jian et al. (2011) presented a comprehensive analysis of both CIR and CME structures observed at 1 AU in the ecliptic plane over the last solar cycle. In particular, they produced a comprehensive list of SIs and CIR-associated structures, including F and R shocks, which act as the starting point for the present analysis. First, we investigate the flow deflections occurring at SIs both during the recent minimum and the previous one. From these, we compute the orientation of the SIs. Second, we analyze the occurrence rate of both F and R CIR-associated shocks through solar cycle 23. To understand these results, we analyze global MHD solutions for the same time periods, focusing our discussion here on the recent minimum.

This recent solar minimum, "agreed by panel" to have occurred in December 2008 (NOAA/SWPC, 2011) but more generally considered to be defined by an interval rather than a point in time (Gibson et al., 2011), appears to have been unique in a number of ways, at least within the time span of a century (Phillips, 2009). In particular, there were marked differences in the structure of the solar wind during the minimum marking the end of solar cycle 22 (September 1996) and the most recent minimum, marking the end of solar cycle 23 (December 2008) (Emery et al., 2009; Riley et al., 2010, 2011; Gibson et al., 2011). At least in part, these differences were likely driven by a reduced polar photospheric flux, which was lower by $\approx 40\%$ (Svalgaard and Cliver, 2007), producing polar coronal holes that were noticeably smaller (Kirk et al., 2009), and more equatorial coronal holes (Riley et al., 2011). Also related to the unique distribution of magnetic flux in the photosphere was the ubiquitous presence of unipolar (pseudo-) streamer structure during much of the recent minimum interval (Riley and Luhmann, 2011). In previous studies, we investigated the large-scale structure of the inner heliosphere using global MHD models at these two minima (e.g., Riley et al., 2001, 2010), comparing them with *in situ* measurements from ACE and Ulysses.

2. Techniques for estimating the orientation of CIRs/SIs

A number of techniques have been developed for inferring the orientation of SIs, CIRs, and the shocks associated with them. Siscoe (1972) applied a variance analysis to the velocity vectors across five stream interfaces, associating the direction of minimum variance with the normal to the SI. González-Esparza and Smith (1997) extended this technique to account for the fact that while the direction of maximum variance can be unambiguously identified with the plane of the SI, there is ambiguity about the orientations of the intermediate and minimum variance directions, and that the minimum variance direction does not necessarily lie parallel to the SI normal.

Here, we introduce perhaps the simplest method for inferring the orientations of SIs. It has the limitation that meaningful results can only be derived for cases with clear signatures present. More complicated techniques, such as that described by González-Esparza and Smith (1997) can be used to confirm these basic results. However, and as noted by González-Esparza and Smith (1997), while employing the more sophisticated techniques will always yield a result, one must still visually inspect the measurements and compare them with the output from the technique to show that they are robust.

Fig. 1 illustrates how flow is deflected at a SI where fast solar wind is catching up to slower wind ahead. It is important to note that these flows are in the frame of the SI that is moving radially out with the solar wind. In this case, the orientation of the interface is such that fast wind is deflected northward and eastward as it approaches the SI while slower wind flowing back into the SI is deflected westward and southward. The lower panels of Fig. 1 recast these flow deflections in terms of what a spacecraft would measure as the structure passed over it. In this case, the spacecraft is not measuring the lagrangian flow (that is, following a parcel of plasma), but rather the Eulerian flow (at a fixed point). Thus, the instrument first measures essentially radial slow flow ahead of the SI. As the SI approaches, the flow is seen to deflect southward and westward. The spacecraft then intercepts the SI, which it sees as a discontinuous change in flow direction, and becomes immersed in the deflected fast wind, which flows northward and eastward. Far enough from the SI, the flow returns to the radial direction.

In Fig. 2 we have simplified the geometry at the stream interface showing slices in the equatorial and meridional planes. Assuming that the flow into the SI is initially radial, we can use the following relations to compute the azimuthal and meridional tilts of the SI:

$$\tan(\Phi) = \frac{v_t}{v_r} \tag{1}$$

$$\tan(\Theta) = \frac{v_r}{v_n} \tag{2}$$

where (v_r, v_t, v_n) are the velocity components in the RTN coordinate system. In this coordinate system, $\mathbf{e}_r$ points radially away from the Sun, $\mathbf{e}_t$ points in the direction of planetary motion and lies in the equatorial plane, and $\mathbf{e}_n$ completes the system.

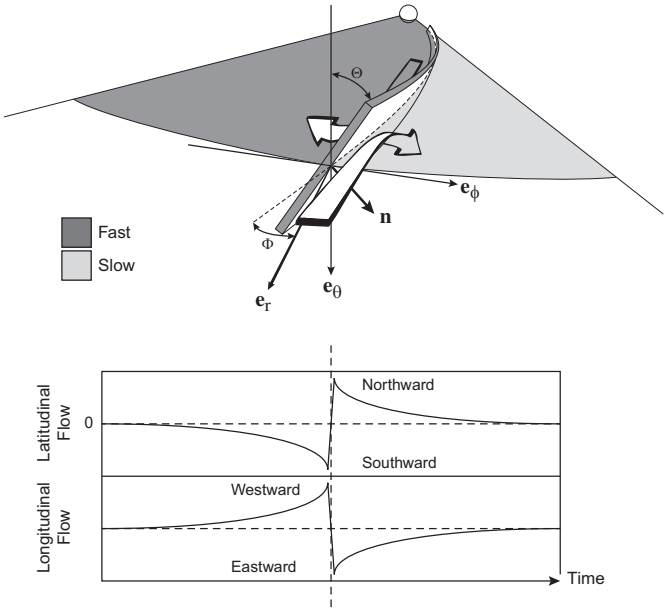

Fig. 1. (Top) An illustration of the flow patterns into and away from a stream interface, in a frame moving with the interface (Adapted from Pizzo, 1991). Fast flow to the east overtakes slower flow to the west and is deflected northward and eastward. Slow wind flows toward the Sun radially and is deflected southward and westward. (Bottom) Schematic flow deflections that would be measured by a spacecraft as the stream interfaced passed over it. Initially slow, radial wind is sampled, which acquires a progressively larger southward and westward component. The spacecraft then passes over the SI (dashed vertical line) and samples the faster wind, which initially contains a large northward and eastward component and progressively diminishes farther away from the interface.

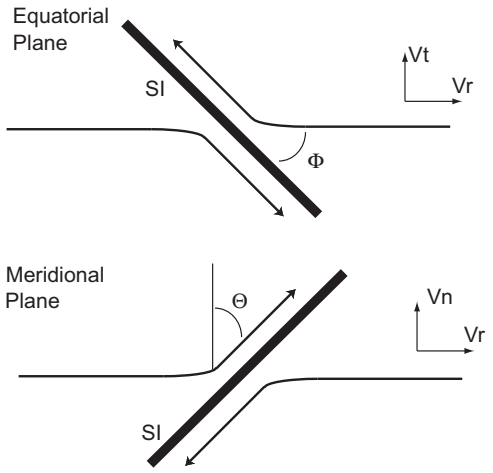

Fig. 2. (Top) A schematic illustrating the flow patterns in the (top) equatorial plane and (bottom) meridional plane. The deflections, Θ and Φ, are also shown, together with the relevant RTN velocity components.

(In effect, $\mathbf{e}_n$ points in the direction of $\mathbf{e}_\theta$ and $\mathbf{e}_t$ points in the direction of $\mathbf{e}_\phi$, where θ and ϕ are the standard angles in the spherical coordinate system.) Using a solar rotation period of $\tau_{rot} = 25.38$ days, we would predict that an interface traveling at 429 km s^{-1} would be tilted in azimuth by 45°. Similarly, speeds of 350 km s^{-1} and 600 km s^{-1} would produce tilts of 55° and 35°, respectively. This makes sense intuitively, since as the speed of the solar wind increases, the Parker spiral angle it makes with the radial should decrease. We also note that from Eq. (2) that, in the limit that $v_n \to 0$ on both sides of the SI, $\Theta \to 90°$, and the SI lies perpendicular to the radial direction, in the meridional plane. To reiterate, the main assumptions of this technique are that: (1) Far from the SI, the flow is radial; and (2) the flow deflections are symmetric in amplitude about the SI.

3. Analysis of the stream interfaces

In a previous study, Jian et al. (2011) identified and catalogued the basic properties of CIRs during solar cycle 23, that is, from 1995 through 2009, which itself was an extension of CIR survey covering 1995–2004 (Jian et al., 2006). They found the CIRs were more prevalent during the recent minimum (occurring at the end of solar cycle 23, December 2008) than during the previous one (September 1996). They also noted the presence of more CIR-associated shocks, which they attributed to different ambient properties of the solar wind during the recent minimum, leading to a lower fast magnetosonic wave speed of the solar wind. Our analysis here builds on these results by investigating the orientation of the SIs observed during solar cycle 23 as well as the occurrence rate of CIR-associated shocks during this same period.

Between 1995 and 2009, Jian et al. (2011) identified 577 CIRs. Since some of them did not recur from one rotation to the next, they were collectively named stream interaction regions, or SIRs, rather than CIRs; however, for simplicity, we will retain the latter term. Jian et al. (2011) used the following criteria to identify CIRs: an overall speed increase; peaks in total pressure (Russell et al., 2005) and proton number density; an increase in temperature; a change in entropy; flow deflections; and field enhancement. The SI itself was chosen to be the point where the total pressure peaked. From the full list, they further identified 36 CIRs with sharp stream boundaries.

In this study, we focus primarily on the orientation of the SIs embedded within these 36 CIRs. We describe two events in detail (one from 1995 (event 'A') and one from 2009 (event 'B')), which capture the general features of most of the SIs studied, and summarize the properties of the remaining ones. In Fig. 3, we show bulk solar wind speed (v), latitudinal and longitudinal flow angles, plasma density (N), and magnetic field strength (B) for the event A. The flow deflections are in the same coordinate system as in Figs. 1 and 2, such that a positive (negative) latitudinal flow is northward (southward) and a positive (negative) longitudinal flow is westward (eastward). The magnetic field strength has been color-coded according to the polarity of the interplanetary magnetic field (IMF). The central dashed line marks the location of the SI as determined by Jian et al. (2011), and the two bounding lines show the intervals used to assess the orientation of the SI. These intervals were chosen subjectively such that they captured the large-scale flow patterns associated with the SI, and in particular, any local maxima, but not so broad that they were contaminated by other dynamical processes. We note several points. First, the SI separates what was originally slow-flowing wind from what was initially fast-flowing wind (Gosling et al., 1978). Before it, slow wind has been accelerated and after it, fast wind has been decelerated. Second, asymmetric peaks in N and B occur at the SI: the bulk of the density enhancement occurring prior to the SI, and the bulk of the field strength enhancement occurring after it. The region of accelerated or decelerated flow stretches from the region of density enhancement before the SI to the region of field strength enhancement after it. Third, the longitudinal (or azimuthal) flow deflections about the SI are consistent with those in Fig. 1: the initially radial flow (0°) is first deflected to the west (positive) then abruptly to the east (negative) as the SI is crossed before returning to radial. Fourth, the latitudinal (meridional) flow deflections are very small and show little change, in particular organized by the SI crossing. Moreover, there is no obvious change at the SI. Fifth, the polarity of the IMF changes 3.75 days before the SI is crossed, marking the traversal of the HCS.

Our second example comes some 14 years later. In Fig. 4 we show the same parameters as in Fig. 3 for an SI observed on day 284, 2009 (event 'B'). With a few differences, the profiles for this event are very similar to event A. The bulk flow profile, longitudinal flow deflections and asymmetric density and field strengths are all remarkably similar. The trailing portion of the field strength enhancement is longer and the latitudinal flow deflection, while also irregular, is suggestive of a small shift from negative (southward) to positive (northward) values across the SI.

Focusing on the longitudinal flow deflections for both events, we can use Eq. (2) to infer the orientation of the SI in the ecliptic plane. Although we could, in principle, pair values equidistant from the SI and compute and ensemble average, a simpler and arguably more robust approach is to estimate the largest flow deflection on either side and use the mean value of this pair to infer the azimuthal orientation of the SI, since our simple cartoon assumes that the deflections are symmetric with respect to the SI. Doing this for event A yielded $\Phi = 29°$ and $\Theta = 9°$. However, given the assumption of symmetric deflections of the opposite sense, we cannot rely on the determination for the orientation in Θ. We also computed the variance matrix eigenvalues and eigenvectors for the interval surrounding the SI, finding that the minimum, intermediate, and maximum eigenvalues were 161, 364, and 17,849. Thus, as reported by González-Esparza and Smith (1997), while the maximum value is well determined, there is degeneracy in the minimum and intermediate values, suggesting the normal to the SI can be only localized to a plane, and not a direction.

Repeating this analysis for event B, we found minimum, intermediate, and maximum eigenvalues of 174, 272, and 1989, again underlining the degeneracy of the minimum and intermediate directions. Using Eqs. (1) and (2), we found $\Phi = 41°$ and $\Theta = 10°$.

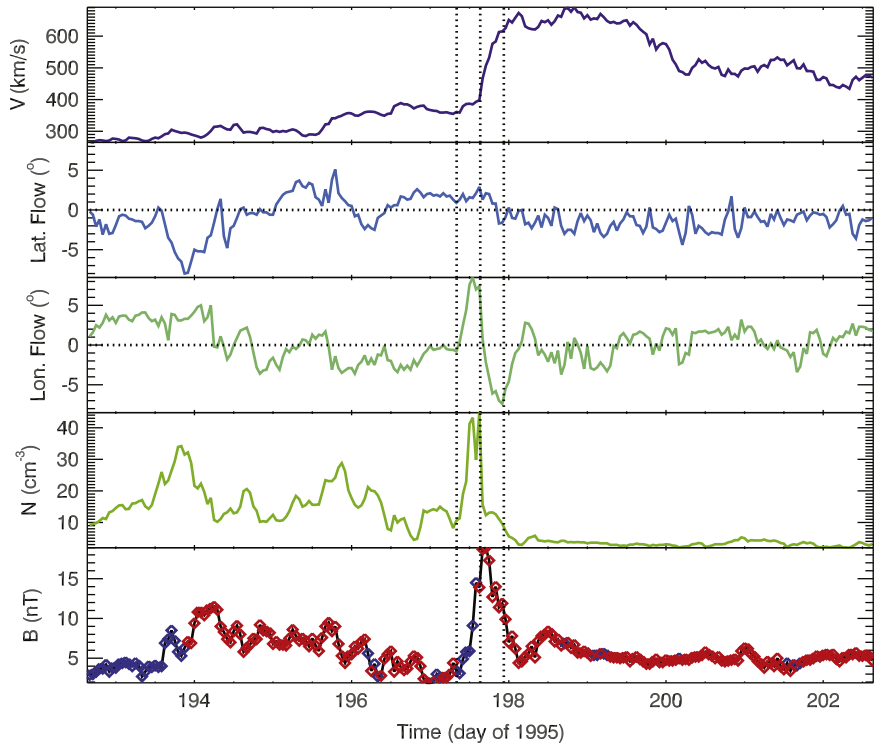

Fig. 3. Time series of bulk solar wind speed (v), latitudinal and longitudinal flow angles, solar wind density (N), and magnetic field strength (B) for an event on day 197 of 1995 (event 'A'). The field strength has been color-coded with the polarity of the interplanetary magnetic field, red indicating outward fields and blue indicating inward fields. The central vertical dashed line marks the location of the SI while the two adjacent vertical dashed indicate the upstream (left) and downstream (right) regions over which the analysis was performed.

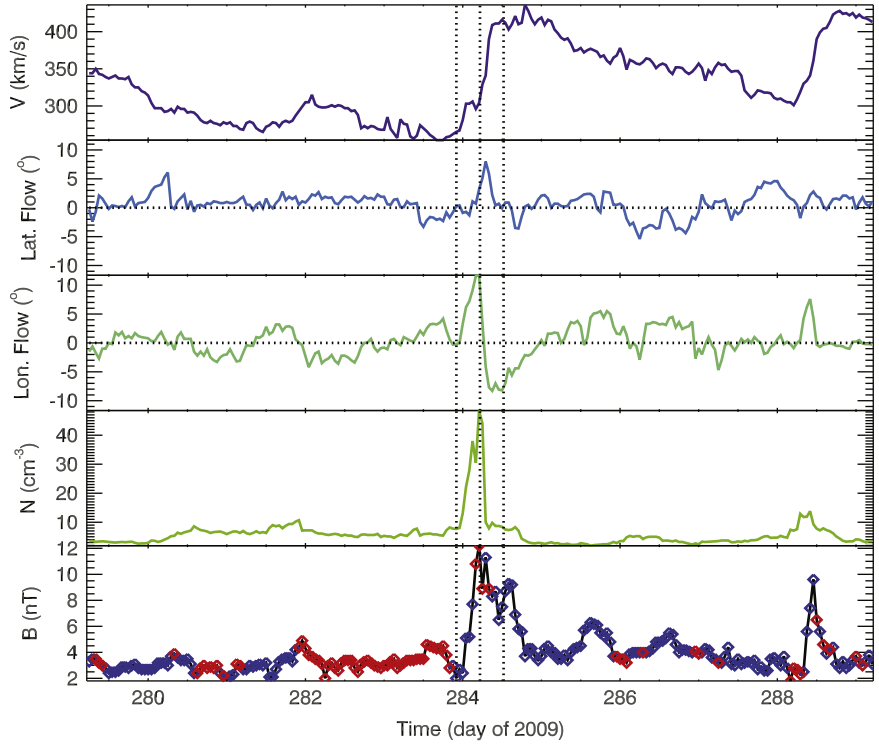

Fig. 4. As Fig. 3 for an SI on day 284 in 2009.

Again, we can only rely on the value determined for Φ, for which the time series meets the basic assumptions of the technique.

It is worth noting that we might anticipate that the azimuthal orientation of the SI would be intermediate between the Parker spiral angles computed for the slow wind ahead of the SI and the fast wind behind it. For event A, for which the speeds of the slow and fast wind ahead of or behind the SI were $\sim 350\ \mathrm{km\ s^{-1}}$ and $\sim 700\ \mathrm{km\ s^{-1}}$, the nominal Parker spiral angles are 51° and 32°,

respectively. Thus, our computed azimuthal orientation of 29° lies at the fast-speed end. For event B, for which the slow and fast wind were $\sim 200\ \mathrm{km\ s^{-1}}$ and $\sim 450\ \mathrm{km\ s^{-1}}$, the Parker spiral angles are 65° and 43°, respectively. Again, our computed angle of 41° lies very near the fast-speed orientation. We are cautious in interpreting these results, however: The orientations determined by Eq. (2) are sensitive to the window chosen. While there are well-determined maxima in the azimuthal flow deflections, and hence azimuthal speeds, the same is not true for the radial speeds, which continue to increase as the window boundaries are moved progressively further from the SI and beyond the peak amplitudes in the azimuthal flow.

Between 1995 and 2009, Jian et al. (2011) identified 36 SIs (or $\approx 20\%$ of the total number) with sharp boundaries where the proton number density and temperature changed rapidly. We analyzed each of these events individually as described above, removing a further six events that did not meet our criterion of sufficiently sharp gradient in speed with either a well-defined density or magnetic field enhancement. Of the remaining 30 events, 27 (90%) showed azimuthal deflections suggesting a shear flow, and discontinuity, in the same sense as in Fig. 1. Only four events (13%) showed a meridional profile as in Fig. 1; two in one sense, a positive deflection followed by a negative deflection, and two in the other sense. However, even for these events, the deflections were not as unambiguous as those for the azimuthal deflections shown in Figs. 3 and 4. In general, the meridional (latitudinal) deflections could be catalogued in the following way: Nine events (30%) displayed flows that drifted continuously through the SI; 10 events (33%) rose to a maximum deflection at the SI (either positive or negative) before returning to near zero; seven events (23%) remained approximately zero throughout the interval surrounding the SI; and three events (10%) were approximately constant, but offset from zero. The fact that the sum of these cases exceeds 30 indicates that there was ambiguity in the classification, and several of the events could be interpreted as being consistent with more than one category, depending on how wide one chose the window for analysis. Finally, no systematic differences were found between the SI properties during the two minima.

4. Analysis of the forward and reverse shocks

We now turn our attention to some properties of the F and R shocks bounding the CIRs observed during solar cycle 23. We note that there is not a one-to-one correspondence between these shocks and the SIs analyzed in the previous section: Some CIRs contain sharp SIs but do not drive shocks, while others drive shocks but do not contain sharp SIs. Again, we start from the study by Jian et al. (2011), who compiled a list of events from Wind and ACE measurements and summarized some of their properties. In particular, they found that, using the total pressure across the shock as a proxy for shock strength, the strength of CIR-associated shocks changed in phase with the solar cycle, being strongest at solar maximum, and weakest at solar minimum. They also concluded that there was no clear dependance on the occurrence rate of CIR-associated shocks with solar cycle, a result we will dispute. Finally, they found that, during the recent minimum, 39% of CIRs had shocks associated with them; more than double the rate for the previous minimum.

Here, we extend the analysis of Jian et al. (2011) to investigate the rate of occurrence of CIR-associated shocks, and the ratio of F to R shocks during the course of the solar cycle, the results of which are both interesting and, perhaps, unexpected. We then interpret the observations with the aid of numerical simulations.

In Fig. 5 we show the variability of F, R, and total CIR-associated shock rates (shocks/year) as a function of year for solar cycle 23. The monthly sunspot number is also shown to give a solar cycle context to the shock variations. Typically, there were $\sim 8-17$ shocks each year around solar minimum, and there was a tendency for the total shock rate to be smaller between 2000 and 2004 than at other times. Perhaps more remarkably, the shock rate was lowest in 2003–2004 during the early declining phase of solar cycle 23, a time typically associated with well-formed CIRs (Riley et al., 2001, 2002, 2003b). Considering the F and R shocks individually, while there was no obvious trend with respect to the F shocks, there was a tendency for more R shocks to be present around the recent minimum (December 2008) than the previous minimum (September 1996).

In Fig. 6, we show the ratio of F to R shocks as a function of solar cycle. In general, from 1998 onward, the ratio of F to R

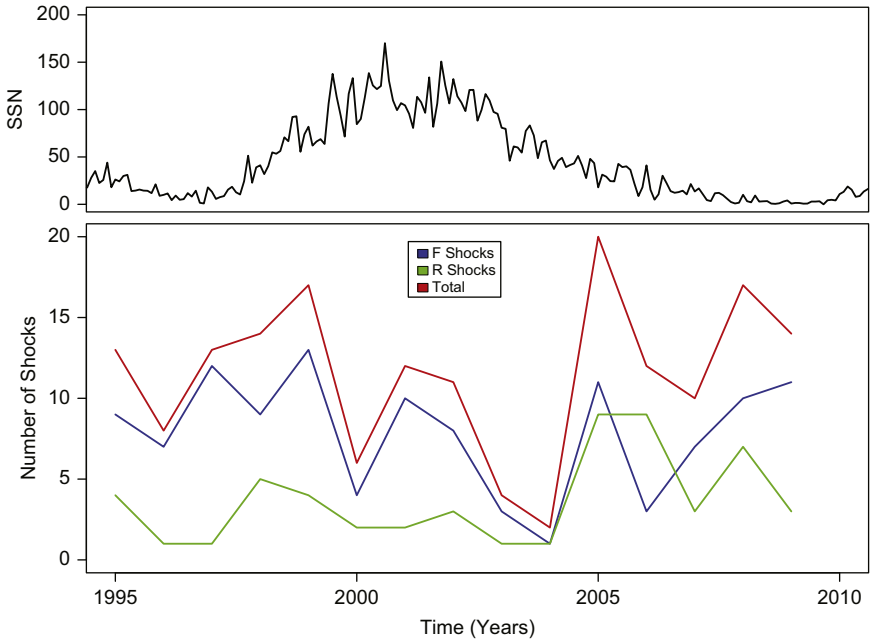

Fig. 5. (Top) The monthly averaged sunspot number as a function of time for the interval 1995–2009 (i.e., solar cycle 23). (Bottom) The annual number of all CIR-associated shocks (red), and forward (blue) and reverse (green) shocks separately. (For interpretation of the references to color in this figure legend, the reader is referred to the web version of this article.)

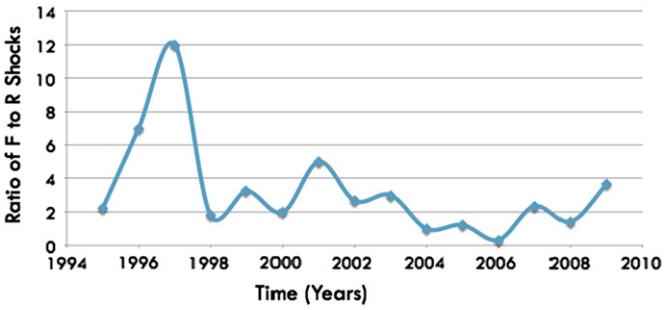

Fig. 6. The ratio of F to R shocks as a function of time for solar cycle 23.

shocks remained relatively stable at $\sim 2-3$, dipping below one only in 2006. However, in 1996 and 1997, the ratio was significantly higher. It is worth emphasizing, however, that in each of these years, only one R shock was observed; thus this peak should be viewed with caution.

5. Interpretation of CIR orientations and shock occurrence rates using global MHD models

Global magnetohydrodynamic (MHD) models of the solar corona and inner heliosphere can be a useful tool for interpreting the global structure associated with *in situ* measurements (e.g., Riley et al., 2001, 2003a). To provide genuine insight, however, the solutions must match the observations we are seeking to interpret. We have found that, in the absence of obvious transient activity, our ambient solar wind solutions do match observations reasonably well (Riley, 2010; Riley et al., 2011), although there remain a number of issues that must be resolved (Riley et al., in press). Here, we restrict our inferences from the model results to a statistical nature. In future studies, we plan to undertake a more detailed event by event comparison.

The modeling technique implemented here is described in more detail by Riley et al. (2001) and references therein. Here we make only a few brief comments. First, we use photospheric synoptic magnetograms to drive the model. This allows us to compute solutions for specific periods of interest, rather than generating idealized or generic solutions. Second, we employ an empirical coupling between the coronal and heliospheric models, which, while from a scientific perspective is not as desirable as a direct coupling, usually produces more accurate heliospheric solutions. Third, unlike other heliospheric models (e.g., Odstrcil et al., 2004) our code is more numerically tolerant approaching the solar poles, allowing us to compare model results directly with Ulysses high-latitude observations (Stevens et al., submitted for publication).

Although we solve the full set of resistive MHD equations, it is worth noting that, to a large extent, the properties of CIRs are controlled by the dynamic pressure of the solar wind. For example, assuming a plasma density of $n \sim 5\ \mathrm{cm}^{-3}$, a bulk speed of $v \sim 500\ \mathrm{km\ s}^{-1}$, a magnetic field strength of $B \sim 5$ nT, and a proton temperature of $T \sim 10^4$ K, we compute a dynamic pressure of 2×10^{-9} Pa, a magnetic pressure of 10^{-11} Pa, and a thermal pressure of 3.5×10^{-12} Pa. Thus, the dynamic pressure exceeds the magnetic pressure by a factor of 100 and exceeds the thermal pressure by a factor of 600. This is not to say that these contributions can always be ignored. We have considered the effects of neglecting the magnetic field and found that while the stream profiles are not significantly effected, there are notable differences in some cases (Riley et al., in press). The generic values we used to derive the pressures at 1 AU may also impact this conclusion. In the slow solar wind, the speed is smaller, and the density and magnetic field strength are greater. However, even in such cases, the dynamic pressure continues to dominate. Finally, it is worth noting that since the dynamic pressure varies as $\sim nv^2$, and both density and speed typically vary by a factor of two between slow and fast wind, it is the velocity variations that have the primary effect in driving CIR structure.

In previous studies (Riley et al., 2010, 2011), we contrasted model solutions for Whole Sun Month (WSM) and Whole Heliosphere Interval (WHI), which occurred between August 8–September 4, 1996 and March 19–April 16, 2008, respectively, and thus illustrated the properties of the heliosphere near each of the last two minima (although the WHI interval might be better described as late-declining phase). We found that, in agreement with *in situ* measurements, the structure of the recent minimum was significantly more complex than during the WSM period, during which time CIRs were systematically tilted due to the simple tilted (or warped) velocity pattern back at the Sun. More recently, Riley et al. (in press) made detailed comparisons between MHD model results and *in situ* measurements for several intervals within the recent solar minimum, both to understand the structure of the large-scale structure of the inner heliosphere and assess the power and limitations of current modeling techniques.

In the present study, we consider the orientation of CIRs during the recent minimum in more detail. CR 2080, which occurred from February 10 through March 9, 2009, serves as a good illustration: It occurred within the broader time period identified as solar minimum (Gibson et al., 2011) and was devoid of any obvious transient activity, such as CMEs. In Fig. 7, we show the global meridional (latitudinal) and azimuthal (longitudinal) speeds, as well as thermal pressure at 1 AU. We note several points: (1) CIR structure is limited to latitudes of $\pm 40^\circ$; (2) two primary features are present – "streaks" that move from low latitudes toward the poles with increasing longitude, and "horseshoe" shaped structures centered about the heliographic equator; (3) azimuthal-speed "streaks" of opposite sign are paired up and located at the same latitudes; (4) similarly, meridional "streaks" are paired up too, however, in this case, the trailing (earlier longitude) lobe is displaced to higher latitudes.

In Fig. 8, we connect the locations of the CIRs with the flow deflections associated with them. The two panels again show meridional and azimuthal speed, however, with an iso-surface of pressure at some arbitrary level overlaid, identifying regions of compression. The locations of the CIRs obviously depends on which iso-surface is plotted. The value chosen here aimed to balance the identification of sufficient structure without complicating the display. From this we see that a spacecraft confined to within $\pm 7.25^\circ$ of the heliographic equator would likely observe systematic azimuthal deflections across a CIR (a spacecraft would appear to propagate from right to left in these plots, moving, at most a few degrees in latitude). On the other hand, while the spacecraft might measure deflections in latitude, these would be at best, of only one sign. Thus, in at least a statistical sense, we expect to see systematic azimuthal flow deflections indicating systematic tilts, but not in latitude. Moreover, it is possible to cut through CIR flanks and produce smooth variations in the latitudinal flow angle as well as asymmetric peaks (that is rising from zero to some maximum and then falling back to zero), or even some constant offset from zero, as observed in some events.

Finally, in Fig. 9, we show a complementary view of these structures in the meridional plane for four equally separated slices in longitude. Panels 1 and 3, in particular, illustrate the "streaks" of Figs. 7 and 8, which appear as compressions (bright regions) moving to higher latitudes with increasing distance from the Sun. At lower latitudes, the "horseshoe" structures appear as blobs in these displays. Based on these results, while we expect

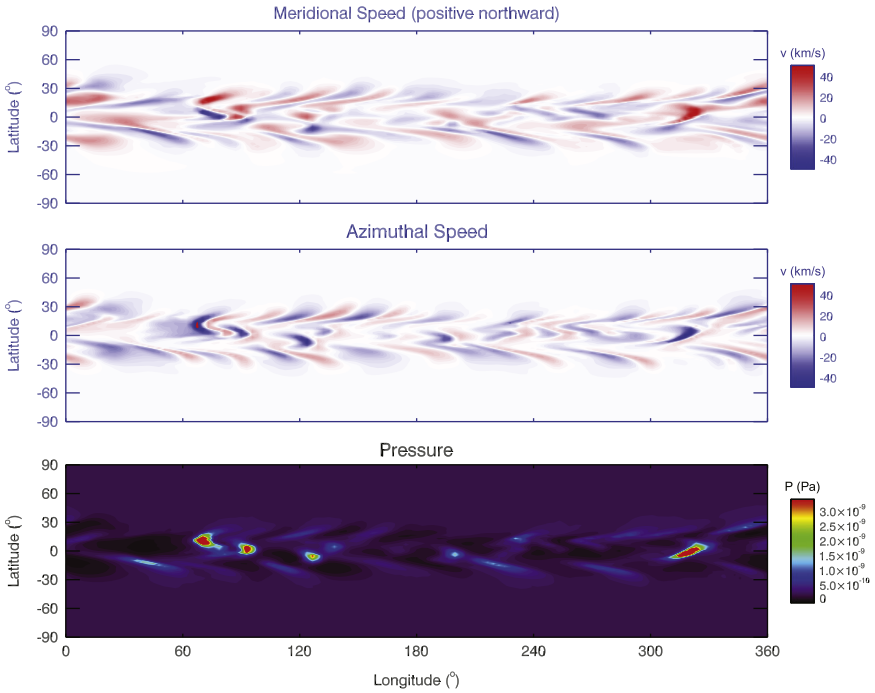

Fig. 7. (Top) Meridional speed, (middle) azimuthal speed, and (bottom) thermal pressure as a function of longitude and latitude at 1 AU for CR 2080.

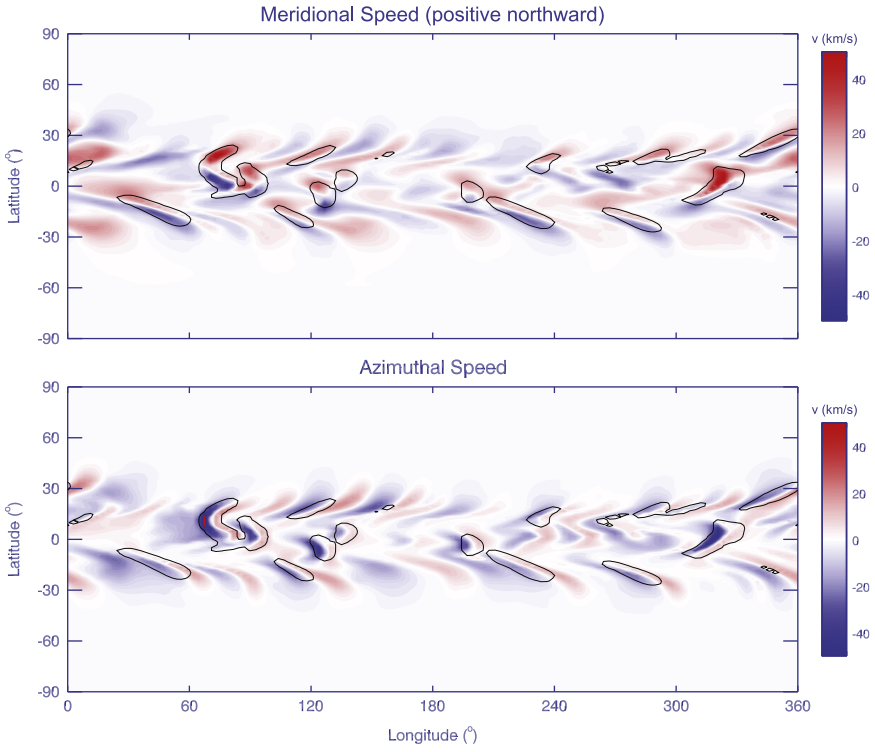

Fig. 8. (Top) Meridional speed (where positive is northward) and (bottom) azimuthal speed as a function of longitude and latitude at 1 AU for CR 2080. Overlaid are contours of thermal pressure at some arbitrary level marking the location of compression regions. These locations coincide with the high pressure regions in Fig. 7.

CIRs and SIs in particular, to be tilted at midlatitudes in the manner illustrated in Fig. 1, in the ecliptic plane, we would not expect to see any systematic tilts. Additionally, we would predict little to no deflections as the interface would lie roughly perpendicular to the radial direction in the meridional plane.

Based on these patterns, we can also suggest why more F than R shocks are observed in the ecliptic plane and why more R shocks were present during the recent minimum than the previous one. In the left panel of Fig. 9, for example, F waves/shocks bound the two most prominent CIRs on the anti-sunward (or leading) side, while R waves/shocks bound the trailing side. As was shown by Gosling et al. (1995) in relation to Ulysses observations, this suggests F shocks are oriented with their outward normals pointing to the equator in both hemispheres, whereas the outward normals for the R shocks point toward the poles (and back to the Sun). The new aspect of this geometry for interpreting

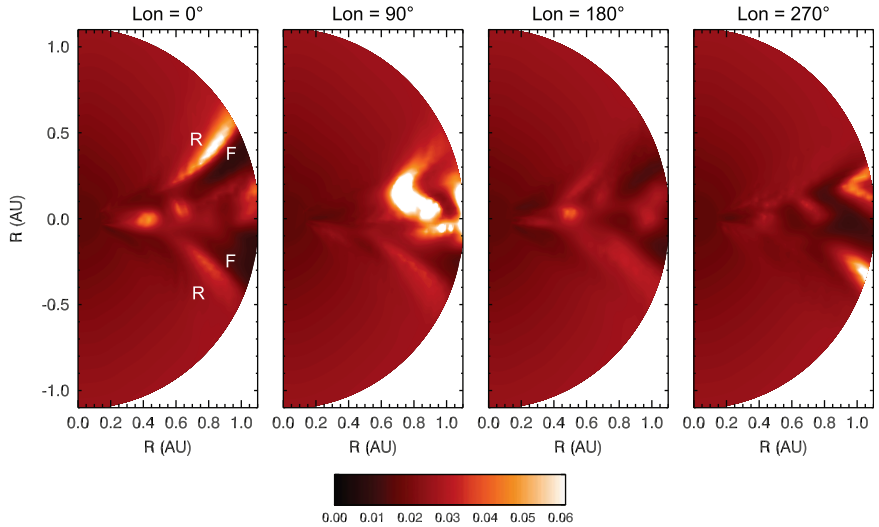

Fig. 9. Meridional cross-sections of scaled pressure at four longitudes for the same interval as Figs. 7 and 8. The pressure has been scaled with heliocentric distance by $r^{10/3}$. In the left-most panel two pairs of F/R waves/shocks have been labeled for illustration.

in-ecliptic measurements is that the flanks of the F shock stretch to lower latitudes than the R shock, because of the tilt of the CIRs. Thus, an in-ecliptic spacecraft sampling this structure (which, ignoring evolutionary effects could be approximated by a radial slice at constant latitude traveling back to the Sun) would be significantly more likely to intercept a F shock than a R shock. Moreover, the main difference between the structure in Figs. 7–9 and that present during the 1996 minimum (Riley et al., 2001) is the presence of the "horseshoe" shaped interaction regions produced by the equatorial coronal holes. These effectively increase the number of R shocks, relative to F shocks, during the recent minimum, and provide an explanation for the peak around 1997 in Fig. 6 (or from a different perspective, the lack of a bump during the most recent minimum).

6. Summary and discussion

In this study, we have analyzed the orientations of SIs during the most recent minimum (December 2008) as well as the previous one (1996), finding that, as previously reported, the east–west flow deflections show a systematic pattern that can be interpreted such that the interfaces are oriented along the nominal Parker spiral direction, with a pitch between that of the slow wind in front of it and the fast wind behind it (Gosling et al., 1978), although based on our analysis, more closely aligned with the fast wind. On the other hand, and as yet unreported, the north–south flow deflections revealed no obvious patterns. In fact, a significant fraction showed relatively little flow deflection near the SI, suggesting that they lay perpendicular to the radial direction in the meridional plane. Global numerical solutions, at least in a statistical sense, are consistent with these results. We suggest that while the Sun's rotation drives the E–W orientations, the latitudinal distribution of solar wind velocity near the Sun drives the N–S orientations. We showed that during these intervals two primary types of interactions were being generated. First, the systematic tilts prevalent in the declining phase of solar cycle 22 (Riley et al., 1996) were occurring well beyond the vicinity of the equatorial (or ecliptic) plane and, thus, the interaction regions measured by Wind/ACE were from the flanks of structures that spanned tens of degrees in latitude. And second, equatorial coronal holes during the recent minimum produced interaction regions with little systematic tilt in the meridional plane, and also increased the relative proportion of R shocks during this time.

The differences observed in the rate of occurrence of R shocks between the recent and previous minima could be explained by the properties of the high-speed streams, which, during the recent minimum were found to be stronger, of longer duration, and more recurrent, at least through the late declining phase (Gibson et al., 2011). On the other hand, as Jian et al. (2011) pointed out, the shock rate could have been modulated by the ambient wind conditions. In particular, the ease at which a shock can form is related to the local magnetosonic speed. Lower this and a pressure wave of some amplitude will be closer to the critical point. Since the magnetosonic speed is constructed from both the sound speed ($\sim T^{1/2}$ and Alfvén speed ($\sim B/n^{1/2}$)), we can use Ulysses measurements made while flying over the poles of the Sun (and hence free from the complication of interaction regions) to estimate whether the magnetosonic speed increased or decreased from one minimum to the next. During the recent minimum, the high-speed solar wind was observed to be cooler ($\sim 14\%$) and less dense ($\sim 17\%$) (McComas et al., 2008). More consequentially, the magnetic field was $\sim 36\%$ lower. Thus, the Alfvén speed was $\sim 9\%$ lower and the sound speed was $\sim 4\%$ lower. Jian et al. (2011) also noted that while the number of shocks increased, they were, generally, weaker. If the increase in the number of R shocks was due to the increased strength of the high-speed streams, we would also expect the R shocks to be generally stronger. On the other hand, if it were to a net decrease in the threshold for the wave to actually steepen into a shock, they would not need to be stronger. Moreover, one, or both of these explanations could account for the dip in shock rate surrounding solar maximum: streams at solar maximum are generally weaker but also, the ambient magnetic field strength is larger than during solar minimum (Riley, 2007).

We offer a third explanation for the increase in the number of R shocks during the recent minimum. During the period approaching, and coincident with the previous minimum, R shocks formed at the trailing edges of CIRs that were tilted and offset from the equatorial plane; their tilt being due to either a tilted dipole geometry, or the equatorward expansion of polar coronal holes. Thus, in-ecliptic spacecraft tended to intercept them, if at all, at their flanks. In contrast, during the recent minimum, and as illustrated by Figs. 7–9 the omnipresence of equatorial coronal holes produced high-speed streams, and hence CIRs whose shocks were more equatorially centered. Thus, all other things being equal, we would expect a larger number of R shocks per Carrington rotation.

This explanation also helps us understand the decrease in the ratio of F to R shocks between the two minima (as shown in Fig. 6): While most, or all F CIR-associated shocks were intercepted in the ecliptic, regardless of their origin from tilted stream profiles, equatorward extensions, or equatorial coronal holes, the R shocks were not. Thus, the decrease in the F/R ratio is an increase in the number of R shocks, not a decrease in the number of F shocks, which is essentially confirmed by Fig. 5.

That the ratio of F to R shocks was greater than one almost every year, and over 10 in 1997, is in apparent contraction to the commonly held view within the scientific community that R shocks associated with CIRs are more likely to form at smaller heliocentric distances than F shocks, and, thus, should be observed more frequently than F shocks. This belief is based on the early 1-D simulations by Hundhausen (1973) (and references therein) who showed that F and R shocks formed at roughly the same time, and therefore, because they bounded a finite-sized interaction region, at different heliocentric distances. Since the R shock is always on the trailing edge of the compression, the implication is that more R shocks would be observed at 1 AU more often than F shocks, in contradiction to the observations.

Our modeling results provide a resolution of this apparent paradox based on the position and orientation of CIRs in the heliosphere. In particular, because CIR dynamics are not centered in the ecliptic, but at latitudes where there are longitudinal gradients in speed back at the Sun, Earth-based spacecraft tend to intercept the CIR structures at their flanks. Thus, except in the case of equatorial coronal holes producing CIRs centered about the equator, we anticipate that F shocks should penetrate to lower latitudes than R shocks. In fact, Ulysses at mid-heliographic latitudes found the opposite (but consistent) result: As it traveled to higher latitudes F shocks disappeared and only R shocks remained (Gosling et al., 1995). In effect, our study has revealed, albeit less clearly, the reverse phenomena in the ecliptic plane.

Our analysis and comparison with model results has been statistical in the sense that we have not attempted to match each observed SI and/or shock with specific model structures. Moreover, we have not attempted to compute the orientation of the shocks bounding the CIRs and compared them either with the observed shocks or the orientations deduced from the flow deflections at the SIs. Although this might be a useful exercise, based on previous studies, we anticipate that the correlation will be relatively low. F and R shocks, for example, often deviate significantly from the larger-scale orientations of the structures they bound, most likely the result of small-scale corrugations in the shock front (Riley and Sonett, 1996). Current global models are capable, at best, of recovering meso- and large-scale structure, in the absence of any wave or turbulence that would also complicate the matter. Instead, we have probed the model results to understand what features in the global modeling would cause such systematic azimuthal flows, but irregular, or non-existent meridional flows, and a stronger prevalence of F to R shocks, as well as a surge in R shocks during the most recent minimum.

Although we have used a fairly sophisticated MHD model to interpret the patterns (and lack thereof, in some cases) we can appeal to simpler illustrations that perhaps explain the measurements more clearly. In Fig. 10 (top), we have drawn four solar velocity profiles. These spherical surfaces are sufficiently close to the Sun that no substantial interaction has yet taken place, but sufficiently far from the Sun that the flow is essentially radial. Cases (a) and (b) are in

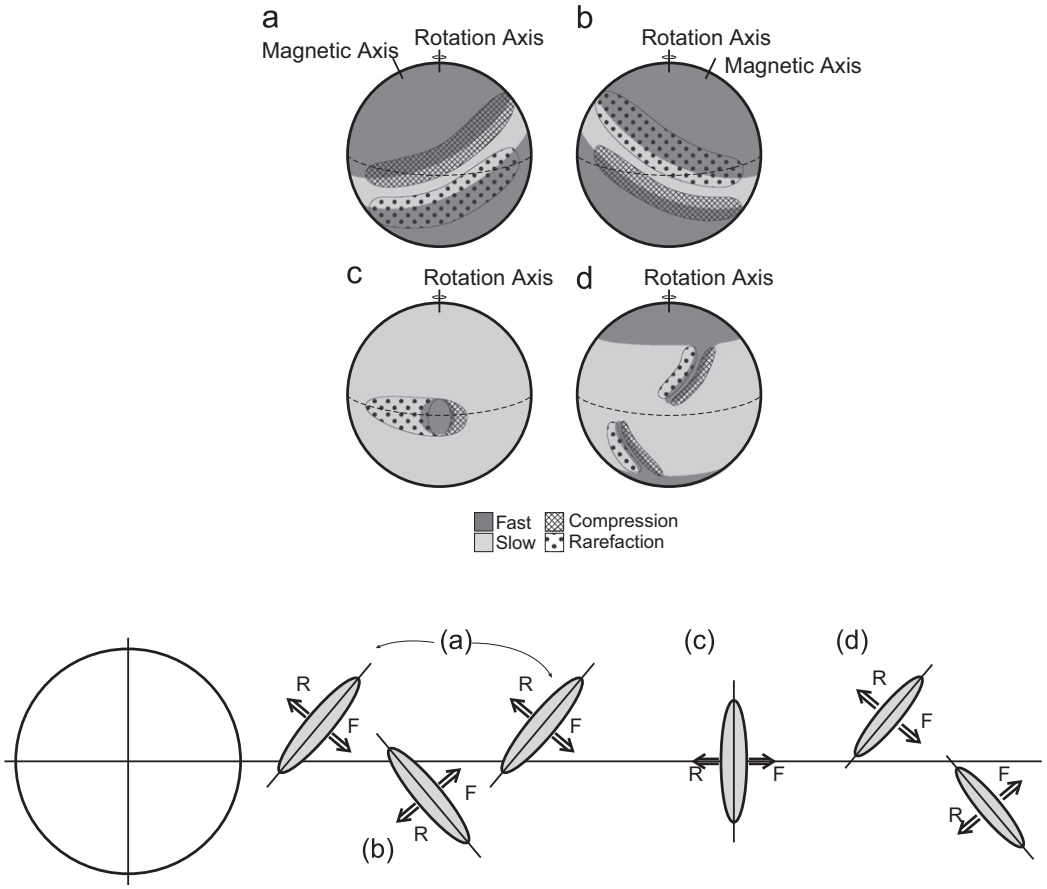

Fig. 10. (Top) An illustration of how different velocity profiles near the Sun (say $30R_{\odot}$) can produce CIRs with particular orientations farther out in the heliosphere (bottom). See text for more details.

fact different views of the same configuration – a tilted dipole, which prevailed during the declining phase of solar cycle 22. Here, a band of slow wind flows out from the magnetic equator, which is tilted with respect to the rotation axis. Focusing on (a) first, slow wind from central meridian is overtaken by faster wind to the east creating a compression region. Similarly, in the southern hemisphere, predominantly fast wind outpaces slower wind to the east creating a rarefaction region. The same processes, but in the opposite hemispheres, occur on the other side of the Sun (b). The bottom part of Fig. 10 shows how these interaction regions (specifically the compression regions) are tilted in the meridional plane, due to the initial gradient of the slow-flow band with respect to heliographic longitude. The F shock bounds the leading edge of the CIR with the R shock trailing it. As drawn, these suggest that, at the least, F shocks intercepted by an in-ecliptic spacecraft will be stronger than the trailing R shock, which will be intercepted further in the flanks of the CIR.

A situation more reminiscent of solar maximum, but also a component of the recent solar minimum is shown in panel (c) of Fig. 10. Here, a fast stream of solar wind emanates from an equatorial coronal hole punching through slower solar wind ahead (originating from the west). A compression region forms on the western edge and a rarefaction trails to the east. Now the orientation of the CIR measured by a spacecraft will depend on its position relative to the center of the coronal hole (or at least the extrapolation of the coronal hole out to our solar wind source radius). However, on average, there will be no systematic tilt, and thus, no meridional deflection of the flow. The F and R shocks will, again on average, be of approximately the same strength. Finally, a third possible configuration is illustrated in panel (d). Typically, such a configuration occurs when well established coronal holes develop an equatorial extension because of a strong but isolated active region at low latitudes, as was the case, for example, at the minimum terminating solar cycle 22 (CR 1913, September 1996). The formation of the compression and rarefaction regions follows a similar explanation as for cases (a)–(c), the main difference here being in how far the CIR penetrates equatorward. Whereas the CIRs in cases (a) and (b) intercepted the equator, in case (d) they would terminate at higher latitudes. Also the tilts of the CIRs and associated shocks would depend on the orientation of the equatorward extension of the hole; in this example producing meridional tilts somewhere between cases (a)/(b) and (c).

In closing, we emphasize that our present study has provided, at best, a statistical interpretation of the Wind/ACE CIR observations. It remains to be seen if the inferences we have drawn hold out on a case by case comparison between measurements and simulation results. These results would, in turn, benefit from a careful analysis of the orientation of the F and R shocks bounding the CIRs.

Acknowledgments

The authors gratefully acknowledge the support of NSF under the Center for Integrated Space Weather Modeling (CISM) program, the LWS Strategic Capabilities Program (NASA, NSF, and AFOSR), NASA's Heliophysics Theory Program (HTP), and the STEREO IMPACT team. Additionally, PR acknowledges support from NASA's Causes and Consequences of the Minimum of Solar Cycle 24 program.

References

Belcher, J.W., Davis Jr., L., 1971. Large-amplitude Alfvén waves in the interplanetary medium, 2. Journal of Geophysical Research 76, 3534–3563.

Burlaga, L.F., 1974. Interplanetary stream interfaces. Journal of Geophysical Research 79, 3717–3725.

Emery, B.A., Richardson, I.G., Evans, D.S., Rich, F.J., 2009. Solar wind structure sources and periodicities of auroral electron power over three solar cycles. Journal of Atmospheric and Solar-Terrestrial Physics 71 (July), 1157–1175.

Gibson, S.E., de Toma, G., Emery, B., Riley, P., Zhao, L., Elsworth, Y., Leamon, R.J., Lei, J., McIntosh, S., Mewaldt, R.A., Thompson, B.J., Webb, D., 2011. The whole heliosphere interval in the context of a long and structured solar minimum: an overview from sun to earth. Solar Physics, doi:10.1007/s11207-011-9921-4, in press.

González-Esparza, J.A., Smith, E.J., 1997. Three-dimensional nature of interaction regions: Pioneer, Voyager, and Ulysses solar cycle variations from 1 to 5 AU. Journal of Geophysical Research 102 (May), 9781–9792.

Gosling, J.T., 1995. Solar wind corotating interaction regions: the third dimension. Reviews of Geophysics 33, 597–602.

Gosling, J.T., Asbridge, J.R., Bame, S.J., Feldman, W.C., 1978. Solar wind stream interfaces. Journal of Geophysical Research 83 (April), 1401.

Gosling, J.T., Bame, S.J., McComas, D.J., Phillips, J.L., Pizzo, V.J., Goldstein, B.E., Neugebauer, M., 1995. Solar wind corotating stream interaction regions out of the ecliptic plane: Ulysses. Space Science Review 72, 99.

Hundhausen, A.J., 1973. Evolution of large-scale solar wind structures beyond 1 AU. Journal of Geophysical Research 78, 2035.

Jian, L., Russell, C.T., Luhmann, J.G., Skoug, R.M., 2006. Properties of stream interactions at one AU during 1995–2004. Solar Physics 239 (December), 337–392.

Jian, L.K., Russell, C.T., Luhmann, J.G., 2011. Comparing solar minimum 23/24 with historical solar wind records at 1 AU. Solar Physics, 155.

Kirk, M.S., Pesnell, W.D., Young, C.A., Hess Webber, S.A., 2009. Automated detection of EUV polar coronal holes during Solar Cycle 23. Solar Physics 257 (June), 99–112.

McComas, D.J., Ebert, R.W., Elliott, H.A., Goldstein, B.E., Gosling, J.T., Schwadron, N.A., Skoug, R.M., 2008. Weaker solar wind from the polar coronal holes and the whole Sun. Geophysical Research Letters 35 (September), 18103.

Neugebauer, M., Snyder, C.W., 1966. Mariner 2 observations of the solar wind, 1, average properties. Journal of Geophysical Research 71 (October), 4469.

NOAA/SWPC, 2011. Solar Cycle Progression 〈http://www.swpc.noaa.gov/Solar Cycle/〉.

Odstrcil, D., Riley, P., Zhao, X.P., 2004. Numerical simulation of the 12 May 1997 interplanetary CME event. Journal of Geophysical Research 109 (February), 2116.

Phillips, T., 2009. Science at NASA: Deep Solar Minimum 〈http://science.nasa.gov/〉.

Pizzo, V.J., 1981. On the application of numerical models to the inverse mapping of solar wind flow structures. Journal of Geophysical Research 86 (August), 6685.

Pizzo, V.J., 1982. A three-dimensional model of corotating streams in the solar wind. III – Magnetohydrodynamic streams. Journal of Geophysical Research 87 (June), 4374.

Pizzo, V.J., 1991. The evolution of corotating stream fronts near the ecliptic plane in the inner solar system. II – Three-dimensional tilted-dipole fronts. Journal of Geophysical Research 96 (April), 5405–5420.

Riley, P., 2007. An alternative interpretation of the relationship between the inferred open solar flux and the interplanetary magnetic field. Astrophysical Journal Letters 667 (September), L97–L100.

Riley, P., 2010. The three-dimensional structure of the inner heliosphere. In: Maksimovic, M., Issautier, K., Meyer-Vernet, N., Moncuquet, M., Pantellini, F. (Eds.), Twelfth International Solar Wind Conference, American Institute Physics Conference Proceedings, vol. 1216; 2010, pp. 323.

Riley, P., Gosling, J.T., Weiss, L.A., Pizzo, V.J., 1996. The tilts of corotating interaction regions at mid heliographic latitudes. Journal of Geophysical Research 101 (A11), 24349.

Riley, P., Linker, J.A., Lionello, R., Mikic, Z. Corotating Interaction Regions during the Recent Solar Minimum: The Power and Limitations of Global MHD Modeling. Journal of Atmospheric and Terrestrial Physics, doi:10.1016/j.jastp.2011.12.013, in press.

Riley, P., Linker, J.A., Mikić, Z., 2001. An empirically driven global MHD model of the corona and inner heliosphere. Journal of Geophysical Research 106, 15889.

Riley, P., Linker, J.A., Mikić, Z., 2002. Modeling the heliospheric current sheet: Solar cycle variations. Journal of Geophysical Research 107 (A7). doi:10.1029/2001JA000299.

Riley, P., Linker, J.A., Mikic, Z., 2010. Global MHD modeling of the solar corona and inner heliosphere for the whole heliosphere interval. Highlights of Astronomy 15, 491–493.

Riley, P., Linker, J.A., Mikić, Z., Odstrcil, D., Zurbuchen, T.H., Lario, D., Lepping, R.P., 2003a. Using an MHD simulation to interpret the global context of a coronal mass ejection observed by two spacecraft. Journal of Geophysical Research 108, 2.

Riley, P., Lionello, R., Linker, J.A., Mikic, Z., Luhmann, J., Wijaya, J., 2011. Global MHD modeling of the solar corona and inner heliosphere for the whole heliosphere interval. Solar Physics, 145.

Riley, P., Luhmann, J.G., 2011. Interplanetary Signatures of Unipolar Streamers and the Origin of the Slow Solar Wind. Solar Physics, doi:10.1007/s11207-011-9909-0, in press.

Riley, P., Mikić, Z., Linker, J.A., 2003b. Dynamical evolution of the inner heliosphere approaching solar activity maximum: interpreting ulysses observations using a global MHD model. Annals of Geophysics 21, 1347.

Riley, P., Sonett, C.P., 1996. Interplanetary observations of solar g-mode oscillations? Geophysical Research Letters 23, 1541–1544.

Russell, C.T., Shinde, A.A., Jian, L., 2005. A new parameter to define interplanetary coronal mass ejections. Advances in Space Research 35, 2178–2184.
Sarabhai, V., 1963. Some consequences of nonuniformity of solar wind velocity. Journal of Geophysical Research 68, 1555.
Siscoe, G.L., 1972. Structure and orientation of solar-wind interaction fronts: Pioneer 6. Journal of Geophysical Research 77, 27–34.
Sonett, C.P., Colburn, D.S., 1965. The SI^{+}–SI^{-} pair and interplanetary forward-reverse shock ensembles. Planetary and Space Science 13 (July), 675.
Stevens, M., Linker, J.A., Riley, P. A study of the sensitivity of global MHD model solutions of the solar corona to boundary conditions. Journal of Atmospheric and Terrestrial Physics, submitted for publication.
Svalgaard, L., Cliver, E.W., 2007. A floor in the solar wind magnetic field. Astrophysical Journal Letters 661 (June), 203.
Wimmer-Schweingruber, R.F., von Steiger, R., Paerli, R., 1997. Solar wind stream interfaces in corotating interaction regions: SWICS/Ulysses results. Journal of Geophysical Research 1021 (August), 17407–17418.

Appendix I

Corotating interaction regions during the recent solar minimum: The power and limitations of global MHD modeling

Riley, P. and Linker, J. A. and Lionello, R. and Mikic, Z.

Published in Journal of Atmospheric and Solar-Terrestrial Physics, 2012.

Journal of Atmospheric and Solar-Terrestrial Physics 83 (2012) 1–10

Contents lists available at SciVerse ScienceDirect

Journal of Atmospheric and Solar-Terrestrial Physics

journal homepage: www.elsevier.com/locate/jastp

Corotating interaction regions during the recent solar minimum: The power and limitations of global MHD modeling

Pete Riley*, Jon A. Linker, R. Lionello, Z. Mikic

Predictive Science, Inc., 9990 Mesa Rim Road, San Diego, CA, United States

ARTICLE INFO

Article history:
Received 4 September 2011
Received in revised form
12 November 2011
Accepted 15 December 2011
Available online 14 January 2012

Keywords:
Corona
Solar wind
Corotating interaction regions
Magnetohydrodynamics
Space weather

ABSTRACT

The declining phase of solar activity cycle 23 has provided an unprecedented opportunity to study the evolution and properties of corotating interaction regions (CIRs) during unique and relatively steady conditions. The absence of significant transient activity has allowed modelers to test ambient solar wind models, but has also challenged them to reproduce structure that was qualitatively different than had been observed previously (at least within the space era). In this study, we present and analyze global magnetohydrodynamic (MHD) solutions of the inner heliosphere (from $1R_S$ to 1 AU) for several intervals defined as part of a Center for Integrated Space weather Modeling (CISM) interdisciplinary campaign study, and, in particular, Carrington rotation 2060. We compare *in situ* measurements from ACE and STEREO A and B with the model results to illustrate both the capabilities and limitations of current numerical techniques. We show that, overall, the models do capture the essential structural features of the solar wind for specific time periods; however, there are times when the models and observations diverge. We describe, and, to some extent assess the sources of error in the modeling chain from the input photospheric magnetograms to the numerical schemes used to propagate structure through the heliosphere, and speculate on how they may be resolved, or at least mitigated in the future.

1. Introduction

Corotating interaction regions (CIRs) and coronal mass ejections (CMEs) are the dominant forces that shape the large-scale structure of the heliosphere. While CMEs are intrinsically transient phenomena, CIRs are assumed to be quasi-stationary. In fact, strictly speaking, CIRs are structures that remain stationary forever in a frame corotating with the Sun. In reality, of course, the processes that produce the slow and fast solar wind are always in flux and the concept of CIRs is an idealization. When dynamically interacting structures appear in the solar wind but do not obviously reappear from one rotation to the next, they may be more strictly labeled stream interaction regions (e.g., Lindsay et al., 1995).

The study of CIRs is important for a number of reasons. First, beyond their intrinsic scientific value, CIRs generate shocks capable of accelerating energetic particles (e.g., Lario and Roelof, 2007). Second, at Earth, they are associated with recurrent geomagnetic activity (e.g. Tsurutani et al., 2006) and may enhance the strength of non-recurrent storms (e.g., Gosling et al., 1990). Third, because, over the last 40 years or so, we have developed a good basic understanding of them, we believe that CIR phenomena may be accessible to physics-based prediction within the foreseeable future (e.g., Riley et al., 2001b).

CIRs form because the plasma expelled from the Sun has a range of speeds. A slow parcel of plasma is compressed by faster plasma behind, creating a region of compression, while faster plasma outrunning slower plasma behind creates an expansion wave, or rarefaction region. Given simple velocity profiles close to the Sun, it is straightforward to infer the basic large-scale properties (at least in a qualitative sense) farther out in the solar wind (Riley et al., this issue). Global heliospheric MHD models can be driven by realistic velocity profiles, computed from coronal MHD solutions, producing a rich and often complex pattern of compression and rarefaction regions (Riley et al., 2011). Often, but not always, the modeled solutions match *in situ* measurements (Riley et al., 2001a).

The declining phase of solar cycle 23, culminating in the prolonged solar minimum that occurred in late 2008, has provided an unprecedented opportunity to study CIR structure in the solar wind in the relative absence of CMEs and other obvious transient phenomena (Riley et al., 2011). As such, it has allowed modelers to test their basic input parameters and model assumptions under pristine conditions (Gibson et al., 2009, 2011). However, this period also produced a number of features that, at least within the span of the space era, were also unique.

* Corresponding author. Tel.: +1 8582175868; fax: +1 8584501953.
E-mail address: pete@predsci.com (P. Riley).

1364-6826/$ - see front matter © 2011 Elsevier Ltd. All rights reserved.
doi:10.1016/j.jastp.2011.12.013

Thus the models have also been challenged to operate in what may be a new environment, raising questions about whether the assumptions made and parameters determined from previous minima hold under these new conditions.

The Center for Integrated Space Weather Modeling (CISM) defined a campaign study to understand the properties of CIRs in the corona and inner heliosphere and their effects throughout the magnetosphere and all the way down to the atmosphere. One of the time periods selected was Carrington rotation (CR) 2060, which occurred between August 14 and September 10, 2007. In this study, we use a global MHD model of the inner heliosphere to define and interpret CIR structure (out to 1 AU) during this interval, as well as other portions of the declining phase of solar cycle 23. In a complementary paper, Wiltberger et al. (this issue) describes a study in which a global magnetospheric model was driven directly with output from the model results that are the subject of the present paper. Stevens et al. (this issue) also provide a complementary analysis of the MHD solutions during the recent solar minimum as well as the previous one, focusing on resolving a long-standing issue with respect to the low interplanetary magnetic field values predicted by global models. In two related studies, we also describe the structure of the heliosphere, including the formation and evolution of CIRs during the "Whole Heliosphere Interval," which occurred between March 19 and April 16, 2007 (Riley et al., 2010a, 2011) as well as more generally during the recent minimum (Riley, 2010). Finally, in this volume, Riley et al. (this issue) use global MHD model results to interpret some properties of stream interfaces (SIs) and CIR-associated shocks observed over solar cycle 23, and particularly during the recent minimum.

In the sections below, we summarize our numerical approach for modeling the large-scale structure of the quasi-stationary inner heliosphere and then present a selection of results to illustrate some of the distinguishing features of the declining phase of solar cycle 23 and the ensuing minimum. We then compare the model results directly with *in situ* measurements by the ACE and STEREO A/B spacecraft and use the model results to provide a global picture of these localized observations. Our comparisons demonstrate that this type of modeling approach can be successful in reproducing the large-scale features suggested by the observations, but also highlights a number of caveats and limitations that must be borne in mind when interpreting the solutions. We discuss each of these in detail and suggest how future developments may address them and lead to better models of the ambient solar wind, ultimately, with predictive capabilities.

2. Modeling approach

Over the last two decades, our group has developed, refined, and applied a number of numerical models for studying the Sun's corona and the heliosphere. As with any model, to make meaningful inferences from the solutions, it is crucial to understand: the assumptions that go into the model; how the boundary conditions are produced; and, in some cases, the numerical schemes that are implemented to solve what are hopefully the relevant equations. To contrast two approaches, we continue to employ both polytropic (Riley et al., 2001a) and thermodynamic (Lionello et al., 2009) coronal models, which treat the energy transport processes in the corona in radically different ways. They trade simplicity and computational requirements for potentially vital physics. However, it is not always the case that the more sophisticated algorithm produces better results. In the case of the polytropic solutions, for example, the fact that they produce remarkably good solutions for the structure of the coronal magnetic field, at the expense of poorer velocity profiles, has led us to develop an *ad hoc* technique for deriving the boundary conditions for the heliospheric model, based on the topology of the magnetic field (Riley et al., 2001a). While we anticipate that a heliospheric model driven directly by output from a thermodynamic solution will ultimately produce more accurate interplanetary solutions, at present, the *ad hoc* prescription typically performs better (of course, the *ad hoc* technique can be used with thermodynamic solutions as well as polytropic solutions; however, this results in a significant computational cost for an arguably marginal gain in the quality of the coronal magnetic field solution).

In this study, we use the CORHEL (CORona-HELiosphere) package; a coupled suite of solar and heliospheric MHD and PFSS models developed by scientists at PSI, Boston University, NOAA, NASA/GFSC, Dartmouth College, and APL. CORHEL aims to supply a simple, coherent interface to these models and includes simple coupling routines so that the output of one model can be used to drive another. Fig. 1 summarizes the main components of CORHEL as well as highlighting areas for potential future development. The chain begins by choosing a photospheric magnetic field map, formatted as a synoptic (or, strictly speaking a diachronic) map of longitude–latitude values covering an entire solar rotation, from one of several solar observatories. In *step*1, the magnetogram is processed in such a way that it can be used to drive the MHD model. This includes: (1) if necessary, converting the measured line-of-sight field to a radial field, assuming that the observed field is everywhere radial; (2) extrapolating the more-resolved

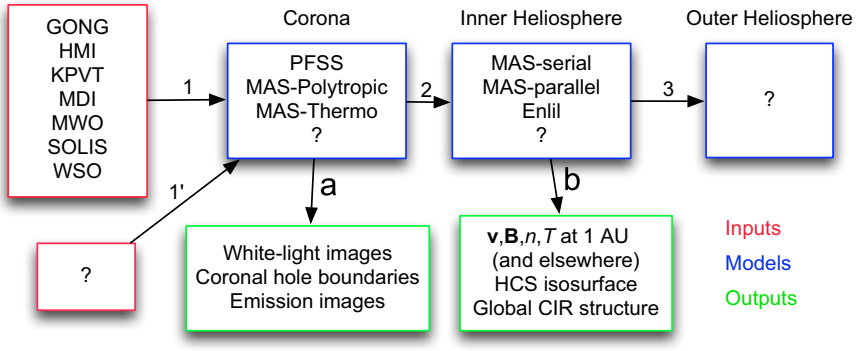

Fig. 1. Flowchart illustrating the inputs, models, and outputs for the CORHEL package. Inputs are shown in red, models in blue, and outputs in green. Potential areas for future development are indicated by the '?' symbols. (For interpretation of the references to color in this figure legend, the reader is referred to the web version of this article.)

mid-latitude fields to the poorly resolved polar regions; and (3) diffusing or filtering the data to a degree that structure relevant to the study is retained but higher frequency features, which might cause numerical issues, are removed. We note that the procedure for processing the magnetograms has undergone significant revision over the last 6 months, and new solutions sometimes depart significantly from previously computed results: typically, but not always, the new results produce a better match with observations. *Step*1 also requires the user to choose appropriate input parameters for the specific coronal model being used. The polytropic version of the coronal model has fewer free parameters than the thermodynamic model, and while this limits the scope of the solutions, we have considerably more experience adjusting them. As noted above, when coupled with the *ad hoc* prescription for deriving the heliospheric model boundary conditions (Riley et al., 2001a), we have found this model usually produces results that are as good as or better than the thermodynamic model, for which much of the underlying physics remains to be explored.

At present, CORHEL supports three coronal models. We have already discussed the MAS polytropic and thermodynamic models. Additionally, we have also implemented a finite-difference potential field source surface (PFSS) model, which includes a current sheet component, and produces speed profiles based on the WSA specification (Arge, personal communication, 2010). Since CORHEL is as much a framework as the models themselves, other coronal models can be easily added provided that they accept (at the least) synoptic maps of the radial component of the photospheric magnetic field, and output (at the least) a global solution for the solar coronal magnetic field.

Step 1′ suggests one of CORHEL's potential opportunities for future growth. Currently, the only observations used to drive the model are line-of-sight measurements of the magnetic field in the photosphere; the rationale being that the magnetic field is the primary driving force for coronal, and hence heliospheric structure, but also that this is one of the most robustly measured parameters. However, as other relevant parameters mature, such as vector measurements of the magnetic field or density and/or temperature low in the corona, it may be possible to incorporate them into boundary conditions for the model. Preliminary steps in this direction have already been made (e.g., Frazin and Kamalabadi, 2005).

Step a highlights that, upon completion, the coronal model produces a set of outputs that can be directly compared with remote solar observations. These include white-light images, coronal hole boundaries (which can be compared with 10830 He, EUV, and/or soft X-ray observations), and emission images (relevant only if the thermodynamic model was run).

In *step* 2, output from the coronal model is used to generate boundary conditions for one of several heliospheric models. For thermodynamic solutions, the output can be used directly to deduce B_r, v_r, n, and T at $20-30R_\odot$, the inner boundary of the heliospheric model. For polytropic solutions, an *ad hoc* scheme, described by Riley et al. (2001a) is used to derive suitable a speed profile map, and pressure balance and momentum flux conservations are used to deduce n and T.

Our recently-developed heliospheric MHD code, MAS in the Heliosphere (MAS-H), has removed some basic limitations in our ability to model structure in the inner heliosphere. Previously, PSI's heliospheric code was both serial and spectral in the azimuthal dimension. As such, runs were limited to grids in ϕ of n^2, and being serial, memory limitations of workstation computers effectively led to runs of 128 azimuthal points, corresponding to a grid spacing of $\phi = 3^\circ$, or 5 h as measured at Earth. MAS-H can be readily run at average resolutions of $< 1^\circ$ in latitude and longitude. CORHEL also supports NOAA's operational inner heliospheric code Enlil, which, in turn, supports cone model CME runs, allowing the user to specify simple configurations for launching ejecta from the inner boundary of the heliospheric code and tracking them as they propagate past 1 AU. Enlil's latitudinal boundaries can be pushed higher, but at increasing computational cost, effectively being limited to $\pm 60^\circ$ in latitude. Thus, for comparisons with Ulysses measurements, for example, (e.g., Riley et al., 2003; Stevens et al., this issue), which require capturing the heliosphere over its entire 4π steradians, it is necessary to use MAS-H.

In *step b* we summarize the main output parameters for the heliospheric model. These include all of the magnetofluid parameters at the location of Earth (or some other location within the heliosphere, nominally out to 5–6 AU) as well as global parameters such as the iso-surface of the heliospheric current sheet (HCS), or large-scale structures such as compression or rarefaction regions.

Physical processes relevant to the outer heliosphere, such as pick-up ions, are not included in our current heliospheric models, rendering them unsuitable beyond perhaps 10 AU. Thus, in an as-yet-to-be-implemented connection, in *step*3 we anticipate how CORHEL could incorporate outer heliospheric models (e.g., Florinski and Pogorelov, 2009), thus being able to compute realistic, event-based solutions all the way from the surface of the Sun out to the edge of the heliosphere.

While it is also possible to envisage CORHEL expanding back through the photosphere and into the convection zone, we believe that, at least currently, photospheric magnetic field measurements are considerably more robust than could be produced from convection/transport models, and, thus, this represents a natural and well-defined boundary. However, that is not to say that the connection could not or should not be made, particularly to study the effects of model-produced photospheric boundary conditions or to study the structure around other magneto-plasma objects, including other stars, for example, where there may be no relevant observations of the surface field.

3. Observations of CIR structure

The several years surrounding CR 2060 (2007–2009) were a period of unusual solar and heliospheric conditions (Riley et al., 2011). The Sun's polar fields were notably weaker than previous near-minima conditions (Svalgaard and Schatten, 2008) and there were significantly more coronal holes producing strong and recurrent high-speed streams.

In Fig. 2 we connect remote solar observations for CR 2060 with *in situ* measurements by the STEREO A and B and ACE spacecraft. Focusing first on the EUV observations, we note several points. First, the northern polar coronal hole is readily visible, while the southern polar coronal hole, if it exists, cannot be seen at all. In fact, during this interval, Earth was situated near its highest point in heliographic latitude [with a B_0 angle (the heliographic latitude of the central point of the solar disk) of 7.1° midway through the rotation]. Thus, the presence of one polar hole and the absence of the other is likely due to an observational selection effect. In fact, analysis of remote solar observations 6 months earlier and later (not shown) reverse the result: the southern polar coronal hole becomes visible at the expense of the northern hole. Second, unlike most previous late declining phases of the solar activity cycle, a number of equatorial and mid-latitude coronal holes were present. Here, we have marked a pair of particularly prominent ones that were relatively persistent from one rotation to the next and generated strong and relatively long high-speed solar wind streams at 1 AU. Third, and related to

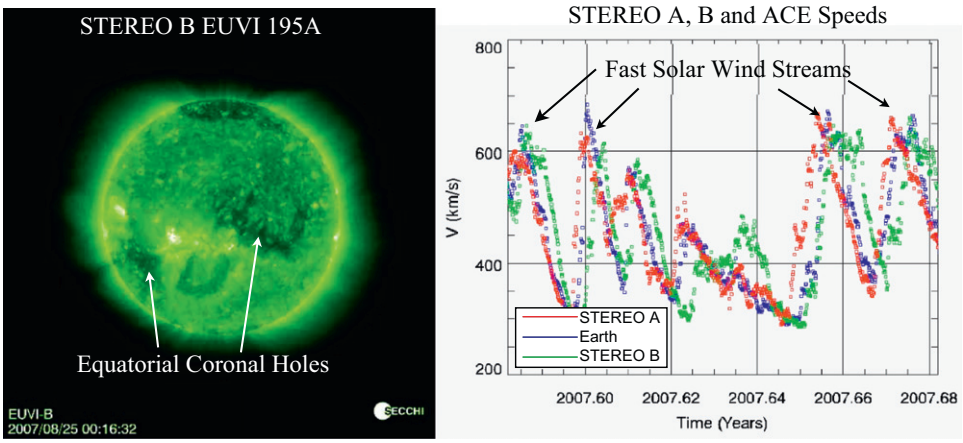

Fig. 2. (Left) EUVI observations from STEREO B at 195 Å on August 25 2007. Two equatorial coronal holes are indicated with the white arrows. (Right) *in situ* measurements of solar wind speed at ~1 AU from the two STEREO spacecraft A and B (red and green) and ACE (blue) for CR 2060. The two fast solar wind streams associated with the coronal holes in the image to the left are indicated by the black arrows. (For interpretation of the references to color in this figure legend, the reader is referred to the web version of this article.)

the previous point, several prominent active regions were present during this interval.

STEREO A/B and ACE bulk solar wind speed measurements over the course of one tenth of a year (~36.5 days) are shown in the right-hand-side of Fig. 2. Since this interval is ~1/3 longer than a solar rotation, the two high-speed streams seen at the beginning of the interval are also seen once more (evolved by one rotation) at the end of the interval. Again, we note several points. First, because STEREO A lies ahead of Earth in its orbit, it becomes immersed in a particular high-speed stream first (red trace). ACE then follows (blue), with STEREO B being last (green). The streams are separated in time by an amount proportional to their angular separation. At ~15° separation (from ACE to STEREO A or ACE to STEREO B), for example, the streams are delayed from one spacecraft to the next by $15^\circ \times 27.27$ days $/360^\circ \approx 1.2$ days. Second, because of their separation, the large-scale stream structure is roughly the same at all spacecraft: All spacecraft observe the same high-speed streams and inter-speed wind. Third, the largest differences in the profiles occurs midway through the rotation during a period of relatively slow wind when both STEREO A and ACE become immersed in a declining speed profile (2007.62) which lasts for ~10 days. While the profiles are virtually identical at STEREO A and ACE, the profile at STEREO B is notably different. In the electronic version of this paper, this figure can also be viewed as a movie highlighting: (1) the evolution of solar wind structure from the launch of the STEREO spacecraft in October 2006 through 2010; and (2) the loss of coherency between the structure measured at the three locations (STEREO A, B, and Earth) as the viewpoints diverge in longitude, and hence time, and, arguably, to a lesser extent, heliographic latitude (Riley et al., 2010b).

4. Model results

In several previous studies, we have described different aspects of the solar corona and heliosphere during this recent declining phase and ensuing minimum (Riley et al., 2010a, 2010b, 2010c, 2011, this issue; Riley, 2010; Riley and Luhmann, 2011). Here, by way of illustration, and to emphasize specific new work, we focus on two aspects: (1) coronal hole boundaries computed from the coronal solution; and (2) the implementation of a new parallel heliospheric code.

One way to assess the quality of the coronal solution is to compare computed coronal hole boundaries with some observed proxy that, in principle, captures the same structure, such as EUV emission images, soft X-ray, or 10,830 He observations.

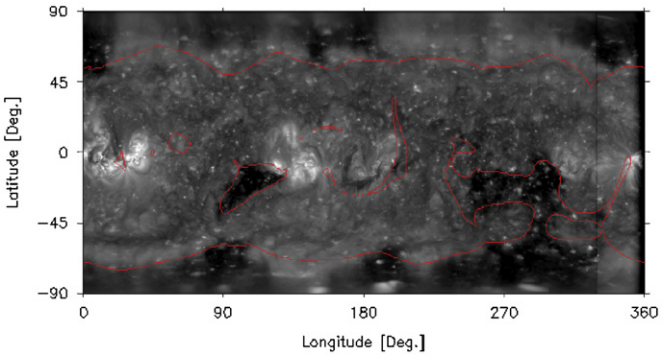

Fig. 3. A comparison of EUVI observations from STEREO A at 195 Å for CR 2051 with the boundaries between open and closed field lines as determined from a polytropic MHD solution (red trace). (For interpretation of the references to color in this figure legend, the reader is referred to the web version of this article.)

In Fig. 3 we compare EUV observations at 195 Å from the SOHO spacecraft with the boundaries of coronal holes from the model. The latter were obtained by tracing out from a longitude-latitude grid at the base of the simulation into the corona. Field lines that extended through the upper boundary ($30R_\odot$) were labeled as "open" while those that closed back down to the solar surface were labeled "closed." In a complementary study, Stevens et al. (this issue) assess the impact of different base densities and temperatures on the quality of the coronal solutions. One measure of this is how well the computed coronal hole boundaries match with EUV emission measurements. In this case, a base temperature of $T_0 = 2.0 \times 10^6$ K was used. This is somewhat higher than our standard values derived from studies based on the minimum marking the end of solar cycle 22 (September, 1996), but produces a qualitatively better match with observations. Focusing on the structure at low and mid latitudes, where there is less likelihood of obscuration from overlying structure, the model captures the two main equatorial coronal holes, and, in particular, the "anvil" shaped structure centered at approximately 285° longitude. There is a mismatch in the location of the northern polar coronal hole, which we believe is likely a combination of poor resolution of this area, coupled with "contamination" from overlying emission. It is worth noting that, at full resolution, EUVI images contain 2048 pixels in sine-latitude, of which approximately 35 pixels lie above 75° latitude at each pole

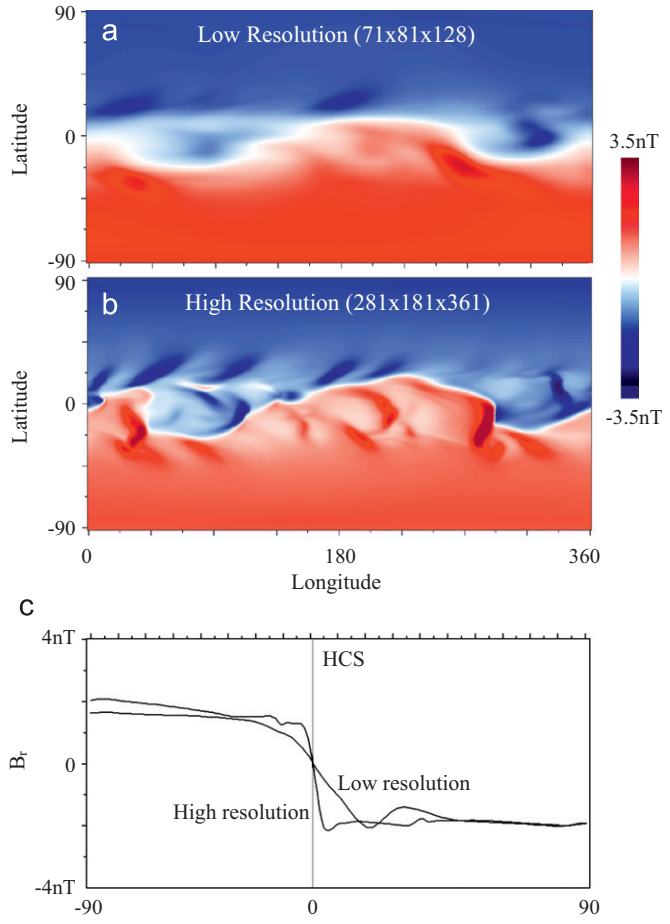

Fig. 4. Comparison of model results at 1 AU using our older serial code (a) and our recently-developed parallel code (b). The serial solution was computed on a grid of $71 \times 81 \times 128$ points whereas the parallel solution was computed with $281 \times 181 \times 361$ points. In (c) Meridional traces from each solution are compared.

when the B_0 angle is zero. When $B_0 \sim 3^\circ$, approximately 22 pixels cover the "obscured" pole and 50 pixels span the "visible" pole. However, the synoptic map shown here retains only 500 pixels in the vertical direction (or 250 from equator to pole), and a mere 5 pixels cover the north pole (above 75°), and 12 pixels cover the south. Thus, we conclude, while the south is poorly resolved, the situation is even worse for the north pole.

A second possibility for the mismatch in the location of the northern polar coronal hole boundary is that the model has overestimated the polar coronal area, presumably because the extrapolated polar fields were too large. As we discuss later, deriving values for the polar fields is a significant challenge for global models, and this explanation for the poor fit cannot be discounted easily, nor can it be readily resolved without direct observations of the Sun's polar regions.

To assess the impact of resolution (as well as some algorithmic changes), in Fig. 4 we compare heliospheric solutions using our older serial code with a recently developed fully parallel code. Although a number of minor improvements were also made between the two codes (such as replacing the spectral solve in azimuth with a finite difference scheme in all three dimensions) the principle improvement has been to allow us to compute solutions at resolutions previously not possible. Here, the numbers of grid points were increased by factors of four, two and a half, and three, in radius, latitude, and azimuth, respectively. Moreover, the lower-resolution solution spanned from $30R_\odot$ to 5 AU, whereas the higher-resolution solution was limited to 1 AU.

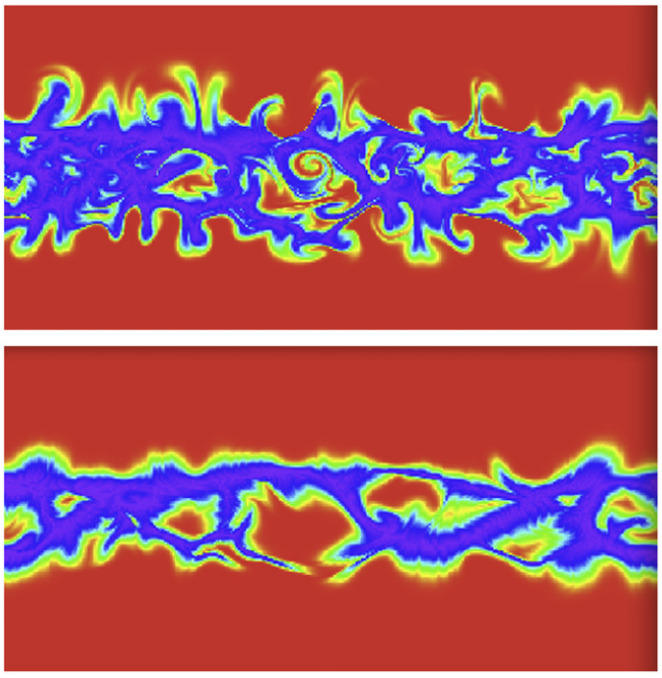

Fig. 5. Comparison of radial speed boundary conditions at $30R_\odot$ for (top) high-resolution simulation and (bottom) low-resolution simulation of CR 2060.

Thus, overall, the number of grid points was effectively increased by a factor of 150. Not surprisingly, the new, more-resolved solutions are producing richer and more complex structure. Although the band of solar wind variability stretches to roughly the same extent in latitude and the grossest features appear in both solutions, beyond that, there are significant differences with obvious impact on the predicted structure of the solar wind at 1 AU in the ecliptic plane.

In Fig. 4(c) we compare traces in latitude at some arbitrary longitude of the radial magnetic field from the two solutions. Although the fields far from the HCS are comparable, nearer to the field reversal, the low-resolution solution spreads out the NS polarity transition, thus leading to smaller predicted field values. Whereas the transition occurs over $\pm 50^\circ$ in the low-resolution solution, it is complete within $\pm 5^\circ$ in the high-resolution. Of course this is still significantly larger than would occur in reality (e.g., Winterhalter et al., 1994), but the change is clearly in the right direction.

The differences between the low- and high-resolution solutions at 1 AU is likely due to two coupled effects. First, higher spatial resolution is maintained in deriving the boundary conditions for the higher-resolution heliospheric solution. And second, the finer-scale structure contained in those boundary conditions is retained as the structure evolves from $30R_\odot$ to 1 AU. In Fig. 5 we compare the main boundary condition driver for the heliospheric solution; the bulk (radial) solar wind flow. Since CIR structure is driven primarily by the velocity profile (Riley, 2010), even a cursory comparison of the two maps suggests that the solutions (at least at low and mid-latitudes) will be different. However, until we compare with actual observations, we cannot be sure whether the added structure adds or subtracts value from the solution.

5. Comparison with observations

We now turn our attention to more direct comparisons of the model results with observations. For the coronal solution, we

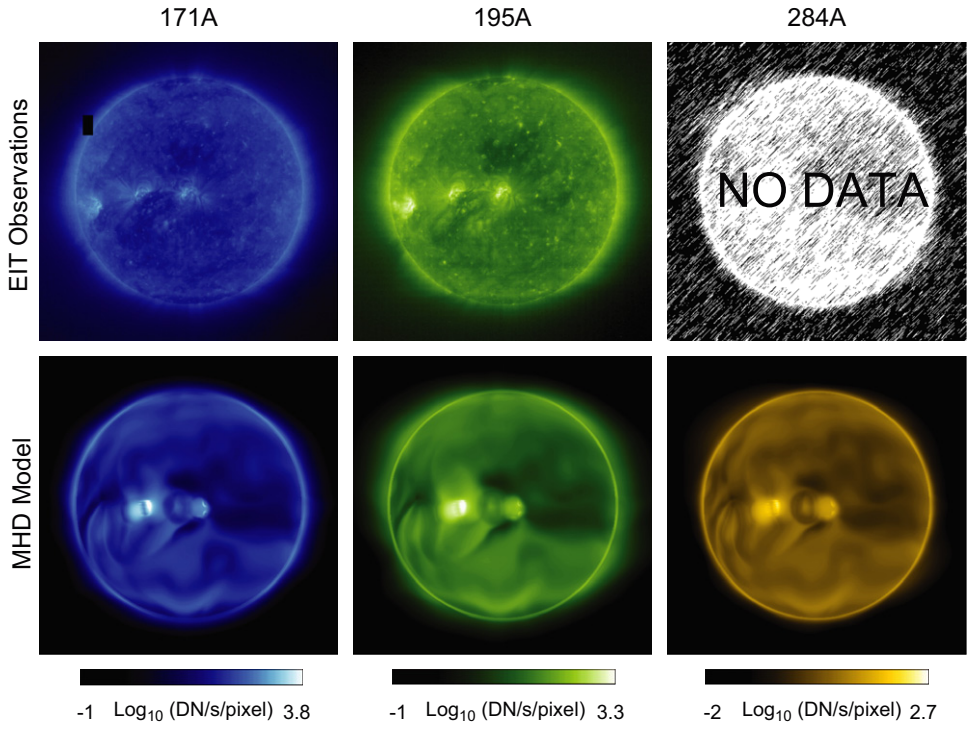

Fig. 6. Comparison of SOHO/EIT observations at 171, 195, and 284 Å with simulated emission images from a global MHD solution (driven by data from MDI) of CR 2068.

compare simulated EUV emission with observations for CR 2068. This requires use of the thermodynamic model since the polytropic solutions cannot reproduce sufficient contrast in density and temperature to yield simulated emission of any value. The quality of the results is also quite sensitive to the thermodynamic parameters chosen (Lionello et al., 2009) and such comparisons are thus a good test of the heating model. For the heliospheric solution, we compare simulated *in situ* measurements of bulk solar wind speed, v, and the magnitude and polarity of the radial component of the interplanetary magnetic field, B_r, both of which have value from a space weather perspective. Ideally, we would also compare B_z, which, together with v_r yields the dawn-dusk electric field imposed across the magnetosphere—the primary driver for geomagnetic activity, and hence the main input parameter for event-based global magnetospheric models (Wiltberger et al., this issue). However, currently, global heliospheric models are not able to generate substantial B_z fields in CIRs, presumably because turbulence and/or wave effects, which provide a seed field that can be enhanced by compression regions and fast CMEs, are not incorporated. Only a modest B_z component is produced from the Russell–McPherron effect (Russell and McPherron, 1973).

Simulated emission images for CR 2068 (i.e., Whole Heliosphere Interval) are compared with SOHO/EIT observations at the same time in Fig. 6. Unfortunately, no data were available from EIT at 284 Å. It is important to note that the comparison is quantitative, and not qualitative, that is, actual counts/second/pixel are compared. Overall, we believe that the model has captured the basic structure of the solar corona as manifested in emission measurements. The general brightness of the disk, limb, and the relative intensity of the active regions compare favorably, as do the basic locations of the coronal holes. One 'glaring' disagreement is the third, east-most active region. While that data clearly show a triplet of active regions, the model has only produced two. Active region heating in the model is sensitive to the local magnetic field strength. Thus, while it is possible that a threshold value was not reached which would have 'lit up' the active region, it is more likely a problem due to the fact that the synoptic map used to generate the solution relied on central meridian data that was more than 21 days old. In reality, the active region seen in the observations probably appeared or evolved while on the far side of the Sun.

Considering next the *in situ* measurements, in Fig. 7 we compare model solutions for CR 2060 using a synoptic photospheric magnetic field map derived from Wilcox Solar Observatory (WSO) measurements. The model matches the stream structure reasonably well. In particular, the initial long-duration of slow wind, followed by a strong and steep high-speed stream on 08/26/2007. The second stream is overestimated by the model, as is the third, to an even greater extent. The polarity of the radial magnetic field measured during this interval consisted of a simple two-sector pattern, initially inward, and switching to outward around 08/30/2007. The smaller-scale reversals not mimicked into model results probably represent waves and/or turbulence, which, as we have noted, are not included in the MHD model. On the left, the global structure of the solar wind velocity from the model is shown at $30R_{\odot}$. This frame corresponds to the blue vertical band in the time series. A movie showing how the global structure of solar wind speed varies as a function of time is included in the electronic version of the paper.

While the previous comparison revealed a few discrepancies between the model results and the observations, as a whole, the match was relatively good, and, particularly in terms of the timing of the fronts of the high-speed streams, which is a feature of significant value from a space weather prediction standpoint. However, the comparison is not always as fair. Even for the same interval, using an input synoptic magnetic field derived from data measured by a different observatory can have a profound effect on the solution. In Fig. 8 we compare the same *in situ* measurements but with model results computed using data from the MDI instrument onboard the SOHO spacecraft. Clearly the model solution fails to reproduce much of the observed stream structure. Although it predicts a stream midway through the rotation, if it is associated with the observed first stream, it lags significantly.

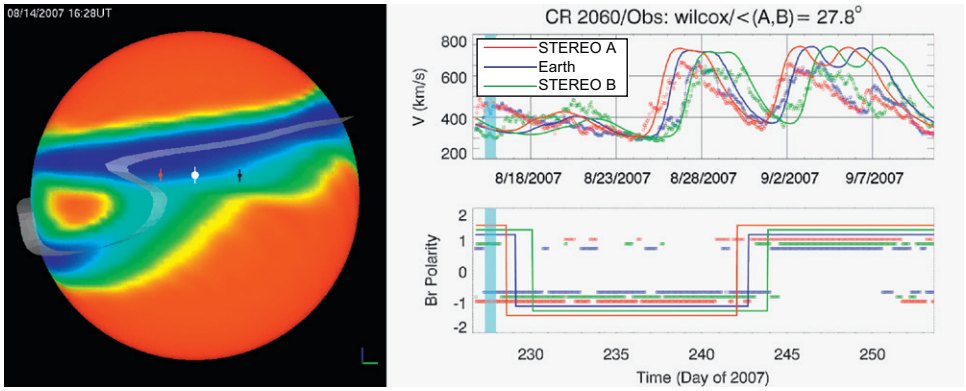

Fig. 7. Times series comparison of solar wind speed and IMF polarity at 1 AU for CR 2060. The model results (solid lines) were obtained by flying the STEREO A, B, and ACE spacecraft through the simulation region. The *in situ* measurements have been smoothed using box-car averages of 12 h. On the left, the global model velocity profile at $30R_{\odot}$ is shown, together with the location of the heliospheric current sheet (grey iso-surface), and the mapped back location of the three spacecraft. In the electronic version of this paper, a movie based on this Figure illustrates how the global solar wind speed pattern changes underneath the spacecraft.

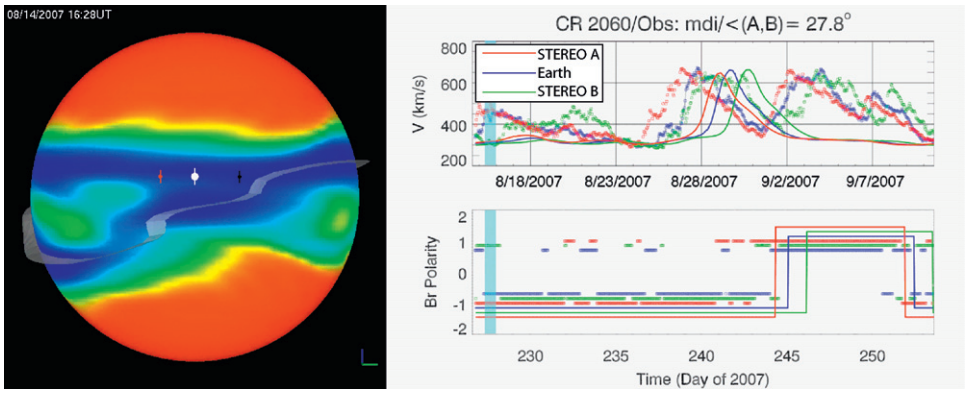

Fig. 8. As Fig. 7 but for a model solution driven by data from SOHO's MDI instrument.

Moreover, none of the subsequent high-speed stream structure appears in the model solution. And, although the model is consistent with a two-sector pattern, the phasing of the sector crossings does not match the observations nearly so well.

We can understand the source of the poor match with the MDI model results from the movie from which Fig. 7 and 8 were extracted. In both solutions, the first stream corresponds to wind from an equatorial coronal hole. However, in the Wilcox solution this stream is faster and broader. The slow-flow band is relatively flat and structureless in the MDI solution, while in the Wilcox solution it is significantly more warped and punctuated by more variable-speed wind. This provides a source of fast wind from the southern polar coronal regions for the last third of the rotation, consistent with the observations. Additionally, the HCS, which traces through the slow-flow band in both solutions extends to higher heliographic latitudes in the Wilcox solution, thus allowing the simulated spacecraft to remain in an outward polarity for a longer period of time.

Tracing the source of these differences to the velocity boundary of the heliospheric solution, however, provides only a partial answer to why the solutions differ so much. Since the only fundamental difference between the two model results lies in the input magnetogram, we must turn to them for a more complete answer. In Fig. 9 we compare the processed synoptic magnetograms for the MDI and Wilcox solutions (top-left and bottom-right). We have also included maps from NSO's SOLIS and GONG facilities for comparison. We also computed solutions using data from SOLIS and GONG (results not shown). SOLIS results were very similar to the results obtained using MDI, that is, relatively poor. Results obtained from GONG were better. In particular, the stream structure during the final third of the rotation was reproduced very well. It is worth reiterating that these are processed synoptic maps. We have applied a pole-fitting algorithm to them to fill in missing, or poorly resolved data and smoothed the entire map to remove high-spatial frequency structure that might cause numerical issues. Focusing first on a comparison of the magnetograms from MDI and Wilcox, beyond the initial similarities in the general features of the largest-scale active regions, we note several differences. First, Wilcox, with its limited resolution captures only the largest-scale structure. Second, whereas the MDI map contains strong and relatively comparable strength polar fields, the polar fields in the Wilcox map are not balanced, with the southern polar field being significantly weaker. More generally, considering the GONG and SOLIS maps, we note that the poles are relatively weak at GONG, but stronger at SOLIS. Moreover, the low- and mid-latitude field strengths are stronger at SOLIS. Generally, both GONG and Wilcox display weaker polar fields everywhere; however, and more importantly, the ratio of the strength of the polar to equatorial fields is lower for GONG/Wilcox than for MDI/SOLIS. With proportionally smaller polar fields, as in GONG/Wilcox, near-equatorial structure can open up and exert more control on the heliospheric solution. Consequently, this has the effect of: (1) opening up equatorial coronal holes further producing stronger high-speed streams; (2) allowing the band of solar wind variability (i.e., the slow, but variable wind) to rise and fall more in latitude; and (3) in turn, allowing the HCS to reach higher heliographic latitudes.

Finally, to assess whether the high-resolution solutions are leading to more accurate solutions near Earth, in Fig. 10 we compare solar wind speed, the radial component of the

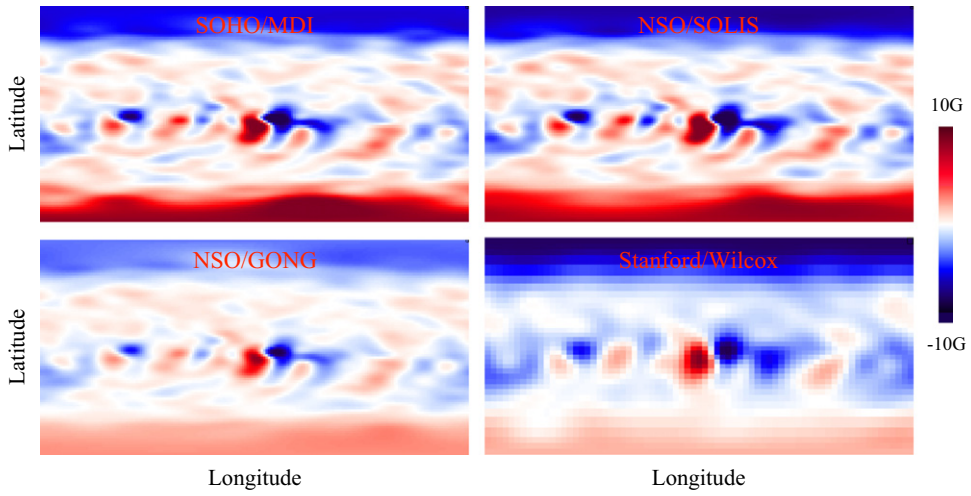

Fig. 9. Comparison of four processed synoptic maps: top-left: SOHO/MDI; top-right: NSO/SOLIS; bottom-left: NSO/GONG; and bottom-right: Stanford/Wilcox.

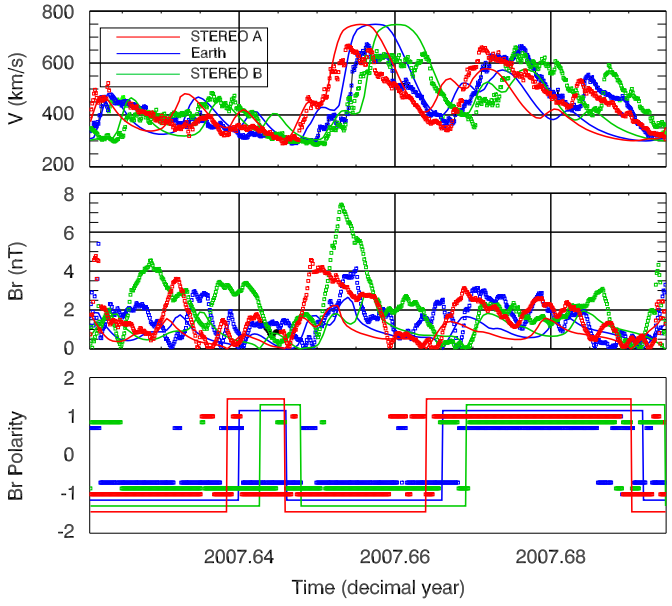

Fig. 10. Times series comparison of solar wind speed, absolute magnitude of the radial component of the magnetic field, and magnetic polarity at 1 AU for CR 2060 using high-resolution heliospheric simulation results. The model results (solid lines) were obtained by flying the STEREO A, B, and ACE spacecraft through the simulation region. The *in situ* measurements (squares) have been smoothed using box-car averages of 12 h.

interplanetary magnetic field (IMF), and the polarity of the magnetic field with observations from STEREO A, B, and ACE. For this solution magnetograms from MDI were used. Comparing with Fig. 8, we see that the added resolution appears to have improved the solution in several key areas. First, the timing of the primary high-speed stream is better phased now in the simulations (particularly at STEREO A). Second, the model solution now produces a double rise at the leading edge of this high-speed stream. Third, speeds of the remaining streams are now more modest in the model solutions, in better agreement with the observations. Fourth, the model solution now includes variability on the scale of several days, and, while the phasing of these peaks and troughs does not obviously match the observations, it is promising that the model solution is at least producing power at these frequencies. In the middle panel, we have also included a comparison of B_r. One of the problems with the heliospheric solutions is that they currently produce field strengths that are a factor of 3 or more lower than measurements at 1 AU. We had anticipated that the higher-resolution solutions would better resolve HCS crossings and limit any numerical diffusion of fields. However, as can be seen, while there is a modest increase in the average field strength, resolution alone cannot explain the mismatch between observations and model solutions.

6. Summary and discussion

In this study, we have applied CORHEL, a suite of MHD models of the solar corona and inner heliosphere, to study CR 2060, and, more generally, the late declining phase and solar minimum of solar cycle 23. Our model results were able to reproduce the essential features of the observed stream structure at 1 AU, as well as the basic structure of the solar corona, as inferred from both comparisons of EUV and white-light observations. As such, they provided a global backdrop with which to interpret and connect remote solar observations and *in situ* measurements. An equally important aspect of our study, however, was to assess some of the current limitations with our modeling procedure. We identified five main areas: (1) boundary conditions derived from synoptic magnetograms from different observatories can give significantly different results; (2) although a particular observatory may perform better for a given rotation, we have not identified one observatory that systematically performs better; (3) the solutions (both coronal and heliospheric) are sensitive to how polar fields are reconstructed; (4) our previous heliospheric solutions, while able to reproduce the grossest-scale features, including the location of the HCS, were limited in their ability to capture meso-scale structure, particularly surrounding the HCS; and (5) heliospheric models, or their inputs, underestimate the radial component (and strength) of the interplanetary magnetic field by a significant factor.

Although our model results have revealed an underlying sensitivity to the magnetogram used to drive the solution, we have not yet identified what aspects of the raw magnetograms or our processing procedure are responsible for producing either better or worse matches with observations. We believe that the polar fields, which are poorly, if at all observed are a crucial component. The noise in raw magnetograms increases significantly with latitude as each latitude bin, as viewed from Earth, becomes increasingly smaller. Moreover, if our assumption that the observed line-of-sight field is in fact radial (which is, in itself a

questionable assumption Harvey et al., 2007), this further compounds the problem: errors in the measurements are multiplied as an increasingly smaller component is converted into a radial vector. Our current technique for addressing these issues is to extrapolate mid-latitude fields to the polar regions; however, this sometimes introduces its own set of errors. It is unlikely, for example, that the polar fields during CR 2060 were as asymmetric as inferred from the map derived from Wilcox observations (lower-left panel of Fig. 9). In spite of this, that map produced, arguably the best match with *in situ* measurements, presenting us with a quandary.

For the purposes of interpreting the global structure of the heliosphere during specific time periods, it may be reasonable to run an ensemble of cases using synoptic maps from different observatories with a range of reasonably defensible processing steps, and choose the solution that best matches most of the observations or some specific aspect under study. This solution can then likely be analyzed with confidence. However, this is clearly not an ideal mode of operation, and, if there is no consistency in the choice of input magnetogram or how it is processed, global MHD models (and PFSS models for that matter) will have limited predictive capability.

Although related to the above point, a distinct issue regarding the preparation of the input magnetograms is how the polar fields are reconstructed. Importantly, our current automated procedure for processing the raw synoptic magnetogram maps frequently produces questionable polar field estimates. While we are currently assessing different approaches for resolving this, a few points are in order. First, there is no shortage of possible techniques to choose from. Liu et al. (2007) compared seven methods for computing polar fields based on various extrapolation techniques. They concluded that a time-dependent interpolation technique relying on the observed polar fields was the best approach. More recently, Sun et al. (2011) have developed a technique using 2-D spatial and temporal interpolation, coupled with a simple flux transport model to compute the unseen values. In contrast, the group at NSO employ two distinct techniques for SOLIS and GONG data, a historical result of the processing routines being developed, at least in part, independently, rather than any systematic choice of the best approach. Second, any successful technique should address the $\pm 7.25^{\circ}$ tilting of the poles such that every 6 months one pole is obscured while the other is (at least partially) observed. Arge and Pizzo (2000) implemented a scheme in the WSA model that uses data from earlier periods when a particular pole was observed to help constrain the polar values when they cannot be measured from Earth. Third, a successful extrapolation technique might weight data based on a noise estimate of the surrounding pixels, giving greater weight effectively to lower latitude pixels for which noise estimates will be lower. Fourth, rather than extrapolating in latitude at a specific time, a more sophisticated approach might extrapolate forward in time as well, incorporating the "run to the poles" streaks that can be seen in the so-called butterfly diagrams of the longitudinally-averaged field on the time scale of a solar cycle or more. Fifth, and finally, flux transport models (e.g., Schrijver and Liu, 2008; Arge et al., 2010) may ultimately offer the best pole-to-pole boundary conditions. Not only can they in principle self-consistently fill in the polar regions based on the migration of lower-latitude magnetic structure, but they can also provide truly synoptic (that is, "at the same time") maps, rather than the asynchronic ("at different times") maps that must necessarily be produced from observations limited by our Earth-centric view of the Sun. Moreover, maps developed by flux transport techniques are intrinsically functions of time, allowing the specification of self-consistent time-dependent boundary conditions for the MHD models.

Although we have not yet made a detailed study, the appearance of the finer-scale structure in the high-resolution heliospheric simulation results is intriguing. Should it account for some or all of the structure seen in the band of solar wind variability, this would allow us to resolve a long-standing question on the origin of the variability of the slow wind: does it originate from temporal or spatial variations at the source, or some combination thereof? Merkin et al. (2011) applied a global MHD model of the inner heliosphere to study the disruption of a heliospheric current sheet fold. They found that at least some finer-scale structure could be self-generated in the solar wind. Preliminary analysis of our results, in contrast suggests that, at least some of the observed structure is reproduced by quasi-steady structure at the inner boundary. However, with only a single-solution to study, any inferences would be premature. We are currently planning a sequence of simulations, which we hope will provide us with meaningful insight into this question.

One of the motivations for developing the new parallel heliospheric code was to assess whether the resolution of the simulations was contributing to the anomalously low field strengths (by a factor of three or more) predicted by the model at 1 AU. To the best of our knowledge, these low values have plagued most heliospheric models, and, until now, no systematic analysis of its origin had been performed. We identified several possible causes for the low computed field strengths. First, a potential source of error lies in the inability of the low-resolution solutions to capture the sharp transition at sector boundaries. Integrating the magnitude of B_r for the two profiles in panel (c) of Fig. 4, for example, would show a net decrease of 5–10% in the average unsigned flux of the low-resolution case. Thus, while it might contribute to lower predicted values, its effect is not sufficient to account for $\times 3$ deficit. Additionally, since the mismatch still occurs over the poles of the Sun during near solar minimum conditions, well away from the HCS, its contribution can be, at most, a minor effect.

A second potential origin for the low model field strengths is that the input magnetograms to the coronal model might be systematically low. We have performed both inter-calibration studies using magnetogram measurements from different observatories, as well as computing global coronal and heliospheric solutions using data from different observatories (Riley et al., submitted for publication), but found only modest effects. A third possibility is that the free parameters in the models might not be allowing enough coronal field to open up into the solar wind, resulting in a lower open flux. In a complementary study, we have investigated the effects of changing the density and temperature at the base of the calculation on the amount of flux opening into the heliosphere (Stevens et al., this issue). We found that, indeed, a modest 10% increase in the base temperature appears to rise the open flux sufficiently to potentially resolve this issue without otherwise reducing the match between other parameters, such as the boundary of coronal holes. Finally, it is worth noting that while we have not yet firmly identified the origin of the low interplanetary field strengths, it is not obviously related to any issues within the heliospheric models themselves, since the problem already exists at their inner radial boundary.

As a final comment, although we have devoted a considerable portion of this study to addressing the deficiencies in current global modeling techniques, we should not overlook the basic successes in being able to reproduce coronal and heliospheric structure during quiescent conditions. The recent delivery of an operational version of the WSA/Enlil coupled models (both of which are included in CORHEL) to NOAA's weather service (Farrell, 2011), a "first" for space weather models, is a testament to the fact that our ability to predict solar wind conditions in the vicinity of Earth is improving. What we have shown here is that

while progress is being made, we still must address a number of important hurdles before we can claim to have succeeded.

Acknowledgments

The authors gratefully acknowledge the support of NSF under the Center for Integrated Space Weather Modeling (CISM) program, the LWS Strategic Capabilities Program (NASA, NSF, and AFOSR), NASA's Heliophysics Theory Program (HTP), and the STEREO IMPACT team. Additionally, PR acknowledges support from NASA's Causes and Consequences of the Minimum of Solar Cycle 24 program. Finally, PR would also like to thank Dr. J. Américo Gonzalez Esparza and the Universidad Nacional Autónoma de México (UNAM) for providing support and facilities while this study was being completed.

Appendix A. Supplementary material

Supplementary data associated with this article can be found in the online version of 10.1016/j.jastp.2011.12.013.

References

Arge, C.N., Henney, C.J., Koller, J., Compeau, C.R., Young, S., MacKenzie, D., Fay, A., Harvey, J.W., 2010. Air force data assimilative photospheric flux transport (ADAPT) model. Twelfth International Solar Wind Conference 1216 (March), 343–346.

Arge, C.N., Pizzo, V.J., 2000. Improvement in the prediction of solar wind conditions using near-real time solar magnetic field updates. Journal of Geophysical Research 105, 10465.

Farrell, P., 2011. New Space Weather Forecasting Model Going Operational with National Weather Service. 〈www.bu.edu/cas/news/press-releases/cism/〉.

Florinski, V., Pogorelov, N.V., 2009. Four-dimensional transport of galactic cosmic rays in the outer heliosphere and heliosheath. Astrophysical Journal 701 (August), 642–651.

Frazin, R.A., Kamalabadi, F., 2005. On the use of total brightness measurements for tomography of the solar corona. Astrophysical Journal 628 (August), 1061–1069.

Gibson, S.E., de Toma, G., Emery, B., Riley, P., Zhao, L., Elsworth, Y. Leamon, R.J., Lei, McIntosh, S., Mewaldt, R.A., Thompson, B.J., Webb, D. 2011. The whole heliosphere interval in the context of a long and structured solar minimum: an overview from sun to earth. Solar Physic, 422. doi:10.1007/s11207-011-9921-4. 〈http://adsabs.harvard.edu/abs/2011SoPh..tmp..422G〉, (Provided by the SAO/NASA Astrophysics Data System).

Gibson, S.E., Kozyra, J.U., de Toma, G., Emery, B.A., Onsager, T., Thompson, B.J., 2009. If the Sun is so quiet, why is the Earth ringing? A comparison of two solar minimum intervals. Journal of Geophysical Research 114 (September), 9105.

Gosling, J.T., Bame, S.J., McComas, D.J., Phillips, J.L., 1990. Coronal mass ejections and large geomagnetic storms. Geophysical Research Letters 17, 901.

Harvey, J.W., Branston, D., Henney, C.J., Keller, C.U., 2007. SOLIS and GONG Teams, 2007. Seething horizontal magnetic fields in the quiet solar photosphere. Astrophysical Journal Letters 659 (April), L177–L180.

Lario, D., Roelof, E.C., 2007. Energetic particles during the first and third Ulysses southern high-latitude excursions: probing global corotating interaction region structure beyond 5 AU. Journal of Geophysical Research 112 (September), 9107.

Lindsay, G.M., Russell, C.T., Luhmann, J.G., 1995. Coronal mass ejection and stream interaction region characteristics and their potential geomagnetic effectiveness. Journal of Geophysical Research 100 (Sep.), 16999–17014.

Lionello, R., Linker, J.A., Mikić, Z., 2009. Multispectral emission of the sun during the first whole sun month: magnetohydrodynamic simulations. Astrophysical Journal 690 (January), 902–912.

Liu, Y., Hoeksema, J.T., Zhao, X., Larson, R.M., 2007. MDI Synoptic Charts of Magnetic Field: Interpolation of Polar Fields. American Astronomical Society Meeting Abstracts #210. Bulletin of the American Astronomical Society, vol. 38; 2007, pp. 129.

Merkin, V.G., Lyon, J.G., McGregor, S.L., Pahud, D.M., 2011. Disruption of a heliospheric current sheet fold. Geophysical Research Letters 381 (July), 14107.

Riley, P., 2010. The three-dimensional structure of the inner heliosphere. in: Maksimovic, M., Issautier, K., Meyer-Vernet, N., Moncuquet, M., Pantellini, F. (Eds.), Twelfth International Solar Wind Conference, American Institute of Physics Conference Proceedings, vol. 1216; 2010, pp. 323.

Riley, P., Linker, J.A., Gonzalez-Esparza, J.A., Jian, L., Russell, C., Luhmann, J. Interpreting some properties of CIRs and their associated shocks during the recent solar minimum using global MHD simulations. Journal of Atmospheric and Terrestrial Physics, this issue.

Riley, P., Linker, J.A., Mikić, Z., 2001a. An empirically-driven global mhd model of the corona and inner heliosphere. Geophysical Research Letters 106, 15889.

Riley, P., Linker, J.A., Mikić, Z., Lionello, R., 2001b. Mhd modeling of the solar corona and inner heliosphere: Comparison with observations. in: Song, P., Singer, H.J., Siscoe, G.L. (Eds.), Space Weather, Geophysical Monograph Series, vol. 125. AGU, Washington, DC, pp. 159.

Riley, P., Linker, J.A., Mikic, Z., 2010a. Global MHD modeling of the solar corona and inner heliosphere for the whole heliosphere interval. Highlights of Astronomy 15, 491–493. doi:10.1017/S1743921310010367. 〈http://adsabs.harvard.edu/abs/2010HiA....15..491R〉. (Provided by the SAO/NASA Astrophysics Data System).

Riley, P., Lionello, R., Linker, J.A., Mikic, Z., Luhmann, J., Wijaya, J., 2011. Global MHD modeling of the solar corona and inner heliosphere for the whole heliosphere interval. Solar Physics, 145.

Riley, P., Luhmann, J.G., 2011. Interplanetary signatures of unipolar streamers and the origin of the slow solar wind. Solar Physics, 417 doi:10.1007/s11207-011-9909-0. 〈http://adsabs.harvard.edu/abs/2011SoPh..tmp..417R〉. (adsnote = Provided by the SAO/NASA Astrophysics Data System).

Riley, P., Luhmann, J., Opitz, A., Linker, J.A., Mikic, Z., 2010b. Interpretation of the cross-correlation function of ACE and STEREO solar wind velocities using a global MHD Model. Journal of Geophysical Research (Space Physics) 115 (November), 11104.

Riley, P., Mikić, Z., Linker, J.A., 2003. Dynamical evolution of the inner heliosphere approaching solar activity maximum: interpreting ulysses observations using a global mhd model. Annals of Geophysics 21, 1347.

Riley, P., Mikic, Z., Linker, J.A., Harvey, J., Henney, C.J., Hoeksema, T., Liu, Y., Ulrich, R., Bertello, L. A multi-observatory inter-calibration of line-of-sight diachronic solar magnetograms and implications for the open flux of the heliosphere. Astrophysical Journal. Submitted for publication.

Riley, P., Mikic, Z., Linker, J.A., Schwadron, N.A., McComas, D.J., 2010c. On the relationship between coronal heating, magnetic flux, and the density of the solar wind. Journal of Geophysical Research 115, 6104. doi:10.1029/2009JA015131.

Russell, C.T., McPherron, R.L., 1973. Semiannual variation of geomagnetic activity. Journal of Geophysical Research 78, 92–108.

Schrijver, C.J., Liu, Y., 2008. The global solar magnetic field through a full sunspot cycle: observations and model results. Solar Physics 252 (October), 19–31.

Stevens, M., Linker, J.A., P., R. A study of the sensitivity of global MHD model solutions of the solar corona to boundary conditions. Journal of Atmospheric and Terrestrial Physics, this issue.

Sun, X., Liu, Y., Hoeksema, J.T., Hayashi, K., Zhao, X., 2011. A new method for polar field interpolation. Solar Physics 270 (May), 9–22.

Svalgaard, L., Schatten, K.H., 2008. Predicting solar cycle 24. AGU Fall Meeting Abstracts, A1593.

Tsurutani, B.T., Gonzalez, W.D., Gonzalez, A.L.C., Guarnieri, F.L., Gopalswamy, N., Grande, M., Kamide, Y., Kasahara, Y., Lu, G., Mann, I., McPherron, R., Soraas, F., Vasyliunas, V., 2006. Corotating solar wind streams and recurrent geomagnetic activity: a review. Journal of Geophysical Research 111 (June), 7.

Wiltberger, M., Huang, C.L., Qain, L., Wang, W., Burns, A.G., Solomon, S.C. CMIT study of CR2060 and 2068 comparing L1 and MAS solar wind drivers. Journal of Atmospheric and Terrestrial Physics, doi:10.1016/j.jastp.2012.01.005, this issue.

Winterhalter, D., Smith, E.J., Burton, M.E., Murphy, N., McComas, D.J., 1994. The heliospheric plasma sheet. Journal of Geophysical Research 99 (April), 6667.

Appendix J

Interplanetary Signatures of Unipolar Streamers and the Origin of the Slow Solar Wind

Riley, P. and Luhmann, J. G.

Published in Solar Physics, 2012.

Solar Phys (2012) 277:355–373
DOI 10.1007/s11207-011-9909-0

Interplanetary Signatures of Unipolar Streamers and the Origin of the Slow Solar Wind

P. Riley · J.G. Luhmann

Received: 23 May 2011 / Accepted: 11 November 2011 / Published online: 16 December 2011

Abstract Unipolar streamers (also known as pseudo-streamers) are coronal structures that, at least in coronagraph images, and when viewed at the correct orientation, are often indistinguishable from dipolar (or "standard") streamers. When interpreted with the aid of a coronal magnetic field model, however, they are shown to consist of a pair of loop arcades. Whereas dipolar streamers separate coronal holes of the opposite polarity and whose cusp is the origin of the heliospheric current sheet, unipolar streamers separate coronal holes of the same polarity and are therefore not associated with a current sheet. In this study, we investigate the interplanetary signatures of unipolar streamers. Using a global MHD model of the solar corona driven by the observed photospheric magnetic field for Carrington rotation 2060, we map the ACE trajectory back to the Sun. The results suggest that ACE fortuitously traversed through a large and well-defined unipolar streamer. We also compare heliospheric model results at 1 AU with ACE *in-situ* measurements for Carrington rotation 2060. The results strongly suggest that the solar wind associated with unipolar streamers is slow. We also compare predictions using the original Wang–Sheeley (WS) empirically determined inverse relationship between solar wind speed and expansion factor. Because of the very low expansion factors associated with unipolar streamers, the WS model predicts high speeds, in disagreement with the observations. We discuss the implications of these results in terms of theories for the origin of the slow solar wind. Specifically, premises relying on the expansion factor of coronal flux tubes to modulate the properties of the plasma (and speed, in particular) must address the issue that while the coronal expansion factors are significantly different at dipolar and unipolar streamers, the properties of the measured solar wind are, at least qualitatively, very similar.

Keywords Interplanetary medium · Solar wind · Sun: corona, evolution, magnetic fields

P. Riley (✉)
Predictive Science, Inc., 9990 Mesa Rim Road, Suite 170, San Diego, CA, USA
e-mail: pete@predsci.com

J.G. Luhmann
Space Science Laboratory, University of California, Berkeley, Berkeley, CA, USA
e-mail: jgluhman@ssl.berkeley.edu

1. Introduction

The recent and prolonged solar minimum occurring at the end of solar cycle 23 (December 2009) has provided a unique opportunity to investigate the Sun and its extended atmosphere (the heliosphere) under pristine, quiescent conditions. In contrast to the previous minimum (September 1996) the structure of the corona was punctuated by the ubiquitous presence of "unipolar" helmet streamers (Hundhausen, 1972), also known as pseudo-streamers (Wang, Sheeley, and Rich, 2007). Whereas the standard helmet streamer, or "dipolar" streamer bridges between coronal holes of opposite polarity, unipolar streamers separate coronal holes of the same magnetic polarity. To accomplish this, two loops are embedded within them. Importantly, while dipolar streamers culminate in stalks with an embedded current sheet, no current sheet is embedded within unipolar streamers since the field lines on either side of the stalk have the same polarity. Figure 1 shows a selection of views for Carrington rotation (CR) 2060 illustrating the these principles. These views illustrate the general features of the solar corona surrounding this period. Simulated white light images, obtained by integrating the model density along the line of sight with an appropriate weighting function for electron scattering of light, are displayed together with a selection of field lines equally spaced in latitude. Closed field lines are colored green while open field lines that are directed away from the Sun are colored red and those directed toward the Sun are colored blue. A selection of dipolar and unipolar streamers are indicated, as is the latitude of the *Ulysses* and ACE spacecraft at these times. Although most of the unipolar streamers can be identified by the double loop structure under the streamer, note that the one in panel (c) cannot be resolved this way, at least on this scale. Instead, the closely spaced field lines alerts us to its presence, suggesting a very small expansion factor.

Identifying and interpreting interplanetary signatures of phenomena observed in the corona can be challenging, complicated by the fact that the plasma undergoes significant evolution as it travels from the solar surface to 1 AU (or beyond). In the absence of obviously transient phenomena such as coronal mass ejecta, three quasi-corotating features in the solar wind are germane to this study: The stream interface (SI), the heliospheric current sheet (HCS), and the heliospheric plasma sheet (HPS), all of which have been associated with features or processes originating in the corona.

The SI is simply a boundary that separates what was originally slow and dense solar wind with what was fast, tenuous wind (Sonett and Colburn, 1965). Although this boundary can exist at the trailing edge of high-speed streams, that is, where fast solar wind outruns slower wind behind it, the term is usually used to refer to the leading edge of high-speed streams where fast wind runs into slower wind ahead, compressing and accelerating it (Gosling *et al.*, 1978).

The HCS is the extension of the neutral line in the corona identifying the boundary between outwardly directed and inwardly directed heliospheric magnetic field lines. Although its presence is often associated with SIs (Gosling *et al.*, 1978), with the HCS preceding the SI by a day or so, they are only loosely related, and, as we will see, during times when unipolar streamers are present (Wang, Sheeley, and Rich, 2007; Wang *et al.*, 2010), it is quite possible for SIs to exist in the absence of an HCS crossing.

Finally, the HPS is a region surrounding the HCS of enhanced density but depressed magnetic field strength (Winterhalter *et al.*, 1994). Thus it is a region of significantly enhanced plasma β, where β is the ratio of thermal plasma pressure to magnetic pressure. The thickness of the HCS has been estimated to be approximately 320 000 km (Winterhalter *et al.*, 1994; Gosling *et al.*, 1981), and typically occurs within regions of slow wind (that is, they are not associated with stream interactions). Gosling *et al.* (1981) mapped these events back

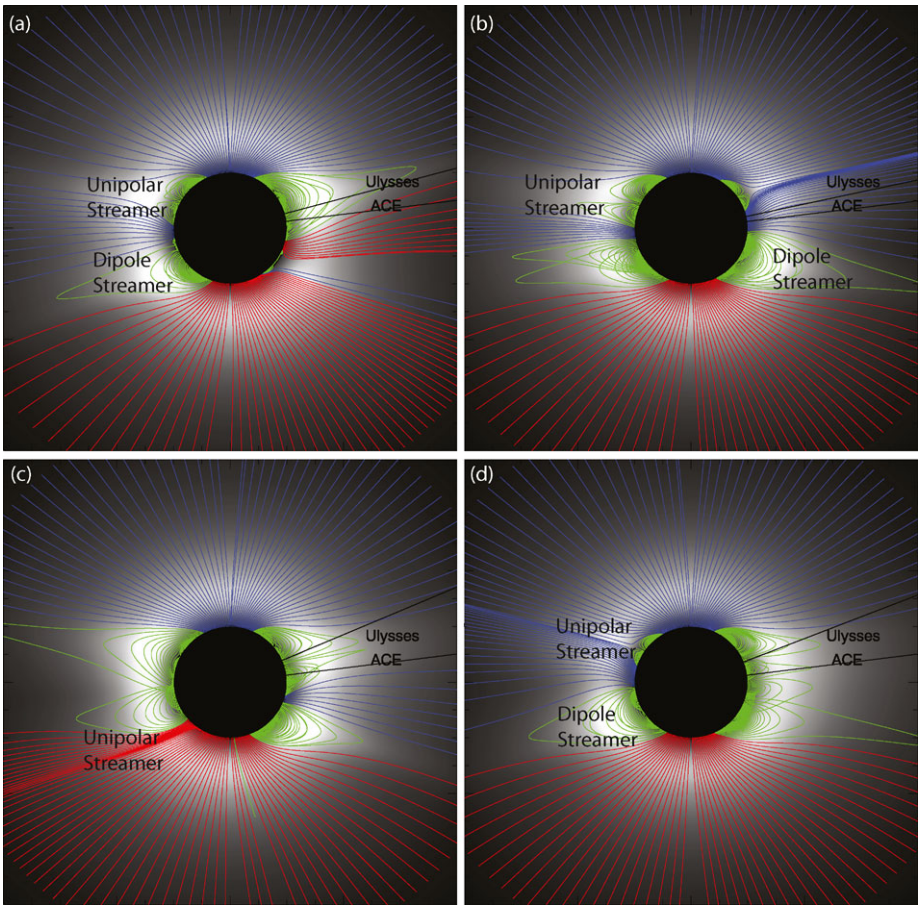

Figure 1 A selection of meridional slices from a global MHD simulation of CR 2060, which occurred between 14 August 2007 and 10 September 2007. Grey-scale images are simulated polarized brightness (pB) images and the colored lines are magnetic field lines drawn from equally spaced points in latitude on the solar surface. The field lines have been color-coded so that blue/red lines are field lines that open into the heliosphere and are inwardly/outwardly directed, while green field lines connect back to the Sun at both ends, *i.e.*, they are closed field lines.

to the Sun finding a strong association with coronal streamers. Thus, it is expected that there should be a relatively strong connection between HCSs and HPSs. Winterhalter *et al.* (1994) found that the latter are almost always present when the former are observed (although Crooker *et al.* (2004a) found that approximately half of the HCs analyzed were embedded in an HPS). On the other hand, it is possible for HPSs to be observed in the absence of HCSs. Neugebauer *et al.* (2004), for example, identified consecutive fast solar wind streams of the same polarity. They found that the interaction region between the two had many of the same features as intervals between streams that contained a sector boundary. In particular, quantities not expected to evolve with stream dynamics, such as helium abundances and heavy ion charge states, were not substantially different from their HCS-related counterparts. They did, however, find some differences in their dynamical properties: non-HCS regions were

shorter in duration, had a higher minimum speed, and lower peak and mean densities. They found no obvious correlation between these intervals and coronal streamers.

The origin of the solar wind, and particularly the slow solar wind has remained elusive since the two basic properties of the wind were first measured in 1962 (Neugebauer and Snyder, 1962). While the fast solar wind is thought to originate from within coronal holes, we cannot point to a definitive location or basic physical mechanism for producing the slow solar wind. Although it has been long known that the slow, and variable solar wind is associated with the edges of coronal streamers (Gosling *et al.*, 1981), as yet, we have not been able to narrow it down further, at least in a way that the scientific community agrees upon. Two distinct ideas on its origin have arisen. (Of course, there are more models and even finer classifications of slow solar wind, but for simplicity, we limit our discussion to these two ideas.) The first, which we will call the "expansion factor" (EF) model, relies on the geometrical properties of groups of the fields lines, or flux tubes as they expand into the heliosphere. In analogy with Bernoulli flow (and this is strictly an analogy – the Bernoulli effect is much too small to account for the difference in speed between the slow and fast wind), flow along flux tubes that expand the most leads to the slow solar wind, whereas flow along flux tubes that expand only modestly produce fast wind. It turns out that the expansion factor is smallest deep within coronal holes and largest adjacent to dipolar streamers (Wang and Sheeley, 1990). Crucially, Wang, Sheeley, and Rich (2007) argued that the expansion factor associated with field lines near unipolar streamers is very small (sometimes as low as one), leading them to predict that solar wind from unipolar streamers would be fast. Although the EF model was originally conceived because of an observed inverse correlation between expansion factor and measured solar wind speed at 1 AU, over the years, a theoretical basis for explaining how expansion factor can modulate not just speed, but density, composition, and charge state has been developed (Wang and Sheeley, 2003; Cranmer, van Ballegooijen, and Edgar, 2007; Wang, Ko, and Grappin, 2009; Cranmer, 2010).

A competing concept for the origin of the slow solar wind relies on the idea that it originates from within a boundary layer (BL) adjacent to the coronal streamers. The leading idea for generating such a boundary layer is a process of magnetic reconnection between open and closed field lines at coronal hole boundaries, although other ideas, such as Kelvin–Helmholtz instabilities have been considered (Suess *et al.*, 2009). A principal strength of such a model lies in its intrinsic ability to account for the difference in composition and abundance states of the slow and fast wind, which are sufficiently different that they imply distinct origins for slow and fast wind. Moreover, the composition and charge states measured in the slow wind are quite close to those measured within coronal streamers (*e.g.*, Uzzo *et al.*, 2003). Since it is apparently necessary for an open magnetic field line to reconnect with one of the streamer loops, the term "interchange reconnection" has arisen to describe the way a closed field line opens while the open field line closes (*e.g.*, Crooker *et al.*, 2004b). While we generically refer to all incarnations of such models as interchange reconnection, we emphasize that the concepts behind them can be quite different (Wang, Hawley, and Sheeley, 1996; Fisk, 1996; Antiochos *et al.*, 2011). The main point, however, is that the boundary between open and closed field lines provides an environment for reconnection to take place. And, in particular, it is not sensitive to whether there are one, two, or even three arcades underneath the streamer structure. Previously, we used a global MHD simulation to demonstrate how differential rotation could drive reconnection at the boundary of coronal streamers (Lionello *et al.*, 2005), substantiating the findings of Wang, Hawley, and Sheeley (1996). Additionally, we showed that the regions where closed magnetic loops reconnect with open field lines may not be distributed uniformly along the boundaries of coronal holes; they are concentrated on

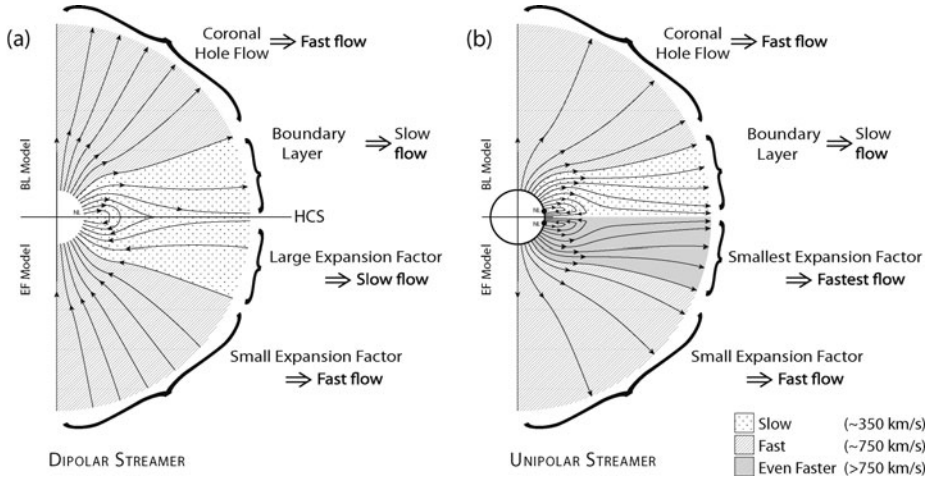

Figure 2 An illustration of the salient features of the EF and BL models for: (a) a dipolar streamer and (b) a unipolar streamer.

the eastward borders of streamers, which may or may not be related to the studies by Suess *et al.* (2009) and Liu *et al.* (2010), who showed that tracers of composition (*e.g.*, He/H, and O^{6+}/H) are preferentially located to one side of the HCS. For the purposes of this study, however, it is sufficient to limit our delineation between EF and BL models.

Figure 2 illustrates the basic features and predictions of the EF and BL models for both dipolar (left) and unipolar (right) streamer geometries. For dipolar streamers, both models predict slow solar wind on either side of the HCS. The width of the slow-flow band is determined in the BL model by the details of where the reconnection is taking place, or the scale over which an instability is occurring, but is presumably limited to some distance away from the closed loops. The boundary of the slow-flow band in the EF model is determined by an interesting property of the time-independent Parker equations, namely, that for rapidly expanding flux tubes, there may be more than one location for the critical point, the most stable of which is that one furthest from the Sun (Cranmer, van Ballegooijen, and Edgar, 2007).

Figure 2(b) illustrates the situation for the case of a unipolar streamer. The concepts for the generation of slow solar wind under the BL model are unaltered: Reconnection, for example, still occurs between open and closed field lines. (Of course it remains to be demonstrated how reconnection can occur within a geometry where all field lines are apparently pointing in the same direction.) However, the situation now changes within the EF scenario. Here, the structure associated with the double loops defining the unipolar streamer promote expansion factors that can be as low as one (see Figure 4). Under such conditions, the EF model would be expected to produce speeds even higher than in the fast solar wind (> 750 km s^{-1}).

The areal expansion factor, f_s, can be defined (Wang and Sheeley, 1997) as

$$f_s = \left(\frac{R_\odot}{R_1} \right)^2 \frac{B_r(R_\odot, \theta_o, \phi_o)}{B_r(r_1, \theta_1, \phi_1)}. \tag{1}$$

This expression relates the amount by which a flux tube expands from one location (r_o, θ_o, ϕ_o), say at the solar surface ($r_o = R_S$) to another, higher up. Typically, the source surface ($\approx 2.5 R_\odot$) is used for potential field source surface (PFSS) models, and the outer

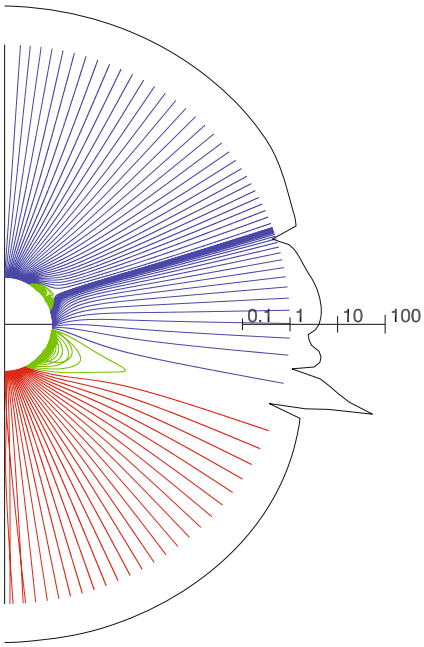

Figure 3 Expansion factor (at $30R_{\odot}$, solid line) is plotted logarithmically as a function of latitude and compared with a set of magnetic field lines drawn out to $6R_{\odot}$ for CR 2060 at 215° longitude.

boundary of the simulation region ($20-30R_{\odot}$) is used for MHD models, the main issue usually being that the field lines are fully radial by this height. This expansion factor is above and beyond the field expansion that would occur for a monopole field ($f_s \sim 1/r^2$). To better understand the relationship between streamer structure and expansion factor, in Figure 3 we compare expansion factor with a trace of field lines at 215° longitude for CR 2060. Although the field lines are only traced out to $6R_{\odot}$, by this distance, they are essentially radial. The expansion factor (which, practically speaking, is computed by tracing along each field line from the outer boundary of the simulation ($30R_{\odot}$) back to the solar surface ($1R_{\odot}$)) is plotted as a logarithmic polar profile to emphasize the wide variation in values ($0.65-93$ for this meridional slice). From this comparison we note several interesting points. First, as the cartoon in Figure 2 illustrated, small expansion factors are associated with unipolar streamers and large expansion factors are associated with dipolar streamers. Second, at least within this geometry, the expansion factors are asymmetric with respect to the inferred centroid (or stalk) of the streamer structure (the HCS in the case of the dipolar streamer and a quasi-radial trace from the spline of the unipolar streamer). The expansion factor is largest equatorward of the dipolar streamer and smallest equatorward of the unipolar streamer. Third, regions of low expansion factor (< 1) bound the large expansion factor associated with the dipolar streamer, with the lowest values occurring at the current sheet.

The basic features of both the BL and EF models are reflected in two empirically based models for computing the speed of the solar wind in the heliosphere. (Of course, in reality, the empirically based models preceded and perhaps even motivated the subsequent theoretical ideas.) First, the original Wang–Sheeley (WS) model (Wang and Sheeley, 1990) uses an observed negative correlation between solar wind speed and the super-radial expansion of the solar magnetic field. Second, Predictive Science, Inc.'s "Distance from the Coronal Hole Boundary" (DCHB) model (Riley, Linker, and Mikić, 2001) specifies speed at the base of the corona as a function of the perpendicular distance from the coronal hole boundary and maps this speed out along field lines to $30R_{\odot}$. In effect, we consider a "boundary layer"

adjacent to the last closed streamer field line that is where the reconnection takes place, opening up the streamer field lines.

Although the derivation of solar wind speed at, say, $30R_{\odot}$ in the WS and DCHB models is empirical (or "*ad hoc*"), and hence subject to optimization in the absence of any improvement in our understanding of the physical mechanisms involved, the prescriptions can be related to the aforementioned different ideas (BL and EF) on the origin of the solar wind. Thus, in principle, it may be possible to derive some physical insight from comparisons of the two approaches. In the case of the WS model, which relies on the expansion factor of the local flux tube to govern the resulting speed, density, and temperature of the escaping solar wind, detailed physics-based models have been developed to produce the correct plasma properties driven by waves and turbulence (Cranmer, 2010), as well as the unique compositional differences between slow and fast solar wind (Laming, 2004). The DCHB model, on the other hand, which linked to the idea of a boundary layer for the origin of the slow solar wind (Fisk, 1996; Antiochos *et al.*, 2011) provides a natural explanation for the composition and charge state distributions in the slow solar wind, as well as speed, density, and temperature, at least in a qualitative sense. Thus, should the WS or DCHB models perform significantly better than the other, this would lend support for either the EF or BL model, respectively. Of course, it is important to stress this would remain a tentative inference since, by definition, empirical models have surrendered some degree of physical insight for the goal of gaining better matches with observations. Additionally, theories are subject to revision based on new constraints. Thus, any deficiency in a model may be used to further develop the theory behind it.

In their original paper, Wang and Sheeley (1990) determined a relationship between solar wind speed (V) and expansion factor (f_s) using very broad velocity bins of size $\Delta v = 100\ \mathrm{km\,s^{-1}}$ applied to solar wind data between $450\ \mathrm{km\,s^{-1}}$ and $750\ \mathrm{km\,s^{-1}}$ (a bin on either end collected all speeds outside this range). Here, following and generalizing Arge and Pizzo (2000) we write a continuous form of relationship between solar wind speed and expansion factor:

$$V_{\mathrm{WS}}(f_s) = V_{\mathrm{slow}} + \frac{V_{\mathrm{fast}}}{(f_s)^{\delta}} \tag{2}$$

where v_{slow} is the lowest solar wind speed expected as $f_s \to \infty$ and α is some coefficient also to be determined, although Wang (2010, private communication) suggests that $\delta = 1$ is justified. The specification of velocity then depends only on the expansion factor of the field line.

Using values from Wang and Sheeley (1990), we performed a least-squares fit to derive $V_{\mathrm{slow}} = 377.5\ \mathrm{km\,s^{-1}}$ and $V_{\mathrm{fast}} = 1863\ \mathrm{km\,s^{-1}}$. Since this expression can potentially lead to speeds well beyond those that have been observed by *Ulysses*, we also impose a minimum and maximum speed of 350 and 800 $\mathrm{km\,s^{-1}}$. These values could also be considered free parameters. Although Arge (2004) derived set of best-fit parameters (which are sensitive to the solar observatory used to create the photospheric field map), the precise values of these parameters are not that important for the current study, and for simplicity, we retain the parameters originally derived in the study by Wang and Sheeley (1990).

The DCHB model depends on the angular, minimum (perpendicular) distance from the coronal hole boundary to specify solar wind speed. This is computed at the base of the corona and the speeds are mapped along field lines to the reference sphere, $30R_{\odot}$, in this case. We can express the relationship as

$$V_{\mathrm{DCHB}}(d) = V_{\mathrm{slow}} + \frac{1}{2}(V_{\mathrm{fast}} - V_{\mathrm{slow}})\left(1 + \tanh\left(\frac{d-\alpha}{w}\right)\right) \tag{3}$$

where d is the minimum, or perpendicular distance from an open-closed boundary, that is, from a CH boundary, at the base of the corona, α is a measure of how thick the slow-flow band is, and w is the width over which the flow is raised to coronal hole values (Riley, Linker, and Mikić, 2001). The parameters $V_{\rm slow}$ and $V_{\rm fast}$ are analogues (but, because of the difference in formulation, likely to be different) of the same-named parameters in the WS model. At the boundary between open-closed fields, this expression reduces to $v_{\rm slow}$, whereas, far from such a boundary, that is, deep within a coronal hole, it reduces to $v_{\rm fast}$. For the DCHB model, then, the specification of the velocity profile depends on the minimum distance of the field line foot-point to a coronal hole boundary.

Figure 4 shows the location of the coronal hole boundaries (at the base of the corona), the distance from the nearest coronal hole boundary (d), and the expansion factor of coronal magnetic fields ($f_{\rm s}$), both at $30R_{\odot}$. Comparison of the computed coronal hole boundaries with the two lower panels shows how the topology of the magnetic field, as it winds through the corona, imports structure and complexity to both of these quantities. The imprints of equatorward extensions of the polar coronal holes, as well as isolated equatorial coronal holes can be recognized but their structure couldn't have been predicted without knowing the coronal magnetic field. Comparison of the second and third panels allows us to recognize the similarities and differences between the WS and DCHB models. In the middle panel, the location of the HCS is overlaid. Around this, d is low, and $f_{\rm s}$ is high. From Equations (2) and (3) we can infer that both models would predict slow wind around the HCS. It is, however, the arcs branching off from the HCS, in particular, in the southern hemisphere in the longitude range $75-210°$, and in the northern hemisphere in the range $180-285°$ that imply different predictions. At these locations, d is again low, suggesting slow solar wind, but $f_{\rm s}$ is extremely low suggesting very fast wind. In fact, on the basis of Equation (2) alone, speeds from these regions would far exceed the speed over within the polar coronal holes.

It is important to distinguish the DCHB model from an earlier prescription based on the minimum angular distance from the heliospheric current sheet (Hakamada and Akasofu, 1981). In the latter, the wind speed is assumed to be slow in a band within some angular minimum distance from the heliospheric current sheet, computed at some reference height (say $2.5R_{\odot}$ for PFSS models or $20-30R_{\odot}$ for MHD models) and fast everywhere else. On the other hand, the DCHB model specifies the slow wind along bands at the base of the corona, adjacent to the open-closed field line boundaries. This speed profile is then mapped along field lines to some reference height. Except for very idealized geometries, such as a tilted dipole field, these would be expected to yield quite different results. The DCHB model attempts to describe the wind profile near its source, whereas the technique based on distance from the HCS attempts to describe the profile at some point of relative equilibrium. Wang and Sheeley (1997) compared the WS and angular distance from the HCS models finding that the latter produced significantly poorer correlations with *in-situ* measurements at Earth.

Finally, it is important to distinguish between the WS and DCHB models and a third empirically based model, which is, arguably, the most well known and implemented. The Wang–Sheeley–Arge (WSA) has been successively refined since its initial development in the late 1990s at NOAA's Space Weather Prediction Center (SWPC) and was recently a key component in the first research model transitioned to space weather operations (Farrell, 2011). Initially, it developed via a set of minor adjustments to the WS model, tuning the free parameters using more thorough comparisons with *in-situ* observations. More recently, the relationship between speed and $f_{\rm s}$ has been generalized, and a term similar to that in the DCHB model has also been added (Arge *et al.*, 2003). In fact, in its current form, the best-fit parameters for the WSA model render it virtually identical to the DCHB model. Ironically,

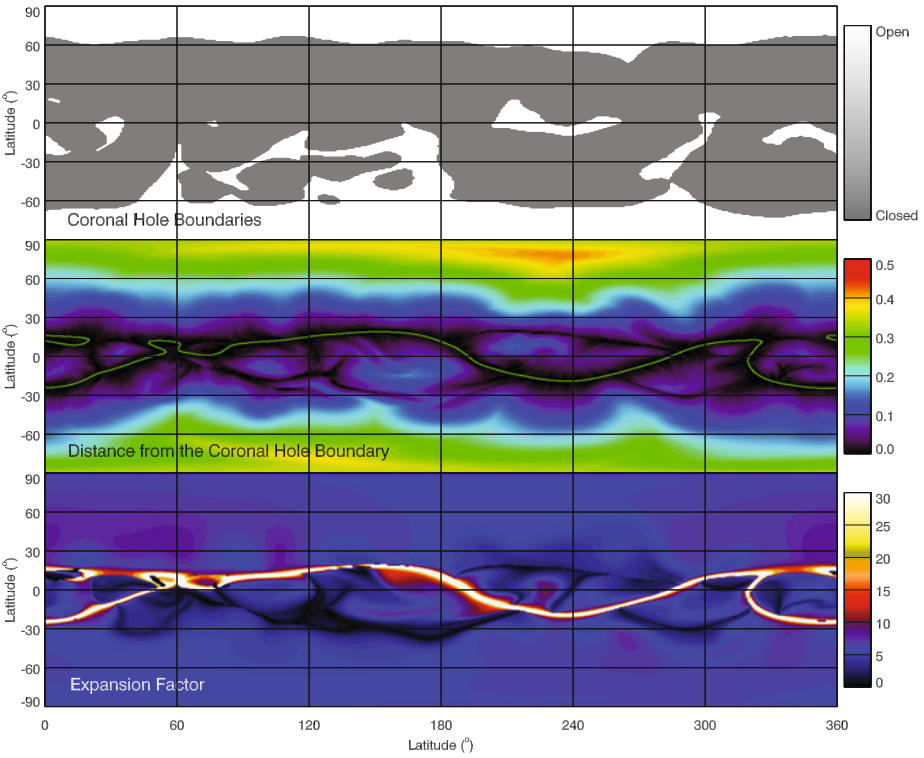

Figure 4 Computed coronal hole boundaries at $1R_{\odot}$ (top), distance from the coronal hole boundary at $30R_{\odot}$ (middle), and expansion factor at $30R_{\odot}$ (bottom) for CR 2060.

we believe that the residual effects of the WS model in the WSA model serve only to reduce its ability to match solar wind streams (Riley *et al.*, 2011).

2. Unipolar Streamers in the Corona

We begin our analysis by summarizing the structure of the solar corona during the interval between 14 August 2007 and 10 September 2007, that is, CR 2060. We chose this time period for our case study for several reasons. First, it is one of the more quiescent rotations during the interval spanning the last solar minimum (marking the end of solar cycle 23), and there were no obvious signatures of transient activity during the interval. Second, well-developed unipolar streamers were observed (see Figure 1). And third, and most importantly, the ACE spacecraft, located at 7.1° N latitude was positioned such that its trajectory took it directly through plasma emanating from one of the unipolar streamers.

To assess how well our MHD model has reproduced the large-scale streamer structure during CR 2060, in Figure 5 we compare our simulated polarized brightness estimates with brightness observations by the SECCHI instruments on board STEREO. The particular combination of STEREO A/B and COR1/2 images were selected from the full set available at http://secchi.nrl.mil/synomaps based on the quality of the images. At least for this rotation, we found that the combination of COR1 from STEREO B at lower altitudes and COR2 from

STEREO A at higher altitudes resulted in the best set. Since the model used here relied on the polytropic approximation, we are limited to a qualitative assessment of model results. In spite of this, the comparison demonstrates that the model has captured the overall features of the streamer structure existing during CR 2060. In particular, we note the following: *i*) There is a dominant streamer pattern tracing through all longitudes that first rises into the northern hemisphere, drops across the equator at $\approx$180° and finally returns to the northern hemisphere. As we will show later, this pattern tracks the location of the HCS as determined from the model.

3. Solar Wind Speed from Unipolar Streamers

The stream structure of the solar wind at 1 AU in the ecliptic plane (from ACE measurements) is shown in the bottom panel of Figure 6. We have plotted both solar wind speed, color-coded according to the observed polarity of the interplanetary magnetic field, together with plasma density (green) as a function of Carrington longitude, ballistically mapped back from 1 AU to the Sun. In this presentation of the data, time increases from right to left. Thus, a fast stream will evolve – as it moves away from the Sun – by steepening at its leading (right) edge and becoming shallower at its trailing (left) edge. The former leads to compression fronts, while the latter produces expansion waves, or rarefaction regions (Sarabhai, 1963). The density enhancement at $\approx$255° longitude (labeled 'B') likely marks the location of a SI, separating fast wind to its left from slow wind to its right. The pattern within the magnetic polarity of the flow is, to a first approximation, two-sector, with the first half of the interval being outward (red) magnetic field and the second half being inward (blue). It is, however, more complex, with "pockets" of opposite polarity embedded within the larger scale pattern.

The middle and top panels of Figure 6 indicate where the ACE observations map back to on the surface of the Sun, using the MHD solution. To accomplish this, the trajectory was ballistically mapped back to $30R_{\odot}$, after which the MHD solution was then used to trace along field lines to their source at the base of the corona. In the middle panel, the red and blue lines show where points on the ACE trajectory map to at the base of the corona. The color-coding is based on the polarity of the interplanetary magnetic field, as measured by ACE. The color contours show the observed photospheric magnetic field, while the black contours mark the neutral line, that is, where $B_{\mathrm{r}} = 0$. Finally, the ACE trajectory and mapping is overlaid on the computed coronal holes for this solution, color-coded by the direction of the photospheric field.

Comparing the mapped ACE polarities with the observed photospheric field (middle panel) suggests a reasonable match between the two. There are some obvious disagreements, such as the outward IMF mapping into the northern polar coronal hole around longitudes 280 – 300°, but overall, the large-scale polarity appears to trace back correctly. Where the comparison is poor, it could suggest: *i*) there are inaccuracies in the model solution – computed coronal holes are larger/smaller than in reality, for example; or *ii*) there were processes not incorporated in the model, such as long period Alfvén waves, turbulence, or transient activity.

Returning to the bottom panel of Figure 6, we can interpret the interval between the first-two streams ($\approx$105° longitude) as a non-HCS interaction region (Neugebauer *et al.*, 2004), whereas the second trough, at $\approx$200° longitude contains an embedded HCS. Moreover, the first two streams likely originate from the mid-latitude extension of the southern polar coronal hole, whereas the boundary between the second and third streams separates distinct

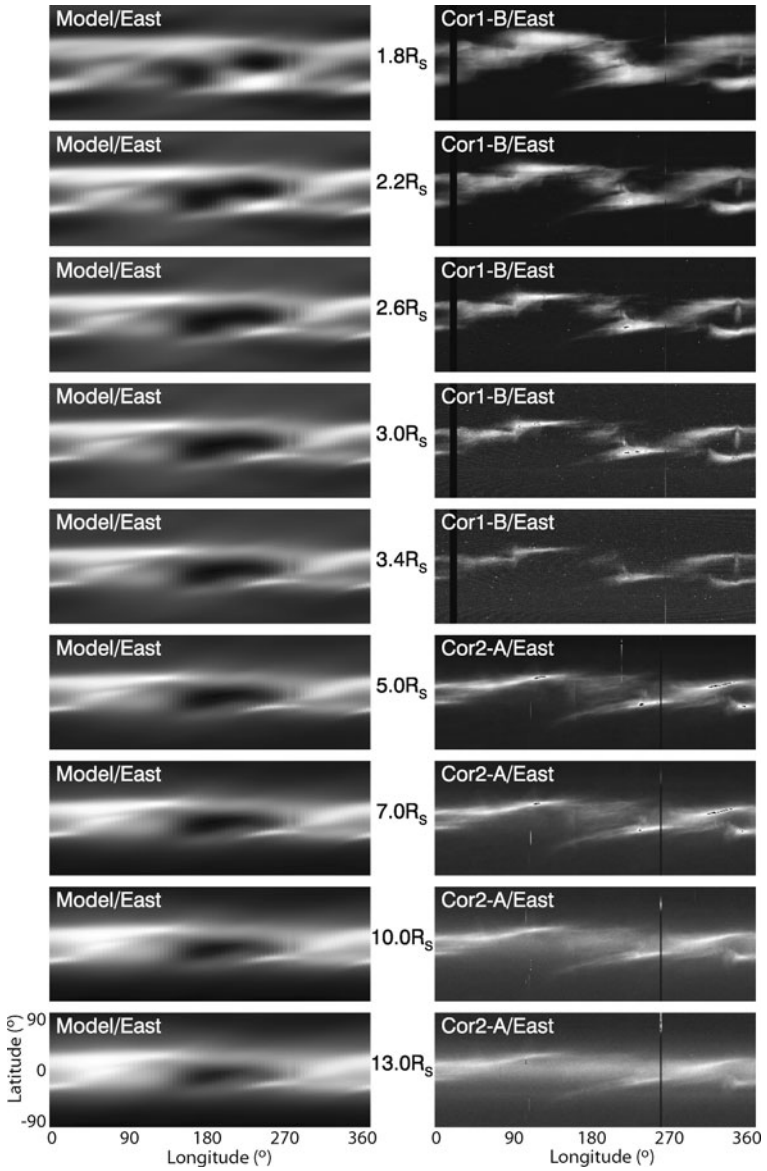

Figure 5 Comparison of model results with white light synoptic maps from COR1 and COR2 instruments on board STEREO A and B spacecraft. The images were assembled from east limb observations and have been arbitrarily scaled to bring out the structure contained within each.

locations (the southern extension and an equatorial coronal hole at $\approx 240°$ longitude. Finally, if we assume that the boundary between 360° and 0° longitude is periodic, that is, that the large-scale structure from 2059 through 2061 did not change appreciably, then the slow and essentially mono-polarity wind from 300° through 40° contains plasma from two distinct equatorial coronal holes, both with negative polarity.

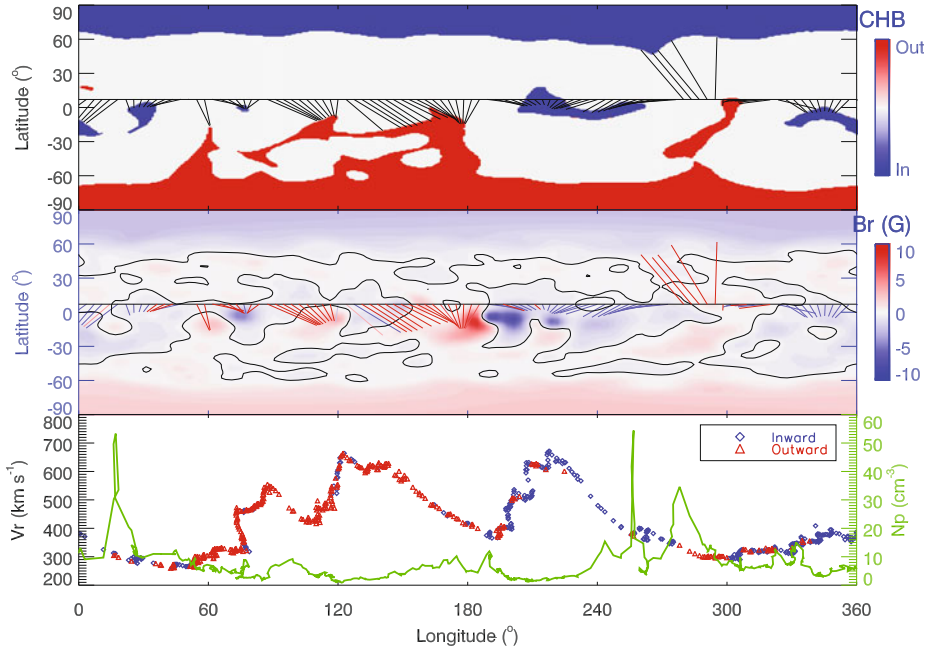

Figure 6 (Top) Coronal holes for CR 2060 computed from the MHD solution and color-coded according to the observed underlying photospheric magnetic field. The trajectory of the ACE spacecraft is superimposed, together with the mapped source regions of the plasma measured at ACE. (Middle) Photospheric magnetic field (color contours), location of the neutral line (black line), and mapped source regions of ACE measurements color-coded according to the observed *in-situ* polarity of the magnetic field embedded in the plasma. (Bottom) Ballistically mapped ACE speed (red/blue) and plasma density (green). The speed has been color–coded according to the measured polarity of the *in-situ* magnetic field.

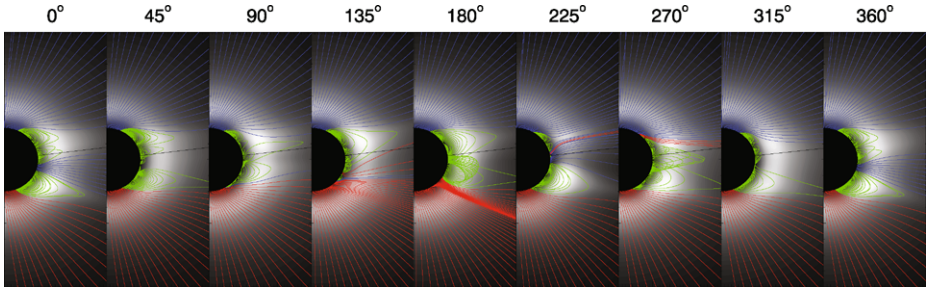

Figure 7 (Top) Selection of meridional slices of *pB* with field lines superimposed, equally spaced in longitude. Field lines colored blue (red) open into the heliosphere and are inward (outward), while field lines drawn in green are closed. The sold black line indicates the latitude of the ACE spacecraft during this interval.

In Figure 7, we have computed polarized brightness (*pB*) and overlaid field lines at a selection of Carrington longitudes. Field lines colored red/blue are open and directed outward/inward. Field lines that are colored green are closed, that is, they attach back to the Sun at both ends. Also shown is the latitude of the ACE spacecraft, which changed only modestly during the 25.38 days. These frames roughly match with the x-axis in Figure 6. We can identify two clear unipolar structures. First during the last 30° and first 30° of the

rotation, a large unipolar streamer is present off the northwest limb. A much more compact unipolar streamer is also seen at $\approx 225°$. Based on ACE's latitude during this interval, we can infer that it missed the compact unipolar streamer but likely sampled and spent a significant amount of time within the major one. In fact, it is possible that the density enhancement labeled 'A' in Figure 6 (bottom panel) is a direct measurement of the HPC associated with this unipolar streamer. In contrast, the density enhancement labeled 'B' is more likely a signature of the SI, separating the fast stream to the left from the slow stream to the right. Finally, event 'C' is probably a crossing of the HCS embedded within a HPS.

4. Model Predictions of Solar Wind Speed from Unipolar Streamers

Armed with an understanding of the basic stream structure measured by ACE and its likely connectivity with structure back at the Sun, we turn our attention to the question of what the WS and DCHB models predict for the structure of the solar wind at Earth during this time period. Panels (a) and (b) in Figure 8 compare velocity maps at $30R_{\odot}$ computed from the WS and DCHB prescriptions. Several points are readily apparent. First, both models match at latitudes away from the "band of solar wind variability," that is, from deep within the polar coronal holes. Second, following the trace of the HCS (white line in (a) and black line in (b)), both models predict slow solar wind. However, the band over which this slow wind exists is extremely thin ($\approx \pm 1°$) for the WS model. In contrast, the HCS-associated band in the DCHB model is $\approx \pm 10°$. Third, where the two models differ most significantly is at the "conjugate" latitudinal point, that is, a trace in longitude that very roughly follows the negative value of the HCS. Of particular note is the spur branching off from the HCS at 200° longitude in the northern hemisphere and merging back into the vicinity of the HCS at $\approx 300°$. Whereas in the DCHB model this is a slow-flow region flanking faster flow from a coronal hole, in the WS model, the spur consists of wind traveling even faster than flow from deep within polar coronal holes. Importantly, and fortuitously, this spur is positioned such that ACE became immersed within it by $\approx 240°$.

The ACE trajectory through these velocity profiles have been extracted and compared with ACE *in-situ* measurements in panels (c) and (d) of Figure 8. In panel (c), the ACE data have been ballistically mapped back to $30R_{\odot}$ to compare with the model results. In panel (d), the model results have been mapped from the Sun to 1 AU using the technique described by Riley *et al.* (2011).

Thus, the two comparisons in (c) and (d) are both limited in that there are assumptions in taking one dataset in or out to the location of the other. However, with this in mind, both views are also useful for interpreting the data, and the differences between the comparisons can be used to estimate the potential errors introduced by each mapping technique. Note further that the streams migrate to the left from $30R_{\odot}$ to 1 AU, since we are using Carrington coordinates. Here, we focus on the high-speed stream centered at $\approx 220°$ in panel (c) or $\approx 180°$ in panel (d), and the remaining portion of the interval. While both the WS and DCHB models reproduce the basic structure of this stream (and the earlier one to the left), they differ significantly in their prediction of the wind following it. The WS model, as we have shown, predicts extremely fast wind from unipolar streamer regions, in which the spacecraft was immersed in during this interval. We have computed speed profiles using a range of free parameters in Equation (1), but the results remain unaltered: the original WS model predicts very fast wind from the slowly expanding field lines surrounding unipolar streamers (Wang, Sheeley, and Rich, 2007; Wang *et al.*, 2010). On the other hand, and by construction, the DCHB predicts slow (and dense) solar wind emanates from the boundary of any type of

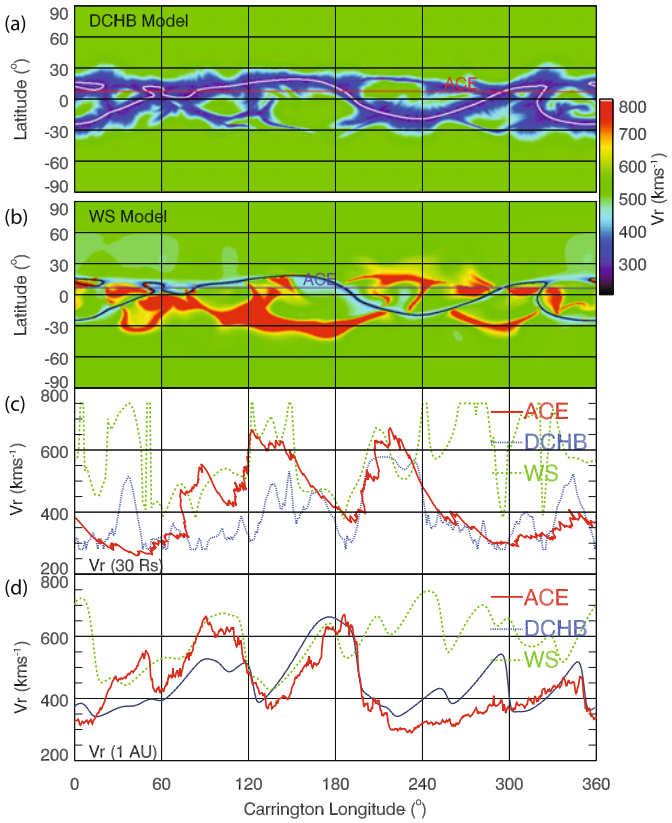

Figure 8 (a) Solar wind speed map at $30R_{\odot}$ produced by the DCHB model. Superimposed are: *i*) The HCS (white curve); and *ii*) the trajectory of the ACE spacecraft (red). (b) Solar wind speed map at $30R_{\odot}$ produced from the WS model. The HCS and ACE trajectory as also shown as black traces. (c) Solar wind speed at $30R_{\odot}$ as determined from: *i*) ballistically mapping ACE it in-situ measurements back from 1 AU (red, solid); *ii*) extracting from the DCHB model (blue, dotted); and *iii*) extracting from the WS model (green, dashed). (d) Solar wind speed at 1 AU. Both the DCHB and WS model results were 'evolved' using the technique described by Riley *et al.* (2011).

streamer structure. The origin of these flows can be traced back to the relevant parameters d and f_s in Figure 4. Comparison with ACE measurements suggest a prolonged interval of slow solar wind, consistent with the predictions of the DCHB model.

It is also worth noting that the high-speed stream that appears at 200° has very different origins in the DCHB and WS prescriptions. In the former, the spacecraft is immersed in an equatorial coronal hole for $\approx 40°$ (see Figure 6), whereas the high-speed wind in the WS profile is produced by the unipolar streamer.

A final point worth noting from Figure 8 is the richness in the variability of the slow-flow band. Considering the smoothing and filtering of the input magnetogram, it is quite remarkable that such complexity is produced. Of course, both because the solar wind tends to dampen out higher-frequency perturbations preferentially, and because the numerics of the code tend to do the same (through numerical diffusion), much of this structure is lost by 1 AU. It would be interesting to assess whether some or all of this fine-scale structure

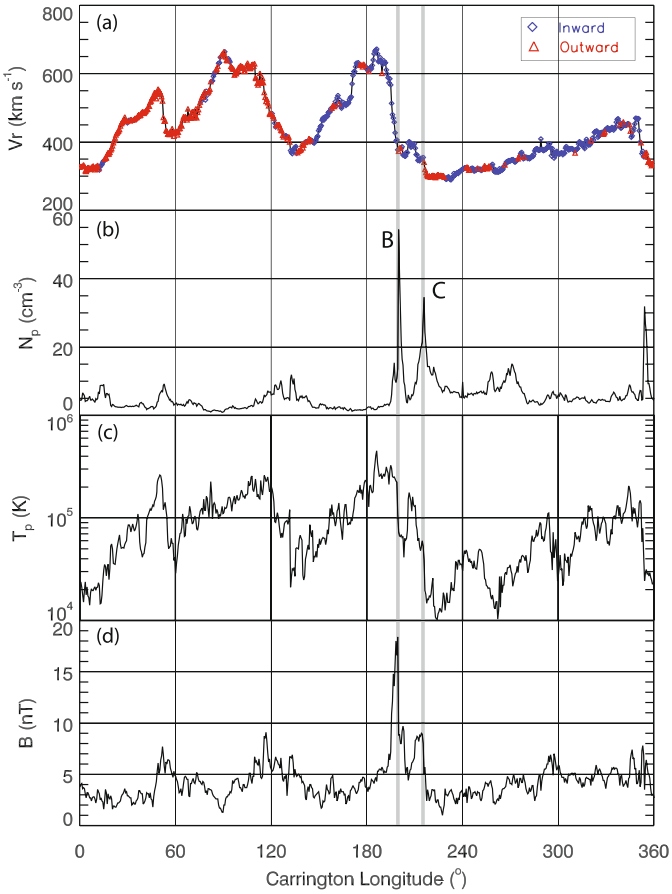

Figure 9 (a) Solar wind speed; (b) number density; (c) proton temperature; and (d) magnetic field strength as a function of Carrington longitude (at 1 AU) for Carrington rotation 2060. Two density enhancements, labeled 'B' and 'C,' are discussed in more detail in the text.

is real. As models become ever more capable of simulating smaller-scale phenomena, the computed results should retain more and more of this texture.

Finally, in Figure 9 we summarize solar wind speed, number density, proton temperature, and magnetic field strength for Carrington rotation 2060. Unfortunately, composition and charge state data during this interval were not available through the level 2 data products at the ACE Science Center. Two of the density enhancements from Figure 8 are also identified. Enhancement B, which showed a sharp rise of about one order of magnitude coincided with an abrupt drop in speed from the fast stream at $\approx 180°$ from the slower wind ahead. It is also coincident with a peak in magnetic field strength and a discontinuous drop in speed, signatures that are all consistent with an SI. The polarity of the field remains inward throughout the period surrounding enhancement B. In contrast, the density enhancement C is apparently associated with an albeit brief polarity change from inward to outward (with increasing longitude), but no significant change in speed. We suggest that this event is a crossing of the HPS and that there is a HCS embedded within it.

5. Summary and Discussion

In this study, we have used ACE *in-situ* measurements, in conjunction with a global MHD model of the solar wind to test a distinguishing prediction between two empirically based models, which in turn may reflect the basic features of two theories for the origin of the solar wind. Specifically, models relying on the expansion factor of the coronal field lines (EF models) predict that solar wind originating from unipolar (pseudo) streamers should be fast; perhaps even faster than wind originating deep within well-established, large polar coronal holes. In contrast, boundary layer models (such as the interchange reconnection model) predict that wind originating from the boundary between open and closed field lines should be slow, regardless of whether the underlying loop structure produces unipolar or dipolar streamers. Thus, we suggest that wind from unipolar streamers is slow, like wind from dipolar streamers. This is consistent with the basic premise of BL models, but in conflict with the EF model. Our analysis was possible because of a serendipitous confluence of three factors during CR 2060: *i*) there was no obvious transient activity; *ii*) well-developed unipolar streamers were present; and *iii*) ACE was positioned in latitude such that it could sample unipolar streamer wind directly.

Our results are in apparent disagreement with several aspects of the studies by Wang and colleagues. Wang, Sheeley, and Rich (2007) identified outflowing material, which they associated with a unipolar streamer, that was traveling at ≈ 200 km s^{-1} at $\approx 3 R_{\odot}$. By comparison, similar profiles from within dipolar streamers during the same interval showed speeds of ≈ 100 km s^{-1} at the same distance. However, this assumes that the outflows being measured are, in fact, fiduciaries of the ambient solar wind flow. Sheeley *et al.* (1997) has argued that these blobs are swept along "like leaves" by the ambient flow. Nevertheless, it is quite possible that they are propagating either faster or slower than the underlying quiescent flow.

Wang *et al.* (2010) identified what they claimed to be signatures of unipolar streamers in ACE *in-situ* measurements. One such case is event B in Figure 9. They argued that the high-density enhancement was a crossing of the HPS associated with the interplanetary extension of the unipolar streamer stalk. However, we have interpreted this, and other events identified by Wang *et al.* (2010) as SIs. Gosling *et al.* (1978) showed that SIs are interfaces that separate flow that was originally hot, tenuous, and fast with flow that was cooler, denser, and slower. Without exception, the events identified by Wang *et al.* (2010) occurred at the leading edges of high-speed streams, which would be expected to compress the plasma producing the density enhancement observed. Moreover, we believe the event labeled B in Figure 9, which occurred $\approx 15^{\circ}$ further in longitude, or ≈ 1.1 days preceding the SI is the HPS, and, the change in polarity coincident with it suggests that a current sheet was also crossed.

Our comparison between WS-derived speeds and 1 AU observations do not invalidate the results of Wang and colleagues (Wang and Sheeley, 1990; Wang, 1994; Wang *et al.*, 1997, 2010). Their comparisons are on such a large temporal scale (a single figure in their studies may include more than 30 years of data) that the patterns being matched represent only the grossest features of the system. Whether they predict the correct phase of even the existence of a specific high-speed stream within a single Carrington rotation cannot be determined. The WS model does predict the appearance of slow solar wind in the vicinity of the HCS, *i.e.*, associated with dipolar streamers, and thus, in the absence of unipolar streamers, it should be able to track the basic features of the slow solar wind. It is only because of the appearance of unipolar streamers in the recent solar minimum that the WS model appears to fail. It is worth emphasizing that although the WS predicts fast solar wind in the vicinity of unipolar streamers, in disagreement with observations, the underlying PFSS model used to

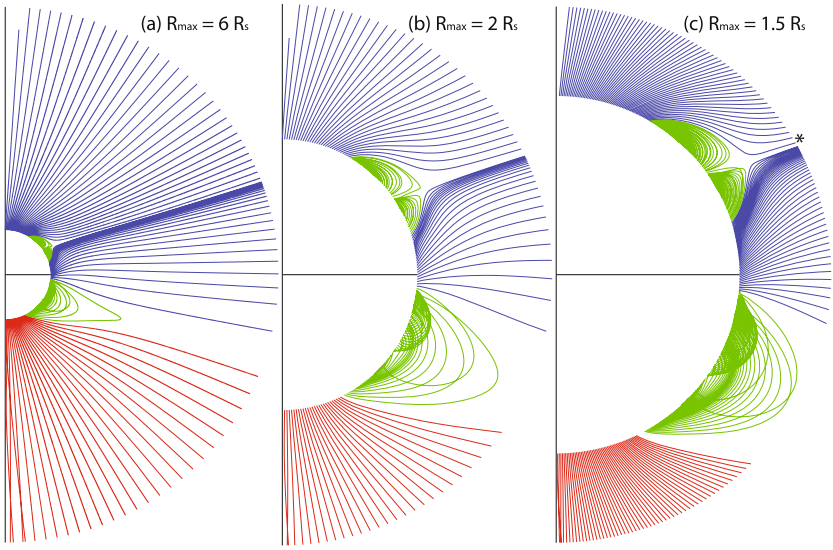

Figure 10 A selection of magnetic field lines for CR 2060 at a longitude of 215° are shown at successively smaller scales: (a) $R_{\max} = 6R_{\odot}$; (b) $R_{\max} = 2R_{\odot}$; and (c) $R_{\max} = 1.5R_{\odot}$. For (a) and (b), 185 field lines equally separated in latitude were drawn. For (c), 370 field lines were drawn. The apparently intersecting field lines is a projection effect due to field lines having different ending longitudes.

reconstruct the structure of the coronal magnetic field remains valid. For many applications, the PFSS technique is a useful and accurate tool (Riley *et al.*, 2006).

Although our results suggest that the WS and, in principle, the EF model, are in conflict with the observations of unipolar streamer structure in the solar wind, the relationship between the magnetic structure of the corona and expansion factor is more complex than has generally been appreciated (Figure 3). In Figure 10, we show three progressively more resolved views of the same meridional slice as in Figure 3. Although expansion factor typically increases with increasing height along a particular field line, such that f_s computed between the base ($r = 1R_{\odot}$) and some height sufficiently far from the Sun that the magnetic field lines are all radial (*e.g.*, $6R_{\odot}$) is a maximum value, for unipolar streamers this may not be the case. In particular, following the two field lines just poleward of the unipolar streamer stalk in panel (c) (marked with the asterisk), $f_s(r)$ first increases until $\approx 1.25R_{\odot}$ and subsequently decreases. Thus, computing f_s at some fixed height well above the base of the corona fails to capture this variation, and it is possible that theoretical models relying on large values of f_s to produce slow wind could be saved if this local structure is capable of modulating solar wind speed (Y.-M. Wang, private communication, 2011). Alternatively, issues with the empirically based WS model near unipolar streamers may be averted if the maximum value of f_s computed along each field line is used to compute solar wind speed, rather than its value relatively high in the corona. However, this remains to be investigated.

In closing, it is worth noting that our ability to differentiate between the two empirical models (WS and DCHB, and, by inference, the EF and BL theories) is based on the presence of unipolar streamer structure was facilitated by the unique properties of the current minimum. Our conclusions are based on a careful analysis of a single Carrington rotation. To substantiate them now requires a systematic statistical analysis of coronal stream structure and *in-situ* measurements both during the recent minimum and contrasting it with structure

from the earlier one (September 1996). Ultimately, these comparisons should lead to better-constrained empirical models of the ambient solar wind structure in the vicinity of Earth, and, hopefully, provide key constraints for theories of the origin of the slow solar wind.

Acknowledgements PR gratefully acknowledges the support of NASA's Causes and Consequences of the Minimum of Solar Cycle 24 program, the LWS Strategic Capabilities Program (NASA, NSF, and AFOSR), the NSF Center for Integrated Space Weather Modeling (CISM), NASA's Heliophysics Theory Program (HTP), and the STEREO IMPACT team. The authors would also like to thank the referee for valuable suggestions that significantly improved the quality of this paper. PR would also like to thank Dr. J. Americo Gonzalez-Esparza and the Universidad Nacional Autónoma de México (UNAM) for providing support and facilities while this study was being completed.

References

Antiochos, S.K., Mikić, Z., Titov, V.S., Lionello, R., Linker, J.A.: 2011, A model for the sources of the slow solar wind. *Astrophys. J.* **731**, 112. doi:10.1088/0004-637X/731/2/112.

Arge, C.N.: 2004, Working with the photospheric magnetic field observations from Mount Wilson, Wilcox, and Kitt Solar Observatories. AGU, Fall Meeting, SH52A-02.

Arge, C.N., Pizzo, V.J.: 2000, Improvement in the prediction of solar wind conditions using near-real time solar magnetic field updates. *J. Geophys. Res.* **105**, 10465. doi:10.1029/1999JA900262.

Arge, C.N., Odstrcil, D., Pizzo, V.J., Mayer, L.R.: 2003, Improved method for specifying solar wind speed near the Sun. In: Velli, M., Bruno, R., Malara, F., Bucci, B. (eds.) *Solar Wind Ten*, *AIP Conf. Proc.* **679**, 190. doi:10.1063/1.1618574.

Cranmer, S.R.: 2010, An efficient approximation of the coronal heating rate for use in global Sun-heliosphere simulations. *Astrophys. J.* **710**, 676. doi:10.1088/0004-637X/710/1/676.

Cranmer, S.R., van Ballegooijen, A.A., Edgar, R.J.: 2007, Self-consistent coronal heating and solar wind acceleration from anisotropic magnetohydrodynamic turbulence. *Astrophys. J. Suppl.* **171**, 520. doi:10.1086/518001.

Crooker, N.U., Huang, C., Lamassa, S.M., Larson, D.E., Kahler, S.W., Spence, H.E.: 2004a, Heliospheric plasma sheets. *J. Geophys. Res.* **109**, 3107. doi:10.1029/2003JA010170.

Crooker, N.U., Kahler, S.W., Larson, D.E., Lin, R.P.: 2004b, Large-scale magnetic field inversions at sector boundaries. *J. Geophys. Res.* **109**, 3108. doi:10.1029/2003JA010278.

Farrell, P.: 2011, New space weather forecasting model going operational with National Weather Service. www.bu.edu/cas/news/press-releases/cism/.

Fisk, L.: 1996, Motion of the footpoints of heliospheric magnetic field lines at the Sun: Implications for recurrent energetic particle events at high heliographic latitudes. *J. Geophys. Res.* **101**, 15547. doi:10.1029/96JA01005.

Gosling, J.T., Asbridge, J.R., Bame, S.J., Feldman, W.C.: 1978, Solar wind stream interfaces. *J. Geophys. Res.* **83**, 1401. doi:10.1029/JA083iA04p01401.

Gosling, J.T., Asbridge, J.R., Bame, S.J., Feldman, W.C., Borrini, G., Hansen, R.T.: 1981, Coronal streamers in the solar wind at 1 AU. *J. Geophys. Res.* **86**, 5438. doi:10.1029/JA086iA07p05438.

Hakamada, K., Akasofu, S.: 1981, A cause of solar wind speed variations observed at 1 AU. *J. Geophys. Res.* **86**, 1290. doi:10.1029/JA086iA03p01290.

Hundhausen, A.J.: 1972, *Coronal Expansion and Solar Wind*, Springer, New York, 7.

Laming, J.M.: 2004, On collisionless electron-ion temperature equilibration in the fast solar wind. *Astrophys. J.* **604**, 874. doi:10.1086/382066.

Lionello, R., Riley, P., Linker, J.A., Mikić, Z.: 2005, The effects of differential rotation on the magnetic structure of the solar corona: magnetohydrodynamic simulations. *Astrophys. J.* **625**, 463. doi:10.1086/429268.

Liu, Y.C.M., Galvin, A.B., Popecki, M.A., Simunac, K.D.C., Kistler, L., Farrugia, C., Lee, M.A., Klecker, B., Bochsler, P., Luhmann, J.L., Jian, L.K., Moebius, E., Wimmer-Schweingruber, R., Wurz, P.: 2010, Proton enhancement and decreased O^{6+}/H at the heliospheric current sheet: implications for the origin of slow solar wind. In: *Twelfth International Solar Wind Conference*, *AIP Conf. Proc.* **1216**, 363. doi:10.1063/1.3395875.

Neugebauer, M., Snyder, C.W.: 1962, Solar plasma experiment. *Science* **138**, 1095. doi:10.1029/2004JA010456.

Neugebauer, M., Liewer, P.C., Goldstein, B.E., Zhou, X., Steinberg, J.T.: 2004, Solar wind stream interaction regions without sector boundaries. *J. Geophys. Res.* **109**, 10102.

Riley, P., Linker, J.A., Mikić, Z.: 2001, An empirically-driven global MHD model of the corona and inner heliosphere. *J. Geophys. Res.* **106**, 15889. doi:10.1029/2000JA000121.

Riley, P., Linker, J.A., Mikić, Z., Lionello, R., Ledvina, S.A., Luhmann, J.G.: 2006, A comparison between global solar magnetohydrodynamic and potential field source surface model results. *Astrophys. J.* **653**, 1510. doi:10.1086/508565.

Riley, P., Lionello, R., Linker, J.A., Mikic, Z., Luhmann, J., Wijaya, J.: 2011, Global MHD modeling of the solar corona and inner heliosphere for the Whole Heliosphere Interval. *Solar Phys.* **145**. doi:10.1007/s11207-010-9698-x.

Sarabhai, V.: 1963, Some consequences of nonuniformity of solar wind velocity. *J. Geophys. Res.* **68**, 1555. doi:10.1029/JZ068i005p01555.

Sheeley, N.R., Wang, Y.M., Hawley, S.H., Brueckner, G.E., Dere, K.P., Howard, R.A., Koomen, M.J., Korendyke, C.M., Michels, D.J., Paswaters, S.E., Socker, D.G., St. Cyr, O.C., Wang, D., Lamy, P.L., Llebaria, A., Schwenn, R., Simnett, G.M., Plunkett, S., Biesecker, D.A.: 1997, Measurements of flow speeds in the corona between 2 and 30 R_{Sun}. *Astrophys. J.* **484**, 472. doi:10.1086/304338.

Sonett, C.P., Colburn, D.S.: 1965, The SI^{+}–SI^{-} pair and interplanetary forward-reverse shock ensembles. *Planet. Space Sci.* **13**, 675. doi:10.1016/0032-0633(65)90046-2.

Suess, S.T., Ko, Y.K., von Steiger, R., Moore, R.L.: 2009, Quiescent current sheets in the solar wind and origins of slow wind. *J. Geophys. Res.* **114**, A04103. doi:10.1029/2008JA013704.

Uzzo, M., Ko, Y.K., Raymond, J.C., Wurz, P., Ipavich, F.M.: 2003, Elemental abundances for the 1996 streamer belt. *Astrophys. J.* **585**, 1062. doi:10.1086/346132.

Wang, Y.M.: 1994, Two types of slow solar wind. *Astrophys. J. Lett.* **437**, L67. doi:10.1086/187684.

Wang, Y.M., Sheeley, N.R.: 1990, Solar wind speed and coronal flux-tube expansion. *Astrophys. J.* **355**, 726. doi:10.1086/168805.

Wang, Y.M., Sheeley, N.R.: 1997, The high-latitude solar wind near sunspot maximum. *Geophys. Res. Lett.* **24**, 3141. doi:10.1029/97GL53305.

Wang, Y.M., Sheeley, N.R.: 2003, The solar wind and its magnetic sources at sunspot maximum. *Astrophys. J.* **587**, 818. doi:10.1086/368302.

Wang, Y.M., Hawley, S.H., Sheeley, N.R.: 1996, The magnetic nature of coronal holes. *Science* **271**, 464. doi:10.1126/science.271.5248.464.

Wang, Y.M., Sheeley, N.R., Rich, N.B.: 2007, Coronal pseudostreamers. *Astrophys. J.* **658**, 1340. doi:10.1086/511416.

Wang, Y., Ko, Y., Grappin, R.: 2009, Slow solar wind from open regions with strong low-coronal heating. *Astrophys. J.* **691**, 760. doi:10.1088/0004-637X/691/1/760.

Wang, Y.M., Sheeley, N.R., Phillips, J.L., Goldstein, B.E.: 1997, Solar wind stream interactions and the wind speed–expansion factor relationship. *Astrophys. J. Lett.* **488**, L51. doi:10.1086/310918.

Wang, Y.M., Robbrecht, E., Rouillard, A.P., Sheeley, N.R., Thernisien, A.F.R.: 2010, Formation and evolution of coronal holes following the emergence of active regions. *Astrophys. J.* **715**, 39. doi:10.1088/0004-637X/715/1/39.

Winterhalter, D., Smith, E.J., Burton, M.E., Murphy, N., McComas, D.J.: 1994, The heliospheric plasma sheet. *J. Geophys. Res.* **99**, 6667. doi:10.1029/93JA03481.

Appendix K

Ensemble Modeling of the Ambient Solar Wind

Riley, P., Linker, J. A., and Mikić, Z.

Published in Solar Wind 13, 2012.

JOURNAL OF GEOPHYSICAL RESEARCH: SPACE PHYSICS, VOL. 118, 600–607, doi:10.1002/jgra.50156, 2013

On the application of ensemble modeling techniques to improve ambient solar wind models

Pete Riley,[1] Jon A. Linker,[1] and Zoran Mikić[1]

Received 24 September 2012; revised 19 December 2012; accepted 25 January 2013; published 25 February 2013.

[1] Ensemble modeling is a method of prediction based on the use of a representative sample of possible future states. Global models of the solar corona and inner heliosphere are now maturing to the point of becoming predictive tools; thus, it is both meaningful and necessary to quantitatively assess their uncertainty and limitations. In this study, we apply simple ensemble modeling techniques as a first step towards these goals. We focus on one relatively quiescent time period, Carrington rotation 2062, which occurred during the late declining phase of solar cycle 23. To illustrate and assess the sensitivity of the model results to variations in boundary conditions, we compute solutions using synoptic magnetograms from seven solar observatories. Model sensitivity is explored using (1) different combinations of models, (2) perturbations in the base coronal temperature (a free parameter in one of the model approximations), and (3) the spatial resolution of the numerical grid. We present variance maps, "whisker" plots, and "Taylor" diagrams to summarize the accuracy of the solutions and compute skill scores, which demonstrate that the ensemble mean solution outperforms any of the individual realizations. Our results provide a baseline against which future model improvements can be compared.

Citation: Riley, P., J. A. Linker, and Z. Mikić (2013), On the application of ensemble modeling techniques to improve ambient solar wind models, *J. Geophys. Res. Space Physics*, *118*, 600–607, doi:10.1002/jgra.50156.

1. Introduction

[2] Since their modest beginnings in the late 1960's [*Hundhausen and Gentry*, 1968], numerical approaches for studying the structure of the solar corona and inner heliosphere have blossomed into sophisticated 3-D, time-dependent, massively parallel, and necessarily complex models [e.g., *Downs et al*., 2011; *Riley et al*., 2012a]. As the models evolved and proliferated over the years, being applied to different scientific questions, they have diverged from one another, emphasizing different observations and relevant physics. The Hybrid Heliospheric Modeling System with Pickup Protons (HHMS-PI) model, for example, combines a magnetohydrodynamic (MHD) model of the solar wind [*Detman et al*., 2006] with a numerical description of pickup protons from neutral hydrogen [*Intriligator et al*., 2012]. Our global model, CORHEL (corona-heliosphere), couples a range of coronal models each driven by the observed line-of-sight photospheric magnetic field, with several solar wind models to compute the 3-D structure of the inner heliosphere [*Riley et al*., 2012a].

[3] With the notable exception of the operational version of the Wang-Sheeley-Arge (WSA)-Enlil model (www.bu.edu/cas/news/press-releases/cism/), global solar and heliospheric models share a basic common goal: to understand the physical processes responsible for the solar wind we observe at 1 AU and elsewhere. In other words, they are science-based models, not operational tools. However, as these models have matured over the last 45 years, they have transitioned from simple tools allowing us to understand fundamental processes to being able to accurately reproduce (at least under some conditions) solar wind conditions near earth. As such, they are poised to transition into predictive models, and it appears timely and appropriate to assess the quality and robustness of these solutions.

[4] Initial assessments of solar wind model solutions came in the form of visual comparisons of observed and modeled time series [e.g., *Riley et al*., 2001]. More recently, studies have attempted to find usable metrics to estimate the quality of the solution. For example, *Owens et al*. [2008] computed mean square errors (MSEs) and correlation coefficients (CCs) over an 8 year period for a combination of solar and heliospheric models. They also considered an event-based approach to model validation by tracking the timing of high-speed streams. In addition to emphasizing a parameter that is of high interest to space weather forecasters, such a metric also avoids the problem that relatively small offsets in the arrival of high-speed streams can a disproportionate effect on the statistical skill score produced by MSEs or CCs.

[5] Thus far, "ensemble" modeling techniques have only been applied to global heliospheric problems in a rudimentary way. By way of illustration, we provide three examples.

[1]Predictive Science, San Diego, California, USA.

Corresponding author: P. Riley, Predictive Science, 9990 Mesa Rim Road, Suite 170, San Diego, CA 92121, USA.
(pete@predsci.com; linkerj@predsci.com; mikicz@predsci.com)

2169-9380/13/10.1002/jgra.50156

First, our group regularly computes several ambient coronal and heliospheric solutions for each Carrington rotation (CR) [*Riley et al*., 2012b]. Each solution is driven by a synoptic map derived from one of up to seven solar observatories, and the predicted *in situ* measurements at 1 AU can vary substantially. Second, *Jian et al*. [2011] compared the output from a handful of global heliospheric runs in which the input synoptic magnetogram, the coronal model, and even the version of the model were varied, finding that while there was a notable improvement from use of the latest models, it was difficult to determine which combination of synoptic map/coronal model was superior. And third, *Lee et al*. [2012] studied the 15 February 2011 halo CME by constructing an "ensemble" of solutions by (1) varying the input parameters for the WSA-Enlil cone model and (2) using several input synoptic magnetograms. While these studies can be illustrative in pointing out the sensitivity of the solutions to the inputs and free parameters, they provide no rigorous or quantitative feedback for improving the solutions. Because of this, it is probably misleading to associate the term "ensemble" with these types of investigations, which are perhaps better described more generically as parametric studies (Even a basic definition of "ensemble" goes beyond a mere collection or group of objects. It refers to a group of complementary parts that contribute to a single effect, such as an "ensemble" of musicians).

[6] Ensemble forecasting is more rigorously defined as a method of prediction that relies on the use of a representative sample of possible future states to derive a prediction. One of the appealing aspects of such an approach is that it offers a rigorous method for computing confidence bounds of the solution by estimating the uncertainty in the ensemble [*Wilks*, 2006]. Moreover, the mean of the ensemble of forecasts is or should be more accurate than the forecast from any individual member, the reason being that the random or unpredictable regions of the forecast tend to cancel one another while the aspects of the forecast that the majority of the models agree on are not removed [*Warner*, 2010]. In its simplest interpretation, ensemble modeling is essentially a method of nonlinear filtering [*Wilks*, 2006]. A further feature of ensemble forecasting is that the probability distribution function of a variable can be used to infer information about more extreme events.

[7] For terrestrial weather forecasting, the uncertainty in the solutions can be divided into two main causes. The first is due to imperfect initial conditions. Unlike the Earth's lower atmosphere, however, small errors in the initial conditions in the solar corona are not likely to cause a substantial divergence of the solutions. Thus, the proverbial butterfly flapping its wings in the corona will, at worst, be fried to a crisp, and the remains convected out into the solar wind. Our "initial condition" issue then is replaced by a "boundary condition" problem. Specifically, the use of line-of-sight magnetograms from different solar observatories can lead to substantially different solutions [*Riley et al*., 2012a].

[8] The second source of errors can be termed "model formalism." This includes the physical processes that are included in the algorithms, as well as the parameterization of the model. For example, coronal models typically rely on either Potential Field Source Surface (PFSS) or MHD approximations, which have unique advantages and disadvantages [*Riley et al*., 2006]. Additionally, time-dependent effects can also alter coronal structure through field shear and twist. These effects cannot be captured by PFSS models or even equilibrium MHD models, instead requiring a time-dependent solution driven by evolving photospheric magnetic fields [*Riley et al*., 2006]. Finally, different sets of free parameters must be specified within each [*Riley and Luhmann*, 2012].

[9] In this report, we compute a representative set of model realizations for one relatively quiescent time period (CR 2062) to introduce and explore the utility of applying ensemble modeling techniques to global solar and heliospheric numerical models. These are tentative first steps, which we hope will lay the foundation for more comprehensive studies in the future.

2. Modeling Approach

[10] The process of generating a global solution describing the plasma and magnetic field properties of the corona and inner heliosphere is relatively complicated. Figure 1 illustrates the main decisions one must make if using the CORHEL global coronal and heliospheric modeling suite [*Riley et al*., 2012a]. One first chooses a synoptic map derived from observations by one of seven solar observatories. These raw maps must then be processed to provide sufficiently robust radial magnetic field boundary conditions for the model. The procedure involves smoothing the maps, balancing the flux, and extrapolating observed mid-latitude fields to the poorly or even completely obscured polar regions, a process that can significantly impact the solutions [*Riley et al*., 2012a]. Next, one chooses a particular coronal model. Currently, the choices are a PFSS model and one of two types of MHD models. In the simpler polytropic MHD algorithm, the energy equation is replaced by a polytropic relationship, and γ is set to 1.05. The resulting solutions are relatively accurate in terms of the large-scale structure of the magnetic field but inaccurate with respect to the properties of the plasma. In contrast, the thermodynamic MHD approach, while computationally more challenging, yields much more accurate plasma properties. These solutions can then be used to drive, either directly or indirectly, a heliospheric model. Here we show two possible models: Enlil and MAS (Magnetohydrodynamics Algorithm outside a Sphere). We do not believe that this portion of the modeling chain is particularly sensitive to the type of model used, and in fact, to these options, we could add an even simpler mapping technique to evolve the plasma and field from $30R_S$ to 1 AU [*Riley and Lionello*, 2011]. Associated with each model are a distinct set of free parameters. In the polytropic MHD approach, for example, we are free to specify the plasma temperature and density at the base of the corona. Resolution of the solution too is effectively a free parameter of the model but one that the results should not be sensitive to.

3. Modeling Results

[11] To illustrate the concepts of ensemble modeling, as applied to the ambient structure of the solar wind, we computed $\sim$ 40 realizations using the CORHEL model suite. For each one, we chose to vary (1) the input synoptic magnetogram (GONG, MDI, MWO, SOLIS, or WSO),

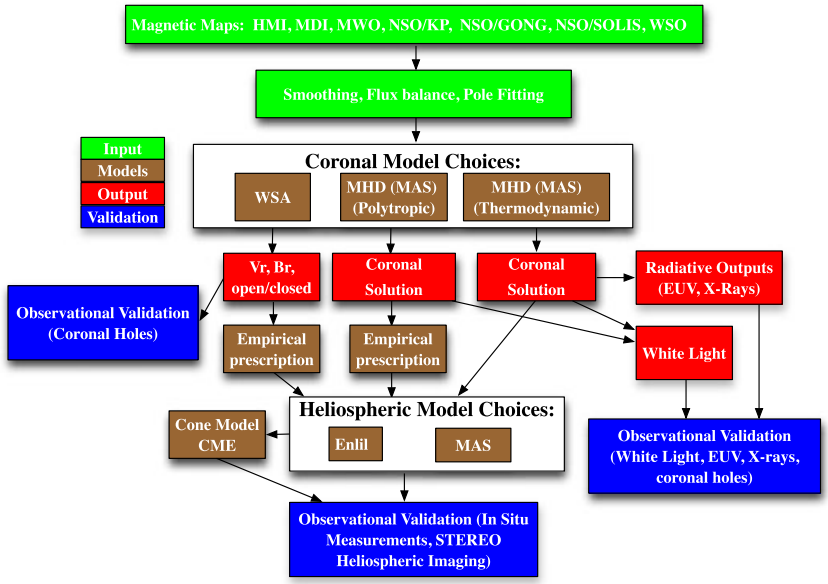

Figure 1. A schematic illustrating how a typical global coronal/heliospheric ambient solution is constructed. Model inputs are shown in green, the models are shown in brown, the output from the models (which is, in some scenarios, also an input into the subsequent model) is shown in red, and the validation procedures are shown in blue.

(2) the coronal model (MAS or WSA/PFSS), (3) the base temperature (1.8×10^6K or 2.5×10^6K), and (4) the spatial resolution ($101 \times 100 \times 128$ or $201 \times 150 \times 256$). In practice, of course, there are an almost limitless number of choices that could be varied, leading to a potentially intractable number of solutions. We chose this limited set because we believe the model results are relatively sensitive to them and they illustrate the essential features of ensemble modeling techniques. An additional pragmatic constraint is that ensemble modeling of the global solar wind can be computationally expensive. Our higher-resolution simulations typically require $\sim$ 25,000 h of Central Processing Unit (CPU) time on either NASA's Pleiades or NSF's Ranger supercomputers. Thus, ensemble modeling techniques can, in principle, quickly consume a large fraction of our yearly allocation.

[12] A selection of realizations for CR 2062 is summarized in Figure 2. These maps show solar wind speed at $30R_S$ as a function of longitude (x axis) and latitude (y axis). The panel titles summarize the parameters that were modified. In particular, we (1) used magnetograms from GONG, MDI, MWO, SOLIS, and WSO; and (2) constructed solutions using both our MHD coronal model (MAS) and the WSA/PFSS model. These two models represent more than just different numerical approaches. In addition to different assumptions, such as the existence of a source surface, they incorporate two distinct ideas for the origin of the solar wind [*Riley and Luhmann*, 2012] and so produce different values of the bulk solar wind speed at the inner boundary of the heliospheric model. The solutions are, at least superficially, similar: fast solar wind at high latitudes and slower wind organized about the heliomagnetic equator. Beyond this, however, there are some notable differences. First, the structure of the band of slow wind differs dramatically from one model to another. The WSA solutions, for example, do not tend to produce slow-flow arcs that split from the main slow-flow band and then rejoin. In fact, they predict the opposite: wind that is faster than that predicted from deep within polar coronal holes. These regions are associated with pseudo (or unipolar) streamers, and one of the distinguishing features between the two ideas for the origin of the slow solar wind is whether plasma from these locations is fast [*Wang et al.*, 2007] or slow [*Riley and Luhmann*, 2012].

[13] Given these solutions, and with no *a priori* information about which is better or worse, we can estimate the variance between them and thus infer where the model solutions agree and disagree [*Epstein*, 1969]. Figure 3 summarizes the standard deviation (s.d., i.e., the square root of the variance) for CR 2062, using the realizations shown in Figure 2. The ensemble mean is also overlaid, but its interpretation is more difficult here and we defer a discussion of it until later. This presentation of the s.d. emphasizes several interesting points. First, away from the "band of solar wind variability," all realizations predict fast, quiescent solar wind, in agreement with Ulysses polar observations [e.g., *Riley et al.*, 1997] and the corresponding s.d. is effectively zero. Second, near the equator, the models agree best in an "island" extending from 60° to 240°, which traces the locus of the heliospheric current sheet (not shown). Third, the realizations disagree the most between $\sim$ 130° and 180° longitude at mid-southern heliographic latitudes. This maps back to the location of a pseudo streamer (Figure 2). Fourth, the degree to which the models differ is substantial: In many regions where near-Earth spacecraft would sample, the s.d. is of the order of $\sim$ 100 km s^{-1}.

[14] The information shown in Figure 2 can also be summarized in more detail for specific trajectories through the region. In Figure 4, we show the ensemble solution, that is, the average speed through the heliographic equator,

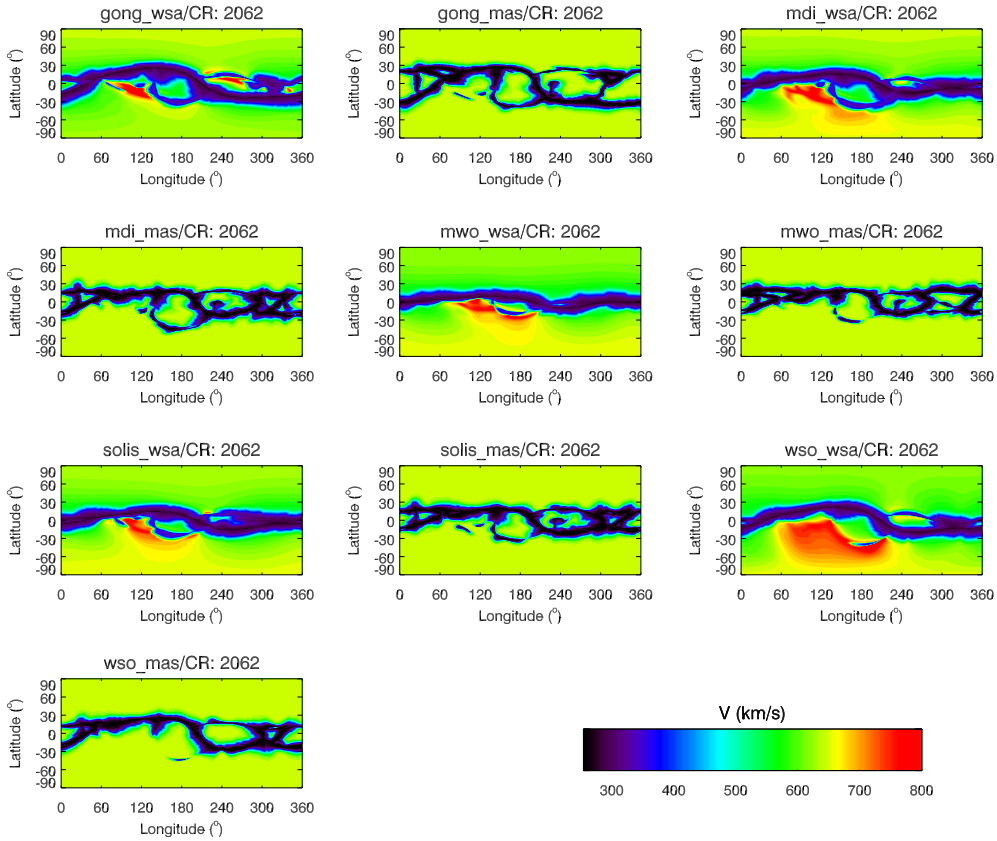

Figure 2. A subset of realizations computed for CR 2062 are shown as a function of longitude (*x* axis) and latitude (*y* axis). For each solution, either the input magnetogram (GONG, MDI, MWO, SOLIS, or WSO) or the coronal model (MAS or WSA) was varied.

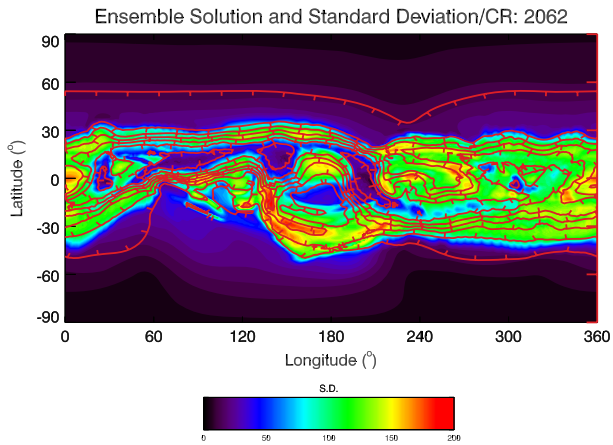

Figure 3. The ensemble mean (red contours) and standard deviation (color contours) for the realizations shown in Figure 2 as a function of Carrington longitude and heliographic latitude. The tick marks on each contour show the direction of decreasing speed.

together with various statistical information, which are explained in the figure caption. Of particular note is that the variance is lowest when the speed is lowest and highest when the speed is highest. (This is also apparent but more difficult to discern in Figure 3.) This makes intuitive sense: It is easier for models to agree when there is no structure, such as long periods of slow, or fast wind, but more difficult to predict the location (phase) of sharp stream fronts, that is, the boundaries between slow and fast wind. This is particularly true at stream interfaces, where fast wind is flowing into slower wind. At such locations, the gradient from slow to fast is sharp, and so small offsets in the location of this boundary will translate into large model variances.

4. Comparison With Observations

[15] Using the results from the heliospheric portion of the simulations, we can compare the ensemble solution with *in situ* measurements. Figure 5 compares in situ measurements (red) of the bulk solar wind speed as measured by the ACE spacecraft with the ensemble model solution (black) at 1 AU in the ecliptic plane. Again, the boxes with "whiskers" summarize the statistical properties of the realizations. We note that the ensemble model has captured the three streams (located between 0° and 240° longitude) but misses the region of prolonged low-speed wind from 240° to 360°. This is, we believe, an intrinsic limitation of using synoptic magnetograms to compute solutions that are fundamentally time-dependent phenomena. We note also that the individual realizations (not shown) displayed considerably more variation both in magnitude and phasing of the streams. Thus, one of the basic effects of ensemble averaging is to reduce the amplitude of the variations.

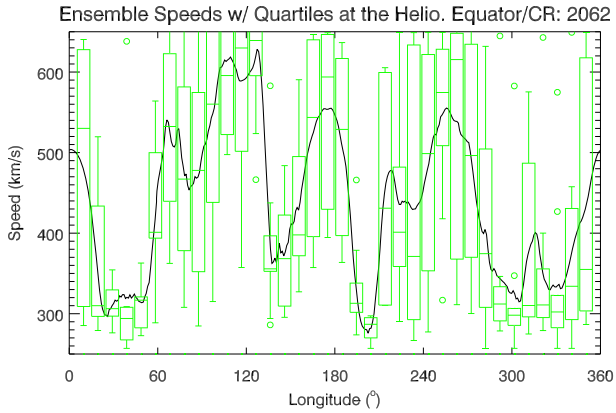

Figure 4. "Whisker" plot of model realizations from Figure 2 at $30R_S$ in the equatorial plane. The solid black line is the ensemble solution, and the green boxes with "whiskers" summarize the variability of the realizations. The median value is indicated by the short horizontal line, while the tops and bottoms of the boxes mark the 25th and 75th quantiles. The tips of the "whiskers" mark the maximum and minimum values. When these maxima are more than three sigma from the median, they are marked with an open circle.

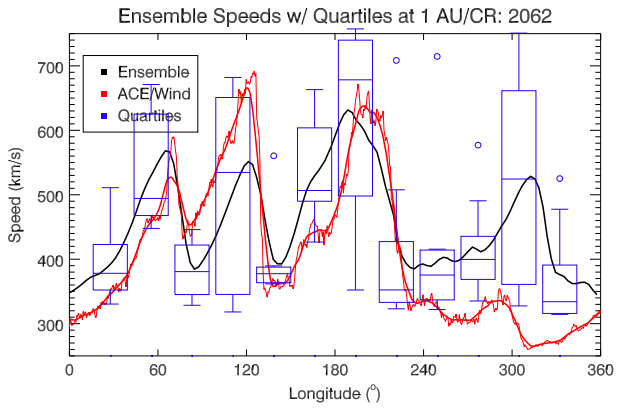

Figure 5. Comparison of ensemble model solution (black) with ACE *in situ* measurements (red; 1 h and 1 day averages). For details on interpreting the boxes with "whiskers," see Figure 4 caption.

[16] A simple technique for assessing the performance of each realization as well as the ensemble solution is to compute the root mean square error (RMSE) or difference between in situ measurements and the model results. Table 1 summarizes these values when compared with ACE measurements. The "persistence" model simply involves taking the observed average solar wind speed during the entire Carrington rotation and using this as the prediction of speed for the interval. Thus, strictly speaking, it is really just the standard deviation (s.d.) of the ACE measurements. It should also be noted that "persistence" in a meteorological sense typically refers to, say, a forecast that some future weather pattern will be the same as a pattern already observed. Our definition here, nevertheless, turns out to be a relatively stringent requirement; requiring that the model beat the s.d. of the observations is quite challenging. The results in Table 1 suggest that there are modest differences in the RMSEs from different observatories and that the RMSE for the ensemble solution is lower than any of the realizations, including persistence, which is of course encouraging. It is somewhat alarming that persistence appears to beat some of the individual realizations. However, it must be realized that phase offsets within what are otherwise good predictions (say, predicting all three streams but being offset by 12 h) can lead to large RMSEs. Additionally, and perhaps more importantly, the flat-line prediction of the "persistence" model has no useful predictive information: Predicting a large, fast stream, even only to within a day or so, has considerably more intrinsic scientific worth and, from an operational point of view, potentially more actionable value.

Table 1. Root Mean Square Errors for Model Realizations for CR 2062.

Magnetogram	Model	RMSE (km/s)
GONG	WS	47.7
GONG	MAS	73.8
MDI	WSA	39.5
MDI	MAS	50.8
MWO	WSA	44.2
MWO	MAS	63.1
SOLIS	WSA	42.9
SOLIS	MAS	43.4
WSO	WSA	37.9
WSO	MAS	56.6
	Ensemble	34.2
	Persistence/s.d.	41.1

5. Assessing Model Performance and Sensitivity: Taylor Diagrams

[17] Even the relatively limited number of realizations we have discussed here produces a considerable amount of data that can be difficult to digest and assess. To concisely summarize the degree to which the model results match observations across many realizations, *Taylor* [2001] developed what has come to be known as a "Taylor diagram," which combines correlation, centered RMSE, and variances.

[18] Figure 6 summarizes five high-resolution runs using the MAS model, driven by data from one of five solar observatories. The radial distance from the origin indicates standard deviation, while the angular direction shows correlation coefficient. The observations thus become a single point on the x axis (black diamond) since they are exactly correlated with themselves, and the model results (red diamonds) are distributed at various locations in this parameter space. Both the correlation of the model results with the data and the degree to which its variance matches the observations are key aspects for providing useful forecasts. Additionally, it turns out that when the correlation coefficient is displayed as its arc cosine, there is a simple geometric relationship between the centered RMSE, the s.d., and the correlation coefficient. (Note that the difference

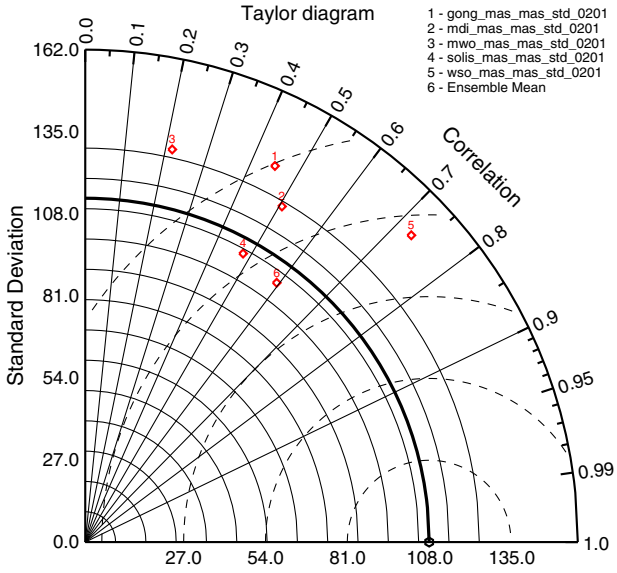

Figure 6. A "Taylor diagram" for summarizing the performance of model runs. The radial distance away from the origin gives the standard deviation of the model result (red diamonds) and data (black diamond). The correlation coefficient (R) between the data and the model result is shown by its azimuthal position. The scale increases as $cos^{-1}R$. The dashed partial circles centered on the black diamond mark contours of constant centered RMSE. See *Taylor* [2001] for further details.

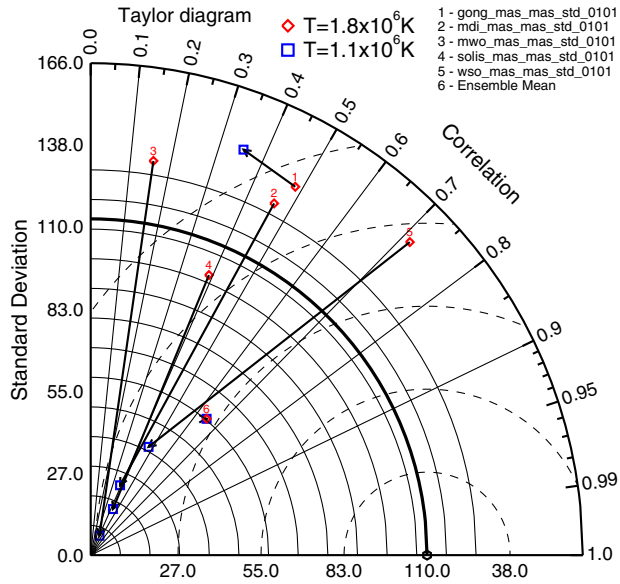

Figure 7. As in Figure 6 except that the blue squares mark the new locations of the solutions when the base temperature is dropped from 1.8×10^6K to 1.1×10^6K. The arrows connect each pair of solutions and show the change in performance that the temperature decrease induces.

between the centered RMSE and the RMSE in Table 1 is that in the former, prior to computing the RMSE, the average values of the data and model are first subtracted.) Specifically, contours of centered RMSE lie on circles centered around the observation point (dashed circles in Figure 6). Thus, the optimum model is the one that lies closed to the observation point, or, equivalently, on the smallest radial dashed circle. Solutions with high correlation coefficient, then, are penalized in this view if the s.d. is substantially smaller or larger than the s.d. of the observations. Model 4, for example, although having a lower correlation coefficient than model 2, provides a closer match in terms of variance and is thus arguably better. Similarly, the ensemble mean of these five cases produces a marginally better solution than the best individual realization (model 5), which has a higher correlation coefficient.

[19] Using the Taylor diagram, we can assess changes in the performance of a model resulting from modifications to it. For example, in Figure 7, we explore the effects of reducing the base coronal temperature in the polytropic MAS model from 1.8×10^6K to 1.1×10^6K, that is, a reduction by one third. We emphasize that this change is primarily to illustrate the application of ensemble modeling techniques: In reality, we do not believe such large changes would lead to solutions that are more consistent with either remote solar observations or in situ measurements. The red diamonds mark the reference solutions, and the blue squares mark the location of the new solutions, with the arrows connecting one to the other. Even without reviewing the individual time series, we can see that all variability

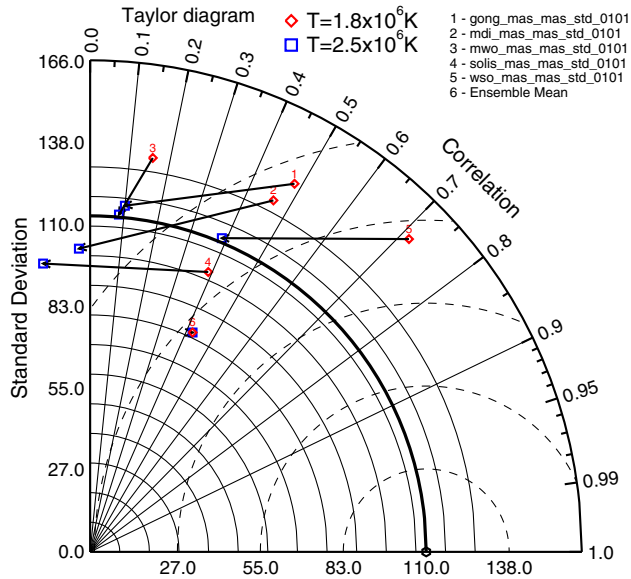

Figure 8. As in Figure 6 except that the blue squares mark the new locations of the solutions when the base temperature is raised from 1.8×10^6K to 2.5×10^6K. The arrows connect each pair of solutions and show the change in performance that the temperature increase induces.

in the solar wind solutions has been removed. Physically, we can understand this change as follows: By decreasing the coronal-base temperature, the thermal pressure of the plasma is reduced. Fewer magnetic field lines are opened up, which in turn causes more of the smaller equatorial coronal

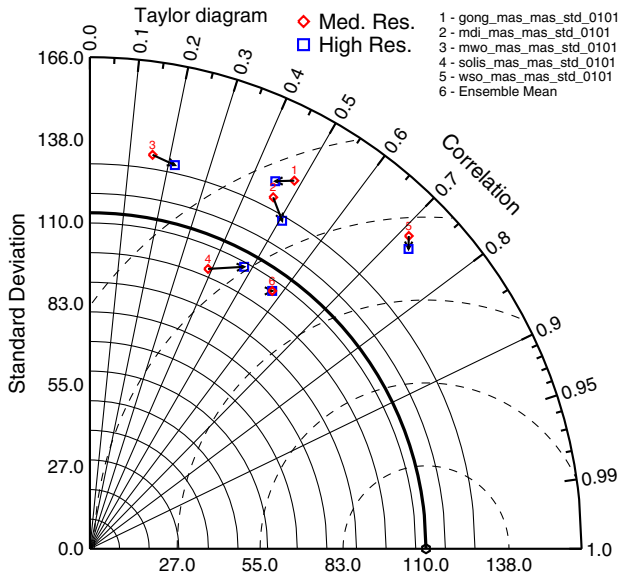

Figure 9. As in Figure 6 except that the blue squares mark the new locations of the solutions when the number of grid points in the model is increased from $101 \times 100 \times 128$ to $201 \times 150 \times 256$. The arrows connect each pair of solutions and show the direction that the change in resolution induces.

holes to close down. Thus, there are less fast streams at low latitudes penetrating the otherwise slower wind associated with the streamer belt, resulting in less variability in the speed of the wind there. It is worth noting, however, that at least on the basis of the centered RMSE, the solutions are no worse.

[20] Another possibility we can explore is an increase in temperature. Again, for the purposes of illustration, we increase the base temperature by one third, from 1.8×10^6K to 2.5×10^6K. This is summarized in Figure 8. Here there is a clear tendency for the solutions to become worse with a higher base temperature. More field lines are opened at lower latitudes, resulting in larger equatorial coronal holes. Slow wind still flows from the edges of open-closed field lines, however, so the variability of the wind is still maintained. The decrease in correlation results from the broadening and misalignment of high-speed streams.

[21] As a final example, in Figure 9, we show how the solutions change when the number of grid points in the simulation is increased from $101 \times 100 \times 128$ to $201 \times 150 \times 256$. Reassuringly, this change results in only a modest change in the performance of the solutions, suggesting that we can explore ensemble techniques at computationally feasible resolutions. In the future, however, as we constrain other, as yet poorly known free parameters, it may be necessary to evaluate the effects of less sensitive factors such as spatial resolution on the quality of the solutions.

6. Discussion

[22] In this report, we have applied some relatively simple terrestrial weather ensemble forecasting concepts to models of the ambient solar corona and inner heliosphere. Although there are some fundamental differences between the Earth's lower atmosphere and the Sun's corona, our results suggest that ensemble modeling techniques can be adapted and successfully applied to assess and improve the performance of global solar and heliospheric models. These are clearly "first steps," but ones that we believe lay a foundation from which more rigorous methods can be developed. We showed that at least for the time period analyzed and the models/parameters chosen, the ensemble prediction outperforms any of the individual realizations. Furthermore, using "Taylor" diagrams, we were able to assess the relative merits of each of the individual solutions as compared with the ensemble mean. Ultimately, it may be possible to implement these techniques at "third party" institutions, such as NASA's Community Coordinated Modeling Center (CCMC). This would allow users and developers to both track the intrinsic improvement within a single model and compare the relative strengths and weaknesses of different models.

[23] Our numerical "experiments" to estimate the sensitivity of the model results to both boundary conditions and model formalism suggest that substantial improvements in performance can be achieved by careful exploration of the relevant parameter space. Three substantial problems, however, pose significant and potentially long-term handicaps for improving the quality of the model solutions. First, our limited view of the Sun's poles forces us to either extrapolate mid-latitude, well-observed data poleward [*Riley et al.*, 2012a] or use flux transport models that attempt to reconstruct the polar regions using physical transport processes coupled with data assimilation [*Arge et al.*, 2010]. Second, our current reliance on synoptic maps (which are built up from daily observations taken over 25.38 days) as inner radial boundary conditions cannot be rigorously defended: The model implicitly assumes that this map is synchronic; that is, it is a snapshot of the surface of the photosphere at one point in time, which it clearly is not. Furthermore, because the first and last slices for each Carrington rotation are separated by more than 25 days, the model's requirement that the azimuthal boundary be periodic necessarily leads to artifacts. Third, our assumption that the Sun's structure does not change appreciably during the course of a solar rotation is an idealization that is not met in reality. Sequences of synchronic maps derived from flux transport models could be used to drive a time-dependent model of the ambient solar wind which may eliminate or at least mitigate all of these concerns. Ideally, of course, a "sentinels" mission consisting of a fleet of spacecraft, each carrying a magnetograph, which together could image the entire solar surface simultaneously, would provide the ultimate boundary conditions for global models. In reality, our first step towards realizing this vision may come from combining magnetograms obtained from Solar Orbiter (currently scheduled for launch in January 2017) with those from near-Earth space and/or ground-based observatories.

[24] **Acknowledgments.** The authors gratefully acknowledge the support of NASA (Causes and Consequences of the Minimum of Solar Cycle 24 program, LWS Strategic Capabilities program, Heliophysics Theory Program, and the STEREO IMPACT team) and NSF (Center for Integrated Space Weather Modeling (CISM) program).

References

Arge, C. N., C. J. Henney, J. Koller, C. R. Compeau, S. Young, D. MacKenzie, A. Fay, and J. W. Harvey (2010), Air force data assimilative photospheric flux transport (ADAPT) model, *Twelfth Int. Sol. Wind Conf.*, *1216*, 343–346, doi:10.1063/1.3395870.

Detman, T., Z. Smith, M. Dryer, C. D. Fry, C. N. Arge, and V. Pizzo (2006), A hybrid heliospheric modeling system: Background solar wind, *J. Geophys. Res.*, *111*, A07102, doi:10.1029/2005JA011430.

Downs, C., I. I. Roussev, B. van der Holst, N. Lugaz, I. V. Sokolov, and T. I. Gombosi (2011), Studying extreme ultraviolet wave transients with a digital laboratory: Direct comparison of extreme ultraviolet wave observations to global magnetohydrodynamic simulations, *Ap. J.*, *728*, 2, doi:10.1088/0004-637X/728/1/2.

Epstein, E. S. (1969), Stochastic dynamic prediction1, *Tellus*, *21*, 739–759.

Hundhausen, A. J., and R. A. Gentry (1968), The propagation of blast waves in the solar wind, *Astron. J.*, *73*, 63.

Intriligator, D. S., T. Detman, G. Gloecker, C. Gloeckler, M. Dryer, W. Sun, J. Intriligator, and C. Deehr (2012), Pickup protons: Comparisons using the three-dimensional MHD HHMS-PI model and Ulysses SWICS measurements, *J. Geophys. Res. Space Phys.*, *117*, A06104, doi:10.1029/2011JA017424.

Jian, L. K., C. T. Russell, J. G. Luhmann, P. J. MacNeice, D. Odstrcil, P. Riley, J. A. Linker, R. M. Skoug, and J. T. Steinberg (2011), Comparison of observations at ACE and Ulysses with Enlil model results: Stream interaction regions during Carrington rotations 2016–2018, *Sol. Phys.*, *273*, 179–203, doi:10.1007/s11207-011-9858-7.

Lee, C. O., C. N. Arge, D. Odstrčil, G. Millward, V. Pizzo, J. M. Quinn, and C. J. Henney (2012), Ensemble modeling of CME propagation, *Sol. Phys.*, p. 79, doi:10.1007/s11207-012-9980-1.

Owens, M. J., H. E. Spence, S. McGregor, W. J. Hughes, J. M. Quinn, C. N. Arge, P. Riley, J. Linker, and D. Odstrcil (2008), Metrics for solar wind prediction models: Comparison of empirical, hybrid, and physics-based schemes with 8 years of L1 observations, *Space Weather*, *6*, S08001, doi:10.1029/2007SW000380.

Riley, P., and R. Lionello (2011), Mapping solar wind streams from the Sun to 1 AU: A comparison of techniques, *Sol. Phys.*, pp. 575–592, doi:10.1007/s11207-011-9766-x.

Riley, P., and J. G. Luhmann (2012), Interplanetary signatures of unipolar streamers and the origin of the slow solar wind, *Sol. Phys.*, *277*, 355–373, doi:10.1007/s11207-011-9909-0.

Riley, P., J. A. Linker, and Z. Mikić (2001), An empirically-driven global MHD model of the corona and inner heliosphere, *J. Geophys. Res.*, *106*, 15,889, doi:10.1029/2000JA000121.

Riley, P., J. A. Linker, Z. Mikić, R. Lionello, S. A. Ledvina, and J. G. Luhmann (2006), A comparison between global solar magnetohydrodynamic and potential field source surface model results, *Astrophys. J.*, *653*, 1510, doi:10.1086/508565.

Riley, P., J. A. Linker, R. Lionello, and Z. Mikic (2012a), Corotating interaction regions during the recent solar minimum: The power and limitations of global MHD modeling, *J. Atmos. Sol. Terr. Phys.*, *83*, 1–10, doi:10.1016/j.jastp.2011.12.013.

Riley, P., M. Stevens, J. A. Linker, R. Lionello, Z. Mikic, and J. G. Luhmann (2012b), Modeling the global structure of the heliosphere during the recent solar minimum: Model improvements and unipolar streamers, in *American Institute of Physics Conference Series, American Institute of Physics Conference Series*, edited by Heerikhuisen, J., G. Li, N. Pogorelov, and G. Zank, vol. 1436, American Institute of Physics, Melville, NY, 337–343, doi:10.1063/1.4723628.

Riley, P., et al. (1997), Ulysses solar wind plasma observations at high latitudes, *Adv. Space Res.*, *20*, 15.

Taylor, K. (2001), Summarizing multiple aspects of model performance in a single diagram, *J. Geophys. Res.*, *106*, 7183.

Wang, Y.-M., N. R. Sheeley, and N. B. Rich (2007), Coronal pseudostreamers, *Astrophys. J.*, *658*, 1340, doi:10.1086/511416.

Warner, T. (2010), *Numerical Weather and Climate Prediction*, Cambridge University Press. New York, NY.

Wilks, D. (2006), *Statistical Methods in the Atmospheric Sciences*, International Geophysics Series, Academic Press, London.

Appendix L

On the application of ensemble modeling techniques to improve ambient solar wind models

Riley, P. and Linker, J. A. and Mikić, Z.

Published in J. Geophys. Res., 2013.

Ensemble Modeling of the Ambient Solar Wind

Pete Riley, Jon A. Linker, and Zoran Mikić

Predictive Science Inc., 9990 Mesa Rim Rd., Suite 170, San Diego. CA 92121.

Abstract. Ensemble modeling is a method of prediction based on the use of a representative sample of possible future states. Global models of the solar corona and inner heliosphere are now maturing to the point of becoming predictive tools, thus, it is both meaningful and necessary to quantitatively assess their uncertainty and limitations. In this study, we apply simple ensemble modeling techniques in a first step towards these goals. We focus on one relatively quiescent time period, Carrington rotation 2062, which occurred during the late declining phase of solar cycle 23 and assess the sensitivity of the model results to variations in boundary conditions, models, and free parameter values. We present variance maps, "whisker" plots, and Taylor diagrams to estimate the accuracy of the solutions, which demonstrate that the ensemble mean solution outperforms any of the individual realizations. Our results provide a baseline against which future model improvements can be compared.

Keywords: Ensemble Modeling, Solar Corona, Inner Heliosphere, Global MHD Modeling, In Situ Observations
PACS: 96.60.P-, 96.60.pc, 96.50.Bh, 96.50.Ci, 96.50.Qx, 96.50.sh, 96.50.Wx, 96.50.Xy

INTRODUCTION

Ensemble forecasting is a method of prediction that relies on the use of a representative sample of possible future states to derive a prediction. One of the appealing aspects of such an approach is that it offers a rigorous method for computing confidence bounds of the solution by estimating the uncertainty in the ensemble [1]. Moreover, the mean of the ensemble of forecasts is, or should be more accurate than the forecast from any individual member; the reason being that the random, or unpredictable regions of the forecast tend to cancel one another, while the aspects of the forecast that the majority of the models agree on are not removed [2].

For terrestrial weather forecasting, the uncertainty in the solutions can be divided into two main causes. The first is due to imperfect initial conditions. Unlike the Earth's lower atmosphere, however, small errors in the initial conditions in the solar corona are not likely to cause a substantial divergence of the solutions, and our "initial condition" issue then is replaced by a "boundary condition" problem. Specifically, the use of line-of-sight magnetograms from different solar observatories can lead to substantially different solutions [3].

The second source of errors can be termed "model formalism." This includes the physical processes that are included in the algorithms, as well as the parameterization of the model. For example, coronal models typically rely on either Potential Field Source Surface (PFSS) or magnetohydrodynamic (MHD) approximations, which have unique advantages and disadvantages [4]. Moreover, different sets of free parameters must be specified within each [5].

In this report, we compute a representative set of model realizations for two relatively quiescent time periods during the previous solar minimum to introduce and explore the value of applying ensemble modeling techniques to global solar and heliospheric numerical models. These are tentative first steps, which we hope will lay the foundation for more comprehensive studies in the future.

MODELING RESULTS

The process of generating a global solution for the plasma and magnetic field properties of the corona and inner heliosphere can be quite complex [3], involving the freedom to choose, for example: the solar observatory from which to derive the boundary condition on the radial magnetic field and the type of coronal and heliospheric model. Associated with each choice, are a further set of free parameters.

To illustrate the concepts of ensemble modeling, as applied to the ambient structure of the solar wind, we have computed ~ 50 realizations using the CORHEL model suite. For each one, we varied: (1) the input synoptic magnetogram; (2) the coronal model; (3) the base temperature; and (4) the spatial resolution of the simulation. In practice, there are an almost limitless number of choices that could be varied, leading to a potentially intractable number of solutions. We chose this limited set because we believe the model results are relatively sensitive to them, and they illustrate the essential features of ensemble modeling techniques.

A selection of realizations for CR 2062 are summarized in Figure 1. These maps show solar wind speed at $30R_S$ as a function of longitude (x-axis) and latitude (y-axis). The panel titles summarize the parameters that were modified. In particular, we: (1) used magne-

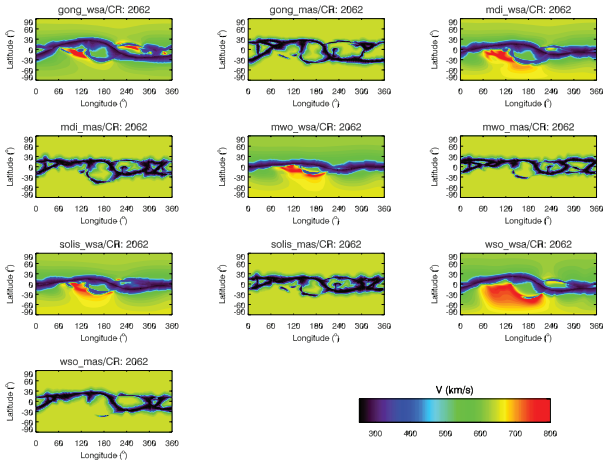

FIGURE 1. A subset of realizations computed for CR 2062 are shown as a function of longitude (x-axis) and latitude (y-axis). For each solution, either the input magnetogram (GONG, MDI, MWO, SOLIS, or WSO) or the coronal model (MAS or WSA) was varied.

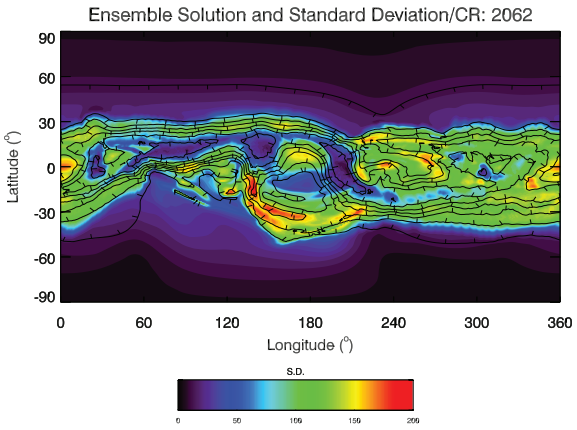

FIGURE 2. The ensemble mean (black contours) and standard deviation (color contours) for the realizations shown in Figure 1 as a function of Carrington longitude and heliographic latitude. The tick marks on each contour show the direction of decreasing speed.

tograms from GONG, MDI, MWO, SOLIS, and WSO; and (2) constructed solutions using both our MHD coronal model (MAS) and the WSA prescription, which includes a PFSS model. These two models represent more than just different numerical approaches. In addition to different assumptions, such as the existence of a source surface, they incorporate two distinct ideas for the origin of the solar wind [5] and so produce different values of the bulk solar wind speed at the inner boundary of the heliospheric model. The solutions are qualitatively similar: fast solar wind at high latitudes, and slower wind organized about the heliomagnetic equator. Beyond this, however, there are some notable differences. First, the structure of the band of slow wind differs dramatically from one model to another. The WSA solutions, for example, do not tend to produce slow-flow arcs that split from the main slow-flow band and then rejoin. These are associated with unipolar- or pseudo-streamers, and one of the distinguishing features between the two ideas for the origin of the slow solar wind is whether plasma from these locations is fast [6] or slow [5].

Given these solutions, and with no *a priori* information about which is better or worse, we can estimate the variance between them, and thus infer where the model solutions agree and disagree [7]. Figure 2 summarizes the standard deviation (s.d., i.e., the square root of the variance) for CR 2062, using the realizations shown in Figure 1. The ensemble mean is also shown as black contours. Of particular note is that the variance is lowest when the speed is lowest and highest when the speed too is highest. This makes intuitive sense: It is easier for models to agree when there is no structure, such as long periods of slow, or fast wind, but more difficult to predict the location of sharp stream fronts, that is, the boundaries between slow and fast wind. This is particularly true at stream interfaces, where fast wind is flowing into slower wind. At such locations, the gradient from slow to fast is sharp, thus, small offsets in the phasing of this boundary will translate into large model variances.

The presentation of the s.d. in Figure 2 emphasizes several interesting points. First, away from the "band of solar wind variability," all realizations predict fast, quiescent solar wind, in agreement with Ulysses polar observations (e.g., [8]). Second, near the equator, the models agree best in an "island" extending from 60° to 240°, which traces the locus of the heliospheric current sheet (not shown). Third, the realizations disagree the most between $\sim$ 130° and 180° longitude at mid-southern heliographic latitudes. This maps back to the location of a pseudo-streamer (See also Figure 1).

COMPARISON WITH OBSERVATIONS

Using results from the heliospheric portion of the simulations, we can compare the ensemble solution, and the statistical properties of the realizations with ACE observations at 1 AU in the ecliptic plane. Figure 3 compares *in situ* measurements (red) of the bulk solar wind speed as measured by the ACE spacecraft with the ensemble model solution (black). The boxes with "whiskers" summarize the statistical properties of the realizations. We note that the ensemble model has captured the three streams (located between 0° and 240° longitude, but misses the region of prolonged low-speed wind from 240° to 360°. This is, we believe, related to the issue that synoptic maps, built up from earth-based observations,

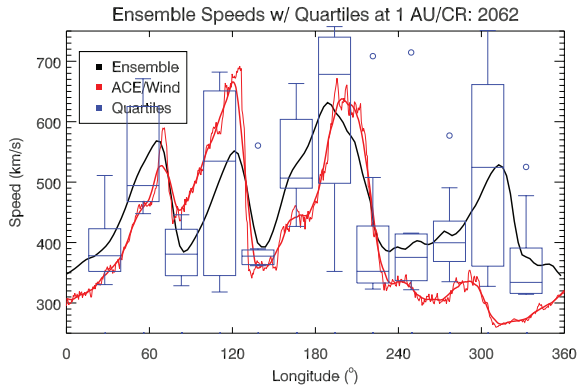

FIGURE 3. Comparison of ensemble model solution (black) with ACE *in situ* measurements (red; 1-hour and 1-day averages). The blue boxes with "whiskers" summarize the variability of the realizations. The median value is indicated by the short horizontal line, while the tops and bottoms of the boxes mark the 25th and 75th quantiles. The tips of the "whiskers" mark the maximum and minimum values. When these maxima are more than three sigma from the median, they are marked with an open circle.

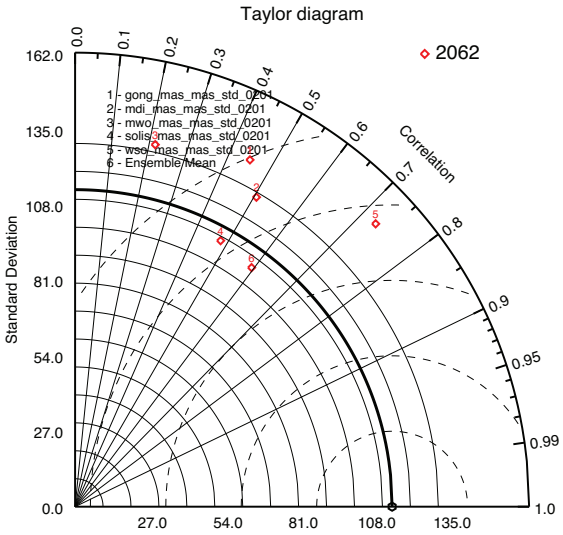

FIGURE 4. A "Taylor diagram" for summarizing the performance of model runs. The radial distance away from the origin gives the standard deviation of the model result (red diamonds) and data (black diamond). The correlation coefficient (R) between the data and the model result is shown by its azimuthal position. The scale increases as $cos^{-1}R$. The dashed partial circles centered on the black diamond mark contours of constant centered RMSE. See [9] for further details.

are not periodic in longitude, as must be assumed by the model.

TAYLOR DIAGRAMS

Even the relatively limited number of realizations we have discussed here contain a considerable amount of data, which can be difficult to digest and assess. To concisely summarize the degree to which the model results match observations across many realizations, Taylor [9] developed what has come to be known as a "Taylor diagram," which combines correlation, centered RMSE, and variances.

Figure 4 summarizes five high-resolution runs using the MAS model, each driven by data from a different solar observatory. The radial distance from the origin indicates standard deviation in solar wind, while the angular direction shows correlation coefficient. The observations thus become a single point on the x-axis (black diamond) since they are exactly correlated with themselves, and the model results (red diamonds) are distributed at various locations in this parameter space. Both the correlation of the model results with the data and the degree to which its variance matches the observations are key aspects for providing useful forecasts. Additionally, it turns out that when the correlation coefficient is displayed as its arc cosine, there is a simple geometric relationship between the centered RMSE. Specifically, contours of centered RMSE lie on circles centered around the observation point (dashed circles in Figure 4). Thus, the optimum model is the one that lies closed to the observation point, or, equivalently, on the smallest dashed circle. Solutions with high correlation coefficient, then, are penalized in this view if the s.d. is substantially smaller or larger than the s.d. of the observations. Model 4, for example, although having a lower correlation coefficient than model 6, provides a closer match in terms of variance. Similarly, although the ensemble mean of these five cases does not produce a higher correlation coefficient than the best single realization (model 5), overall, it is marginally a better solution.

Using the Taylor diagram, we can assess changes in the performance of a model resulting from modifications to it. For example, in Figure 5, we explore the effects of reducing the base coronal temperature in the polytropic MAS model from 1.8×10^6K to 1.1×10^6K, that is, a reduction by one third. The red diamonds mark the reference solutions and the blue squares mark the location of the new solutions, with the arrows connecting one to the other. Even without reviewing the individual time series, we can see that all variability in the solar wind solutions has been removed. Physically, we can understand this change as follows: By decreasing the coronal-base temperature, the thermal pressure of the plasma is reduced. Fewer magnetic field lines are opened up, which in turn causes more of the smaller equatorial coronal holes to close down. Thus, there are less fast streams at low lati-

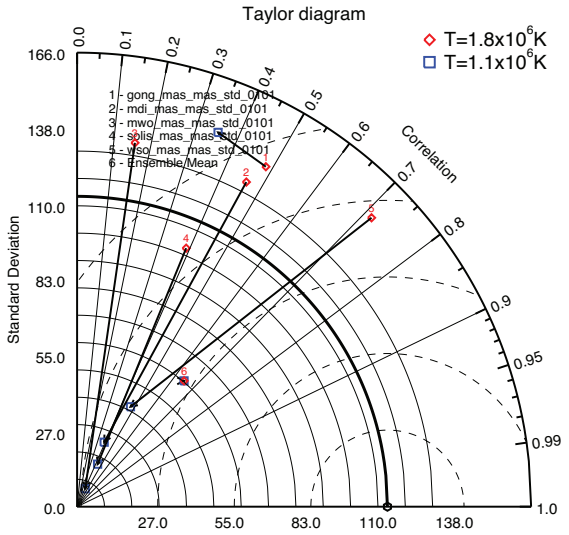

FIGURE 5. As Figure 4 except that the blue squares mark the new locations of the solutions when the base temperature is dropped from 1.8×10^6K to 1.1×10^6K. The arrows connect each pair of solutions and show the change in performance that the temperature change induces.

tudes punching through the otherwise slower wind associated with the streamer belt, resulting in less variability in the speed of the wind there.

DISCUSSION

In this report, we have applied some relatively simple terrestrial weather ensemble forecasting concepts to models of the ambient solar corona and inner heliosphere. Although there are some fundamental differences between Earth's lower atmosphere and the Sun's corona, we believe that ensemble modeling techniques can be adapted and successfully applied to both assess and improve the performance of global solar and heliospheric models.

Our numerical "experiments" to assess the sensitivity of the model results to both boundary conditions and model formalism suggests that substantial improvements in performance can be achieved by careful exploration of the relevant parameter space. Three substantial problems, however, pose significant and potentially long-term handicaps for improving the quality of the model solutions. First, our limited view of the Sun's poles forces us to extrapolate mid-latitude, well-observed data poleward [3]. Second, our current reliance on synoptic maps, which are built up from daily observations taken over 25.38 days, as inner radial boundary conditions cannot be rigorously defended: The model implicitly assumes that this map is synchronic, that is, it is a snapshot of the surface of the photosphere at one point in time, which it clearly is not. Furthermore, because the first and last slice for each Carrington rotation are separated by more than 25 days, the model's requirement that the boundary condition be periodic, necessarily leads to artifacts at the boundary. Third, our assumption that the Sun's structure does not change appreciably during the course of a solar rotation is an idealization that is not met in reality. Several developments may resolve these issues. First, sequences of synchronic maps derived from flux transport models could be used to drive a time-dependent model of the ambient solar wind [10]. Second, magnetograms constructed from simultaneous observations by Solar Orbiter (currently scheduled for launch in January 2017) and earth-based magnetographs and/or ground-based observatories may be used to produce "quasi-synchronic" maps.

ACKNOWLEDGMENTS

The authors gratefully acknowledge the support of NASA (Causes and Consequences of the Minimum of Solar Cycle 24 program, LWS Strategic Capabilities program, Heliophysics Theory Program, and the STEREO IMPACT team) and NSF (Center for Integrated Space Weather Modeling (CISM) program).

REFERENCES

1. D. Wilks, *Statistical Methods in the Atmospheric Sciences*, International Geophysics Series, Academic Press, 2006, ISBN 9780127519661, URL `http://books.google.com/books?id=\_vSwyt8\_OGEC`.
2. T. Warner, *Numerical Weather and Climate Prediction*, Cambridge University Press, 2010, ISBN 9780521513890, URL `http://books.google.com/books?id=6RQ3dnjE8lgC`.
3. P. Riley, J. A. Linker, R. Lionello, and Z. Mikic, *J. of Atmos. and Solar-Terr. Phys.* **83**, 1–10 (2012).
4. P. Riley, J. A. Linker, Z. Mikić, R. Lionello, S. A. Ledvina, and J. G. Luhmann, *Astrophys. J.* **653**, 1510 (2006).
5. P. Riley, and J. G. Luhmann, *Sol. Phys.* **277**, 355–373 (2012).
6. Y.-M. Wang, N. R. Sheeley, and N. B. Rich, *Astrophys. J.* **658**, 1340 (2007).
7. E. S. Epstein, *Tellus* **21**, 739–759 (1969).
8. P. Riley, S. J. Bame, B. L. Barraclough, W. C. Feldman, J. T. Gosling, G. W. Hoogeveen, D. J. McComas, J. L. Phillips, B. E. Goldstein, and M. Neugebauer, *Adv. Space Res.* **20**, 15 (1997).
9. K. Taylor, *J. Geophys. Res.* **106**, 7183 (2001).
10. C. N. Arge, C. J. Henney, J. Koller, C. R. Compeau, S. Young, D. MacKenzie, A. Fay, and J. W. Harvey, *Twelfth International Solar Wind Conference* **1216**, 343–346 (2010).

Appendix M

A Multi-Observatory Inter-Comparison of Line-of-Sight Synoptic Solar Magnetograms

Riley, P. and Ben-Nun, M. and Linker, J.A. and Mikic, Z. and Svalgaard, L. and Harvey, J. and Bertello, L. and Hoeksema, T. and Liu, Y. and Ulrich, R.

Published in Solar Physics, 2013.

Solar Phys
DOI 10.1007/s11207-013-0353-1

A Multi-Observatory Inter-Comparison of Line-of-Sight Synoptic Solar Magnetograms

P. Riley · M. Ben-Nun · J.A. Linker · Z. Mikic · L. Svalgaard · J. Harvey · L. Bertello · T. Hoeksema · Y. Liu · R. Ulrich

Received: 22 February 2013 / Accepted: 20 June 2013

Abstract The observed photospheric magnetic field is a crucial parameter for understanding a range of fundamental solar and heliospheric phenomena. Synoptic maps, in particular, which are derived from the observed line-of-sight photospheric magnetic field and built

P. Riley (✉) · M. Ben-Nun · J.A. Linker · Z. Mikic
Predictive Science, 9990 Mesa Rim Road, Suite 170, San Diego, CA, USA
e-mail: pete@predsci.com

M. Ben-Nun
e-mail: mbennun@predsci.com

J.A. Linker
e-mail: linkerj@predsci.com

Z. Mikic
e-mail: mikicz@predsci.com

L. Svalgaard · T. Hoeksema · Y. Liu
Stanford University, Stanford, CA, USA

L. Svalgaard
e-mail: leif@leif.org

T. Hoeksema
e-mail: todd@solar2.stanford.edu

Y. Liu
e-mail: yliu@solar2.stanford.edu

J. Harvey · L. Bertello
NSO, Kitt Peak, Tucson, AZ, USA

J. Harvey
e-mail: jharvey@noao.edu

L. Bertello
e-mail: bertello@noao.edu

R. Ulrich
UCLA, Los Angeles, CA, USA
e-mail: ulrich@astro.ucla.edu

Published online: 25 July 2013

up over a period of 27 days, are the main driver for global numerical models of the solar corona and inner heliosphere. Yet, in spite of 60 years of measurements, quantitative estimates remain elusive. In this study, we compare maps from seven solar observatories (Stanford/WSO, NSO/KPVT, NSO/SOLIS, NSO/GONG, SOHO/MDI, UCLA/MWO, and SDO /HMI) to identify consistencies and differences among them. We find that while there is a general qualitative consensus, there are also some significant differences. We compute conversion factors that relate measurements made by one observatory to another using both synoptic map pixel-by-pixel and histogram-equating techniques, and we also estimate the correlation between datasets. For example, Wilcox Solar Observatory (WSO) synoptic maps must be multiplied by a factor of 3 – 4 to match Mount Wilson Observatory (MWO) estimates. Additionally, we find no evidence that the MWO saturation correction factor should be applied to WSO data, as has been done in previous studies. Finally, we explore the relationship between these datasets over more than a solar cycle, demonstrating that, with a few notable exceptions, the conversion factors remain relatively constant. While our study was able to quantitatively describe the relationship between the datasets, it did not uncover any obvious "ground truth." We offer several suggestions for how this may be addressed in the future.

Keywords Sun: Corona, evolution · Magnetic fields · Solar wind · Interplanetary medium · Potential field source surface model

1. Introduction

The Sun's photospheric, and by extension, coronal magnetic field is a crucial parameter that modulates a range of solar phenomena. The open, unsigned magnetic flux, *i.e.*, the component of the solar magnetic field that opens up into the heliosphere, in particular, is of fundamental scientific importance (*e.g.* Riley, 2007). For example, its long-term (on the time-scale of ≈ 100 years) changes undoubtedly affect the transport of cosmic rays (Lockwood, 2001). These long-term variations in cosmic ray fluxes, if present, may affect both technology and space, and even terrestrial climate (Bering *et al.*, 1998). Lockwood, Stamper, and Wild (1999) argued that the average open flux has risen by 40 % from 1964 to 1999 and, by correlation and then extrapolation using *aa* (a measure of the disturbance level of the Earth's magnetic field based on magnetometer observations at two approximately antipodal stations), by 131 % from 1900 to 1999. In contrast, Svalgaard and Cliver (2005) computed an index based on Bartel's historical *u* index of geomagnetic activity, and used it to infer that the average interplanetary magnetic field increased by only ≈ 25 % between 1900 and 1950, and has decreased since then. Most recently, Lockwood and Owens (2011) have suggested that the Sun, and by inference, its global heliospheric magnetic field, is entering a grand solar minimum period, potentially as deep as that thought to have occurred during the Maunder minimum.

An important aspect of these analyses concerns how raw solar magnetograms are processed to produce a line-of-sight, or radial estimates of the photospheric magnetic field in physical units.

Wang and Sheeley (1995), for example, have argued that a saturation correction factor derived for magnetograms at the Mount Wilson Observatory (MWO) should be applied to data measured at the Wilcox Solar Observatory (WSO). Their rationale was empirically based: it provided a significantly better match between the computed open flux (using a potential field source surface (PFSS) model) and the measured radial component of the

interplanetary magnetic field at 1 AU (B_r^{IMF}). Svalgaard, Duvall, and Scherrer (1978), in contrast, argued that WSO data require only a constant factor (1.85) to convert the measured values into units of gauss (G). Since these correction factors can, in places, differ by more than a factor of two, the choice of which one to use can be crucial.

A number of studies have attempted to inter-calibrate line-of-sight magnetograph measurements from one or more observatories (*e.g.* Jones, 1989, 1992a, 1992b; Jones *et al.*, 1993, 2004; Cauzzi *et al.*, 1993; Jones and Ceja, 2001; Berger and Lites, 2002; Thornton and Jones, 2002; Tran *et al.*, 2005; Wenzler *et al.*, 2006; Demidov *et al.*, 2008; Ulrich *et al.*, 2009; Pietarila *et al.*, 2013; Liu *et al.*, 2012). Typically, they were undertaken to resolve uncertainties in one dataset, under the assumption that the other data were more accurate. Our approach in this study, however, is to attempt to find a "ground truth" by comparing each of the seven observatories' data with every other observatory, in the hope that a consensus result may be found. Specifically, we analyze data from The Global Oscillation Network Group (GONG), Mount Wilson Observatory (MWO), Wilcox Solar Observatory (WSO), The Kitt Peak Vacuum Telescope (KPVT), Synoptic Optical Long-term Investigations of the Sun (SOLIS), the *Michelson Doppler Imager* (MDI) onboard the *Solar and Heliospheric Observatory* (SOHO) spacecraft (Scherrer *et al.*, 1995), and the *Helioseismic and Magnetic Imager* (HMI) onboard the *Solar Dynamics Observatory* (SDO) spacecraft. This combination was chosen because they represent the most often analyzed and used datasets, spanning and overlapping the greatest interval of time. Moreover, with the exception of KPVT, which was the predecessor of the SOLIS instrument, and MDI, which was retired recently, all of the observatories are currently producing synoptic maps.[1]

Unlike previous studies, we make the starting point for our analysis the synoptic maps, that is, latitude-longitude maps made up of 27 days of measurements, instead of the raw disk magnetograms. These are the maps that global numerical models rely on (Riley *et al.*, 2011; Bertello, Petrie, and Tran, 2010; Petrie, Canou, and Amari, 2011; Luhmann *et al.*, 2012) and thus represent an important basic dataset to investigate and assess. However, we must recognize that the process of making such maps, in and of itself, has the potential for introducing errors and even purposeful differences between the observatories. For example, our analysis will implicitly assume that the relationship between maps is a simple linear one, depending only on latitude, which is not likely to be the case.

Our goal in this study is limited to a quantitative comparison of the synoptic maps. Yet this in itself is a worthwhile objective. As Lord Kelvin wrote: "... when you can measure what you are speaking about, and express it in numbers, you know something about it; but when you cannot measure it, when you cannot express it in numbers, your knowledge is of a meager and unsatisfactory kind; it may be the beginning of knowledge, but you have scarcely in your thoughts advanced to the state of Science, whatever the matter may be." (Stellman, 1998). Here then, our study aims to place our current state of knowledge with respect to synoptic maps on Lord Kelvin's 'scale of science.' We first attempt to identify a "ground truth" for magnetic field values given in synoptic maps, and, failing that, to quantify the variability among them, which, at least to some extent, provides an estimate for their uncertainty.

[1] Since SOLIS replaced KPVT, we collectively refer to these data as "SOLIS" when we present long-term analyses, acknowledging that prior to Carrington rotation (CR) 2008, the data were obtained by KPVT.

2. Construction of Photospheric Synoptic Magnetograms

Magnetographs rely on a variety of techniques to infer the magnetic field in the photosphere. At MWO and WSO, for example, a Babcock solar magnetograph records the Zeeman polarization in the wings of an absorption line of iron at 5250 Å (*e.g.* Ulrich, 1992). Other lines are also measured to provide a true zero level of the instrument, such as the magnetically insensitive line of Fe I at 5124 Å at WSO.[2] By measuring the amount and sense of the circular polarization, the line-of-sight component of the magnetic field can be recovered. At NSO/KPVT, the 8688 Å line of Fe I is used to derive the LOS magnetic field (although 5507 Å was used for CR 1855 through 1862). Additionally, two distinct instruments were used: Between CR 1625 and CR1853, a 512-channel Babcock type instrument was used, while after CR 1855 a CCD spectromagnetograph was used. To convert the raw measurements into G, a conversion factor of 1.46 is required. Both MDI and GONG use interferometric techniques to measure the opposite states of polarization of the Ni I 6768 Å line.

Zeeman-splitting measurements must be carefully processed to infer the line-of-sight component of the photospheric magnetic field. Once obtained, assuming the field is vertical, a radial component can be derived. At MWO, two Fe I lines have been studied in detail: 5250 Å and 5233 Å. The former suffers from the problem that the magnetograph signal does not scale linearly with the line-of-sight component of the field, *i.e.*, it becomes saturated. Ulrich (1992) derived a correction factor for MWO 5250 Å observations of the form

$$g_{\mathrm{MWO}} = 4.5 - 2.5\sin^2(\rho), \tag{1}$$

where ρ is the heliocentric angular distance away from disk center. Thus, multiplication of 5250 Å measurements by the factor given in Equation (1) would convert them to the 5233 Å measurements. This led Wang and Sheeley (1995) to apply the same correction factor to WSO data. However, Svalgaard, Duvall, and Scherrer (1978) found from their 5250 Å measurements at WSO that the line-of-sight photospheric field varied exactly as $\cos(\rho)$, and they inferred a constant saturation factor, $g_{\mathrm{WSO}} = 1.8$ (which has since been revised to 1.85 (Svalgaard, 2006)). The corrections for MWO and WSO measurements continue to be investigated. Recent work (Ulrich *et al.*, 2009; Demidov and Balthasar, 2009; Demidov and Balthasar, 2012) produced different and contradictory versions of Equation (1).

Beyond instrumental differences, we should note that the choice of wavelength itself necessarily means that we are not observing at the same height in the solar atmosphere. Thus, although the differences would be expected to be modest, strictly speaking, the instruments are not measuring exactly the same altitude in the solar atmosphere.

An additional practical difference is that the resolution of the disk magnetograms produced by different observatories (and even intra-observatory) varies dramatically. At the NSO KPVT, for example, the pixel size of images was 1.0″ for the 512-channel Babcock instrument and 1.14″ for the spectromagnetograph. Until 2010 SOLIS's resolution was 1.125″, becoming 1.0″ after that. Full-disk scan times have ranged from 40 min for the 512-channel Babcock instrument to 11 min for SOLIS. Ground-based observations, while in principle providing higher-resolution images, suffer from seeing effects that reduce the resolution to that of space-based instruments. The effective resolution of the disk magnetograms then defines the appropriate resolution at which synoptic maps can be made.

[2]Strictly speaking, the 5124 Å line does have a slight Zeeman sensitivity – $g = -0.013$ (Landi Degl'Innocenti, 1982).

Table 1 Sources of synoptic magnetograms used in this study: WSO data were obtained from wso.stanford.edu/synoptic/; GONG data were obtained from gong2.nso.edu/archive/patch.pl?menutype=s; Kitt Peak Vacuum Telescope (KPVT) data were obtained from nsokp.nso.edu/kpvt/synoptic/mag/; SOLIS data were obtained from solis.nso.edu/vsm/vsm_maps.php; MWO data were obtained from howard.astro.ucla.edu/pub/obs/synoptic_charts/FITS_files/; MDI data were obtained from soi.stanford.edu/magnetic/synoptic/carrot/M/; and HMI data were obtained from jsoc.stanford.edu/ajax/exportdata.html. For consistency, all data were downloaded on 1 October 2012, and analyzed thereafter.

Observatory	Type	Grid size	Dates available (mm/dd/year)	CRs available
WSO	LOS	73×30	05/27/1976 to 09/11/2012	1642 – 2127
GONG	Radial	360×180	08/25/2006 to 06/16/2010	2047 – 2097
KPVT	Radial	360×180	02/18/1975 to 09/26/2003	1625 – 2007
SOLIS	Radial	360×180[a]	08/30/2003 to 09/11/2012	2007 – 2127
MWO	LOS	971×512	06/28/1996 to 08/15/2012	1911 – 2126
MDI	Radial	3600×1080	05/05/1996 to 12/24/2010	1909 – 2104
HMI	Radial	3600×1440	04/22/2010 to 09/11/2012	2096 – 2127

[a]SOLIS maps are also available on 1800×900 grids.

Table 1 summarizes the main attributes of the synoptic maps we analyzed here. Column one gives the name of the observatory, while column two gives the type of measurement produced. In fact, all observatories measure only the line-of-sight component of the magnetic field; however, some convert this value into a "radial" field, under the assumption that the total field is radial, while others do not. Column three gives the grid size of the synoptic maps. These are the canonical values, although some of the observatories have special data products where the resolution may be different. Columns four and five give the dates and CRs over which the data are available.

Constructing synoptic maps, that is, maps of the radial photospheric magnetic field as a function of Carrington longitude versus latitude, can be a complex process. Some of the questions the observers must face in assembling them from disk images include the following: i) How is one to average data taken at different times during the day, or over multiple days, and, in the case of GONG, data from multiple observatories at different geographical locations? ii) How does one account for differential rotation for data taken at different times that were averaged together? iii) How does one fill in data in the polar regions, where because of geometrical effects one can observe not as well (or not at all) from Earth's vantage, due to the $\pm 7.2^\circ$ tilt of the Earth's orbit with respect to the heliographic equatorial plane? For this study, our initial assumption in comparing the synoptic maps is that they have been processed in such a way as to reproduce the most accurate synoptic maps possible. However, we recognize that differences between them may reflect differences in how they are assembled, and not necessarily differences in the original data.

Unfortunately, synoptic maps themselves are not the best data product for driving MHD models. The name itself, synoptic, means "affording a general view of the whole," which suggests that the maps are a single snapshot in time; however, the maps are assembled using observations from near-Earth observatories taken during the course of a solar rotation, *i.e.*, at different times, and should, technically, be called diachronic maps. A more useful map for a global model would be a synchronic'(or true synoptic) map, that is, a snapshot of the entire solar surface at a single point in time. Such a map is not possible now or in the foreseeable future with our limited Earth-centric view of the Sun.

A step toward more synchronic maps can be made by accounting for the differential rotation that occurs as disk images are added to the synoptic map progressively farther around

the far-side of the Sun. Potential field source surface (PFSS) modeling suggests that these pseudo-synchronic maps, which include the effects of differential rotation, may produce better predictions of stream structure in the vicinity of Earth (Bertello, Petrie, and Tran, 2010). These results require further substantiation, however, and such maps are not produced as a matter of course by the other observatory teams, making them less than ideal for the present study. Flux evolution models arguably also provide a more accurate map of the photospheric magnetic field (Arge *et al.*, 2010). However, they remain very much a topic of research and are not yet regularly produced over a sufficiently long time span to be of use here.

Finally, we should note that some of the maps (but not all) have been re-processed over the years. The MDI data, for example, are currently (as of 1 October 2012) labeled LEVEL 1.8.2, reflecting a major re-processing of both the disk and synoptic products in December 2008. Unfortunately, time histories of previous versions are typically not made available, and we should emphasize that the results we derive here are sensitive to the version of the data analyzed. Thus, for clarity, all observatory data were downloaded on 1 October 2012, and the complete analysis described here was performed on those data.

3. Magnetogram Inter-Comparison

We begin our analysis by making some qualitative comparisons between the synoptic maps. We then turn to two quantitative approaches, linear regression and histogram equating, to estimate the relationship between flux measured at one observatory and another, before finally considering the possible temporal evolution of these relationships over more than a solar cycle.

Figure 1 summarizes all available synoptic maps as a function of longitude and $\sin(\lambda)$ from five solar observatories for CR 2047. These data have been plotted at their original resolution, that is, the resolution at which the maps were published, which can be quite different from the native resolution of the disk magnetograms. For example, the native resolution of WSO disk images is 23×11. Each map's color table was constructed by setting the range to be $\pm 5 \times |\tilde{x}|$, where $|\tilde{x}|$ is the median of the absolute value of each synoptic map. For the most part, the data are provided in self-describing FITS files that include the optional FSCALE or BSCALE keywords. For the WSO maps, which are supplied as text files, the data were converted from micro-tesla to gauss by multiplying by 0.01. The WSO data were neither corrected using the factor of 1.85, as advocated by Svalgaard (2006), nor using the MWO correction factor (Equation (1)), as proposed by Wang and Sheeley (1995). In the broadest sense then, the maps are reasonably similar to one another. The resolutions of these maps are 73×30 (WSO), 360×180 (GONG and SOLIS), 971×512 (MWO), and 3600×1080 (MDI). We note the ever-smaller scale features that appear with increasing resolution. The smallest-scale fields (outside active regions (ARs)) in the MWO are notable for their absence, when compared with SOLIS (panel above) or MDI (panel below). It is quite possible that these are not measured fields but noise in the data, which would be consistent with MWO's known low noise levels. On the other hand, the relative strength of the ARs at MWO is stronger (more saturated) than those for MDI. Thus, there is the suggestion that the fields do not scale linearly with strength between at least some of the observatories.

Figure 2 shows a second comparison for CR 2097, which occurred between 19 May 2010 and 16 June 2010. By this time, measurements of SDO's HMI were available. We note, again, the strong qualitative similarity between the magnetograms. WSO fields appear generally weaker, but we must bear in mind that the resolution of these data are at least a factor of five lower than the next-lowest resolved datasets, and some 50 times lower than

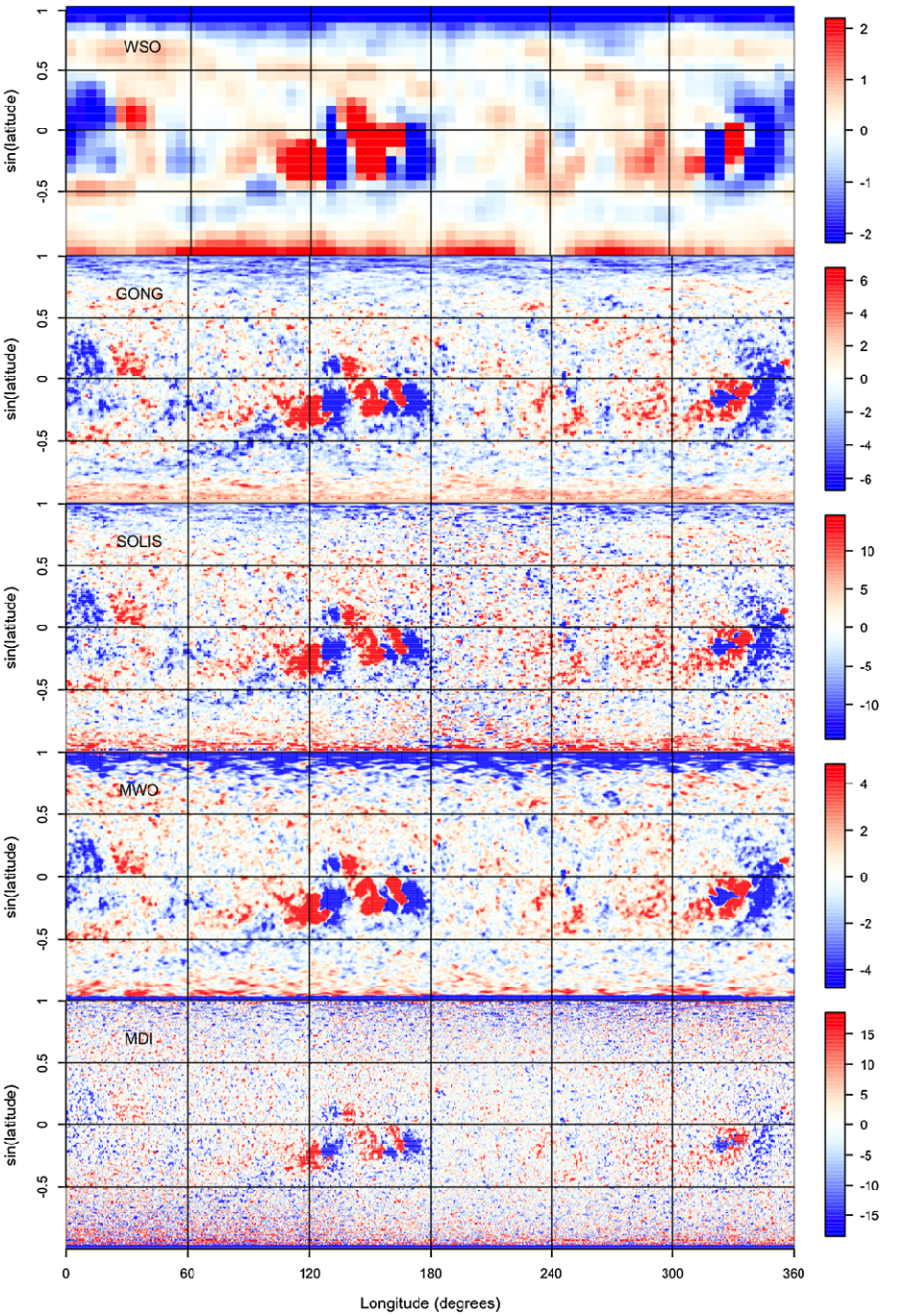

Figure 1 Comparison of synoptic maps (as a function of longitude and sin(λ)) for five solar observatories for CR 2047. From top to bottom: Wilcox Solar Observatory (WSO); Global Oscillation Network Group (GONG); Synoptic Optical Long-term Investigations of the Sun (SOLIS), Mount Wilson Observatory (MWO); and *Michelson Doppler Imager* (MDI). All data are in their original resolution: WSO 73 × 30; GONG 360 × 180; SOLIS 360 × 180; MWO 971 × 512; and MDI 3600 × 1080. The ranges for the color bars were set to $\pm 5 \times |\tilde{x}|$, where $|\tilde{x}|$ is the median of the absolute value of each synoptic map.

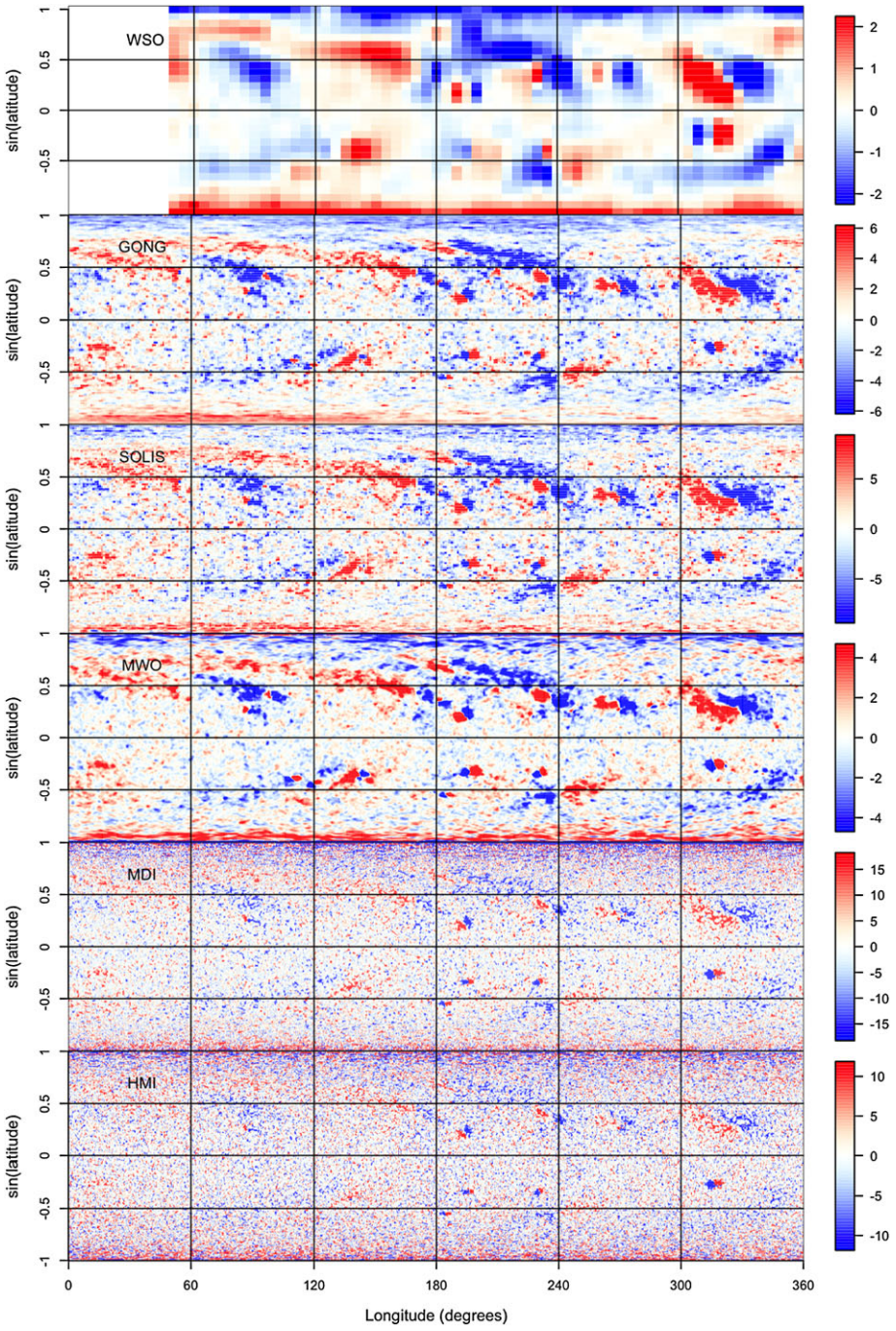

Figure 2 The same as Figure 1, except for CR 2097, which was also observed by SDO's HMI, with a resolution of 3600 × 1800.

HMI. MWO/MDI and GONG/SOLIS match well in terms of AR-scale fields, while the small-scale salt-and-pepper fields in the ten-times more resolved MDI and HMI are very similar, at least in a statistical sense.

In Figure 3 we have box-car-smoothed the data from GONG, SOLIS, MWO, and MDI for CR 2047 to match the resolution at WSO. In principle, these maps should match very closely, and, to a first appearance, they do. The AR structure at all observatories except WSO is remarkably similar, with the notable exception that the fields are weaker at MWO. Additionally, the quiet-Sun regions of MWO are weaker than at the other four observatories. Unfortunately, the smoothing procedure did not have the anticipated effect of converting the maps into WSO-proxies: The fields at WSO are still generally weaker than at other observatories. Also, more finer-scale structure is retained at the other observatories than at WSO. Although the data were smoothed on spatial scales matching WSO, they are still plotted at their native resolution, and so, in some sense, they still retain more information than does WSO.

4. Regression Analysis

To make a quantitative comparison of the synoptic maps, we constructed scatter plots and applied a selection of regression-fitting techniques to estimate the slope of the lines, which, in turn, gives us a measure of the conversion factor, that is, the coefficient necessary to take data from one observatory and convert them into data from another observatory. We also separated the data by $\sin(\lambda)$ bins for several reasons. First, the data become noisier with increasing distance from the equator to the poles. Thus, we can estimate the quality of the fits to the data by monitoring quantities such as correlation coefficients as a function of latitude. Second, it allows us to investigate whether there are any underlying latitudinal dependencies in the conversion factors, as has been proposed, for example by Wang and Sheeley (1995), for WSO data.

We begin by comparing data from GONG and MWO for CR 2047. Figure 4 shows scatterplots of the field at GONG (x-axis) and MWO (y-axis) as a function of $\sin(\lambda)$. From the top-left to the bottom-right panel, $\sin(\lambda)$ runs from -1 ($-90°$) to $+1$ ($+90°$). Focusing first on the low- and mid-latitude regions (middle panels) we note that i) the correlation is high (> 0.96), ii) the relationship is linear, and iii) the slopes of the best-fit lines are all close to 1.9. We also found that particularly when the scatter is large, it is useful to compute several estimates of the slope: In cases where they differ significantly (top and bottom rows), caution is appropriate in deciding whether the results are robust. Moving progressively closer to the poles, the correlation breaks down, such that by $|\sin(\lambda)| > 0.6$, the correlation coefficient has decreased significantly (< 0.5).

5. Histogram Equating

The technique of histogram equating was first applied to magnetogram comparisons by Jones *et al.* (1992). These authors found that pixel-by-pixel comparisons, such as those in Section 4, are complicated and prone to either intrinsic errors such as the timing of the measurements, or processing errors, such as filtering to account for the differences in spatial resolution of the instruments. A simpler approach, they argued, is to assume that the two instruments only observed the same statistical distribution of flux. Therefore, the only difference between cumulative histograms of two magnetograms is due to different scales

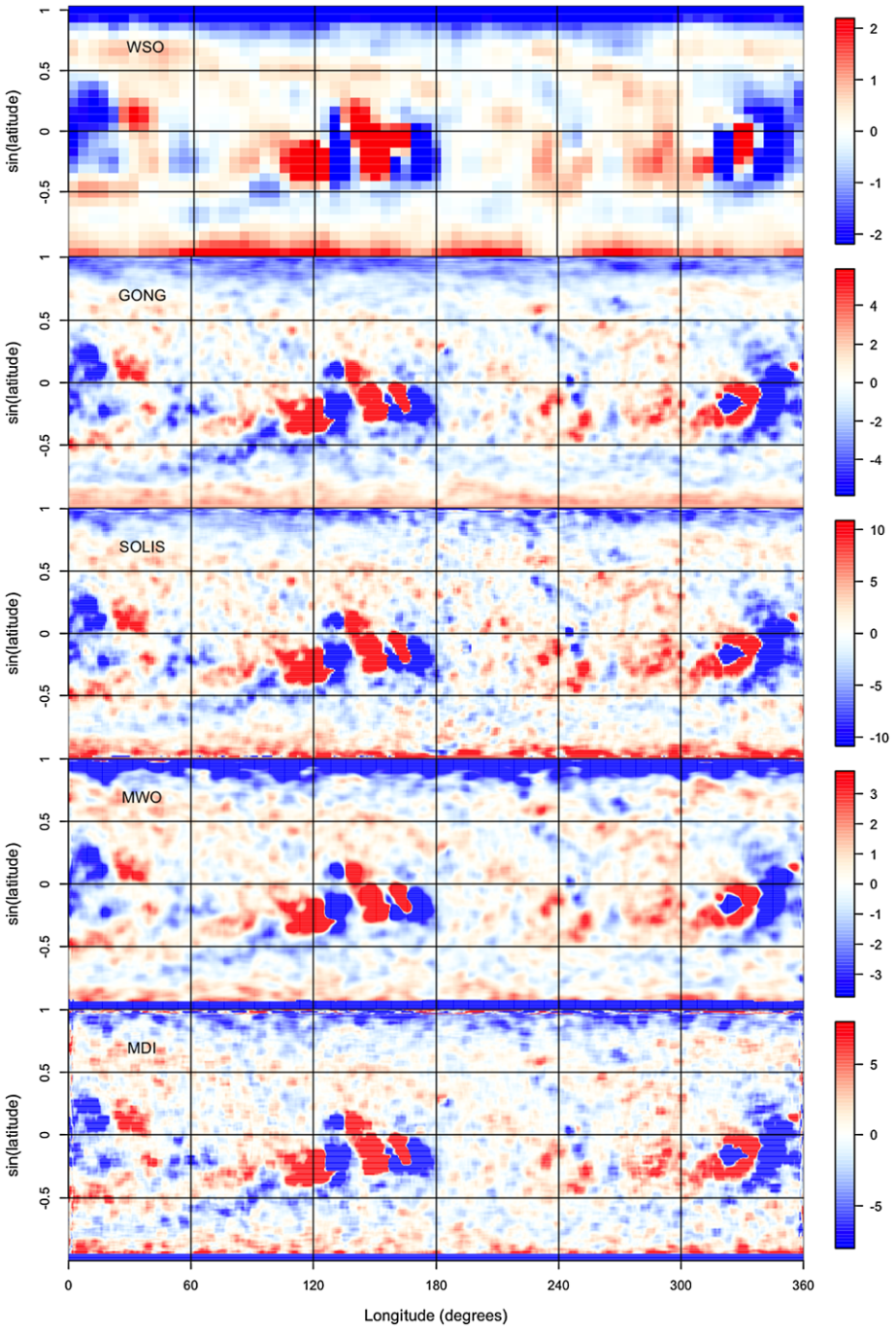

Figure 3 The same as Figure 1 (*i.e.*, for CR 2047), but the individual magnetograms have been box-car smoothed in both sin(λ) and longitude by the ratio of their resolution to that of WSO.

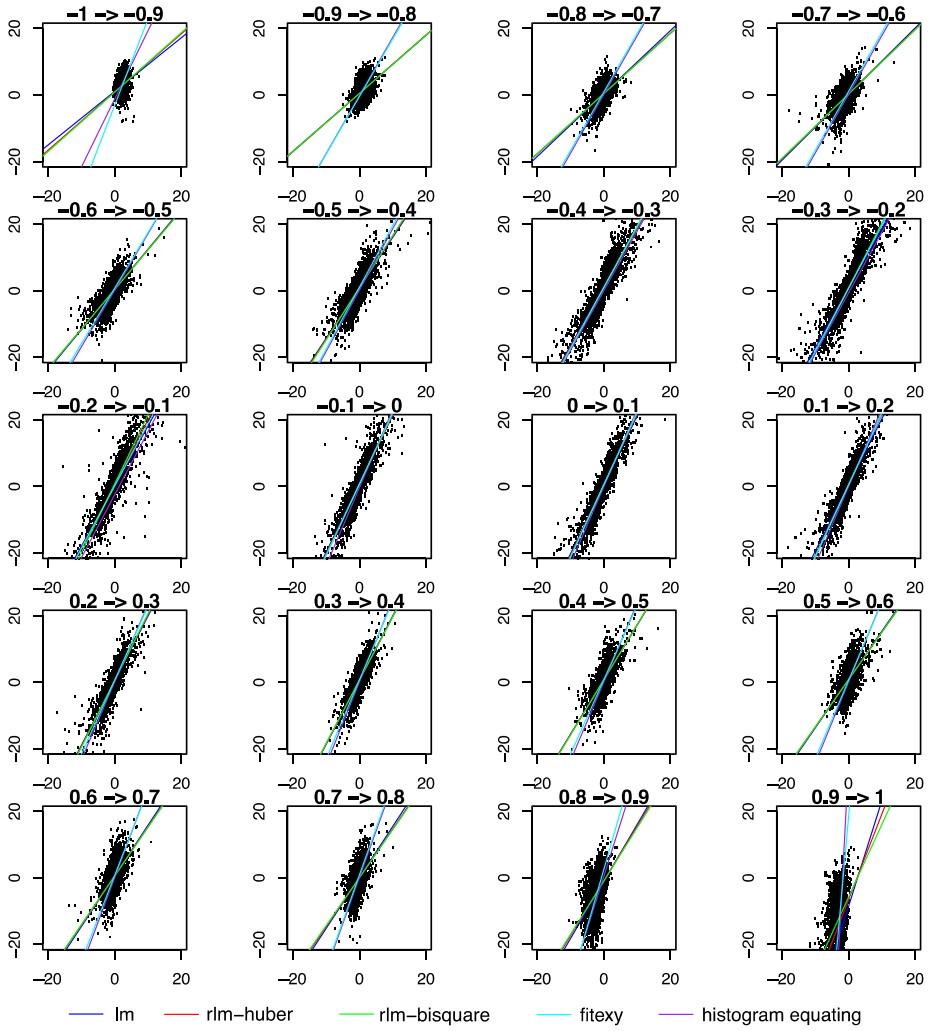

Figure 4 Correlation analysis for GONG (x-axis) and MWO (y-axis) for CR 2047 as a function of $\sin(\lambda)$. The panels start at $-90°$ (top left) and end with $+90°$ (bottom right) in equidistant steps of 0.1, in $\sin(\lambda)$. Both the x- and y-axes range from -20 Gauss to $+20$ Gauss. In each panel five straight lines are fitted to the data: blue – linear regression, red – robust linear regression with Huber weights, green – robust linear regression with bi-square weights, cyan – fitexy and purple – histogram equating (see text for more details).

of measurement. Additionally, this technique allows one in principle to identify conversion factors that are a function of flux. In practice, however, it should be noted that histogram equating must be used with care, and, in particular, the technique is quite sensitive to spatial resolution. In comparisons of GONG magnetograms, for example, it was found that 10-min averaged magnetograms taken at different times of day (but at the same GONG site) displayed diurnal variations that tracked seeing.

Here, we follow the technique explicitly outlined by Wenzler *et al.* (2006). Briefly, we first separated and ordered each of the n_{points} measurements into either positive or negative flux. We defined n_{bins} to be the number of bins (= 100 for comparisons not involving WSO,

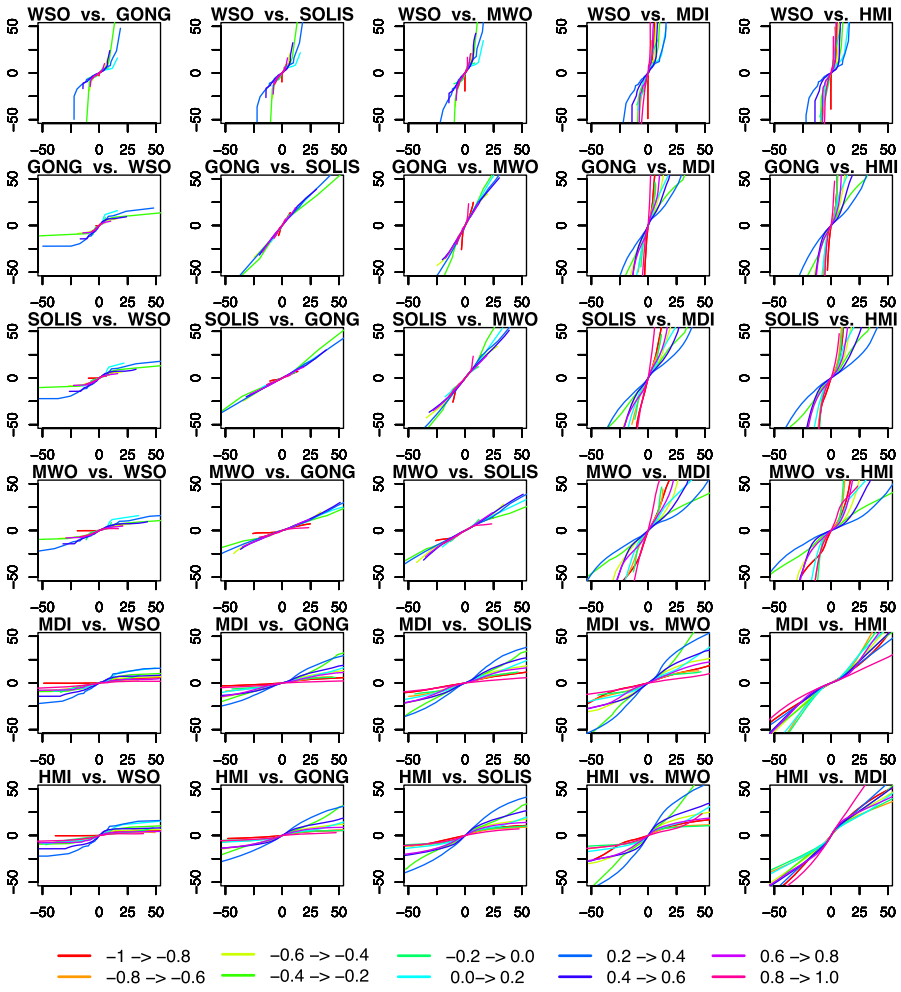

Figure 5 Comparison of histogram-equating tables for six observatories: WSO, GONG, SOLIS, MWO, MDI, and HMI for CR 2097. The leading diagonal comparison that would compare the same observatory with itself has been removed. The different-colored lines show comparisons for the bands in $\sin(\lambda)$ as indicated by the key at the bottom. All field strengths are in gauss.

and 50 if WSO is used) that each half of the measurements are apportioned, then sequentially grouped $\approx n_{\text{points}}/(2 \times n_{\text{bins}})$ into each bin. For each bin, we computed the mean field value. This then led to the so-called histogram-equating tables. Plots of these equating tables from one observatory against another one relate the strength of the field at one observatory to the strength at another observatory as a function of that flux.

Figure 5 compares histogram equating tables between the six observatories for CR 2097. In each panel, the different curves represent bands in $\sin(\lambda)$. The green to blue curves, for example, show the relationship between the fields within the vicinity of the solar equator, and are presumably the most accurate. We note several points. First, where the lines are straight, the conversion factor between the strengths of fields at one observatory and the other is independent of the strength of the flux. This can be seen in the MWO *vs.* SOLIS

comparisons. Similarly, where the curves have a strong S shape, there is a significant dependency on the conversion factor as a function of field strength, *i.e.*, a saturation effect. There are many examples of this, including MWO *vs.* HMI and WSO *vs.* GONG. The S shape may be regular, in which case for that comparison the field from the observatory along the y-axis saturates when the x-axis field reaches a certain value. Alternatively, the curve may be inverted, in which case the observatory plotted along the x-axis saturates with sufficiently strong field strengths from the y-axis observatory. It makes sense, intuitively, that the complementary plot (*i.e.*, observatory A *vs.* observatory B and observatory B *vs.* observatory A) will have regular and inverted shapes (see, *e.g.*, WSO *vs.* HMI and HMI *vs.* WSO). We note also that there is a strong symmetry between the positive and negative sides of each curve. Finally, we emphasize that in these comparisons we are limiting ourselves to the bulk measurements, which for the most part fall within the range of $-50 \rightarrow +50$ G. We believe that the deformities giving rise to the S shape are produced from sunspots, which are not likely to obey the same relationships as the lower-intensity fields from quiet-Sun and coronal-hole regions.

While the previous comparison highlighted the effects of $\sin(\lambda)$, in Figure 6 we compare equating tables for the five observatories that were contemporaneously taking measurements between CR 2047 and 2097. Thus, we are exploring the temporal variability of these curves. For each panel, we only retained data that fell within ± 0.5 in $\sin(\lambda)$, discarding polar values, which have the lowest signal-to-noise ratios. The slope and shape of the curves here should again give us a measure of the relationship between each pair of observatories, but now, the spread or variance in the curves within each panel gives us a measure of change over time. This may represent intrinsic random errors, and hence a measure of the limitations of such an approach, or may hint at systematic variations during the course of a solar cycle, which could, in principle, be incorporated into the conversion factor. A few points are in order. First, some comparisons result in straight, tightly grouped curves, such as those between SOLIS, GONG, and MWO. Comparisons involving either WSO or MDI lead to stronger S-shaped profiles. Moreover, this dependence with flux strength does not disappear when WSO and MDI are compared directly. Second, and this also relates to Figure 5, where a tightly grouped set of straight lines exists, a single conversion factor is defensible. However, where the profile is S-shaped and the lines are spread out, caveats of using a single conversion factor become significant.

6. Conversion Factors: Comparison of Techniques and Temporal Variations

In this section, we compare the linear regression and histogram-equating techniques for estimating the conversion factors, estimate their accuracy, and assess to what extent they vary over time.

Figure 7 summarizes the conversion factors for all combinations of the six observatories for CR 2097, obtained using the synoptic map pixel-by-pixel and histogram-equating techniques, and plotted as a function of $\sin(\lambda)$. Each panel shows the factor necessary to convert the data into one of the five other observatories. Thus, the middle-right panel, for example, shows that MWO data must be multiplied by a factor ≈ 5 for it to match the MDI measurements. (A subset of these data is summarized numerically in Tables 2 and 3.) We note several points. First, there seems to be little obvious trend with latitude: Although there is significant variability, the curves are, to a first approximation, flat. In particular, the WSO slopes show no evidence for a conversion factor proportional to $\sin^2(\lambda)$, which we would

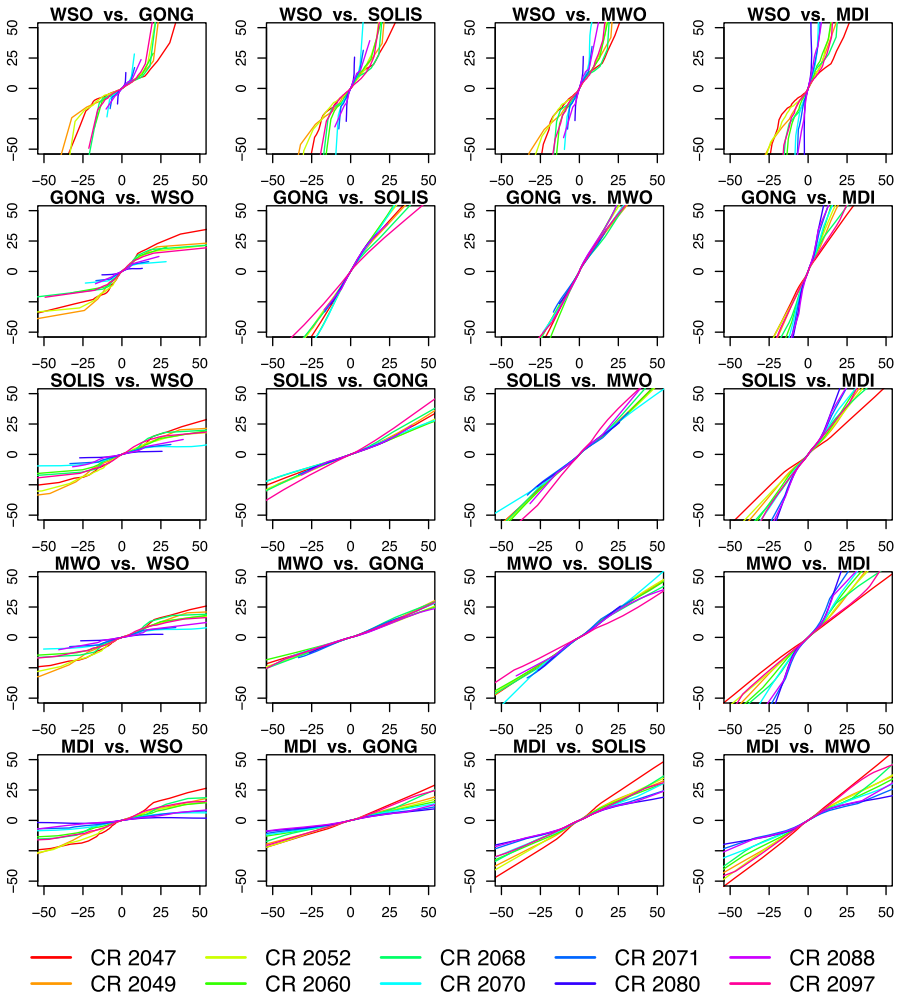

Figure 6 The same as Figure 5, but here, the different-colored lines show results for a selection of Carrington rotations from CR 2047 to CR 2097, as indicated by the key at the bottom.

anticipate if Equation (1) held for WSO data. Second, although often similar, the two techniques (pixel-by-pixel and histogram equating) show some significant differences. This is most apparent at high latitudes, where the data are the noisiest.

In Figure 8, we assess the accuracy of the slopes shown in Figure 7 via Pearson correlation coefficients (χ). As expected, the correlation for both the synoptic map pixel-by-pixel and histogram-equating techniques is best at low- and mid-latitudes and falls beyond $|\sin(\lambda)| = 0.5$. Generally speaking, the correlations for the histogram-equating technique are consistently better than for the pixel-by-pixel comparisons. Additionally, we note that the histogram-equating correlations are lowest where the histogram-equating tables (Figures 5 and 6) display the most nonlinear response (*i.e.*, S-shaped curve), such as between WSO and MDI or HMI and WSO.

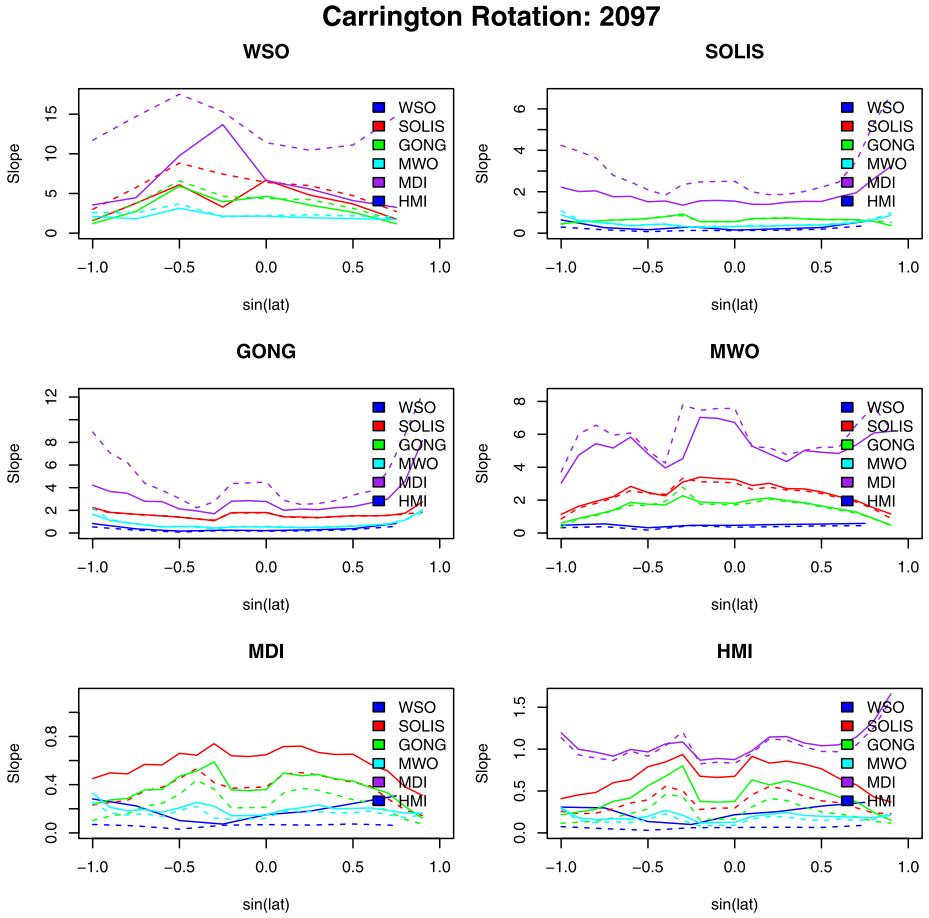

Figure 7 Conversion factors (slopes of pixel-by-pixel comparison, or linear regression of histogram equation tables) for six observatories compared against each other and plotted as a function of $\sin(\lambda)$. The solid line in each panel represents the pixel-by-pixel comparison while the dashed line represents the histogram-equating technique. Each observatory is assigned a different color. Each panel shows the factor necessary to convert the data into one of the five other observatories. Thus, the middle-right panel, for example, shows that MWO data must be multiplied by a factor ≈ 5 for it to match the MDI measurements. (See also Tables 2 and 3.)

To assess the variability of the conversion factors over time, we repeated the analysis previously described for CR 2097 for a selection of Carrington rotations spanning CR 1913 to CR 2127. We retained only data for which $|\sin(\lambda)| < 0.5$. Figure 9 summarizes these results. The curves start and stop at different times, depending on when the particular observatory was collecting data. Thus, GONG (top right) and HMI (bottom right), which only began taking measurements for CR 2047 and CR 2096, respectively, show the shortest traces. In contrast, WSO, SOLIS (made up of KPVT and SOLIS), and MWO show the longest traces because they have effectively been taking continuous measurements for 35 – 40 years. As a first approximation, we might conclude that the profiles are relatively flat, suggesting no obvious temporal evolution in the conversion factor. That is, there is no obvious trend, which might occur if an instrument response function changed during this interval, or periodicity, which might occur if the conversion factors were sensitive to the solar cycle. That is not to

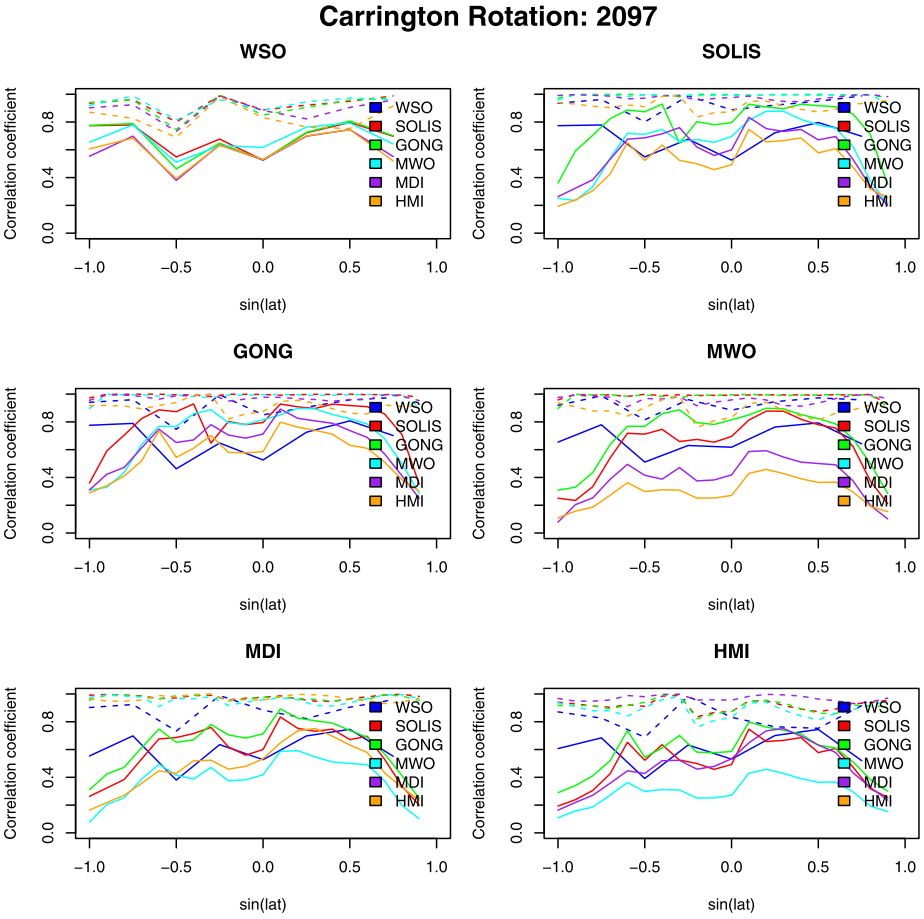

Figure 8 The same as Figure 7, except that correlation coefficients for CR 2097 are plotted as a function of $\sin(\lambda)$.

say that such variations are not present, only that they are not easily discerned. There are, however, some noteworthy points. First, the sharp rise (by a factor of ≈ 2.6) in the WSO-to-MDI conversion factor (top left panel). This started at $\approx$ CR 2050 and appears to have ceased before CR 2090. It should be noted, however, that this effect is amplified because of the already high conversion factor (≈ 12.5). Viewed as a reciprocal (bottom-left panel), the effect is not even noticeable. Since all traces in the WSO panel show this excursion, we infer that this is likely an artifact in the WSO dataset during this period. Second, the replacement of KPVT by SOLIS appears to be relatively seamless. The transition occurred around CR 2008, and while there is a drop in conversion factor (*e.g.*, middle-left panel), there is no systematic change to any of the profiles. Third, MDI and HMI, similarly dovetail nicely into one another (*e.g.*, middle-right panel). This is perhaps not surprising since the two datasets are produced by the same team at Stanford and the method for processing the original magnetograms is the same.

Tables 2 and 3 summarize numerically some of the results displayed in Figures 5 through 9. In Table 2, for example, we can see that WSO data must be multiplied by a

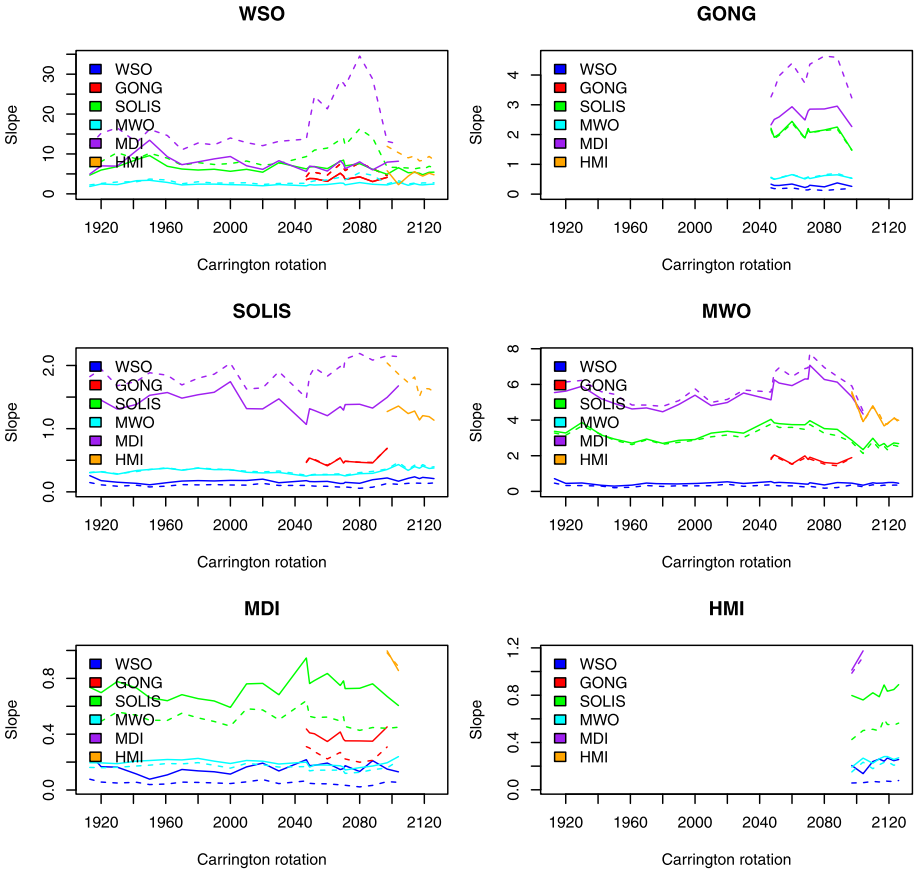

Figure 9 The same as Figure 7, except that the conversion factors are plotted as a function of Carrington rotation covering CR 1913 to CR 2127.

factor of $\approx 2-2.7$ to match data from MWO. This is close to the factor of 1.85 that Svalgaard (2006) has long advocated using for WSO data. Similarly, GONG must be multiplied by a factor of ≈ 2.2 to match data at SOLIS. This is consistent, although a little higher than the known deficit between GONG and SOLIS measurements.

Table 3 provides conversion factors for MWO as a function of Carrington rotation, that is, the factor that MWO measurements must be multiplied by for them to match data at the other observatory. Thus, MWO data must be multiplied by $1/3-1/2$ to match WSO observations, which is consistent with the values from Table 2.

From all of these comparisons, we conclude several points. First, there is no obvious "ground truth." That is, no two observatories consistently produce conversion factors of 1.0. There are pairs that have been made to match (KPVT/SOLIS and MDI/HMI), but no independent pairs. Second, the conversion factors are substantial, ranging up to an order of magnitude. Third, even for specific pair-wise comparisons, the conversion factor varies substantially over the course of a solar cycle.

Table 2 Inferred conversion factors for CR 2097. In each entry the first (second) number gives the slope from the pixel-by-pixel (histogram-equating) comparison, that is, reading down and to the left, this is the number you would need to multiply data from observatory 1 such that it matched data from observatory 2.

	WSO	GONG	SOLIS	MWO	MDI	HMI
WSO	1.0/1.0	$4.14 \pm 1.24/4.59 \pm 1.26$	$4.91 \pm 1.48/6.68 \pm 1.54$	$2.24 \pm 0.51/2.49 \pm 0.68$	$7.95 \pm 3.82/13.16 \pm 3.09$	$5.81 \pm 2.84/11.91 \pm 3.52$
GONG	$0.26 \pm 0.08/0.19 \pm 0.08$	1.0/1.0	$1.48 \pm 0.24/1.48 \pm 0.22$	$0.53 \pm 0.05/0.53 \pm 0.08$	$2.27 \pm 0.39/3.23 \pm 0.82$	$1.93 \pm 0.52/3.08 \pm 0.96$
SOLIS	$0.22 \pm 0.07/0.13 \pm 0.04$	$0.69 \pm 0.11/0.69 \pm 0.10$	1.0/1.0	$0.35 \pm 0.05/0.36 \pm 0.04$	$1.50 \pm 0.08/2.15 \pm 0.27$	$1.27 \pm 0.16/2.04 \pm 0.35$
MWO	$0.46 \pm 0.09/0.36 \pm 0.11$	$1.90 \pm 0.19/1.89 \pm 0.33$	$2.87 \pm 0.38/2.76 \pm 0.34$	1.0/1.0	$5.31 \pm 1.09/5.92 \pm 1.36$	$5.8 \pm 1.69/5.49 \pm 1.38$
MDI	$0.15 \pm 0.07/0.06 \pm 0.02$	$0.45 \pm 0.07/0.31 \pm 0.08$	$0.67 \pm 0.04/0.44 \pm 0.05$	$0.20 \pm 0.04/0.16 \pm 0.03$	1.0/1.0	$1.0 \pm 0.10/0.98 \pm 0.10$
HMI	$0.21 \pm 0.09/0.06 \pm 0.02$	$0.55 \pm 0.14/0.30 \pm 0.11$	$0.80 \pm 0.09/0.42 \pm 0.10$	$0.19 \pm 0.05/0.15 \pm 0.05$	$1.01 \pm 0.10/0.99 \pm 0.13$	1.0/1.0

Table 3 Inferred conversion factors and their standard deviations for a range of Carrington rotations from 1913 through 2126. The values have been scaled to MWO, so that MWO data from CR 1913 must be multiplied by 0.46 to match the values observed at WSO at this time. Where no data are available, dashes are present.

CR	WSO	GONG	KPVT	SOLIS	MWO	MDI	HMI
1913	0.46 ± 0.27	–	3.28 ± 0.43	–	1.00	5.99 ± 1.24	–
1920	0.33 ± 0.08	–	3.15 ± 0.53	–	1.00	6.14 ± 1.33	–
1930	0.33 ± 0.14	–	3.67 ± 1.02	–	1.00	6.23 ± 2.10	–
1942	0.30 ± 0.15	–	3.19 ± 0.68	–	1.00	5.59 ± 1.71	–
1950	0.21 ± 0.03	–	2.88 ± 0.53	–	1.00	5.45 ± 1.07	–
1961	0.24 ± 0.05	–	2.62 ± 0.21	–	1.00	4.84 ± 0.54	–
1970	0.33 ± 0.06	–	2.89 ± 0.18	–	1.00	4.84 ± 0.43	–
1980	0.28 ± 0.06	–	2.64 ± 0.27	–	1.00	4.77 ± 0.48	–
1990	0.32 ± 0.10	–	2.75 ± 0.23	–	1.00	5.09 ± 0.26	–
2000	0.31 ± 0.05	–	2.87 ± 0.31	–	1.00	5.75 ± 0.92	–
2010	0.32 ± 0.08	–	–	3.06 ± 0.32	1.00	4.99 ± 0.78	–
2017	0.32 ± 0.07	–	–	3.22 ± 0.29	1.00	5.41 ± 0.68	–
2020	0.41 ± 0.14	–	–	3.16 ± 0.37	1.00	5.16 ± 0.91	–
2030	0.28 ± 0.14	–	–	3.16 ± 0.37	1.00	5.68 ± 0.91	–
2047	0.36 ± 0.13	1.79 ± 0.28	–	3.77 ± 0.30	1.00	5.57 ± 0.76	–
2049	0.34 ± 0.13	2.06 ± 0.54	–	3.74 ± 0.46	1.00	6.67 ± 0.86	–
2052	0.31 ± 0.17	1.85 ± 0.30	–	3.56 ± 0.34	1.00	6.93 ± 1.91	–
2060	0.31 ± 0.15	1.52 ± 0.18	–	3.59 ± 0.26	1.00	6.44 ± 1.02	–
2068	0.25 ± 0.13	1.87 ± 0.20	–	3.48 ± 0.35	1.00	6.89 ± 1.58	–
2070	0.24 ± 0.07	1.73 ± 0.15	–	3.71 ± 0.38	1.00	6.94 ± 1.24	–
2071	0.29 ± 0.09	1.82 ± 0.11	–	3.75 ± 0.24	1.00	7.74 ± 0.96	–
2080	0.18 ± 0.03	1.53 ± 0.21	–	3.26 ± 0.36	1.00	6.95 ± 0.69	–
2088	0.21 ± 0.05	1.44 ± 0.12	–	3.13 ± 0.53	1.00	6.45 ± 1.52	–
2097	0.36 ± 0.11	1.89 ± 0.33	–	2.76 ± 0.34	1.00	5.92 ± 1.36	5.49 ± 1.38
2104	0.26 ± 0.08	–	–	2.13 ± 0.27	1.00	4.50 ± 0.92	3.89 ± 0.92
2110	0.37 ± 0.14	–	–	2.80 ± 0.30	1.00	–	4.73 ± 1.10
2114	0.37 ± 0.14	–	–	2.39 ± 0.38	1.00	–	4.73 ± 1.10
2117	0.35 ± 0.11	–	–	2.54 ± 0.16	1.00	–	3.80 ± 0.73
2119	0.33 ± 0.19	–	–	2.34 ± 0.31	1.00	–	3.78 ± 0.92
2123	0.35 ± 0.19	–	–	2.59 ± 0.18	1.00	–	4.16 ± 0.85
2126	0.35 ± 0.14	–	–	2.52 ± 0.30	1.00	–	3.88 ± 0.88

7. Summary and Discussion

In this report, we have compared synoptic maps from seven observatories in an effort to find a "ground truth" estimate for the photospheric magnetic field. We found that the maps generally agree with one another but that there are some significant quantitative differences. We provided several tables of conversion factors so that data from one observatory can be converted to data that would match measurements made at another observatory, but temporal variations over a solar cycle suggest that care must be taken in how they are used.

The differences we found between the synoptic maps can substantially affect the global PFSS and MHD models, particularly in the computation of the open, unsigned heliospheric flux. Consider a PFSS solution, for example. Since the magnetic field is potential, solutions are found by solving Laplace's equation: $\nabla^2 \chi = 0$, where χ is a scalar potential. In the simplest application of this model, the only free parameter is the radius of the source surface, that is, the distance from the Sun where all field lines are required to become radial. This is typically taken to be $2.5 R_S$. What this means is that multiplication of the photospheric magnetic field boundary condition by some constant factor results in the open flux that passes through the source surface increasing by that same amount. Alternatively, the amount of open flux can be modulated by moving the source surface in (out) and increasing (decreasing) the amount of open flux. Although the situation is more complicated with MHD models because of the relative strengths of plasma and magnetic field pressures, similar effects are found (Stevens *et al.*, 2012). Thus, given the free parameters in the model, it should be possible to take any input synoptic map and make the open flux agree with *in-situ* measurements. In fact, there seems to be a notable deficit. That is, MHD models predict field strengths that are substantially (2 – 3 times) lower than are observed at 1 AU (Riley *et al.*, 2012). This may be the result of using photospheric field strengths that are too low, or from a new idea, that a significant amount of unipolar flux is present (but not well observed) near the poles of the Sun (Linker *et al.*, 2012).

There are many possible sources of the differences we see from one synoptic map to another. First, for ground-based instruments, seeing caused by atmospheric turbulence can effectively blur the resulting image. Similarly, telescope jitters, which could result from a number of sources, including tracking problems, stability of the telescope, and temperature variations, can reduce the effective resolution of the instrument. Second, incorrect calibration of the polarization modulation, leading to potentially nonlinear errors in the conversion of instrument units to real units. Third, the choice in the spectral line could lead to intrinsic differences between the maps. As is well known, different spectrum lines may be formed at different heights in the expanding magnetic flux of network features, thus, different lines may not measure the same magnetic fields. Fourth, the algorithms used to convert the raw data measured by the instruments could contain errors. In the specific case of synoptic maps, this is additionally complicated by the extra steps in converting the disk magnetograms to Carrington maps and conserving flux in this transformation. Fifth, we must recognize that for these line-of-sight measurements, an average of the magnetic field strength over a particular area is not the same as the average of a line shift over that area, which is then converted into field strength. Thus, our assumption that we can degrade the spatial resolution of a more highly-resolved map to that of a lower-resolution map by simple averaging is strictly not true. Sixth, the line-of-sight component of the photospheric field includes an increasing contribution from poorly resolved, but rapidly changing horizontal fields as one approaches the limb (including the poles). This should not be treated as a radial field, but in practice often is. And, while it is difficult to assess its impact, to the extent that it does not average to zero within a particular pixel, it may be a source of discrepancy between different datasets.

An additional and distinct set of problems arises from instrumental effects, which can appear at different observatories, at different times, and for both known and (at least initially) unknown reasons. Several examples serve to illustrate this problem. First, toward the end of the MDI mission, the zero-level drifted. Second, there is a known scaling problem with GONG in the sense that it measures signals that are approximately 70 % of what they should be. The reason is not clear: The field measurement is simply the difference between the Doppler-shift images made in left- and right-circularly polarized light. The velocities are what one anticipates from solar rotation and the circular polarization modulation has

been measured to be essentially 100 % efficient. Third, the modulator in the SOLIS instrument slowly degraded from 2003 to 2006, resulting in weaker signals. This was corrected in March 2006, resulting in higher signals. Fourth, the cameras in the SOLIS instrument were replaced in late 2009, resulting in another jump in the signal. These effects are not immediately evident in the analysis presented here. And fifth, and again concerning SOLIS, the current modulator has a spatial variation across the disk such that the signals from the west limb are weaker than those from the east limb. This effect is corrected for by a calibrating function, but it is not known how stable the phenomenon is.

This study did not resolve the illusive problem of finding an underlying "ground truth" for the photospheric magnetic field. It might have been tempting to infer from the seamless continuity between KPVT/SOLIS and MDI/HMI pairs that one of these might have provided the most accurate estimate of the photospheric field. However, these continuities were accomplished by design and are not the result of independence. MDI and SOLIS, at least using synoptic map pixel-by-pixel comparisons, resulted in conversion factors that were very close to one. Since the instruments/observatories are managed independently by different teams at different locations, does this provide any evidence for a "ground truth?" Unfortunately, and again, the data-processing pipelines are not strictly independent. Liu *et al.* (2012) described that they used a previous analysis by Tran *et al.* (2005), which compared MDI and MWO magnetograms to bring the MDI measurements into agreement with MWO values. While the logic behind the application of the MWO correction factor appears to be theoretically justified, such bootstrapping prevents us from inferring this as evidence of a "ground truth."

Another limitation of the present study, and one of our own making, is the use of synoptic maps instead of magnetograms. Our rationale for this was that these maps are used to drive global numerical models and thus represent a practical starting point for the comparison. However, significant processing has occurred between magnetograms and maps. The relationship between a resolution element in the synoptic map and the original magnetogram, in particular, is quite remote. At WSO, for example, the native pixel size is 3 arcmin. The raw magnetograms are composed of 11 scan lines in latitude and 23 positions in longitude; the apertures in the longitude direction overlapping by 50 %. These are then remapped into heliographic coordinates and interpolated using a polynomial smoothing function, which produces a regular map with 5-degree steps in Carrington longitude and 30 points in sin-latitude. These magnetograms are then used to construct the synoptic maps, which involves using all observations of a given point within 55° of central meridian to construct an average value. No adjustment for any radial projection is made in this process. Ultimately, it may be that no "ground truth" can be found from an analysis of the synoptic maps: Instead, we must directly compare the disk magnetograms.

There are at least several avenues we could pursue to resolve some of the issues raised here. First, we could compare our conversion factors with those obtained by looking at the mean magnetic field of the Sun (MMFS), that is, the strength of the line-of-sight component of the photospheric field averaged over the entire visible hemisphere (Scherrer *et al.*, 1977). However, it is not clear whether the factors obtained from such a comparison would be expected to match those obtained here. In fact, MMFS comparisons between SOLIS and HMI produce substantially different results than resolved-image comparisons (Pietarila *et al.*, 2013). Second, we could analyze the disk magnetograms directly. This would allow us to at least separate out intrinsic differences between the measurements and differences introduced through the process of assembling the maps. Three preliminary but independent studies by co-authors of this paper, however, do not appear to be converging on a consensus view. It appears that the results are sensitive to one of a number of potential effects: i) How

the data are binned, ii) which intervals are chosen, and iii) what fitting techniques are applied to the scatterplots. We are currently designing more focused investigations to remove these contaminations, or at least assess their effects on the results.

In closing, we reiterate that the main point of this study was to quantitatively assess the differences between synoptic magnetograms from a selection of solar observatories, and if possible, identify a "ground truth" dataset. While successful on the former, we were not able to find evidence to support using one dataset over another. PFSS and MHD numerical models may be able to help us resolve this; however, the presence of free parameters within the model will make such a study challenging. On the other hand, the unique nature of the recent protracted solar minimum may provide the necessary conditions to accurately connect the magnetic flux observed *in situ* at 1 AU with that observed in the photosphere through a global model, if used in conjunction with other observed constraints, such as the measured bulk solar wind speed, location of coronal hole boundaries, and disk emission profiles.

Acknowledgements The authors gratefully acknowledge the support of the LWS Strategic Capabilities Program (NASA, NSF, and AFOSR), the NSF Center for Integrated Space Weather Modeling (CISM), NASA's Heliophysics Theory Program (HTP), the Causes and Consequences of the Minimum of Solar Cycle 24 program, the STEREO/IMPACT, STEREO/SECCHI, and SDO/HMI instrument teams. Wilcox Solar Observatory data used in this study were obtained via the web site http://wso.stanford.edu courtesy of J.T. Hoeksema. The Wilcox Solar Observatory is currently supported by NASA. The SOLIS, GONG and KPVT programs are managed by the National Solar Observatory, which is operated by AURA, Inc. under a cooperative agreement with the National Science Foundation. SOHO/MDI is a project of international cooperation between ESA and NASA. The MWO data included in this study are from the synoptic program at the 150-Foot Solar Tower of the Mt. Wilson Observatory. The Mt. Wilson 150-Foot Solar Tower is operated by UCLA, with funding from NASA, ONR and NSF, under agreement with the Mt. Wilson Institute. HMI data are courtesy of the Joint Science Operations Center (JSOC) Science Data Processing team at Stanford University.

References

Arge, C.N., Henney, C.J., Koller, J., Compeau, C.R., Young, S., MacKenzie, D., Fay, A., Harvey, J.W.: 2010, Air Force data assimilative photospheric flux transport (ADAPT) model. In: Maksimovic, M., Issautier, K., Meyer-Vernet, N., Moncuquet, M., Pantellini, F. (eds.) *Twelfth International Solar Wind Conference*, *AIP Conf. Proc.* **1216**, 343 – 346. doi:10.1063/1.3395870.

Berger, T.E., Lites, B.W.: 2002, Weak-field magnetogram calibration using advanced Stokes polarimeter flux-density maps – I. Solar optical universal polarimeter calibration. *Solar Phys.* **208**, 181 – 210. doi:10.1023/A:1020537923728.

Bering, E.A., Benbrook, J.R., Engebretson, M.J., Arnoldy, R.L.: 1998, Simultaneous electric and magnetic field observations of Pc1 – 2, and Pc3 pulsations. *J. Geophys. Res.* **103**, 6741 – 6762. doi:10.1029/97JA03327.

Bertello, L., Petrie, G.J., Tran, T.: 2010, The impact of different global photospheric magnetic field maps on coronal models. In: AGU Fall Meeting, SH31B-1796.

Cauzzi, G., Smaldone, L.A., Balasubramaniam, K.S., Keil, S.L.: 1993, On the calibration of line-of-sight magnetograms. *Solar Phys.* **146**, 207 – 227. doi:10.1007/BF00662010.

Demidov, M.L., Balthasar, H.: 2009, Spectro-polarimetric observations of solar magnetic fields and the SOHO/MDI calibration issue. *Solar Phys.* **260**, 261 – 270. doi:10.1007/s11207-009-9443-5.

Demidov, M.L., Balthasar, H.: 2012, On multi-line spectro-polarimetric diagnostics of the quiet Sun's magnetic fields. Statistics, inversion results and effects on the SOHO/MDI magnetogram calibration. *Solar Phys.* **276**, 43 – 59. doi:10.1007/s11207-011-9863-x.

Demidov, M.L., Golubeva, E.M., Balthasar, H., Staude, J., Grigoryev, V.M.: 2008, Comparison of solar magnetic fields measured at different observatories: peculiar strength ratio distributions across the disk. *Solar Phys.* **250**, 279 – 301. doi:10.1007/s11207-008-9225-5.

Jones, H.P.: 1989, Magnetograph group summary. In: Winglee, R.M., Dennis, B.R. (eds.) *Max'91 Workshop2: Developments in Observations and Theory for Solar Cycle 22*, *NASA-TM-101893*, 17 – 26.

Jones, H.P.: 1992a, Calibrating the NASA/NSO spectromagnetograph. *Bull. Am. Astron. Soc.* **24**, 814.

Jones, H.P.: 1992b, Comparison of magnetograms by histogram equating. *Bull. Am. Astron. Soc.* **24**, 1252.

Jones, H.P., Ceja, J.A.: 2001, Preliminary comparison of magnetograms from KPVT/SPM, SOHO/MDI and GONG$^+$. In: Sigwarth, M. (ed.) *Advanced Solar Polarimetry – Theory, Observation, and Instrumentation*, *ASP Conf. Ser.* **236**, 87 – 95.

Jones, H.P., Duvall, T.L. Jr., Harvey, J.W., Mahaffey, C.T., Schwitters, J.D., Simmons, J.E.: 1992, The NASA/NSO spectromagnetograph. *Solar Phys.* **139**, 211 – 232. doi:10.1007/BF00159149.

Jones, H., Bogart, R., Canfield, R., Chapman, G., Henney, C., Kopp, G., *et al.*: 1993, A magnetograph comparison workshop. *Bull. Am. Astron. Soc.* **25**, 1216.

Jones, H.P., Harvey, J.W., Henney, C.J., Keller, C.U., Malanushenko, O.M.: 2004, Measurement scale of the SOLIS vector spectromagnetograph. *Bull. Am. Astron. Soc.* **36**, 709.

Landi Degl'Innocenti, E.: 1982, On the effective Lande factor of magnetic lines. *Solar Phys.* **77**, 285. doi:10.1007/BF00156111.

Linker, J.A., Mikic, Z., Riley, P., Downs, C., Lionello, R., Henney, C., Arge, C.N.: 2012, Coronal and heliospheric modeling using flux-evolved maps. In: *Proceedings of Solar Wind 13*, *AIP Conf. Proc.* **1539**, 26 – 29.

Liu, Y., Hoeksema, J.T., Scherrer, P.H., Schou, J., Couvidat, S., Bush, R.I., Duvall, T.L., Hayashi, K., Sun, X., Zhao, X.: 2012, Comparison of line-of-sight magnetograms taken by the Solar Dynamics Observatory/Helioseismic and Magnetic Imager and Solar and Heliospheric Observatory/Michelson Doppler Imager. *Solar Phys.* **279**, 295 – 316. doi:10.1007/s11207-012-9976-x.

Lockwood, M.: 2001, Long-term variations in the magnetic fields of the Sun and the heliosphere: their origin, effects, and implications. *J. Geophys. Res.* **106**, 16021 – 16038. doi:10.1029/2000JA000115.

Lockwood, M., Owens, M.J.: 2011, Centennial changes in the heliospheric magnetic field and open solar flux: the consensus view from geomagnetic data and cosmogenic isotopes and its implications. *J. Geophys. Res.* **116**, 4109. doi:10.1029/2010JA016220.

Lockwood, M., Stamper, R., Wild, M.N.: 1999, A doubling of the Sun's coronal magnetic field during the past 100 years. *Nature* **399**, 437 – 439.

Luhmann, J., Lee, C.O., Riley, P., Jian, L.K., Russell, C.T., Petrie, G.: 2012, Interplanetary conditions: lessons from this minimum. In: Mandrini, C.H., Webb, D.F. (eds.) *Comparative Magnetic Minima: Characterizing Quiet Times in the Sun and Stars*, *IAU Symp.* **286**, 168 – 178. doi:10.1017/S1743921312004802.

Petrie, G.J.D., Canou, A., Amari, T.: 2011, Nonlinear force-free and potential-field models of active-region and global coronal fields during the whole heliosphere interval. *Solar Phys.* **274**, 163 – 194. doi:10.1007/s11207-010-9687-0.

Pietarila, A., Bertello, L., Harvey, J.W., Pevtsov, A.A.: 2013, Comparison of ground-based and space-based longitudinal magnetograms. *Solar Phys.* **282**, 91 – 106. doi:10.1007/s11207-012-0138-y.

Riley, P.: 2007, An alternative interpretation of the relationship between the inferred open solar flux and the interplanetary magnetic field. *Astrophys. J. Lett.* **667**, L97 – L100. doi:10.1086/522001.

Riley, P., Lionello, R., Linker, J.A., Mikic, Z., Luhmann, J., Wijaya, J.: 2011, Global MHD modeling of the solar corona and inner heliosphere for the whole heliosphere interval. *Solar Phys.* **274**, 361 – 375. doi:10.1007/s11207-010-9698-x.

Riley, P., Linker, J.A., Lionello, R., Mikic, Z.: 2012, Corotating interaction regions during the recent solar minimum: the power and limitations of global MHD modeling. *J. Atmos. Solar-Terr. Phys.* **83**, 1 – 10. doi:10.1016/j.jastp.2011.12.013.

Scherrer, P.H., Wilcox, J.M., Svalgaard, L., Duvall, T.L. Jr., Dittmer, P.H., Gustafson, E.K.: 1977, The mean magnetic field of the Sun – observations at Stanford. *Solar Phys.* **54**, 353 – 361. doi:10.1007/BF00159925.

Scherrer, P.H., Bogart, R.S., Bush, R.I., Hoeksema, J.T., Kosovichev, A.G., Schou, J., *et al.*: 1995, The Solar Oscillations Investigation – Michelson Doppler Imager. *Solar Phys.* **162**, 129 – 188. doi:10.1007/BF00733429.

Stellman, J.: 1998, *Encyclopaedia of Occupational Health and Safety*, International Labour Office, Geneva.

Stevens, M.L., Linker, J.A., Riley, P., Hughes, W.J.: 2012, Underestimates of magnetic flux in coupled MHD model solar wind solutions. *J. Atmos. Solar-Terr. Phys.* **83**, 22 – 31. doi:10.1016/j.jastp.2012.02.005.

Svalgaard, L.: 2006, How good (or bad) are the inner boundary conditions for heliospheric solar wind modeling? Presentation at 2006 SHINE Workshop.

Svalgaard, L., Cliver, E.W.: 2005, The IDV index: Its derivation and use in inferring long-term variations of the interplanetary magnetic field strength. *J. Geophys. Res.* **110**, A12103. doi:10.1029/2005JA011203.

Svalgaard, L., Duvall, T.L. Jr., Scherrer, P.H.: 1978, The strength of the Sun's polar fields. *Solar Phys.* **58**, 225 – 239. doi:10.1007/BF00157268.

Thornton, C.E., Jones, H.P.: 2002, Comparison of three solar magnetographs. *Bull. Am. Astron. Soc.* **34**, 1243.

Tran, T., Bertello, L., Ulrich, R.K., Evans, S.: 2005, Magnetic fields from SOHO MDI converted to the Mount Wilson 150 foot Solar Tower scale. *Astrophys. J. Suppl.* **156**, 295 – 310. doi:10.1086/426713.

Ulrich, R.K.: 1992, Analysis of magnetic fluxtubes on the solar surface from observations at Mt. Wilson of λ5250 and λ5233. In: Giampapa, M.S., Bookbinder, J.A. (eds.) *Seventh Cambridge Workshop: Cool Stars, Stellar Systems, and the Sun*, *ASP Conf. Ser.* **26**, 265 – 267.

Ulrich, R.K., Bertello, L., Boyden, J.E., Webster, L.: 2009, Interpretation of solar magnetic field strength observations. *Solar Phys.* **255**, 53 – 78. doi:10.1007/s11207-008-9302-9.

Wang, Y.M., Sheeley, N.R.: 1995, Solar implications of Ulysses interplanetary field measurements. *Astrophys. J. Lett.* **447**, L143 – L146. doi:10.1086/309578.

Wenzler, T., Solanki, S.K., Krivova, N.A., Fröhlich, C.: 2006, Reconstruction of solar irradiance variations in cycles 21 – 23 based on surface magnetic fields. *Astron. Astrophys.* **460**, 583 – 595. doi:10.1051/0004-6361:20065752.

Appendix N

The Day the Sun Stood Still: Using global Thermodynamic MHD Simulations to Infer the Structure of the Solar Corona and Inner Heliosphere during the Maunder Minimum

Pete Riley, Roberto Lionello, Jon A. Linker, Leif Svalgaard, Ed Cliver, Andre Balogh, Jürg Beer, Paul Charbonneau, Nancy Crooker, George Siscoe, Marc DeRosa, Mike Lockwood, Ken McCracken, Matt Owens, Ilya Usoskin, Yi-Ming Wang, and S. Koutchmy

To be submitted to Astrophys. J., 2013.

The Day the Sun Stood Still: Using global Thermodynamic MHD Simulations to Infer the Structure of the Solar Corona and Inner Heliosphere during the Maunder Minimum

Pete Riley, Roberto Lionello, and Jon A. Linker

Predictive Science, 9990 Mesa Rim Road, Suite 170, San Diego, CA 92121, USA.

pete@predsci.com and lionel@predsci.com

Leif Svalgaard

Stanford University, HEPL, Via Ortega, Stanford, CA 94305 USA

leif@leif.org

Ed Cliver

AFRL/RVBXS, Sunspot, CO 88349 USA

ecliver@nso.edu

Andre Balogh

Imperial College, South Kensington Campus, Department of Physics, Huxley Building 6M68, London, SW7 2AZ, UK

a.balogh@ic.ac.uk

Jürg Beer

Surface Waters, Eawag, Ueberlandstrasse 133, P.O. Box 611, 8600 Duebendorf, Switzerland

Juerg.beer@eawag.ch

Paul Charbonneau

Département de Physique, Universit de Montral, C.P. 6128 Centre-Ville, Montral, Qc, H3C-3J7, Canada

paulchar@astro.umontreal.ca

Nancy Crooker and George Siscoe

Center for Space Physics, Boston University,725 Commonwealth Avenue, Boston, MA 02215, USA

crooker@bu.edu and siscoe@bu.edu

Marc DeRosa

Lockheed Martin Solar and Astrophysics Laboratory, 3251 Hanover St., B/252, Palo Alto, CA 94304, USA

derosa@lmsal.com

Mike Lockwood

University of Reading, Department of Meteorology, Earley Gate, P.O. Box 243, Reading, Berkshire, RG6 6BB, UK

lockwood@reading.ac.uk

Ken McCracken

100 Mt. Jellore Lane, Woodlands, NSW, 2575, Australia

jellore@hinet.au

Matt Owens

Department of Meteorology, University of Reading, Reading RG6 6BB, UK

m.j.owens@reading.ac.uk

Ilya Usoskin

Sodankyla Geophysical Observatory, FIN-90014, University of Oulu, Finland

m.j.owens@reading.ac.uk

Yi-Ming Wang

Naval Research Laboratory, 4555 Overlook Ave SW, Washington DC 20375-5252, USA

ilya.usoskin@oulu.fi

and

S. Koutchmy

Institut d'Astrophysique de Paris, CNRS and UPMC, Paris, France

koutchmy@iap.fr

Received _____; accepted _____

To be submitted to Ap. J.

ABSTRACT

Observations of the Sun's corona during the space era have led to a picture of relatively constant, but modulating solar output and structure. Longer-term, more indirect measurements, such as from ^{10}Be, coupled by other albeit less reliable contemporaneous reports, however, suggest periods of significant departure from this standard, which may possibly have produced terrestrial weather effects. The Maunder Minimum, was one such epoch where: (1) Sunspots effectively disappeared for long intervals during a 70-year period; (2) Eclipse 'observations' suggested the distinct lack of a visible K-corona but possible appearance of the F-corona; (3) Reports of aurora were notably reduced; and (4) Cosmic ray intensities at Earth were inferred to be substantially higher. Using a global thermodynamic MHD model, we have constructed a range of possible coronal configurations for the Maunder Minimum period and compared their predictions with these limited observational constraints. We conclude that the most likely state of the corona during the Maunder Minimum was not merely that of the 2008/2009 solar minimum, as has been suggested in several recent studies. Instead, we argue that the Sun's photospheric magnetic field was substantially reduced (by up to an order of magnitude) and this resulted in, and is consistent with the observations associated with this period. We discuss the implications of this work in terms of future long-term space weather forecasting.

Subject headings: Solar Corona; Solar Wind; MHD Simulations

1. Introduction

The "Maunder Minimum" is a period of time between approximately 1645 and 1715 when the observed number of sunspots all but disappeared (Eddy 1976). Although it can be argued how accurate the sunspot record was during this interval, the low numbers cannot be due to a lack of observations; a number of well-known astronomers, including Giovanni Domenico Cassini, regularly made observations of the Sun during this time (ref). During the same period of time, as we will discuss in more detail below, the number of aurora decreased, cosmic ray fluxes increased, and the Sun's corona apparently lost its visible structure. Perhaps even more intriguingly, this period coincided with the so-called "Little Ice Age," during which time both North America and Europe experienced bitterly cold winters (e.g., Luterbacher (2001)).

Broadly speaking, we can differentiate between two distinct ideas for the state of the solar corona during the Maunder Minimum. The first, and original idea was of a corona that was radically different from what we observe today (Eddy 1976; Parker 1976; Suess 1979). The second, and currently more favored interpretation is of a corona that was not significantly different than the one observed during the recent and somewhat unique solar minimum of 2008/2009 (Svalgaard & Cliver 2007; Schrijver et al. 2011; Wang & Sheeley 2013).

In his landmark paper, (Eddy 1976) reviewed an extensive range of available data associated with this time period, including auroral records, sunspots, carbon-14 records, and eclipse observations. From the (i) prolonged absence of sunspots; (ii) reduction in aurora reports; (iii) decrease in ^{14}C (suggesting a significant increase in cosmic ray flux hitting the Earth); and (iv) absence of any structured corona during eclipses, he inferred that, to manifest such phenomena, the solar corona must have existed in a unique configuration. He suggested that "the solar wind would have blown steadily and isotropically, and possibly at

gale force, since high-speed streams of solar wind are associated with the absence of closed structure in the solar corona." He had concluded that, based on eclipse observations, there likely wasn't any K-corona present, and that, in fact, what was observed could have been from dust-scattered light (i.e., the F-corona). When asked about the Maunder minimum, Parker (1976) suggested "In view of the absence of a white light corona, we may conjecture whether the Sun was entirely shrouded in a coronal hole, yielding a fast steady solar wind, or whether there simply was no solar wind at all. I would guess the former, but I know of no way to prove the answer." Suess (1979) expanded on these views: "Firstly, C-14 data indicate an enhanced cosmic ray intensity, with the conclusion that the interplanetary magnetic field was smooth and perhaps of low intensity. Secondly, the apparent absence of a corona during eclipses requires low coronal density, suggesting an absence of closed magnetic loops. Thirdly, the absence of sunspots eliminates the possibility of a solar maximum type of corona of low emission intensity and implies a low large-scale photospheric field intensity. Finally, the absence of mid-latitude aurorae implies either that the solar wind speed or the IMF intensity, or both, were low and not irregular."

More recently, the idea that the Maunder Minimum was radically different than anything witnessed during the space era has come to be replaced with the idea that the recent, and undoubtedly unique solar minimum of 2008/2009 provided an accurate proxy for Maunder Minimum conditions. This perspective has been built up on two primary fronts. First, Svalgaard & Cliver (2007) proposed that there appears to be minimum value that can exist in the strength of the interplanetary magnetic field. It is important to recognize, however, that this is a hypothesis, not a robust empirically-determined result. Although the strength of the IMF has apparently returned to the same approximate value since the start of the space era, there is no guarantee that this must remain so, in fact, the precise value of this "floor" had to be lowered as we witnessed the minimum of 2008/2009. Second, Schrijver et al. (2011) argued that there exists a minimum state of solar magnetic activity,

associated with the presence of small-scale ephemeral regions. They concluded that "the best estimate of magnetic activity...for the least-active Maunder Minimum phases appears to be provided by direct measurements in 2008-2009." In perhaps what could be described as a compromise between these two extreme views, Wang & Sheeley (2013) presented a solution where the photospheric field consisted of ephemeral regions with a reduced, but not absent global dipole. They reasoned that a Sun consisting exclusively of ephemeral regions would generate no IMF, in conflict with the apparent continuation of the solar cycle (albeit much reduced) during the Maunder Minimum (McCracken et al. 2011).

Although our analysis focuses principally on inferring the likely structure of the corona and inner heliosphere during the Maunder minimum period, we are obliged to note that this period roughly coincided with an interval known as the "little ice age," during which time, the temperature in northern Europe was lower than normal (ref), and sufficiently so that the river Thames froze over (Manley 2011). The connection, if any, between the two events, remains a topic of lively debate. Our main contribution to the discussion would be that if, on one hand, we conclude that the Sun during the Maunder minimum period was essentially the same as the 2008/2009 Sun, then it is very unlikely that there can be a causal connection between the Maunder minimum and the little ice age. On the other hand, if the Sun was radially different, then it at least opens the door for a variety of possible mechanisms to connect solar variability with Earth climate.

In this study, we apply a global MHD model to infer the most likely configuration of the solar corona (and by extension, the inner heliosphere) that is consistent with the observations associated with the Maunder Minimum. In section 2, we review, re-analyze, and extend previous studies of the limited, and often indirect observations of the period between 1645 and 1715. Our purpose is not to argue for a particular interpretation, but to identify and assess possible interpretations and estimate their uncertainties, even

qualitatively. In Section 3, we introduce a set of possible configurations of the photospheric magnetic field that may have existed during the Maunder minimum, and use them to drive MHD simulations. In Section 4, we describe our MHD formalism, paying particular attention to the unique aspects that make it applicable and relevant for studying the Maunder Minimum. In Section **??**, we describe the model results and relate them to the 'observations,' allowing us to refute some configurations, whilst finding support for others. In Section 4.5, we apply a simple Bayesian, or conditional argument to assess the two principal hypotheses, which, while not definitively supporting or refuting either, does provide a heuristic way to weigh the various pieces of evidence. Finally, we summarize the main points of this study, and discuss the implications in terms of both understanding the Maunder Minimum and other periods of inactivity, the likelihood of future grand minima, and the possible correlation between such intervals and terrestrial climate.

2. "Observations" during the Maunder Minimum

Although a number studies since J. Eddy's landmark paper (Eddy 1976) have revised, and refined our interpretation of the available but limited "observations" associated with the Maunder minimum, it is worth reviewing them here, both to point out where they lead to definitive inferences and where they remain ambiguous. Additionally, it affords us an opportunity to offer our own interpretation. In particular, using these observations, in Section 4.5, we will apply Bayesian arguments to deduce the most probable configuration of the corona.

The "observations" we consider here are: (1) the sunspot time series; (2) aurora reports; (3) cosmic ray fluxes as inferred from 10-Be and 14-C records; and (4) eclipse observations. Figure 1 summarizes the first three of these records stretching back from near-present day to the Maunder minimum. In the following subsections, we consider each

in more detail.

2.1. Sunspot "Observations"

Figure 1(a) summarizes the sunspot record back in time until 1610 (Svalgaard 2011). This is the parameter that originally defined the Maunder minimum, although the numbers themselves have undergone significant revision since they were first analyzed by G. Spörer and E. W. Maunder in the 1890's (Sporer 1887; Maunder 1894). As a practical definition, we follow the consensus of identifying the Maunder minimum as the time period between ~ 1645 and $\sim 1700-1715$ when sunspots all but disappeared. It is important to emphasize, however, that they did not disappear entirely; there were isolated observations of sunspots throughout this period. On the other hand, there were intervals of up to 25 years with virtually no sunspots being reported (Soon & Yaskell 2003).

The sunspot record is not without error or uncertainty, however. First, we must confront the claim that the reduction in sunspot number was not due processes at the Sun, but from a lack of observations. Hoyt & Schatten (1996) examined how well sunspots were observed during the Maunder Minimum, concluding, perhaps somewhat conservatively, that $68\% \pm 7\%$ of the days were observed. Therefore, the paucity of sunspots was due to them not being observed, not from there being no observations. Second, the apparent lack of sunspots may have been caused by atmospheric effects, such as the presence of volcanic ash masking the sunspots or increasing the threshold for detection. Third, the sunspot record has undergone revision over the years. Thus, the curve shown in Figure 1(a) differs from that of, say, Usoskin (2008) because of a renormalization of the last half century's worth of data. If such recent measurements have been found to be inaccurate, what does this suggest for records originating more than 300 years earlier? Although this could have a qualitative effect on the record, it is unlikely to change the basic, qualitative profile shown

in Figure 1(a).

Assuming that the SSN record is a reliable proxy for the number of sunspots, we infer that at the same, around ≈ 1645 they suddenly 'turned off,' and remained as such until ≈ 1715. Thus, from the perspective of the SSN, the Maunder interval is a period of constant inactivity. It is worth noting here that the point in the solar cycle at which the Maunder Minimum began could have important theoretical ramifications. Mackay (2003) argued that if the Maunder Minimum began at solar maximum, this would have led to a configuration with effectively no unipolar polar fields. In contrast, if it began near, or at solar minimum, strong unipolar polar fields would have been present that may have remained intact to a large extent throughout the interval. On this question, Figure 1(a) is at best ambiguous.

At the risk of over-interpreting the signal, the SSN record during the Maunder Minimum further suggests that sunspots did cluster into perhaps half-a-dozen or so small peaks that may be suggestive of a continued solar cycle within the Maunder Minimum. Additionally, these cluster peaks, and the underlying base, tended to decrease slightly, perhaps suggesting that the Sun sank to even lower states of inactivity during the 70-year period. Finally, we note that the Maunder Minimum period terminated suddenly, or rather that solar activity resumed quite suddenly after 1700.

2.2. Aurora "Observations"

Records of aurora date back thousands of years (Siscoe 1980). Yet, again, interpreting them is fraught with danger. Does the absence of an aurora mean that one didn't occur, or just that it wasn't reported? Additionally, different records provide, at best, only threshold indicators of geomagnetic activity. Consistent observations at mid-latitudes, for example, will not contain modest geomagnetic events that reveal themselves only at the highest

geomagnetic latitudes. Perhaps the strongest statement we can make is that if an aurora was observed, then it probably happened (there not being any other obvious phenomena that could mimic this effect), whereas, if none were reported, it may or may not mean that none occurred. Thus, the auroral record, at least older than a century, at best, provides a lower limit of geomagnetic activity.

In spite of these limitations, several records exist and have been analyzed in detail. Here, we rely on the record reconstructed by Réthly & Berkes (1963), however, our conclusions would not be affected had we used other researcher's work (e.g., Schröder (1992)). We consider the raw counts and smoothed profile shown in Figure 1(b) to make the following points. First, geomagnetic activity did not cease during the MM period. Second, activity was higher both before and after the Maunder minimum. Third, there is even a tentative suggestion of a solar cycle modulation in the number of aurora days.

The presence of any aurora indicates that the Sun, through the solar wind, was connected to the Earth's upper atmosphere. To generate aurora requires a dawn-dusk electric field, which in turn, requires a roughly radially-directed solar wind carrying a B_z magnetic field. Additionally, at least some of the electrons and ions bombarding the atmospheric oxygen and nitrogen atoms presumably come directly from the solar wind. We conclude then, that Parker's suggestion that there might not be any solar wind at all, is not consistent with these observations.

Since these observations were made at mid-European latitudes, we can also infer that they were probably related to relatively substantial geomagnetic storms. This, in turn suggests that they originated not from corotating interaction regions (CIRs), which would tend to produce minor events, but from coronal mass ejections (CMEs). Further, we could anticipate that these CMEs were associated with the appearance of the relatively few sunspots that were present, signaling the presence of active regions. It is from active

regions that the strongest (i.e., fastest and largest field strengths) are typically produced. Unfortunately, the limited number of auroral sightings during the Maunder minimum (one at most in any one year, except once when two were observed) does not allow us to make a meaningful correlation between sunspot number and number of aurora. In contrast, later in the record, there is a significantly clearer correlation between the temporal location of the peaks in the two time series (although no obvious association in their amplitude).

In the context of modern times, how geomagnetically quiet was the Maunder Minimum? Unfortunately, these data had ceased to be recored by 1962. At most, during most of the MM period, only one aurora was observed at mid-latitudes in a single year, but during most years, no aurora were reported. In fact, during the 70 year period, only 5-6 events we reported. This once in more than a decade frequency is considerably lower than the time period from 1900-1963, when the Réthly & Berkes (1963) records stopped. Unfortunately, aurora are not generally counted in modern times. Therefore, we again conclude that these aurora data likely represent a lower limit for geomagnetic activity.

As a final point, we note that to penetrate to mid-latitudes, the solar source must be relatively significant. Thus, it is unlikely that corotating interaction regions (CIRs) alone could have produced them. Instead, coronal mass ejections (CMEs) associated with the very limited number of sunspots that were present probably produced the observed aurora.

2.3. Cosmic Ray Fluxes inferred from Cosmogenic Records

Cosmogenic isotopes are rare isotopes created when a high-energy cosmic ray interacts with the nucleus of an atom in the earth's atmosphere. The two principal products are ^{10}Be and ^{14}C. Here, we focus principally on the former, since it is more directly relatable to cosmic ray intensities (Steinhilber et al. 2012). High-energy galactic cosmic

ray particles impact atmospheric nitrogen or oxygen, producing ^{10}Be, which then become attached to aerosols. Depending on where the ^{10}Be is produced it may take from weeks (troposphere) to one-two years (stratosphere) before being deposited in the polar ice caps. Since climate/precipitation effects can modulate the ^{10}Be concentrations within the ice, care must be taken when interpreting the records as a measure of cosmic ray intensities. The general consensus, however, is that ^{10}Be records provide, primarily, a measure of production rates (Usoskin 2008).

In panel (c) of Figure 1 we show the ^{10}Be record as reported by Berggren et al. (2009). The individual circles are yearly measurements of concentration. The black/blue curve represents an 11-year running average. We note several points. First, the solar cycle is clearly seen, particularly since 1895 (the beginning of the "Gleissberg" minimum). Second, the absolute concentration varies by a factor of ~ 2.5 over the 400-year interval. Third, the three established minima (Maunder, Dalton, and Gleissberg) all coincide with local peaks in concentration. Fourth, a striking feature is that, unlike the Sunspot record, the Maunder minimum as viewed through $10^{B}e$ was not steady. The Be-10 data steadily increased from 1.75×10^4 atoms/g to over 3×10^4 during the 70-year interval. Thus, at least from a cosmic ray perspective, the Maunder minimum period was a period of evolution, not constancy.

We might reasonably infer, that, if as the record suggests, the CR flux increased by almost a factor of two, this suggests a commensurate decrease in the strength of the interplanetary magnetic field. In fact, the relationship between CR flux and the strength of the IMF is considerably more complicated (Usoskin 2008). We will return to this point in Section 2.5, where we consider the modulation potential.

The ^{10}Be record also calls into question the idea that the Maunder Minimum interval is substantially the same as the 2008/2009 minimum. First, the recent minimum is a snapshot of the Sun in time, whereas, we have argued here that the Maunder minimum was

an evolving configuration. Second, if the recent minimum is related, to which part of the Maunder interval can we associate it with? Presumably, it would be the beginning, since we have not yet seen the 70 years of little-to-no sunspots or the continual increase in cosmic ray fluxes. Thus, we conclude that at best, the 2008/2009 minimum may turn out to be the first minimum that defined the start of a new grand minimum, but that the ensuing coronal and heliospheric conditions are likely to be significantly (up to a factor of two in field strength) different.

Finally, in panel (d) of Figure 1 we show yearly averages of the ^{14}C record as reported by Reimer et al. (2004). Again, a large value of ^{14}C, suggests a stronger flux of cosmic rays, which in turn suggests a lower interplanetary field, possibly in conjunction with a relatively flat HCS. We note the almost monotonic increase from 1600 until shortly after 1700, consistent with the 10^Be record. Between then and until 1955, it appears to generally decrease, except for two 'recoveries' when it increases. The first occured at $\sim$ 1800 and the second, shortly before $\sim$ 1900, and coincide with the Dalton and Gleissberg minima. Above-ground nucear tests began in 1955 rendering the time series from this point forward useless for present purposes. In fact, secular variations after $\approx$ 1900 are probably dominated by the anthropogenic effects of fossil fuel burning (Usoskin 2008).

Comparing the ^{14}C and ^{10}Be profiles, we note that, at the largest scales, they convey a similar trend in the inferred flux of cosmic rays. The three grand minima (seen as maxima in these records) are approximately co-temporal and the general variations about some reference point, say 1600, are reasonably matched. One notable exception is that while the peak ^{10}Be values during the Maunder and Dalton intervals match one another, they are substantially different in the ^{14}C record, perhaps the result of being superimposed on a monotonic decrease from 1700 until at least 1955.

We conclude from these records that the cosmic ray flux was larger during the

Maunder Minimum than at any time over the last 400 years. Moreover, the flux of particles systematically increased during the 70-year interval, suggesting that the minimum was only "flat" in terms of sunspots. If anything, the true Maunder minimum was not an interval, but a point in time that occurred circa 1700.

2.4. Eclipse "Observations"

Observations of eclipses during the MM period are strongly suggestive, but not conclusive, that the structured corona observed in modern times during eclipses disappeared (Eddy 1976). Here, we build upon, and add to the evidence compiled by J. Eddy. As he noted, of the 63 possible solar eclipses known to have occurred between 1645 and 1715, only eight passed through Europe, and, of those four (1652, 1698, 1706, and 1708) were captured by reports sufficiently detailed to be of use for this study.

Dr. John Whybard gives an account of his, and that of the vice-prefect's observations of the 1652 solar eclipse in Carrickfergus, located in County Antrim, Northern Ireland (Wing 1656). He stated that the corona "had a uniform breadth of half a digit, or a third of a digit at least, that it emitted a bright and radiating light, and that it appeared concentric with the sun and moon when the two bodies were in conjunction."

As reported by Grant (Grant 1852), MM. Plantade and Capies observed the eclipse of 1706 at Montpellier, located on the south coast of France, in a way that was "clearer and more precise than any other that had been hitherto recorded." They observed that "as soon as the sun was totally eclipsed, there appeared around the moon a very white light forming a kind of corona, the breadth of which was equal to about 3". Within these limits the light was everywhere equally vivid, but beyond the exterior contour, it was less intense, and was seen to fade off gradually into the surrounding darkness, forming an annulus around the

moon of about 8 degrees diameter."

It is interesting to note that neither of these reports is consistent with a structured corona. Had the Sun displayed a dipolar or quadrupolar configuration, such as any of the eclipses viewed in, say, the last century, we might have expected the observers to note this fact.

The eclipse of 1715, which was well observed from London, is an interesting case. Halley himself reported that there "appeared a luminous ring around the moon as on the occasion of the eclipse of 1706." R. Cotes, on the other hand wrote "besides this ring, there appeared also rays of a much fainter light in the form of a rectangular cross...The longer and brighter branch of this cross lay very nearly along the ecliptic, the light of the shorter was so weak that I did not constantly see it." Eddy (1976) interpreted the longer, brighter branch to be a description of a solar minimum streamer belt configuration and the shorter branch to be polar plumes. The discrepancy between these two accounts raises several issues. First, it is possible that earlier accounts failed to acknowledge that there was an underlying structure. Or, second, that the structured K-corona had returned to the Sun by the time of this observation.

The eclipse of 1766, which was observed "in the Southern Ocean by the persons on board the French ship of war the Comte d'Artois," provides clear evidence that "normal" solar conditions had returned. Although totality only lasted some 53 seconds, the observers noted "a luminous ring about the moon, which had four remarkable expansions situate at a distance of 90 [degrees] from each other." From this we can infer that a quadrupolar streamer structure was visible. Additionally, it bolsters support for the interpretation that had this structure been present in 1652, it would have been noted.

Finally, we remark that during the eclipses of 1652, 1698, 1706, and 1708, the corona was described as "dull or mournful," and often as "reddish," which Eddy (1976) suggested

might describe how the zodiacal light component (i.e., the F-corona) might look to an observer in the absence of a K-corona.

In summary then, we conclude that: (1) the corona during the MM was likely featureless, at least to the extent that it wasn't commented on; (2) the coronal light that was present was "reddish" and (3) coronal features returned sometime between 1708 and 1766. Given the qualitative nature and questionable reliability of the reports, we must assign large uncertainties to these inferences.

2.5. Cosmic Ray Modulation Potential

Variations in cosmogenic radionuclide records, and, in particular ^{10}Be and ^{14}C, are believed to provide a measure of solar activity. To a rough approximation, their values indicate the flux of cosmic rays impinging the upper atmosphere. However, the transport and deposition mechanisms for both species is relatively complex and quite different from one another, meaning that interpretation does not come without important caveats. Usoskin (2008) has explored – in detail – the various processes that affect cosmogenic records.

A number of both empirical and physics-based models have been developed to recover unbiased estimates of "solar activity." Here, we focus on the so-called modulation potential, ϕ. As suggested by its name, ϕ is intended to capture the variability in the observed cosmic ray flux in the vicinity of Earth. Because these fluxes are modulated on a global scale, ϕ is a global heliospheric quantity, capturing the physical processes of: (1) diffusion of particies due to scattering; (2) convection in the solar wind; (3) adiabatic losses; and (4) particle drifts. Without belaboring the details, the following empirical estimate for ϕ provides an intuitive way to understand it:

$$\phi = \phi_o + \phi_1 \left(\frac{F}{F_o} \right)^{1+\frac{\alpha}{\alpha_o}} (1 + \beta p) \quad (1)$$

where F is the open solar flux, α is the tilt angle of the HCS, and p is the global magnetic polarity; $p = 1(-1)$ for positive (negative) polarity periods. Best fit values for the constants are: $\phi_o = 150$MV, $\phi_1 = 86$MV, $F_o = 2.5 \times 10^{14}$Wb, $\alpha_o = 91°$, and $\beta = -0.03$ (Alanko-Huotari et al. 2006).

From Equation (1), we can see that during solar minimum periods, when $\alpha \to 0°$, the modulation potential is linearly proportional to the open flux in the heliosphere. During elevated periods of activity (and in the extreme that $\alpha \to 90°$) the modulation potential is more sensitive (up to the square) of the open flux. Intuitively, this makes sense: During periods of higher activity, as the heliospheric magnetic field strength increases and the latitudinal extent of the HCS broadens there is a larger barrier for cosmic rays to impact the Earth. In contrast, when the HCS becomes flat, and the field strength reduces, the structure of the solar wind provides no impediment to the propagation of these particles. Of the two parameters, since α varies between 10° and 90° every 11 years, it doesn't impact ϕ as much as F, which varies by more than a factor of two. Moreover, α must oscillate between these extremes every cycle, and cannot drift beyond them on longer times scales as can F. Therefore, we conclude that long-term variations in ϕ likely represent changes in the large-scale heliospheric magnetic field strength.

Armed with this simplified picture, we can now interpret several reconstructions of the modulation potential shown in Figure 2. The solid colored lines show various estimates of ϕ using both ^{10}Be and ^{14}C records. The black solid line is an eleven-year running mean of monthly averages (black points) of ϕ derived from neutron monitor measurements. The approximate match between the cosmogenic records and the neutron monitor measurements gives us some confidence that present day values can be, at least roughly, compared with

historical estimates, particularly during the deepest portion of the Maunder Minimum ($\approx$ 1700). However, more important than the absolute values, is the variability in the cosmogenic data between 1600 and 2000. If we assume that, to first order, ϕ is providing a proxy for the strength of the heliospheric magnetic field, then its strength during the Maunder Minimum was as much as $500/50 = 10$ times lower than it was during the decade 2000-2009. Additionally, the field strength during the early 1600's, which, it could be argued was the beginning of a long term, monotonic decrease in field strength, is approximately the same as the inferred field strength today, reinforcing the suggestion by Lockwood & Owens (2011) that we may be entering a grand solar minimum, similar to the Maunder interval.

These profiles also reinforce the idea that the Maunder minimum was not an extended interval of constant inactivity, as might be inferred from the sunspot record, but a progressive drop, culminating in an absolute minimum (what we have termed "the day the Sun stood still") roughly located at 1700.

3. Candidate Scenarios for the Sun's Photospheric Magnetic Field during the Maunder Minimum

The Sun's photosphere provides a convenient boundary from which to base our calculations. First, the photospheric magnetic field is well observed by both ground-based and space-based solar observatories. Second, the transition from a flow-dominated to a magnetic field-dominated environment occurs at the photosphere. In principle then, assuming that all of the salient physical processes are included in the models, and that the model results are not strongly dependent on the values of free parameters (i.e., coefficients in the formulation of the relevant physics that are not well constrained), specification of the photospheric magnetic field should be sufficient to reconstruct the global structure of the corona and inner heliosphere. Such models are frequently applied to data from the modern

era driven by the observed photospheric magnetic field, in an effort to understand the large-scale structure of the corona and inner heliosphere, and generally match the observed large-scale structure of the inner heliosphere (e.g., Riley et al. (2012b,a)).

The distribution of magnetic field in the photosphere during the Maunder minimum, however, is subject to considerable speculation. We have reasonably reliable evidence that few, to no sunspots were observed during this period, suggesting the absence of active regions. Theoretically, several studies have speculated on various aspects of the Maunder Minimum solar field. Schrijver et al. (2011) have argued that small-scale fields associated with ephemeral regions must have persisted during even the deepest portion of the interval. Mackay (2003) proposed that the Maunder Minimum must have commenced at, or near solar minimum. Had it started at solar maximum, there would be no reversal of the polar fields, in apparent conflict with evidence that the solar cycle continued to operate during this 70-year period. Thus, one approach to deducing the photospheric field during this interval is to construct a range of possible scenarios, based on these constraints, and test their predictions against the available, albeit limited "observations."

We can safely discount the extreme possibility, raised (but not necessarily advocated) by Parker (1976), that the entire visible magnetic field disappeared. While this would provide an obvious means for removing all sunspots, we know: (1) that there were very occasional sunspots during the Maunder interval; (2) there were occasional geomagnetic storms; and (3) at least the suggestion of a solar cycle still operating during this interval. The continued, sporadic appearance of sunspots suggests that magnetic flux continued to emerge in the photosphere, albeit at a much lower rate. The occasional geomagnetic storms suggests a continued magnetic connection between the solar surface and Earth's magnetosphere. And, the maintenance of a solar cycle suggests that the field did not "extinguish" itself, which, from a theoretical perspective, would be difficult to envisage.

Thus, we suggest that the most radical scenarios for the Maunder Minimum photosphere may have contained only small-scale ephemeral flux, random in amplitude and position, but substantially lower in magnitude (say, one third to an order of magnitude) than currently-observed ephemeral regions (Figure 3(a)). Evolutionarily, we might anticipate that this state was arrived at slowly as the polar fields decayed but were not replaced by poleward-migrating flux from sunspots, which had disappeared, and this represents some portion late in the Maunder Minimum interval. On the other hand, the most conservative configuration would be that the Maunder minimum period was no different than the recent minimum of 2008/2009, as suggested by Schrijver et al. (2011) (Figure 3(d)). If substantiated, this is an appealing result because all of the modern era measurements, modeling, and inferences could be applied to better understand, and constrain the Maunder interval. Between these two extremes, we consider two alternatives. In the first (Figure 3(b)), we simply multiply the first case by a factor of three, which mimics the distribution of ephemeral flux during modern times and in the absence of active regions and unipolar polar regions. It is important to note that this will not result in a self-similar solution (or even identical solution, as would be the case if this were a PFSS model), because the added flux heats the coronal plasma more strongly, opening up more field lines. In the second intermediary configuration, we add a centered magnetic dipole to scenario 2 (Figure 3(c)). Although this look very similar to Figure 3(b), upon careful inspection, the poles can be seen, at least on larger scales, unipolar. If smoothed sufficiently, this configuration would look similar to Figure 3(d).

Scenarios $1 \rightarrow 4$, then,we believe, are representative of the possible state of the photospheric magnetic field during the Maunder Minimum, containing the two most extreme configurations: an ephemeral-only Sun (1 or 2) and a 2008/9-like Sun (3 or 4). It should be noted, however, that the actual configuration could have been different. If so, we believe that the difference could only be in degree, not form; It is difficult to imagine an

alternative distribution of flux that does not immediately conflict with the observations we have described above.

4. Global MHD Modeling

A global MHD model of the solar corona and inner heliosphere can provide a unique and powerful way to "self-consistently" link the disparate observations discussed in Section 2 and assess the likelihood that any of the scenarios discussed in Section 3 are consistent or in conflict with these observations. The model we describe in the following sections contains the key elements that: (1) The primary driver is the photospheric magnetic field; and (2) the heating of the corona is a function only of the photospheric magnetic field strength. Thus, the magnetic and emission properties of the corona are coupled, and we can, at least in principle, apply the model to epochs with significantly different properties.

4.1. Model Description

The MHD approximation is appropriate for long-scale, low-frequency phenomena in magnetized plasmas such as the solar corona. Using the photospheric magnetic field as the primary driving boundary condition, as described in Section 3, we can attempt to reproduce the Sun's magnetic and emission properties during during the Maunder Minimum by solving the following set of viscous and resistive MHD equations:

$$\nabla \times \mathbf{B} = \frac{4\pi}{c}\mathbf{J}, \tag{2}$$

$$\nabla \times \mathbf{E} = -\frac{1}{c}\frac{\partial \mathbf{B}}{\partial t}, \tag{3}$$

$$\mathbf{E} + \frac{\mathbf{v} \times \mathbf{B}}{c} = \eta \mathbf{J}, \tag{4}$$

$$\frac{\partial \rho}{\partial t} + \nabla \cdot (\rho \mathbf{v}) = 0, \tag{5}$$

$$\frac{1}{\gamma-1}\left(\frac{\partial T}{\partial t}+\mathbf{v}\cdot\nabla T\right) = -T\nabla\cdot\mathbf{v}+\frac{m}{2k\rho}S \quad (6)$$

$$\rho\left(\frac{\partial \mathbf{v}}{\partial t}+\mathbf{v}\cdot\nabla\mathbf{v}\right) = \frac{1}{c}\mathbf{J}\times\mathbf{B}-\nabla(p+p_w)+\rho\mathbf{g}+\nabla\cdot(\nu\rho\nabla\mathbf{v}), \quad (7)$$

$$S = (-\nabla\cdot\mathbf{q}-n_e n_p Q(T)+H_{\rm ch}), \quad (8)$$

where $\mathbf{B}$ is the magnetic field, $\mathbf{J}$ is the electric current density, $\mathbf{E}$ is the electric field, ρ, $\mathbf{v}$, p, and T are the plasma mass density, velocity, pressure, and temperature, $\mathbf{g}=-g_0R_\odot^2\hat{\mathbf{r}}/r^2$ is the gravitational acceleration, η the resistivity, and ν is the kinematic viscosity. Equation (8) contains the radiation loss function $Q(T)$ as in Athay (1986), n_e and n_p are the electron and proton number density (which are equal for a hydrogen plasma), $\gamma=5/3$ is the polytropic index, $H_{\rm ch}$ is the coronal heating term (see below), and $\mathbf{q}$ is the heat flux.

For the present study, we have used a grid of $151\times180\times360$ points in $r\times\theta\times\phi$. The grid resolution is nonuniform in r with the smallest radial grid interval at $r=R_\odot$ being ~ 0.33 m. The angular resolution in θ and ϕ is 1°. A uniform resistivity η was used, corresponding to a resistive diffusion time $\tau_R\sim 4\times10^3$ hours, which is much lower than the value in the solar corona. This is necessary to dissipate structures that cannot be resolved which are smaller than the cell size. The Alfvén travel time at the base of the corona ($\tau_A=R_\odot/V_A$) for $|\mathbf{B}|=2.205$ G and $n_0=10^8$ cm^{-3}, which are typical reference values, is 24 minutes, and so the Lundquist number $\tau_R/\tau_A\approx1\times10^4$. A uniform viscosity ν is also used, corresponding to a viscous diffusion time τ_ν such that $\tau_\nu/\tau_A=500$. Again, this value is chosen to dissipate unresolved scales without substantially affecting the global solution. Our model includes a chromosphere and transition region. However, to efficiently model the coupling between the transition region and corona, required the development of a technique that artificially broadens the transition region, while maintaining accuracy in the corona Lionello et al. (2009).

4.2. Coronal Heating

Global MHD models of the solar corona and inner heliosphere are capable of reproducing the essential features of a range of measurements and observations (e.g., (Riley et al. 2012b,a)). A crucial aspect and limitation of current capabilities concerns the physical mechanisms that heat the corona. While it is generally believed that it must involve the conversion of magnetic energy into heat, it is not clear how this transformation takes place. One scenario involves the dissipation of high-frequency waves, while another relies on the rapid release of energy built up from slow photospheric motions (e.g., Lionello et al. (2009)). Phenomenologically, it is well known that magnetic flux and X-ray radiance are linearly correlated over many orders of magnitude (Fisher et al. 1998; Pevtsov et al. 2003; Riley et al. 2009).

In this study, we take a pragmatic position of specifying the heating as a function of magnetic field strength. Specifically, we assume that the heating of the corona takes the following form:

$$H = H_{\rm QS} + H_{\rm AR} \tag{9}$$

$$H_{\rm QS} = H^0_{\rm QS} f(r) \frac{B_t^2}{B(|B_r| + B_r^c)} \tag{10}$$

$$H_{\rm AR} = H^0_{\rm AR} g(B) \left(\frac{B}{B_0}\right)^{1.2} \tag{11}$$

where: $B_t = \sqrt{B_\theta^2 + B_\phi^2}$, $H^0_{\rm QS} = 1.18 \times 10^{-5}$ erg/cm^{3}s, $B_r^c = 0.55$ G, $H^0_{\rm AR} = 1.87 \times 10^{-5}$ erg/cm^{3}s, and $B_0 = 1$ G, $f(r) = \exp\left(-\frac{r/R_\odot - 1}{0.2}\right)$, and $g(B) = \frac{1}{2}\left(1 + \tanh\frac{B-18.1}{3.97}\right)$.

Although these functions are *ad hoc*, importantly, they depend only on the strength

of the magnetic field, and hence, provided that corona heating too depends only on field strength, should be applicable to a range of values even outside those that have been observed during the space era. Thus, by demonstrating that the model can reproduce observations during the space era, and requiring that the heating profiles depend only on the magnetic field, that is, that there are no additional free parameters, we have confidence that the heating profiles should be applicable when applied to more extreme conditions.

4.3. Computation of the Open Magnetic Flux

Open solar magnetic flux can be practically defined as that flux which threads through some reference sphere, say, the fast-mode critical point, or even 1 AU. Assuming further that, on sufficiently long temporal scales, this flux is independent of position in the heliosphere, as suggested by Ulysses observations (Smith & Marsden 2003), in-situ measurements of the interplanetary magnetic field, B_{IMF}, are a proxy for the open flux. Multi-solar cycle measurements of B_{IMF} demonstrate that the open flux roughly doubles between solar minimum and solar maximum. Owens et al. (2006); Riley et al. (2007); Schwadron et al. (2010) have argued that the measured flux at 1 AU is a contribution from a relatively constant background flux, with an additional contribution from CMEs, which at solar maximum can be as large as the background level.

Therefore, under solar minimum conditions, and for timescales longer than a solar rotation, the average open flux computed from the MHD model should match estimates for $|B_r^{IMF}|$ as measured by in-situ spacecraft or via indirect estimates from cosmogenic records. In particular, following Wang & Sheeley (1995), we estimate the magnitude of the radial interplanetary magnetic field at Earth from the MHD solution to be:

$$|B_r^E| = \frac{|\Phi_{open}|}{4\pi r_E^2} = \frac{1}{4\pi}\Big(\frac{R_s}{215R_\odot}\Big)^2 \int |B_r(R_s,\theta,\phi)| d\Omega \tag{12}$$

where ϕ denotes longitude, $R_\odot$ radius of the Sun, R_s is the radius of the source surface, typically $2.5R_\odot$, r_E is the radius of the Earth, and the solid-angle integral is computed over a sphere at the source surface.

4.4. Model Results

We used the four magnetograms described in Section 3 to compute MHD model solutions of the solar corona from 1 to 30 R_S. The resulting magnetic field configurations are shown in Figure 4. The same starting points were used in each panel, corresponding to a mesh resolution of 10° in latitude and longitude. Focusing first on scenarios 1 and 2, we note the lack of any obvious axis of symmetry, which would be expected given the randomness of the flux. Additionally, the greater number of field lines in scenario 2 illustrates that the flux open to the heliosphere is much larger than in scenario 1. Considering next the bottom two panels, we note the obvious dipolar configuration in both, not surprisingly, most obvious in scenario 3. Qualitatively comparing the number of open field lines we note the large increases from scenarios 1/2 to 3/4.

For each solution, we computed the open magnetic flux, as defined by Equation (12). These are summarized in Table 5. We note that scenario 1 results in the lowest amount of open flux (0.08 nT), then scenario 2 (0.3 nT), followed by scenario 4 and 3 (1.0 and 1.9 nT, respectively). In each case, the proportional difference is less as we move from $1 \rightarrow 2 \rightarrow 4 \rightarrow 3$. The value computed for CR 2085 (scenario 4), is lower than estimates made using near-Earth spacecraft (and earlier observations from Ulysses). However, the relative variations in open flux between models and observations has been shown to match

well (**?**). Stevens et al. (2012) have investigated the known deficit in the open flux produced by the models, suggesting that a better estimate of some of the model parameters (e.g., coronal base temperature) may resolve the difference. Additionally, more recent analysis by Linker et al. (2012) suggests that current synoptic maps may be underestimating the polar field strengths, which would lead to a systematic reduction in the model estimates for the open flux. For our purposes, assuming that the relative differences are reasonably accurate, scenario 1 and 2 predict reductions over 2008 conditions of a factor of ≈ 12 and ≈ 3, respectively. Additionally, it should be noted that the 2008 time period we are comparing to represents a somewhat unique interval where the fields were lower by a factor of 1.6 over the previous space era minima (Smith & Balogh 2008), and general solar activity was estimated to be the lowest it had been in the last century (e.g., Riley et al. (2011)). The range bracketed by scenarios 1 and 2 is consistent with the difference between the curves in Figure 2 when contemporary values are compared with those in 1700.

We next consider the structure of the corona in white light that these scenarios suggest. In Figure 5, we have computed the simulated polarized brightness (pB) for each solution. These are constructed by integrating the plasma along the line of sight with a suitable weighting function (Billings 1966). We have found that the model often matches observed white light images both from spacecraft and ground-based observations during eclipses (Riley et al. 2001; Mikić et al. 2007; Riley 2010; Riley et al. 2012b). Scenario 4, which represents the corona during the last solar minimum displays the typical mid- and low-latitude streamer structure we expect during the declining phases and solar minimum. The recent minimum was unique in that there were a larger number of pseudo-streamers present than during the previous (1996) minimum, which lead to a broader and more structured "belt" of brightness around the equator (Riley & Luhmann 2012). The presence of unipolar polar fields is clearly seen by the dark regions over both poles. Scenario 3, which represents an idealization of scenario 4 by removing any active regions (i.e., no

large-scale fields except for the $m = 0$ component, i.e., the dipole), presents a similar, albeit simpler picture. The closed, dipolar fields bracketing the equator trap plasma that scatters photons to the observer while the polar, open field regions retain only a tenuous outwardly streaming flow of plasma that cannot be easily seen in white light. Scenarios 1 and 2 are both much darker and do not display any axial symmetry. It is likely that scenario 1 would not be visible to the naked eye, especially if contrasted with the relative brightness of the preceding partial eclipse. Scenario 2 is marginally more visible, and appears to show structure. Whether or not this would be reported, or whether only the more dominant effect of a "halo" or "annulus" would be noted by observers of the time is unclear.

The white light we observe from the solar corona is made up of two primary components: the K (kontinuierlich) and F (Fraunhofer) corona. The K-corona is created by sunlight scattering off free electrons, while the F-corona is created by sunlight scattering off dust particles. Close to the Sun, the K-corona dominates. However, beyond perhaps $3R_S$ (the precise number depending sensitively on the point of observations and solar conditions), the brightness of the F-corona exceeds that of the K-corona (Koutchmy & Lamy 1985). It is important to differentiate between brightness, B, and polarized brightness, pB, here: While coronagraphs (and MHD simulations) often display images of pB, at visible wavelengths, the polarization of the F-corona is nearly zero, hence it it not observed in images of pB, even at larger distances. More importantly, our eyes 'see' B. Thus, to directly relate our simulation results to the reports of eclipses during the Maunder Minimum, we should limit ourselves to B.

Figure 6 is an estimate of the of the F-corona as it might have looked during the Maunder Minimum using the formulae by Koutchmy & Lamy (1985). In fact, this picture is indistinguishable from how it would appear today, given that it was formed from asteroid collisions and cometary activity, for which the timescales are much longer. We also have

taken the liberty of using a red color table based on work suggesting that there is a strong reddening of the spectrum (see Koutchmy & Lamy (1985) and references therein). It is, however, by no means certain that if the K-corona disappeared completely, that the remaining F-corona would appear as red as shown here. The main point to make is that the F-corona shows no discernible structure with respect to position angle. Although there is a slight variation between the equator and pole, this would be imperceptible to the naked eye. An observer fortunate enough to witness the F-corona directly would report a smooth annulus or halo surrounding the Sun, possibly reddish in color.

To make a direct comparison between the F- and K-corona during the Maunder Minimum, we computed simulated total brightness (B) images, analogous to those shown in Figure 5. From these, we extracted radial traces taken through the solar equator for each scenario, and compared them with the F-corona brightness estimates discussed above. These are shown in Figure 7. The inset in each panel summarizes the photospheric magnetic field that was used to produce the solution. Comparing scenario pairs 1/2 and 3/4 first, we note the striking result that for the former, the F-corona dominates over the K-corona by $\sim 1.3R_S$. However, for scenarios 3/4 this changeover does not occur until almost $2R_S$. Comparison with Figure 5 suggests that the range between $1.3R_S$ and $2R_S$ is precisely where coronal structure manifests itself in white-light eclipse observations. Given the idealizations and approximations employed to arrive at this result, it is quite remarkable that such a clear delineation occurs. Based on these results, then, we would anticipate that an eyewitness to scenarios 1 or 2 would not observe any structure of the true (K-) corona because it would be obscured by the (potentially red) and structureless F-corona. On the other hand, an observer of scenarios 3 or 4 would likely see helmet streamer, pseudo streamer, coronal hole, and plume structure before being washed out by the F-corona.

4.5. Bayesian Analysis

Our analysis, thus far, has produced only qualitative inferences on the likely state of the corona during the Maunder Minimum. These are subjective, in the sense that two reasonable people could disagree. For example, while the reports of a "red erie glow" during some of the eclipse observations is suggestive of the presence of an F-corona, one could argue that these were the result of local atmospheric effects, or even sensitivities unique to the observer. Baye's theorem provides a way to incorporate various types of evidence to arrive at an estimate for the probability that a given hypothesis is true based on various pieces of evidence. Although its application is sometimes criticized for being subjective, it does provide a quantitative methodology, and it is particularly well suited for comparing exclusive ideas.

Using Bayes's theorem, we can write:

$$\frac{P(H_1|\epsilon)}{P(H_0|\epsilon)} = \frac{P(H_1)}{P(H_0)} \frac{P(\epsilon|H_1)}{P(\epsilon|H_0)} \tag{13}$$

where the term on the left-hand side is the posterior odds, the first term on the right-hand side is the prior odds, and the second term on the right-hand side is the likelihood ratio. It is worth considering these terms in more detail. $P(H_1|\epsilon)$ is the conditional probability that hypothesis H_1 is true, given evidence ϵ. Thus, the posterior odds is the amount by which hypothesis H_1 is more likely than H_0, given the evidence ϵ. The power of Bayes's theorem lies in the fact that the posterior odds are calculated from the terms $P(\epsilon|H_1)$ and $P(\epsilon|H_1)$, that is, the probability that the evidence would have arisen given under each of the competing scenarios. In fact, for a set of n pieces of evidence, we can generalize Equation (14) as follows:

$$\frac{P(H_1|\epsilon)}{P(H_0|\epsilon_1,...,\epsilon_n)} = \frac{P(H_1)}{P(H_0)} \prod_{i=1}^{n} \frac{P(\epsilon_i|H_1)}{P(\epsilon_i|H_0)} \tag{14}$$

Turning to the specific case of distinguishing between the "ephemeral Sun" and "2008 Sun" scenarios, if we assume that these are mutually exclusive hypotheses, and that only two possibilities exist, we need only to construct the likelihood ratios for each piece of evidence, multiply them together and with our prior odds, to estimate the posterior odds.

In table 5, we have summarized each piece of evidence that might support either the conclusion that the Maunder Minimum Sun was "2008-like" or "ephemeral-like." If we further assume that the evidence distinguishes only between the two ideas, then $P(\epsilon|H_1) + P(\epsilon|H_1) = 1$. Thus, if the evidence does not distinguish between either scenario, we might infer that $P(\epsilon|H_1) = P(\epsilon|H_1) = 1/2$. On the other hand, if the evidence favors the ephemeral Sun idea, which most do, $P(\epsilon|H_1) > P(\epsilon|H_1)$. While it is not possible to deduce precise values for $P(\epsilon|H_1)$ or $P(\epsilon|H_1)$ for any of these observations, the key point is that because they are multiplicative, even modest individual biases in favor of one hypothesis over the other can result in a substantial shift in the posterior odds ratio. For example, if each piece of evidence in Table 5 favored one hypothesis over the other in the ratio $\frac{0.6}{0.4}$, then, because the last two rows would cancel one another, the "ephemeral Sun" scenario would be $(\frac{0.6}{0.4})^5 \approx 7.6$ times more likely to be correct than the "2008 Sun." As we noted earlier, however, reasonable minds will disagree. The main point is that the weight of the evidence supports the "ephemeral-only" Sun, and not the 2008/2009 Sun picture. Only one piece of evidence distinguishes between the two scenarios in favor of the latter, while six, arguably independent pieces of evidence favor the former.

5. Discussion

Our analysis appears to safely rule out the ideas that the MM Sun was substantially the same as the recent 2008/2009 minimum (Svalgaard & Cliver 2007; Schrijver et al. 2011; Wang & Sheeley 2013) or that coronal magnetic fields disappeared entirely. The continued modulation of cosmic rays, including the inferred presence of a 22-year cycle, as well as albeit modest auroral activity, requires both some magnetic field and a continuing dynamo process. The lack of any observations reporting coronal structure, the presence of an F corona, and likely decrease in the strength of the IMF also contradict the idea that the MM Sun was no different than in 2008/2009. It is worth noting that Schrijver et al. (2011) and Svalgaard & Cliver (2007) based their conclusions on assumptions or hypotheses, which were extrapolated back to the Maunder Minimum Interval. Schrijver et al. (2011) argued that there is a minimum state, or "floor" in solar activity, associated with small-scale magnetic bipoles (i.e., what we have called ephemeral regions). However, they did not address whether or not polar coronal holes would have been present during the Maunder Minimum. Svalgaard & Cliver (2007) posited a similar "floor" but this time, in terms of the strength of the interplanetary magnetic field. This was based on empirical evidence from the minima of 1976, 1986, and 1996. The floor, however, had to be lowered as the 2008/2009 minimum dropped below the value predicted for it.

Table 5 summarizes the key observations we have analyzed here, as well as TSI, which was considered by Schrijver et al. (2011). It simplifies the interpretation of these observations in terms of the two major candidates: the '2008 Sun' and the 'Ephemeral Sun.' The ephemeral Sun picture is generally consistent with all observations - or at least with the consensus interpretation of them. On the other hand, the 2008 Sun is inconsistent with all, except TSI, which does not act as a distinguishing feature. Of course, arguments can be made that the observations are inaccurate, imprecise, or that their interpretation is

incorrect. And these arguments can be made in favor (or against) each scenario. However, from a purely statistical point of view, we are led to the conclusion that the ephemeral Sun is significantly more consistent with the observations.

An important inference that can be drawn from this work is that the Maunder minimum was not a steady period of inactivity. Instead, it is likely that there was a general progression to a progressively deeper configuration during the 70-year period. Therefore, it may be more reasonable to compare the 2008/2009 solar minimum with the initial descent into the Maunder minimum;however, it is unlikely that the last 5-10 years looked anything like the recent minimum. Thus, we suggest that the Sun's magnetic field continued to evolve during this interval and posit that this evolution is best represented by an ever-decreasing surface field, and, in particular, the gradual decay of the polar fields. These polar fields are the dominant source of the open flux permeating the heliosphere and modulating the flux of cosmic rays hitting Earth's magnetosphere. By 1700, the point in the Maunder Minimum that we associate with "the day the Sun stood still" likely consisted of only small-scale parasitic polarity field, with virtually no large-scale dipolar component, i.e., no unipolar fields.

Our results are in apparent conflict with several numerical studies. Mackay (2003) used a magnetic flux transport model to consider the possible surface magnetic field configurations that may have been present during the Maunder minimum. They concluded that if the grand minimum started at solar cycle minimum, then a large amount of unipolar flux may have persisted in the polar regions of the Sun, whereas, if the minimum had started at solar maximum, there may have been little-to-no large scale magnetic flux on the Sun. Wang & Sheeley (2013) argued that an "ephemeral only" sun was not possible because the inferred interplanetary magnetic field strength would be inconsistent with estimates based on the ^{10}Be record. Their approach for estimating the open flux that a set

of randomly orientated small-scale dipoles would produce, however, rested on a magneto static extrapolation of the large-scale residual field produced by them. Importantly, it did not take into account the fact that small loops would be heated, expand, and often open up; a result that could only be revealed using an MHD approach, as described here. In fact, our results suggest that an ephemeral-only Sun is capable of supplying an open flux that may be 1/10 to 1/3 of the value measured in 2008/2009, clearly consistent with the cosmogenic records.

Our invocation of Bayesian methodology to argue that the "ephemeral-only" Sun is strongly favored may seem awkward. In fact, the case for the the "ephemeral-only" Sun can be made simply by scanning Table 5. However, the Bayesian approach provides two advantages. First, it emphasizes that the individual pieces of evidence combine in a multiplicative fashion to support one hypothesis over the other. Second, it provides a conceptual framework for understanding why arguments that seek to promote an alternative hypothesis by attacking the credibility of the evidence. For example, considering observations of eclipses during the Maunder minimum. While one can argue that there may have been omissions or even biases in the reports, this only goes to the credibility of the evidence, that is, a measure of the error bars. The most probable interpretation remains that these observations tend – even if only slighty – to favor the "ephemeral-only" picture, and they actively refute the "2008/2009" scenario. As with error analysis in general, we derive the best estimate of the parameter by multiplying the individual parameters together, and then, we add the relative individual errors. We may conclude that the errors are large enough that they admit either hypothesis; however, our conclusion remains that the most likely scenario is the "ephemeral-only" Sun.

In closing, our analysis of the available observations during the Maunder Minimum, together with their interpretation within the context of global MHD model results strongly

suggests that this period was unlike anything we have observed in recent times. As such, it once again "opens the door" for the possible connection between the little-ice age, which was observed in Europe and elsewhere, roughly coincident with the Maunder Minimum period.

This work was motivated by discussions during the two ISSI (International Space Science Institute) team workshops on "Long-Term Reconstruction of Solar and Solar Wind Parameters," which occurred in May, 2012 and 2013. PR gratefully acknowledges the support of NASA (Causes and Consequences of the Minimum of Solar Cycle 24 program, LWS Strategic Capabilities program, Heliophysics Theory Program, and the STEREO IMPACT team) and NSF (Center for Integrated Space Weather Modeling (CISM) program).

REFERENCES

Owens, M. J., Merkin, V. G., & Riley, P. 2006, J. Geophys. Res., 111, A03104

Alanko-Huotari, K., Mursula, K., Usoskin, I. G., & Kovaltsov, G. A. 2006, Solar Phys., 238, 391

Athay, R. G. 1986, Astrophys. J., 308, 975

Berggren, A.-M., Beer, J., Possnert, G., Aldahan, A., Kubik, P., Christl, M., Johnsen, S. J., Abreu, J., & Vinther, B. M. 2009, Geophys. Res. Lett., 36, 11801

Billings, D. E. 1966, A Guide to the Solar Corona (New York: Academic Press)

Eddy, J. A. 1976, Science, 192, 1189

Fisher, G. H., Longcope, D. W., Metcalf, T. R., & Pevtsov, A. A. 1998, Astrophys. J., 508, 885

Grant, R. 1852, History of physical astronomy from the earliest ages to the middle of the nineteenth century ..., Harvard astronomy preservation microfilm project (Bohn)

Hoyt, D. V., & Schatten, K. H. 1996, Solar. Phys., 165, 181

Koutchmy, S., & Lamy, P. L. 1985, in Astrophysics and Space Science Library, Vol. 119, IAU Colloq. 85: Properties and Interactions of Interplanetary Dust, ed. R. H. Giese & P. Lamy, 63–74

Linker, J. A., Mikic, Z., Riley, P., Downs, C., Lionello, R., Henney, C., & Arge, C. N. 2012, Proceedings of Solar Wind 13, AIP Conf. Proc., 1539, 26

Lionello, R., Linker, J. A., & Mikić, Z. 2009, Astrophys. J., 690, 902

Lockwood, M., & Owens, M. J. 2011, J. Geophys. Res., 116, 4109

Luterbacher, J. 2001, History and climate: memories of the future, 29

Mackay, D. H. 2003, Sol Phys., 213, 173

Manley, G. 2011, Weather, 66, 133

Maunder, E. W. 1894, Knowledge, 17, 173

McCracken, K., Beer, J., Steinhilber, F., & Abreu, J. 2011, Space Sci. Rev.

McCracken, K. G., & Beer, J. 2007, Journal of Geophysical Research (Space Physics), 112, 10101

McCracken, K. G., Beer, J., & McDonald, F. B. 2005, ISSI Scientific Reports Series, 3, 83

McCracken, K. G., McDonald, F. B., Beer, J., Raisbeck, G., & Yiou, F. 2004, Journal of Geophysical Research (Space Physics), 109, 12103

Mikić, Z., Linker, J. A., Lionello, R., Riley, P., & Titov, V. 2007, in Astronomical Society of the Pacific Conference Series, Vol. 370, Solar and Stellar Physics Through Eclipses, ed. O. Demircan, S. O. Selam, & B. Albayrak, 299–+

Parker, E. N. 1976, in IAU Symposium, Vol. 71, Basic Mechanisms of Solar Activity, ed. V. Bumba & J. Kleczek, 3

Pevtsov, A. A., Fisher, G. H., Acton, L. W., Longcope, D. W., Johns-Krull, C. M., Kankelborg, C. C., & Metcalf, T. R. 2003, Astrophys. J., 598, 1387

Reimer, P. J., Baillie, M. G. L., Bard, E., Bayliss, A., Beck, J. W., Bertrand, C. J. H., Blackwell, P. G., Buck, C. E., Burr, G. S., Cutler, K. B., Damon, P. E., Edwards, R. L., Fairbanks, R. G., Friedrich, M., Guilderson, T. P., Hogg, A. G., Hughen, K. A., Kromer, B., McCormac, G., Manning, S., Ramsey, C. B., Reimer, R. W.,

Remmele, S., Southon, J. R., Stuiver, M., Talamo, S., Taylor, F. W., van der Plicht, J., & Weyhenmeyer, C. E. 2004, Radiocarbon, 46, 1029

Réthly, A., & Berkes, Z. 1963, Nordlichtbeobachtungen in Ungarn, 1523-1960 (Verlag der Ungarischen Akademie der Wissenschaften)

Riley, P. 2010, in Twelfth International Solar Wind Conference, Am. Inst. Phys. Conf. Proc., ed. M. Maksimovic, K. Issautier, N. Meyer-Vernet, M. Moncuquet, & F. Pantellini, Vol. 1216, 323

Riley, P., Linker, J. A., Lionello, R., & Mikic, Z. 2012a, J. Atmos. Solar-Terr. Phys., 83, 1

Riley, P., Linker, J. A., & Mikić, Z. 2001, J. Geophys. Res., 106, 15889

Riley, P., Lionello, R., Linker, J. A., Mikic, Z., Luhmann, J., & Wijaya, J. 2011, Solar Phys., 145

—. 2012b, Solar Phys., 274

Riley, P., Lionello, R., Mikić, Z., Linker, J., Clark, E., Lin, J., & Ko, Y.-K. 2007, Astrophys. J., 655, 591

Riley, P., & Luhmann, J. G. 2012, Solar Phys., 277, 355

Riley, P., Mikic, Z., Linker, J. A., Harvey, J., Hoeksema, T., Liu, Y., Ulrich, R., & Bertello, L. 2009, Submitted to Astrophys. J.

Schrijver, C. J., Livingston, W. C., Woods, T. N., & Mewaldt, R. A. 2011, Geophys. Res. Lett., 38, 6701

Schröder, W. 1992, J. Geomagn. Geoelectr, 44, 119

Schwadron, N. A., Connick, D. E., & Smith, C. 2010, Ap. J. Lett., 722, L132

Siscoe, G. L. 1980, Reviews of Geophysics and Space Physics, 18, 647

Smith, E. J., & Balogh, A. 2008, Geophys. Res. Lett., 35, 22103

Smith, E. J., & Marsden, R. G. 2003, Geophys. Res. Lett., 30, 1

Solanki, S. K., Usoskin, I. G., Kromer, B., Schüssler, M., & Beer, J. 2004, Nature, 431, 1084

Soon, W., & Yaskell, S. 2003, Maunder Minimum: And the Variable Sun-Earth Connection (World Scientific Publishing Company Incorporated)

Sporer, E. 1887, Vierteljahrsschr. Astron. Ges. Leipzig, 22, 323

Steinhilber, F., Abreu, J. A., Beer, J., Brunner, I., Christl, M., Fischer, H., Heikkilä, U., Kubik, P. W., Mann, M., McCracken, K. G., et al. 2012, Proceedings of the National Academy of Sciences, 109, 5967

Stevens, M., Linker, J. A., & Riley, P. 2012, J. Atmos. Solar-Terr. Phys., in press

Suess, S. T. 1979, Plan. Space Sci., 27, 1001

Svalgaard, L. 2010, ArXiv e-prints

Svalgaard, L. 2011, Proceedings of the International Astronomical Union, 7, 27

Svalgaard, L., & Cliver, E. W. 2007, Astrophys. J. Lett., 661, 203

Usoskin, I. G. 2008, Living Reviews in Solar Physics, 5, 3

Usoskin, I. G., Bazilevskaya, G. A., & Kovaltsov, G. A. 2011, Journal of Geophysical Research (Space Physics), 116, 2104

Usoskin, I. G., Solanki, S. K., Schüssler, M., Mursula, K., & Alanko, K. 2003, Physical Review Letters, 91, 211101

Wang, Y.-M., & Sheeley, N. R. 1995, Astrophys. J. Lett., 447, L143

Wang, Y.-M., & Sheeley, Jr., N. R. 2013, Ap. J., 764, 90

Wing, V. 1656, Astronomica Instaurata, Or, A New and Compendious Restauration of Astronomie: In Four Parts ... Whereunto is Added, a Short Catalogue of All the Most Accurate and Remarkable Coelestiall Observations, that Have Been Made by Tycho, Longomontanus, Gassendus, the Landgrave of Hassia, and Others (R. and W. Leybourn)

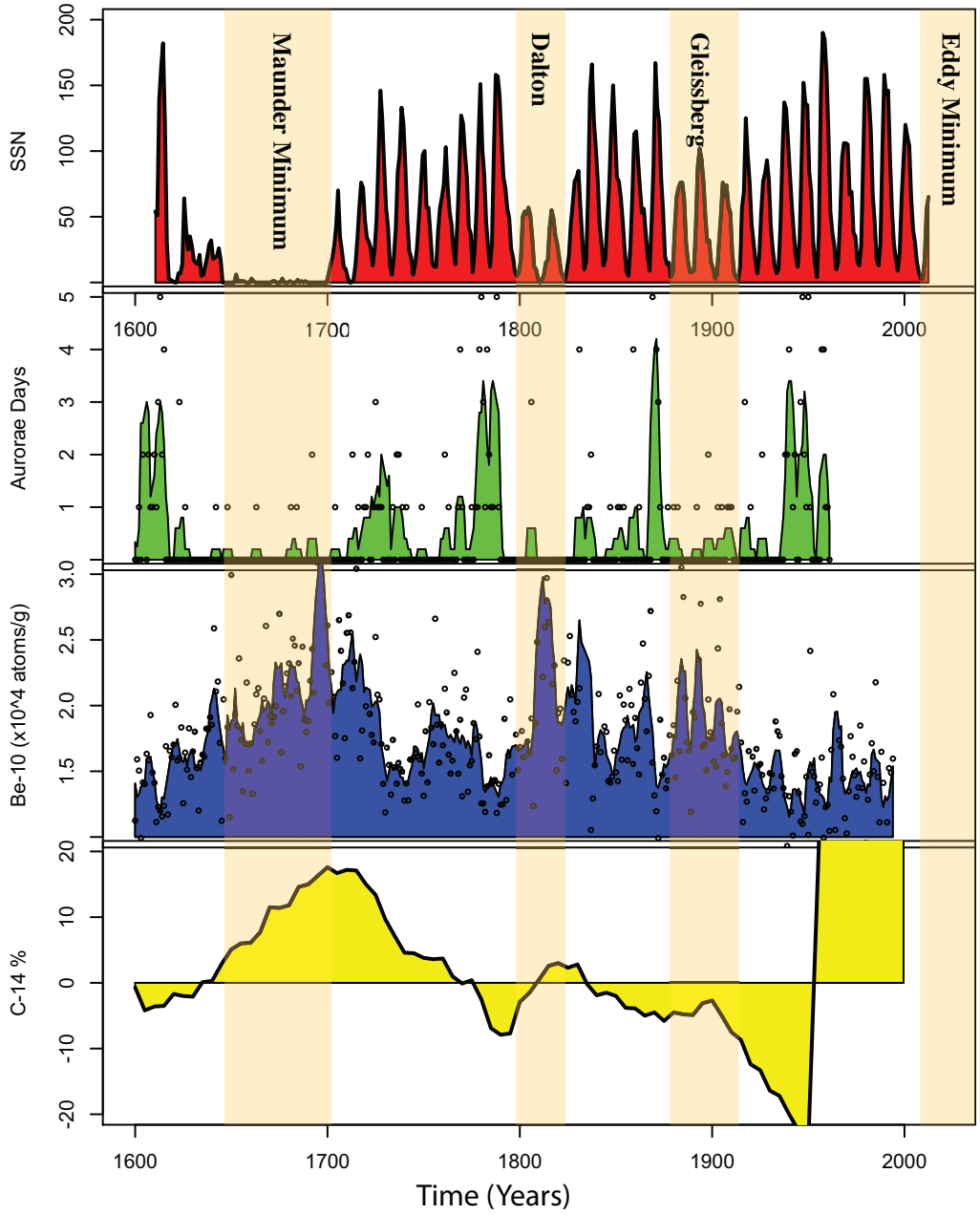

Fig. 1.— The evolution of various solar-related parameters from 1600 through 2012. (a) the yearly sunspot number (Svalgaard 2010). (b) the number of aurora per year (Réthly & Berkes 1963). (c) Beryllium-10 measurements (Berggren et al. 2009). (d) Carbon-14 measurements (Reimer et al. 2004) . See text for more details.

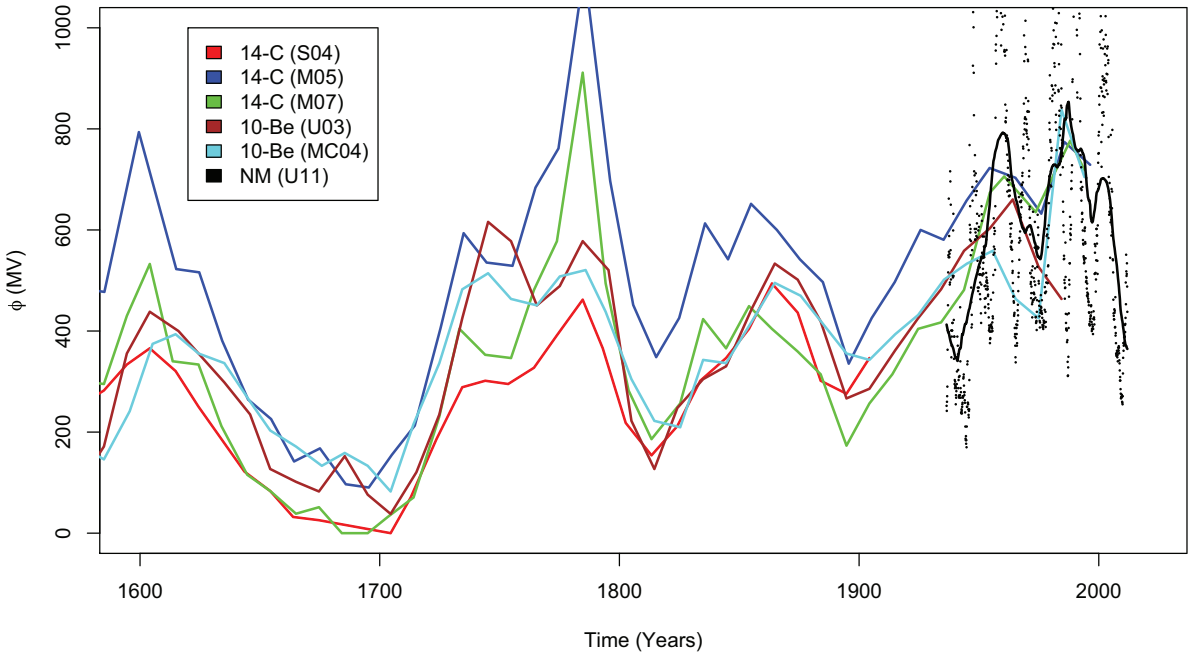

Fig. 2.— Temporal evolution of a selection of estimates for the modulation potential (ϕ). Following Usoskin (2008), S04 refers to Solanki et al. (2004), M05 refers to McCracken et al. (2005), M07 refers to McCracken & Beer (2007), U03 refers to Usoskin et al. (2003), MC04 refers to McCracken et al. (2004), and U11 refers to Usoskin et al. (2011). The first three profiles are based on Carbon-14 records, the next two are based on Beryllium-10, and the final profile shows direct neutron monitor measurements both on monthly averages (dots) and an 11-year running mean (solid black curve).

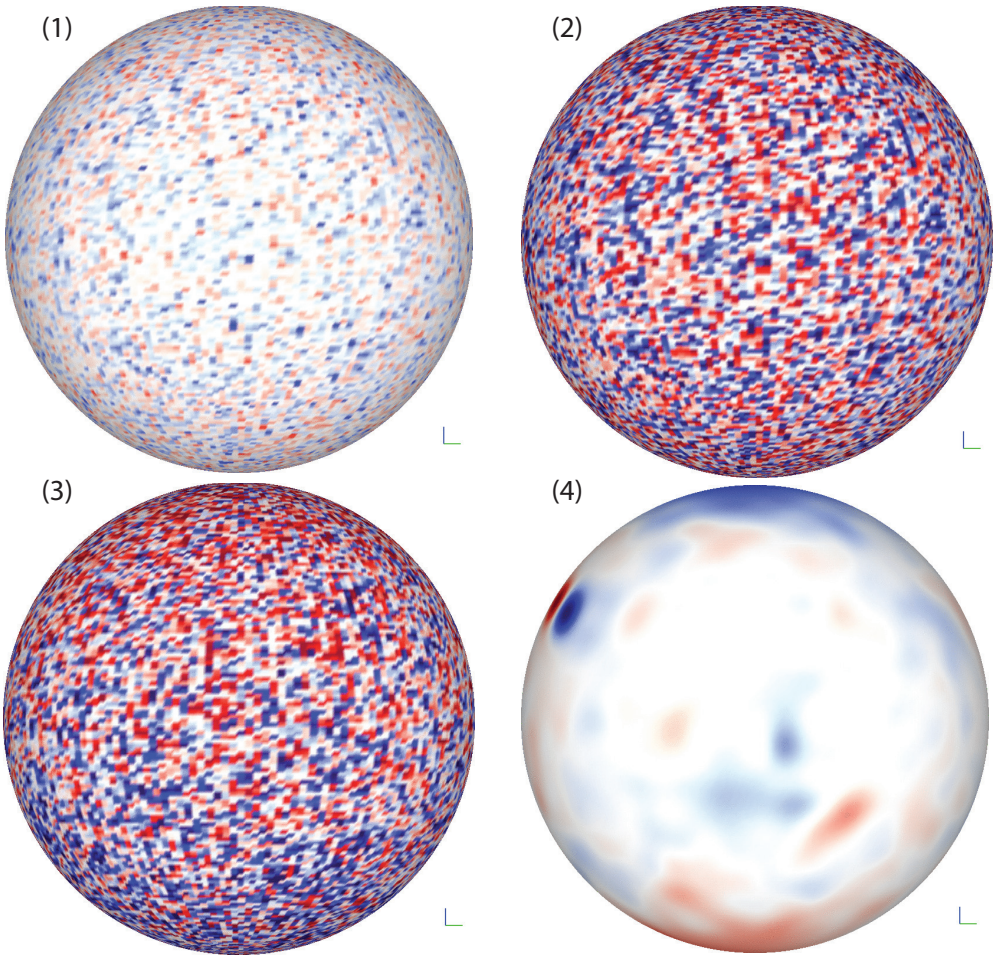

Fig. 3.— Comparison of possible configurations of the Sun's photospheric magnetic field during the Maunder Minimum period. (Top Left) Scenario (1): CR 2072. (Top Right) Scenario (2): A scaled version of the 2072 photosphere. (Bottom Left) Scenario (3): A photosphere composed entirely of ephemeral fields. (Bottom Right) Scenario (4): The complete absence of any photospheric magnetic field.

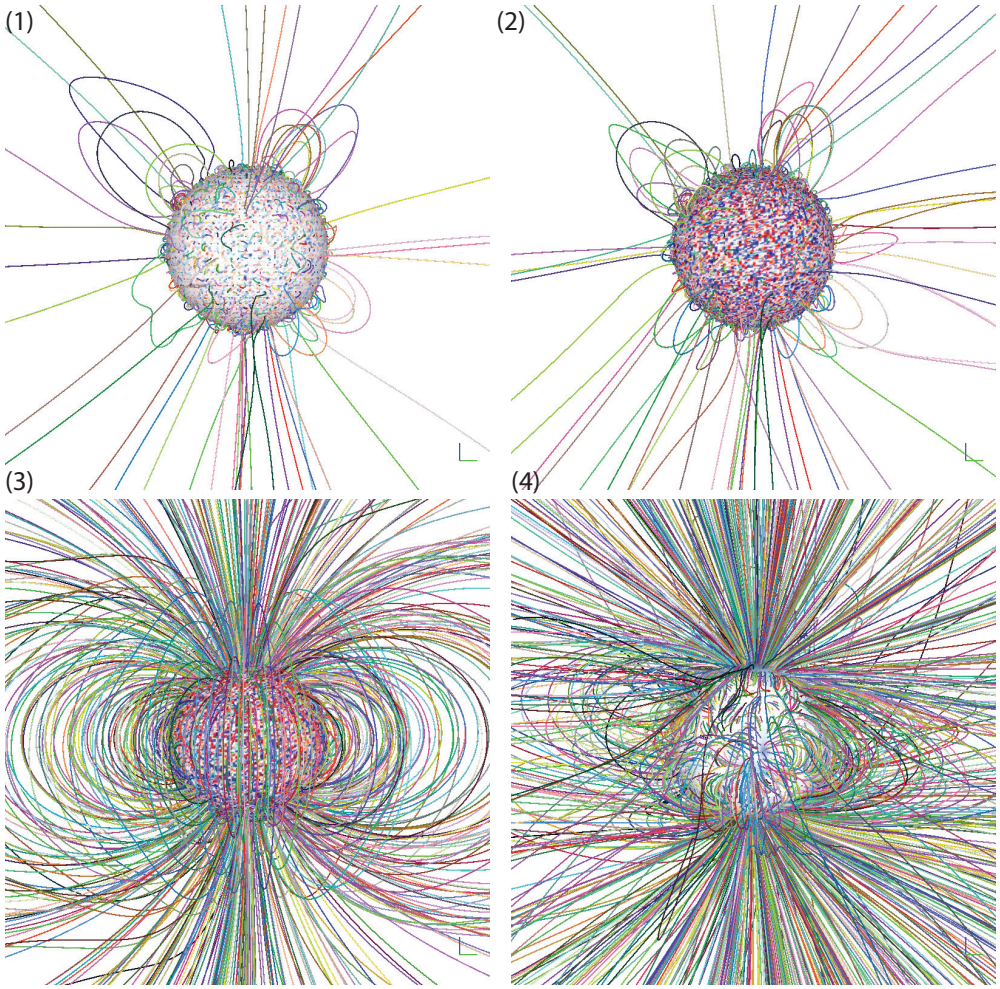

Fig. 4.— As Figure 3 but showing a selection of magnetic field lines drawn from a grid separated by 10° in latitude and longitude.

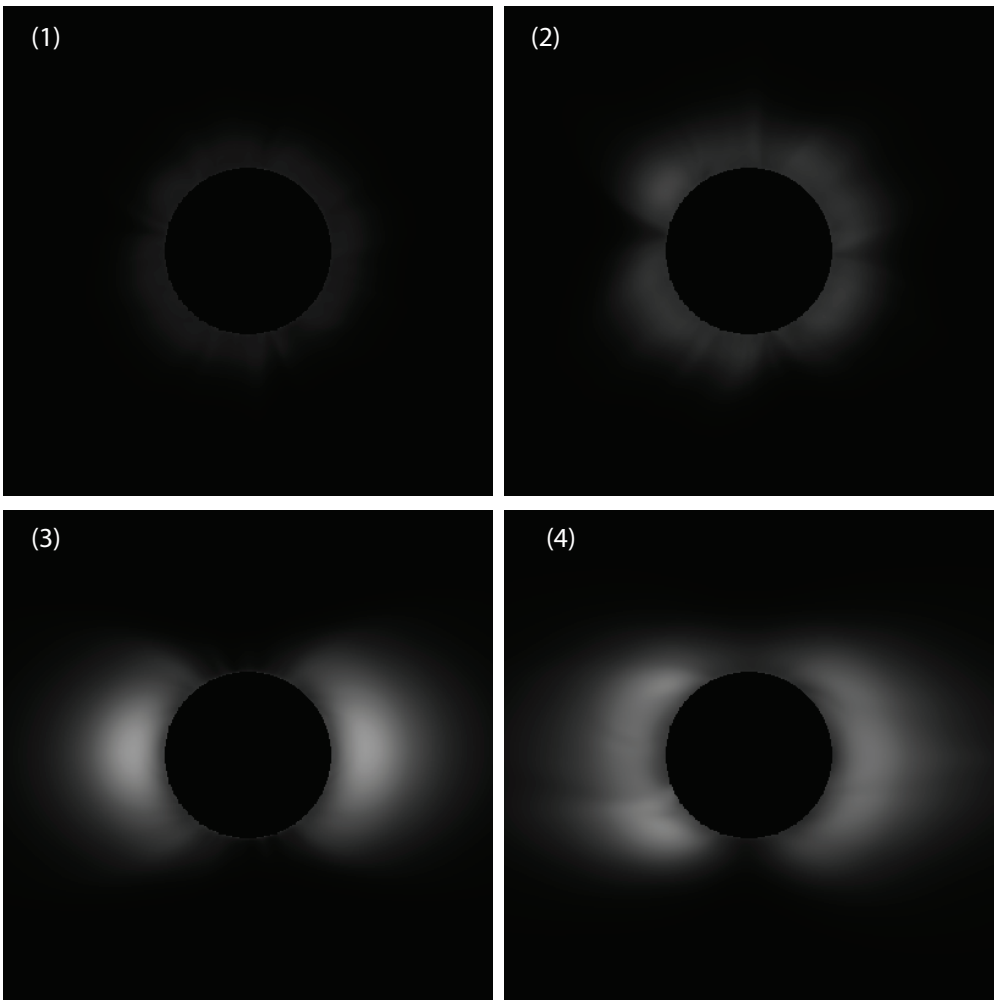

Fig. 5.— As Figure 3 but showing simulated polarized brightness.

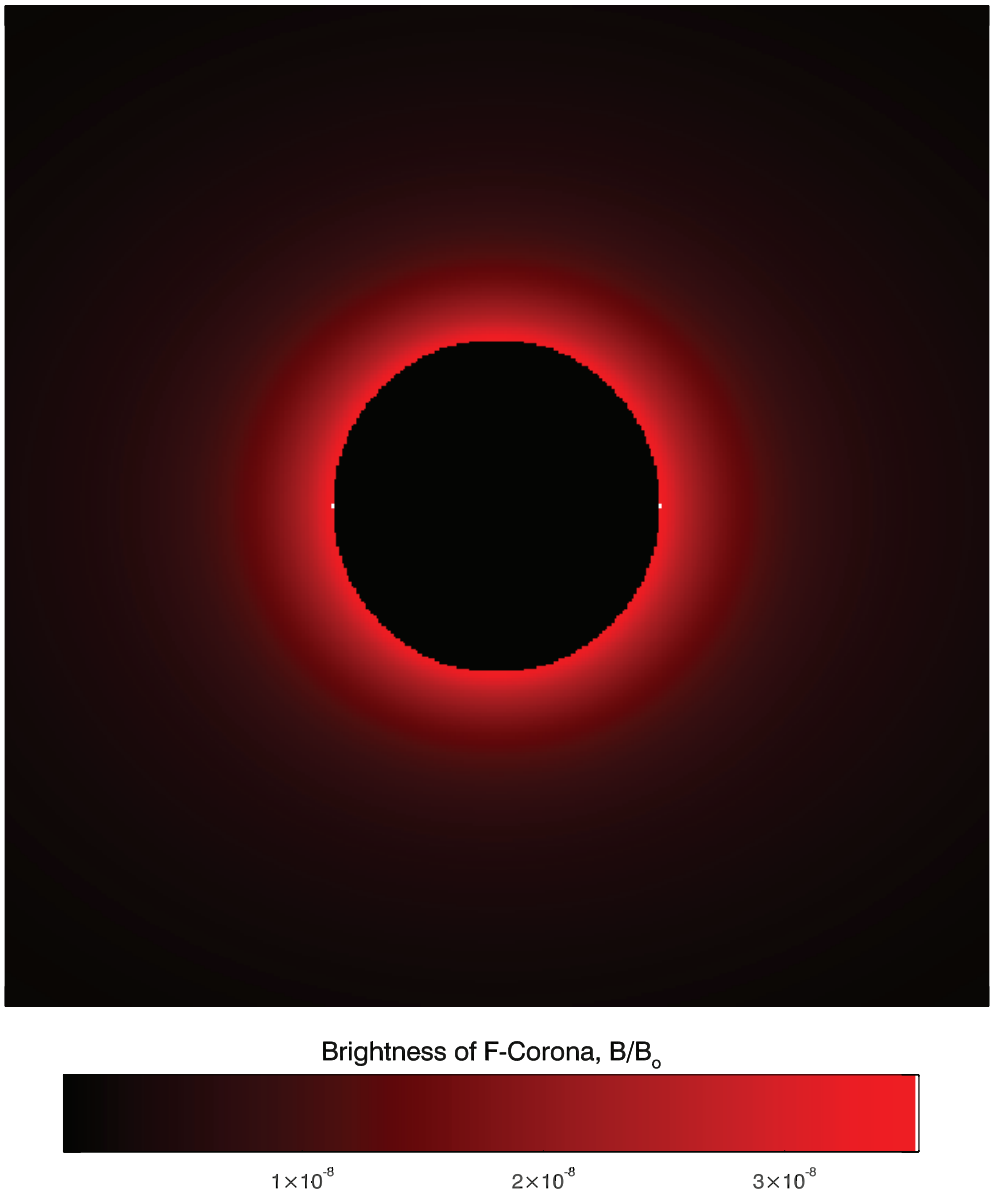

Fig. 6.— Simulated image of the F corona, based on the formula by Koutchmy & Lamy (1985).

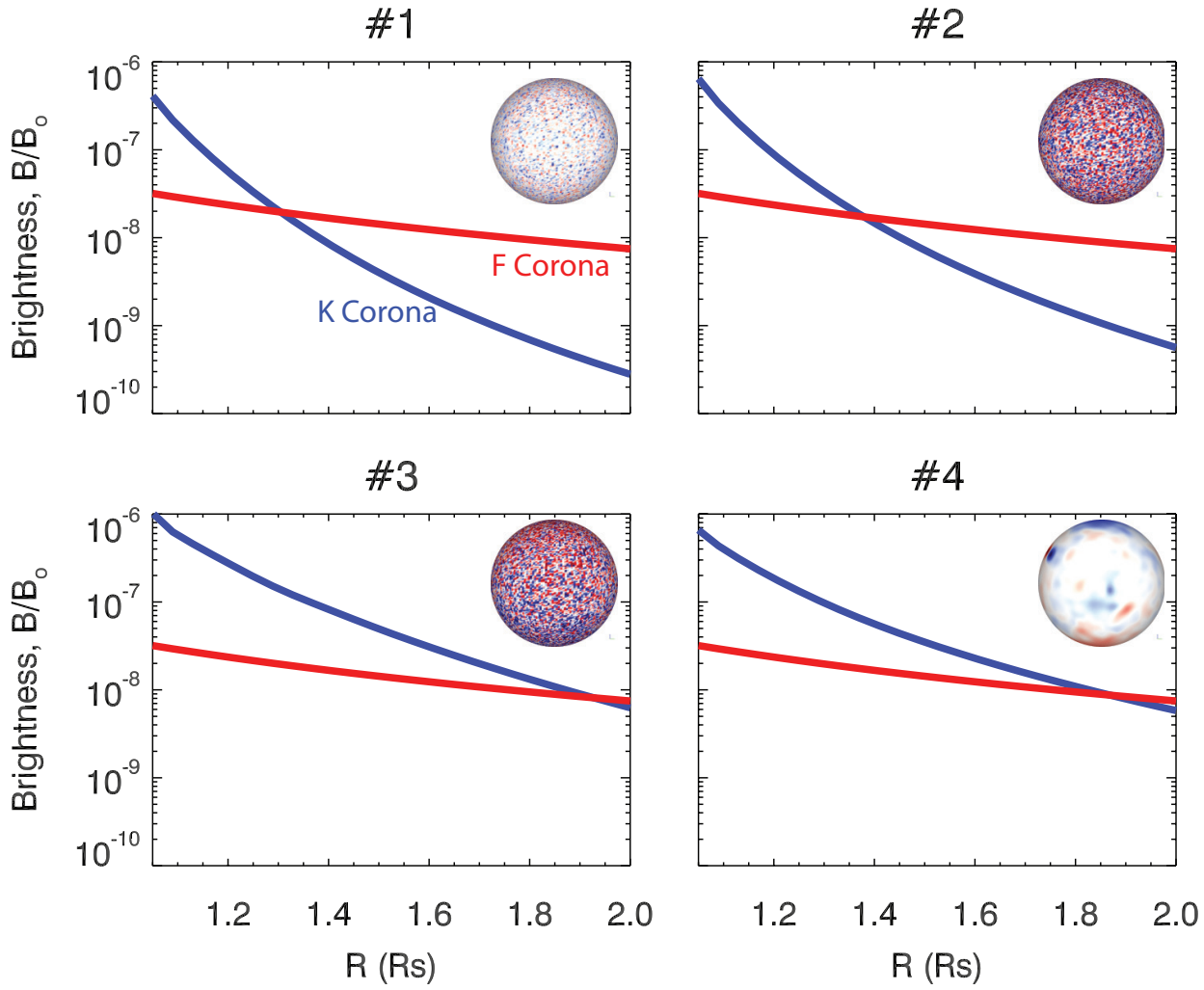

Fig. 7.— Comparison of radial fall-off in brightness for (a) CR 2072 and (b) a 1/10-th scaled version of CR 2072. The K-corona is colored blue and the F-corona is colored red.

Table 1: Open flux estimates.

Model	Description	Open Flux
1	Parasitic polarity only (±3.3 G)	0.08 nT
2	Parasitic polarity only (±10 G)	0.3 nT
3	Parasitic polarity + large-scale dipole	1.9 nT
4	CR 2085 (06/26/09-07/23/09)	1.0 nT

Table 2: Summary of observational evidence for each of two possible MM scenarios.

Observation	2008 Sun	Ephemeral Sun	Notes
SSN	×	✓	Strictly speaking, 2008/2009 cannot represent ∼ 1700 because sunspots were not absent for the last 70 years.
Aurora	?	✓	Difficult to assess because historical records are not currently maintained, and current measures are limited to space era.
^{10}Be	×	✓	When coupled with neutron monitor measurements and converted to modulation potential, 2008 was significantly different than 1700.
^{14}C	×	✓	Unfortunately, natural ^{14}C measurements cannot be extended beyond 1950.
Coronal Structure	×	✓	Eclipse observations during MM are not unambiguous. However, argument can be made that a 2008 eclipse would have been noted.
Red Glow	×	✓	Reports of an "erie" red glow are suggestive of an F-corona (and commensurately fainter, or absent K-corona).
22-year Periodicity	✓	×	Continued solar cycle suggests that circulation still proceeding, implying that polar fields build-up and decay.